

NORTHWESTERN UNIVERSITY

Utilizing Spin-Orbit Coupling to Manipulate the Properties of Inorganic Compounds

A DISSERTATION

SUBMITTED TO THE GRADUATE SCHOOL
IN PARTIAL FULFILLMENT OF THE REQUIREMENTS

for the degree

DOCTOR OF PHILOSOPHY

Field of Chemistry

By

Tyler James Pearson

EVANSTON, ILLINOIS

March 2021

ABSTRACT

Spin-orbit coupling (SOC) underlies myriad phenomena in chemistry and physics. Arbitrary manipulation of spin-orbit coupling would enable precise control over such parameters as magnetic anisotropy, the sensitivity of quantum sensors, and even the selectivity of certain catalytic processes. Herein, I describe my efforts directed towards utilizing SOC as a handle to tune the properties of both molecular magnets as well as both molecular and solid-state defect-based quantum bits. Chapter one provides a discussion of how SOC might be manipulated and a summary of our approach towards tuning it. Chapter two discusses an early success in enhancing magnetic anisotropy in a heterobimetallic molecular complex. Chapter three and four describe some insights that we gained throughout our study of transition metal-main group heterobimetallics featuring direct bonds between transition metals and main group metals.

Chapters five and six describe my efforts to understand the role of spin-orbit coupling both in molecular and solid-state quantum bits. Chapter five details my early exploration of the coherence properties of two octacyanometallate ions with successively higher spin-orbit coupling constants. Chapter six describes my work in examining the relationship between specific phonon modes and the coherence properties of oxygen-deficient double perovskites.

ACKNOWLEDGEMENTS

First and foremost, I would like to thank my amazing doctoral advisor, Danna Freedman. Her commitment to my scientific development was instrumental in my becoming the well-rounded scientist I am today. Her attention to and support of my mental health warrants particular mention. I never felt afraid to tell Danna when I was struggling, and for that I cannot thank her enough. I would also like to thank my candidacy committee, Professors Thomas Meade, Chad Mirkin, and Mercuri Kanatzidis for their thoughtful comments throughout my candidacy exam. Professors Mirkin and Meade continued to serve on my thesis committee and helped me immeasurably with learning to write effective research proposals.

My mentors, coworkers, and friends were constant sources of inspiration and motivation for me throughout my time at Northwestern. Majed Fataftah, Scott Coste, Ryan Klein, Samantha Clarke, and Michael Graham, Joe Zadrozny, and James Walsh turned the Freedman group into the productive learning and research environment that it is today. I'm proud to be graduating as a member of such an esteemed group of people and to have been able to share time in the Freedman lab with this group. Sharing the office with Majed, Scott, and Ryan was the adventure of a lifetime and immeasurably aided my growth as an experimentalist. Raymond Yu, who joined the Freedman group exactly when I did, was always there for me when I needed someone to bounce ideas off or when I needed to complain about something. Chats over strong drinks with Raymond were something of a staple of my time in graduate school, and I cannot thank him enough for being there for me. I am happy to be leaving the Freedman group in the hands of such an enthusiastic and intelligent bunch of people as my younger and more recent colleagues. Mikey Wojnar, Stephen von Kugelgen, Alison Altman, Kelsey Collins, Alexandra Tamerius, Jeremy Amdur, Dan Laorenza, Stephanie Petry, Eric Reisel, and Rianna Greer are some of the best colleagues anyone

could ask for and give me confidence that the Freedman lab is looking at many rich years of scientific productivity down the line.

Much of my work and training would not have been possible without the help of fantastic collaborators. Some of these include Dr. Matthew Krzyaniak, Prof. Michael Wasielewski, Prof. Tyrel McQueen, and Ms. Mekhola Sinha. Almost everything I know about EPR is thanks to Matt. I also want to thank the people who ran facilities I used, in particular Toby Woods and Mark Nilges at UIUC and Candice Klug at MCW. I've had a fantastic time learning a lot of beamline science throughout my PhD. Michael Hu at APS was a phenomenal resource on NRIXS and NRFS, and Alpha N'Diaye at ALS was very helpful for learning XAS and XMCD. It's a shame that some of these studies got cut short due to COVID.

I would be nowhere in life without my fantastic friends. Firstly, I would like to thank the people who were there in the trenches with me. Rebecca Sponenburg, Penelope, and Bento were always a particularly welcome sight to come home to and all were able to get me through anything that graduate school life could throw at me. Jason Khoury, Tyler Slade, and Daniel Chica were fantastic friends from day one, and I'll cherish our football watching parties and bar hangouts forever. I'd be remiss if I didn't also mention the people on the outside who got me through too, particularly Colin Dunn, David Shatan-Pardo, Tim Caradonna, and Junesoo Seong. Finally, I'd like to thank my friends in the Evanston Running Club who welcomed me with open arms and provided me a much-needed outlet in Evanston outside of the bubble of the chemistry department. I want to make extra special mention of my fantastic partner, Laura Jewell, who has been an amazing companion and a constant source of love and support.

During long hours at the bench and commuting, I ended up listening to a lot of Not Another D&D Podcast. It's not the only reason I was able to finish a PhD with my sanity (mostly) intact

but having a constant source of laughs when I was riding the purple line home at night was definitely an important part. Special shout out to the two crew, and thanks from the bottom of my heart to Murph, Emily, Jake, and Caldwell for being awesome. Keep up the Bon Frère behavior.

Finally, I want to thank my family, especially my parents. I cannot remember a time in my life where my parents were not completely supportive of me and my interests, both artistic, scientific, or personal. My dad was at every track and cross country meet holding a stopwatch calling out my splits for me. My parents would drive eight hours (one way!) from Richmond to New Haven multiple times a year while I was an undergraduate to see the YSO concerts in person. I'm blessed beyond belief to have them. I also want to especially thank my dad for being my original inspiration to become a scientist. His constant indulgence of my curiosity as a kid was crucial in keeping me engaged and interested in science as I got older.

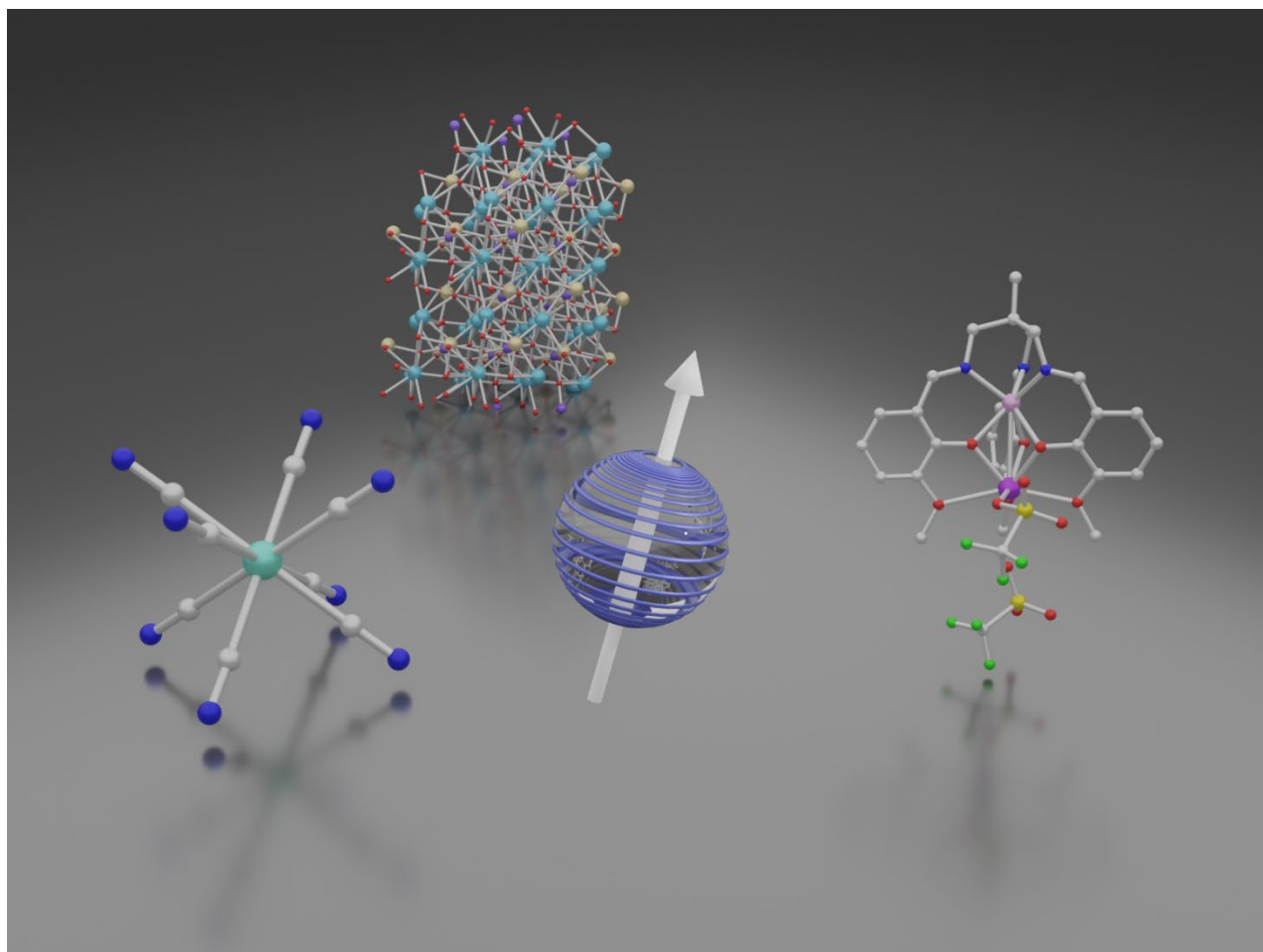
*To my friends,
my family,
the loft, the red couch, and the lap of shame*

TABLE OF CONTENTS

CHAPTER ONE: INTRODUCTION	9
The phenomenon of spin-orbit coupling	10
Harnessing spin-orbit coupling to create magnetically anisotropic compounds	11
Spin-orbit coupling as a design parameter in quantum information	12
CHAPTER TWO: ENHANCEMENT OF MAGNETIC ANISOTROPY IN A MN–BI HETEROBIMETALLIC COMPLEX	14
Introduction:	15
Results and Discussion:	18
Conclusions:	21
Supplementary Information:.....	23
CHAPTER THREE: MAGNETIC ANISOTROPY IN HETEROBIMETALLIC COMPLEXES	32
Introduction	33
Measuring spin-orbit coupling.....	35
Trends within analogous ligand fields.....	36
From ligand-based effects to heterobimetallic complexes	38
SOC transfer via direct, covalent bonding.....	40
Towards interactions between spin and heavy ligand orbitals	44
Experimentally deconvoluting the influences of ligand geometry and SOC	48
Conclusions and Outlook.....	51
Supplementary Information.....	53
CHAPTER FOUR: ORBITAL ENERGY MISMATCH ENGENDERS HIGH-SPIN GROUND STATES IN HETEROBIMETALLIC COMPLEXES	68
Introduction	69
Results and Discussion	70
Conclusions	78
Supplementary Information.....	80
CHAPTER FIVE: OCTACYANOMETALLATE QUBIT CANDIDATES	116
Introduction	117
Results and Discussion	118
Conclusions	124
Supporting Information	125
CHAPTER SIX: INTRODUCTION OF SPIN CENTERS IN SINGLE CRYSTALS OF BA₂CAWO_{6-δ}	155
Introduction	156
Experimental Section.....	158
A. Single crystal growth	158
B. Characterization	158
III. Results and Discussion	159
A. Single crystal growth	159
B. Crystal structure	161

C. Determination of the spin-state of the defect center	164
D. Pulse EPR measurements	164
IV. CONCLUSIONS	171
Supporting Information:	172
CHAPTER SEVEN: ORIGINAL RESEARCH PROPOSAL	196

Chapter One: Introduction



The phenomenon of spin-orbit coupling

As unpaired electrons orbit the nucleus, they generate orbital angular momentum. This orbital moment, L , couples with the spin moment, S , intrinsic to the electron. This interaction, termed the spin-orbit interaction, is responsible for myriad processes which are becoming increasingly important in both applied and fundamental chemistry and physics.¹ Permanent magnetism,² quantum coherence,³ non-trivial topology,⁴ intersystem crossing,⁵ and even catalytic selectivity⁶ are all determined at least in part by the strength of spin-orbit coupling. Thus, finding new ways to arbitrarily manipulate the spin-orbit coupling of paramagnetic transition metal species presents an extremely important research question. My focus has been on manipulating the properties of magnetic transition metal complexes and materials for use in permanent magnetism and as quantum bits through manipulating the degree of spin-orbit coupling which they experience.

When a spin-bearing ion experiences a ligand field – which is almost always the case outside of extreme laboratory conditions⁷ or in interstellar space – the orbitals split in energy. The difference in the ways the orbitals interact with the ligands results in the canonical crystal field splitting in transition metal complexes. A further consequence of this interaction is that the degeneracy of the spin-bearing orbitals is broken, which causes the orbital moment to become quenched. Recently, chemists have discovered that engineering near degeneracy between orbitals related by the L_z operator can unquench orbital angular momentum enough to manifest in slow magnetic relaxation and even magnetic hysteresis.⁸ Such systems with these engineered degeneracies have become well studied in recent years.⁹ Our approach to controlling the magnetic properties attempts to circumvent the precise ligand field engineering required in this approach by utilizing a completely different paradigm. Crucial to our approach is the fact that SOC approximately scales with the square of the effective nuclear charge, Z_{eff}^2 .¹⁰ Therefore, heavier

elements on the periodic table have much higher spin-orbit coupling constants than lighter elements. Thus, we hypothesize that a system wherein we have successfully reconstituted a spin-orbit coupled system will result in high magnetic anisotropy. This proxy for spin-orbit coupling is, conveniently, easy to measure using routine electron paramagnetic resonance spectroscopy and SQUID magnetometry, and therefore the synthesis of magnetically anisotropic complexes is where we started our study of spin-orbit coupling transfer.

Harnessing spin-orbit coupling to create magnetically anisotropic compounds

One area in which we seek to utilize spin-orbit coupling is in the creation of magnetically anisotropic systems. We theorize that by separating the two components of magnetism between two atomic sites – one site to supply the spin moment, and another to supply a high degree of spin-orbit coupling to the system – we can reconstitute a spin-orbit coupled system. As unquenched spin-orbit coupling is crucial in generating high magnetic anisotropy, we anticipated being able to see such transferral of spin-orbit coupling in the magnetic data we collected. We utilized heterobimetallic molecular complexes to study this phenomenon because they allow us to independently tune each of these two components of spin-orbit coupling. Herein, we supply the spin moment using high-spin first row transition metals and we supply the orbital moment to the system by introducing extremely heavy elements with high spin-orbit coupling constants into proximity with the electronic spin.

Transition metals are ideal species to test these hypotheses because they supply almost no intrinsic orbital moment to the system. In transition metals, the unpaired electrons which generate spin-orbit coupling are housed in the d-orbitals which interact strongly with the ligand field causing them to split in energy. This non-degeneracy between the d-orbitals effectively quenches the orbital moment in transition metal complexes. This allows us to separately supply a purely

spin-based moment from an orbitally quenched transition ion and a pure orbital moment from a heavy diamagnetic metal center.

Spin-orbit coupling as a design parameter in quantum information

Quantum information science (QIS) is a broad term which has come to dominate many sectors of chemistry and physics. It is an attempt to aggregate and unify the fields which utilize the quantum properties of matter to perform measurements or operations. Such fields as quantum computation, quantum sensing, quantum metrology, and quantum communication all fall under this umbrella term which has come to dominate the modern scientific literature.¹¹ All these fields rely upon the smallest unit of quantum information, the quantum bit. In analogy to classical bits, which process information by switching between on and off states (0 and 1, true or false, dead or alive, etc.), quantum bits, or qubits, process information fundamentally differently: by utilizing arbitrary superpositions of on and off states. In these systems the stability of the superposition is a primary design feature.¹² In systems for quantum computation, for example, quantum bits should have long, stable superpositions so that they do not decohere during gate operations. Over the years, scientists have discovered that insulating the spin from sources of magnetic noise such as other oscillating electronic or nuclear spins can result in extremely long coherence times. In sensing applications, however, such quantum bits are less useful because of the insulation which makes them good bits for quantum computation makes them much less useful as sensors. Therefore, the ability to tune the lifetimes of quantum bits is extremely important for tailoring them for specific applications. Spin-orbit coupling is an important contributor to the coherence time of quantum bits. As the spin-orbit coupling is increased, the spin interacts more strongly with its ligand field and therefore more strongly experiences the phonon bath of the matrix within which

it resides.¹³ Furthermore, increases in spin-orbit coupling cause the g -value to deviate from $g = 2$, which can result in increased sensitivity of the superposition to external interference.

In the following chapters, I present five studies united by their focus on manipulating and measuring the phenomenon of spin-orbit coupling. Throughout, we discover that the nature of the interaction between different metals and the relationship between the spin center and its environment are extremely important in the manifestation of spin-orbit coupling in the magnetic and coherence properties of paramagnetic species.

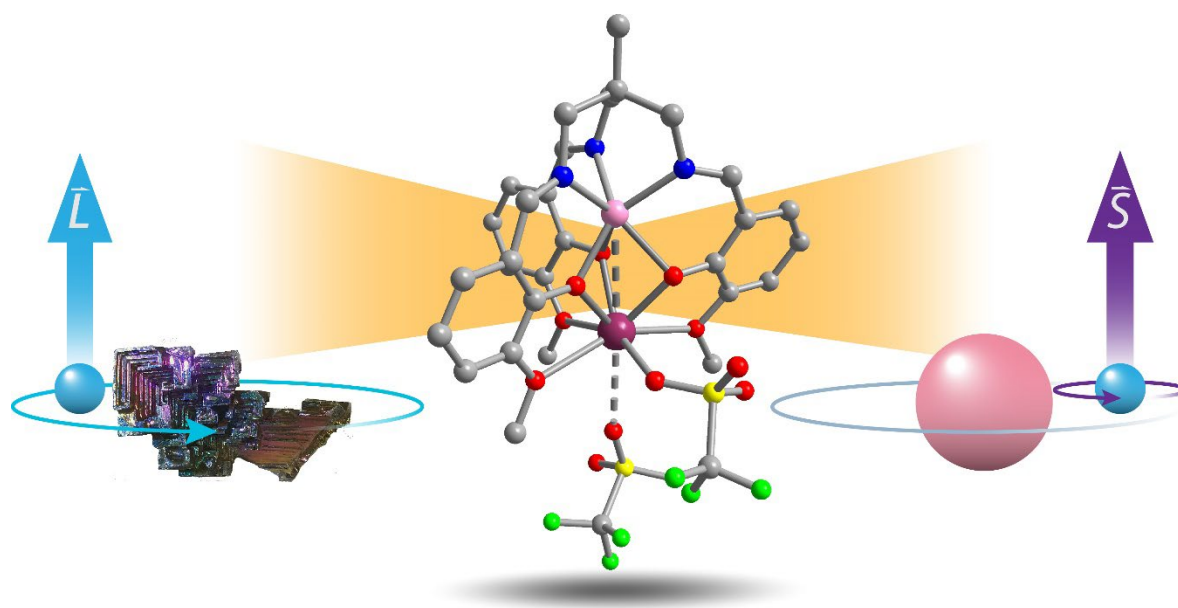
Chapter Two: Enhancement of magnetic anisotropy in a Mn–Bi heterobimetallic complex

Reprinted with permission from:

Pearson, T. J.; Fataftah, M. S.; Freedman, D. E. *Chemical Communications* **2016**, 52, 11394-11397.

Copyright 2016 Royal Society of Chemistry

This section was written in collaboration with the co-authors listed above



Introduction:

Spin-orbit coupling underlies a plethora of emergent phenomena in materials ranging from permanent magnets to exotic materials such as topological insulators.¹ Spin-orbit coupling, which scales as Z_{eff}^4 , arises from the interaction of the two components of a magnetic moment: the spin moment S , and the orbital moment, L . Typically, the spin moment and the orbital moment originate from the same atom, as observed in lanthanides, which possess a fully spin-orbit coupled ground state. Intriguingly, in a select number of systems, heavy diamagnetic atoms bound to spin centres enhance the observed magnetic anisotropy of the electronic ground state of the system. Spectroscopically, this phenomenon manifests in certain excited state dynamics by enhancing the rate of spin-forbidden processes. This well-characterised behaviour is known as the heavy atom effect.² Within the realm of magnetic molecular species, interactions between spin-based magnetic

moments and external sources of orbital angular momentum are largely confined to heavy halide species. From a combination of magnetometry, electron paramagnetic resonance (EPR) spectroscopy, and theoretical investigations, the halide's orbital contribution is well established.³ The aggregate of these studies suggests that the interaction of heavy main group elements with paramagnetic transition metals is a viable approach towards engendering magnetic anisotropy in transition metal complexes. Indeed, this design principle may prove crucial in constructing the next

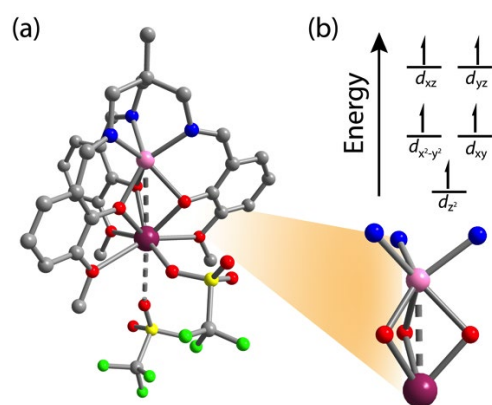


Figure 2.1. (a) The molecular structure of **2** as determined *via* single crystal X-ray diffraction. The dashed line highlights the metal-metal interaction of interest. Pink, purple, red, blue and grey spheres represent Mn, Bi, O, N, and C atoms respectively. Yellow and green spheres represent the sulfur and fluorine atoms of the triflate anions. Hydrogen atoms have been omitted for clarity. (b) Close-up view of the Mn²⁺(μ-O₃)Bi³⁺ interaction of interest as well as a qualitative diagram of the *d*-orbital splitting.

generation of permanent magnetic solid-state materials. Halides, however, are inherently limited in their potential for covalent interactions, thus limiting their contributions to the anisotropy of the electronic ground state. Expanding our synthetic repertoire from halides to other main group elements necessitates a fundamental study of the nature of the magnetic interactions between main group elements and transition metals. Herein, we report the synthesis, structure, and magnetic characterisation of a Mn^{2+} - Bi^{3+} heterobimetallic complex (Figure 2.1) which features a single, isolated $\text{Mn}\cdots\text{Bi}$ interaction at a distance of 3.2163(5) Å, the closest yet reported for a paramagnetic heterodinuclear molecular species. Within this complex the heavy main group element bismuth interacts with a spin-bearing ^6A manganese centre. This complex constitutes an initial step towards understanding the magnetic interaction of bismuth with transition metals.

An investigation of the impact of an orbital angular momentum-bearing diamagnetic element on a spin centre necessitates judicious selection of the proper spin carrier. The confluence of a high spin state, well suited to magnetic measurement, and an isotropic ground state recommend Mn^{2+} as the ideal candidate.⁴ Here, we utilise the zero-field splitting parameters (D and E) to quantify the enhancement of magnetic anisotropy in the ground state of the paramagnetic complex. These parameters arise primarily from mixing of low-lying electronic excited states into the ground state. The extent of mixing is primarily dictated by two factors: the energy separation between the states, and the spin-orbit coupling parameter (λ). Indeed for high-spin d^5 metal ions, such as Mn^{2+} , all electronic excited states require spin-flips, which are energetically prohibitive, thus limiting their contributions to the ground state. Therefore, the axial zero-field splitting, D , is very small in Mn^{2+} complexes, with the highest yet reported being 1.46 cm^{-1} in a five-coordinate polyoxotungstate complex.⁵ Furthermore, depending on the electronic configuration of the excited states, they may contribute both positive and negative values to D in Mn^{2+} complexes, further

restricting the magnitude of D in these species.⁶ In six-coordinate Mn^{2+} complexes, D is typically lowered by the increased strength of the ligand field, with D restricted to approximately 1 cm^{-1} .⁷ In complexes featuring primary coordination spheres consisting only of nitrogen and oxygen donors, D is limited even further, with the highest value reported being 0.32 cm^{-1} and with most values falling in the range of $0.0 - 0.1 \text{ cm}^{-1}$.^{8,9} From these data and supporting theoretical studies,¹⁰ spin-orbit coupling is deemed the dominant factor in generating magnetic anisotropy in Mn^{2+} complexes. Owing to the potential for spin-orbit coupling to modulate the anisotropy of Mn^{2+} ions more significantly than other factors, Mn^{2+} centres are particularly attractive probes for observing enhancement of magnetic anisotropy *via* transferral of spin-orbit coupling onto the Mn^{2+} spin centre. To investigate this phenomenon, we utilised bismuth, the heaviest, non-radioactive¹¹ element on the periodic table, whose spin-orbit coupling constant is thereby significantly higher than other elements.¹² To take full advantage of this high spin-orbit coupling, we incorporated a

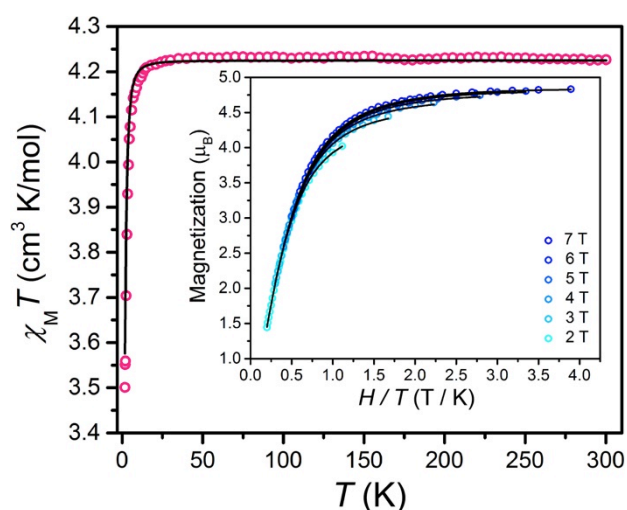


Figure 2.2. Variable temperature dc magnetic susceptibility plot under an applied field of 5000 Oe in the temperature range of 1.8 K to 300 K. Inset: Variable temperature, variable field magnetization data collected between 1.8 K and 10 K. The data were collected between 2 and 7 T in 1 T increments. The black lines in both plots are a simulation of the data with the parameters $D = 0.7 \text{ cm}^{-1}$ and $g_{\text{iso}} = 1.965$.

single Bi^{3+} ion into a Mn^{2+} complex. By creating a heterobimetallic complex featuring a close $\text{Bi}^{3+} \cdots \text{Mn}^{2+}$ contact, the transfer of spin-orbit coupling between the heavy diamagnetic ion and the spin-bearing ion could be indirectly observed through examination of the axial zero-field splitting parameter, D , of the Mn^{2+} centre.

Specifically, to examine this interaction in detail, we focused on molecular model complexes due to the

inherent tunability of molecular species, which renders them particularly attractive platforms upon which to study fundamental magnetic properties. Towards that end, we employed a ligand scaffold featuring two adjacent binding sites. One of these pockets is comprised of three neutral imine donors and three anionic phenolate donors. The coordination chemistry of this pocket is well established as there are several previously reported transition metal complexes of the ligand.¹³ The second pocket features the same three phenolate donors with three additional ethereal donors, which can accommodate a large ion. This oxygen-rich pocket is particularly favourable to Bi³⁺ binding given its oxophilicity. Previous magnetic characterisation of the monometalated Mn²⁺ complex of this ligand has established a benchmark for the magnetic parameters of the Mn²⁺ ion in the absence of Bi³⁺ coordination in the adjacent coordination pocket of the ligand scaffold.^{13a} Within this complex, bismuth interacts through a μ -O₃ bridge with a spin-bearing ⁶A₁ manganese centre. This complex constitutes an initial step towards understanding the magnetic interaction between bismuth and paramagnetic transition metals.

Results and Discussion:

Synthesis of the target complex proceeded *via* deprotonation of 1,1,1-tris[(3-methoxysalicylideneamino)methyl]ethane (**H₃L**) followed by *in situ* metalation with Mn(SO₃CF₃)₂. The sodium salt of the monometalated complex [Na⁺][LMn²⁺] (**1**) was isolated as an orange powder in 90% yield. Reaction of this complex with Bi(SO₃CF₃)₃ in THF resulted in precipitation of the target complex as a yellow powder. Recrystallization of the crude product gave the heterobimetallic product, [LMnBi][SO₃CF₃]₂ (**2**) in modest yield (33%).

Single-crystal X-ray diffraction studies enabled the determination of the molecular structure of **2** (see Figure 2.1). The complex crystallises in the triclinic space group P-1. The Mn²⁺ centre features coordination by three imine donors and by three phenolates in a nearly ideal trigonal

prismatic coordination geometry. The average Mn-N bond length is 2.157(5) Å, which is in good agreement with similar Mn²⁺ species reported in the literature.^{13a} The Mn-O bonds average 2.177(5) Å, comparable to other hetero bi- and trimetallic complexes of this type.^{13b} The distance between the two metal centres is 3.2163(5) Å, the shortest isolated paramagnetic Mn²⁺-Bi³⁺ interaction yet

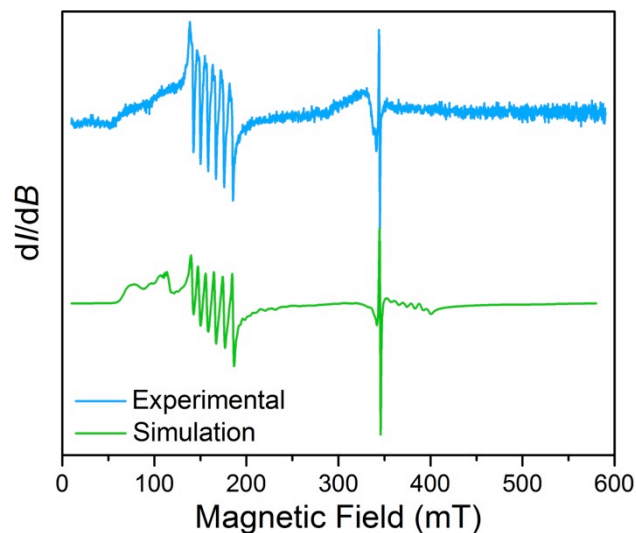


Figure 2.3. Overlay of the experimental (blue) cw-EPR spectrum of a 0.1 mM solution of **2** in butyronitrile collected at X-band frequency (9.63 GHz) at 20 K. The green trace is a simulation using the parameters described in the text.

reported. This proximity of the Mn²⁺ and Bi³⁺ centres prompted us to measure the magnetic properties of the complex, in pursuit of enhancement of the axial zero-field splitting parameter (D), which serves as a probe of the magnetic anisotropy at the Mn²⁺ centre. Initial

magnetic characterisation of **2** (Figure 2.2) proceeded via measurement of its variable temperature dc magnetic susceptibility. Its $\chi_M T$ value of 4.23 cm³ K/mol is slightly less than the spin-only value of 4.37 cm³ K/mol expected for an isotropic $S = 5/2$ species, but is consistent with the assignment of a high-spin d^5 Mn²⁺ ion with an isotropic g -value of 1.96. With decreasing temperature, the value of $\chi_M T$ remains constant until approximately 6 K, which is, again, consistent with a high-spin d^5 ion possessing small zero-field splitting.¹⁴ Below 6 K, contributions from the Zeeman effect and zero-field splitting result in a sharp decrease in the value of $\chi_M T$ to a value of 3.50 cm³ K/mol at 1.8 K.

In order to better quantify the axial and transverse zero-field splitting parameters (D and E), we collected variable-temperature, variable-field magnetisation data (Figure 2.2 inset). Plotting

the magnetisation data as a function of the ratio of field to temperature (H/T) reveals a small splitting between the isofield lines, signifying the presence of non-negligible zero-field splitting. The splitting is indicative of an easy axis of magnetisation, whereby in the absence of an internal magnetic field with preferred orientation, the isofield lines cleanly overlay. Quantification of the axial zero-field splitting proceeded via simulation of the magnetisation data with the Hamiltonian $\hat{H} = g_{\text{iso}}\mu_{\text{B}}\mathbf{S}\mathbf{H} + D[\hat{S}_z^2 - (S(S+1))/3]$ and the Van Vleck equation using the program DAVE 2.0,¹⁵ where D is the axial zero-field splitting, g_{iso} is the isotropic g -value, μ_{B} is the Bohr magneton, \mathbf{S} is the spin quantum number, and \mathbf{H} is the applied magnetic field. The best simulation to the data, presented in Figure 2.2, yielded the following parameters: $D = 0.70(2) \text{ cm}^{-1}$, $g_{\text{iso}} = 1.965(5)$. The dc magnetic susceptibility data were successfully modelled using these values (see Figure 2.2), providing further support for the assignment of these parameters.

Given the relatively small D values intrinsic to Mn^{2+} ions, magnetometry alone is not sufficiently sensitive towards the assignment of the sign of D , nor to any rhombicity (E/D) potentially exhibited by the complex. Thus, to corroborate the assignment and sign of the zero-field splitting parameters, we examined the complex via electron paramagnetic resonance (EPR) spectroscopy at X-band frequency. The spectrum shown in Figure 2.3 was collected on a dilute solution of **2** in a butyronitrile glass. The six-line hyperfine feature centred at 150 mT is indicative of coupling of electronic spin to the $I = 5/2$ ^{55}Mn nucleus. The spectrum was modelled using EasySpin¹⁶ with the following Hamiltonian, $\hat{H} = (g_x + g_y + g_z)\mu_{\text{B}}\mathbf{S}\mathbf{H} + \mathbf{A}\mathbf{I}\mathbf{S} + D[\hat{S}_z^2 - (S(S+1))/3] + E(\hat{S}_x^2 - \hat{S}_y^2)$, where g_i ($i = x, y, \text{ and } z$) are the g -values along the principal x -, y -, and z -directions, \mathbf{A} is the hyperfine coupling tensor, \mathbf{I} is the nuclear spin, E is the transverse zero-field splitting, and the remaining parameters retain their previous definitions. The best simulation provided the following parameters: $g[x,y,z] = [1.95(3), 2.00(3), 2.20(5)]$ $A[x,y,z] = [240(5), 240(5), 50(5)]$

MHz, $D = 0.74(2) \text{ cm}^{-1}$, $E = 0.0505(5) \text{ cm}^{-1}$. These values obtained from simulating the cw-EPR spectrum are an excellent match with those obtained from SQUID magnetometry.

Complexes of Mn^{2+} in analogous N_xO_y primary coordination spheres typically feature very low spin-orbit coupling. This D value of 0.7 cm^{-1} is notably large for Mn^{2+} in a 6-coordinate N_xO_y environment,⁹ with the highest previously reported for Mn^{2+} in such an environment being 0.32 cm^{-1} , as observed for a Mn^{2+} ion in a trigonal prismatic clathrochelate.⁸ The differences in ligand spheres (N_6 vs. N_3O_3) in these six-coordinate N_xO_y complexes have little influence on the D values they exhibit.⁹ This value of D is markedly higher than that of the previously reported monometallated Mn^{2+} complex as well, which exhibits a D value of 0.168 cm^{-1} .^{13a} While the geometry about the spin centre does change between the monometalated complex and the heterobimetallic, these subtle changes in coordination geometry have only minor influences on the D -values of Mn^{2+} ions and do not account for the substantial increase we observe in D . Observation of a D value approximately double the previously-reported highest value for an analogous complex (see ESI, Figure S2.2) indicates that enhanced spin-orbit coupling, originating from the secondary coordination sphere, plays a significant role in enhancing the zero-field splitting parameters for Mn^{2+} in **2**, as further supported by the deviation in g from the free-electron value of 2.0 expected for Mn^{2+} . Note, there are values of D up to 1 cm^{-1} for six-coordinate Mn^{2+} complexes.⁷ However, these complexes typically feature direct coordination by heavy halides, such as iodide and bromide, which encourage high D values owing to their weak ligand field strength and the heavy atom effect, which contributes spin-orbit coupling to the electronic ground state of the Mn^{2+} ion.

Conclusions:

Discovering new ways to enhance magnetic anisotropy is of crucial importance for improving and expanding technologies that rely on permanent magnetic materials. To this end, we

have synthesised and characterised a Mn-Bi heterobimetallic complex which exhibits zero-field splitting values significantly larger than those previously reported for Mn^{2+} ions in similar primary coordination spheres. We hypothesise that Bi^{3+} proximity to the Mn^{2+} spin centre within the complex is the underlying cause for the observed enhancement, even in the absence of direct metal-metal bonding. These results have further implications for the study of bulk transition metal oxides, the properties of which have been hypothesised to be influenced by the anisotropy of the transition metal sites comprising the lattice.¹⁷ Understanding the transferral of spin-orbit coupling between heavy elements and transition metals could shed light on the interesting and useful properties of mixed-metal systems, such as BiMnO_3 and BiFeO_3 .

Supplementary Information:

General Considerations. Manipulations of all compounds were performed under a dinitrogen atmosphere in a Vacuum Atmospheres Nexus II glovebox unless otherwise specified. Glassware was either oven-dried at 150 °C for at least 4 hours or flame-dried prior to use. Acetonitrile (MeCN), diethyl ether (Et₂O), tetrahydrofuran (THF), and dichloromethane (DCM) were dried using a commercial solvent purification system from Pure Process Technology and stored over 3 or 4 Å molecular sieves prior to use. Methanol (MeOH) was also dried and degassed on the solvent system, but was distilled prior to use to remove residual sieve dust. Butyronitrile was distilled from CaH₂, degassed via three consecutive freeze-pump-thaw cycles, and stored over 4 Å molecular sieves prior to use. 1,1,1-tris(aminomethyl)ethane hydrochloride (TAME*3HCl) was prepared by the method described by Ralph et. al.¹⁸ All other reagents were used as received.

[1,1,1-tris[(3-methoxysalicylideneamino)methyl]ethane] (H₃L). An adaptation of a literature procedure was used to isolate **H₃L**.¹⁹ In air, TAME*3HCl (1.28 g, 5.6 mmol) was stirred into a slurry in 100 mL MeOH in a 500 mL round bottom flask. To this slurry 100 mL of a MeOH solution of NaOH (0.72 g, 18.1 mmol) was added. This solution was allowed to stir for approximately 10 minutes until the solution turned clear and colorless. A 70 mL MeOH solution of *ortho*-vanillin was then added (2.57 g, 16.9 mmol). After being allowed to stir for 2 hours, the solvent was removed *in vacuo* and the residue was extracted with 50 mL DCM. This extract was vacuum filtered to remove precipitate. The solution was subsequently filtered again through a pad of celite. The DCM was then removed *in vacuo* to yield a yellow powder. 1.88 g (3.6 mmol, 64% yield). ¹H NMR (500 MHz, dimethyl sulfoxide-*d*₆) – δ 1.06 (s, 3H, CH₃), 3.62 (s, 6H, CH₂), 3.29 (s, 9H, CH₃), 6.83 (t, *J* = 8 Hz, 3H, Ar-CH), 7.03 (d, *J* = 8 Hz, 3H, Ar-CH), 7.06 (d, *J* = 8 Hz, Ar-CH), 8.58 (s, 3H, CH), 13.65 (br s, 2H, Ar-OH)

[Mn^{II}(L)Bi^{III}](OTf)₂. In a 20 mL vial in an N₂ glovebox 144.3 mg (0.28 mmol) of **H₃L** was dissolved in 6 mL THF and stirred. To this mixture was added a solution of 46.4 mg (0.86 mmol) NaOMe in 3 mL MeOH. This was allowed to stir for 30 minutes. After 30 minutes, a solution of 99.1 mg (0.28 mmol) Mn(OTf)₂ in 3 mL MeOH was added. The yellow solution gradually turned orange, and was permitted to stir overnight. The next day, the solvent was removed in vacuo to yield an orange powder. This powder was taken up in 5 mL DCM, filtered through a plug of celite, and then the DCM was removed *in vacuo*. This residue was then dissolved in 5 mL THF and, while stirring, a solution of 182.8 mg (0.28 mmol) Bi(OTf)₃ in 3 mL THF was added dropwise. This reaction was allowed to proceed overnight. The next day, the reaction was filtered through a Buchner funnel and the yellow precipitate was collected. This was purified *via* recrystallization through vapor diffusion of Et₂O into a MeCN solution to yield 105.5 mg (33 %) of crystalline product. IR: 2951(w), 2898(w), 2851(w), 1620(s), 1606(s), 1566(s), 1469(s), 1455(s), 1441(vs), 1402(s), 1388(s), 1367(m), 1316(s), 1281(s), 1265(s), 1239(w), 1225(w), 1190(s), 1167(w), 1075(s), 1030(vs), 1003(s), 965(s), 947(s), 907(m), 845(s), 785(m), 734(s), 629(s), 604(m), 571(m), 513(s), 474(s), 423(m), 411(m) ESI-MS: [C₂₉H₃₀N₃O₆MnBi(OCH₃)⁺ *m/z* = 811.12; Elemental Analysis: Calculated % (Found %), C: 34.52 (34.52), H: 2.80 (2.78), N: 3.90 (3.76)

Magnetic Measurements: All samples were prepared under inert atmosphere and were measured in flame-sealed quartz tubes. Samples were prepared from ground microcrystalline material which was restrained in molten eicosane to prevent torqueing of crystallites. All measurements were conducted on a Quantum Design MPMS-XL SQUID magnetometer from 1.8 to 300 K and applied dc fields of 0-7 T. Diamagnetic corrections for the sample holder and diamagnetism intrinsic to the sample were calculated from Pascal's constants. Prior to full characterization, magnetisation from 0-4 T at 100 K was measured. Linear behavior in this curve indicated no ferromagnetic

impurities. Data agreement was checked between multiple measurements. Fits and simulations were performed with the MagProp package within DAVE 2.0.²⁰

EPR Measurements: All samples were prepared under inert atmosphere and were measured in flame-sealed quartz tubes. Samples were prepared from ground microcrystalline material which was prepared as a 0.1 mM solution in butyronitrile. Simulations to experimental data were performed using EasySpin.²¹

X-ray Diffraction Studies: Single crystals suitable for X-ray analysis were coated with Paratone N oil and mounted on a MiTeGen MicroLoop™ for analysis. Data were collected at 100 K on a Bruker KAPPA APEX diffractometer equipped with a MoK α microsource, a Quazar™ Optics monochromator, and a Bruker APEX II CCD area detector. Raw data were integrated and corrected for Lorentz and polarization effects using Bruker Apex2 v. 2014. 11.²² Absorption corrections were applied using SADABS.²³ Space group assignments were determined through examination of systematic absences, E-statistics, and successive refinement of the structures. Structures were solved using direct methods in SHELXT and further refined with SHELXL-2013²⁴ operated with the OLEX2²⁵ interface.

Other Physical Measurements: Elemental analysis was performed by Midwest Microlab (Indianapolis, IN). Infrared spectroscopy was performed on a Bruker Alpha FTIR spectrometer equipped with an attenuated total reflectance accessory. Solution-phase NMR spectroscopy was performed using a Varian Inova 500 MHz spectrometer. ¹H NMR spectra were referenced to the DMSO residual peak at 2.50 ppm. Electrospray mass spectra were collected in both positive and negative ionization mode on a Bruker AmaZon SL spectrometer equipped with a quadrupole ion trap using MeCN as the carrier solvent.

Discrepancy in g -values between magnetometry and EPR: The differences in the simulated g -values between the magnetometry measurements and the EPR measurements arise from two sources. First, where EPR is a spectroscopic measurement, magnetometry is extremely mass-dependent, which introduces an additional source of error in determining the g -value. The discrepancy in the simulated g -values between magnetometry and EPR is feasible allowing for an 8% margin of error in the sample mass. Additionally, it is difficult to account for g -anisotropy in magnetometry of powdered samples without overparameterizing the model, which is why simulation of magnetometry data proceeded with an isotropic g -value.

Table S2.1. Crystallographic information for the structural refinement of **2**.

Empirical Formula	C ₃₁ H ₃₀ BiF ₆ MnN ₃ O ₁₂ S ₂
Formula weight	1078.62 g/mol
Temperature	100 K
Wavelength	0.71073 Å
Crystal System	Triclinic
Space Group	<i>P</i> -1
Unit Cell Dimensions	<i>a</i> = 9.6023(5) Å, <i>α</i> = 96.095(3)° <i>b</i> = 12.8674(7) Å, <i>β</i> = 105.256(3)° <i>c</i> = 16.9332(9) Å, <i>γ</i> = 104.605(3)°
Volume	1806.25(17) Å ³
<i>Z</i>	2
Density (calculated)	1.983 Mg/m ³
Absorption coefficient	5.43 mm ⁻¹
<i>F</i> ₀₀₀	1054
Crystal color	Yellow
Crystal size	0.087 × 0.070 × 0.034 mm ³
<i>θ</i> range	1.358 – 30.233°
Index ranges	-13 ≤ <i>h</i> ≤ 13 -18 ≤ <i>k</i> ≤ 18 -22 ≤ <i>l</i> ≤ 22
Reflections collected	73675
Independent reflections	10716 [<i>R</i> _{int} = 3.14]
Completeness to <i>θ</i> = 30.233°	99.5%
Absorption correction	Multi-scan
Maximum and minimum transmission	0.680, 0.746
Refinement method	Full-matrix least-squares on <i>F</i> ²
Data / restraints / parameters	10716 / 64 / 552
Goodness-of-fit on <i>F</i> ^{2a}	1.034
Final <i>R</i> indices [<i>I</i> > 2σ(<i>I</i>) = 10626 data] ^b	<i>R</i> ₁ = 3.35 %, <i>wR</i> ₂ = 7.33 %
<i>R</i> indices (all data, 0.80 Å)	<i>R</i> ₁ = 4.33 %, <i>wR</i> ₂ = 7.59 %
Largest diff. peak and hole	3.84 and -1.31 e.Å ⁻³

^a GooF = [Σ[w(*F*_o² - *F*_c²)²] / (n-p)]^{1/2} where n is the number of reflections and p is the total number of parameters refined. ^b*R*₁ = Σ||*F*_o| - |*F*_c|| / Σ|*F*_o|; *wR*₂ = [Σ[w(*F*_o² - *F*_c²)²] / Σ[w(*F*_o²)²]^{1/2}

Table S2.2: Structural parameters for the Mn²⁺ local environment in the monometalated complex previously reported by Sunatsuki et al.,² the heterobimetallic complex **2** from this work, and the complex with the highest *D* value yet reported, a trigonal prismatic Mn²⁺ clatherochelate complex.⁹ The high axial zero-field splitting was attributed to the local environment of the Mn²⁺ center in the clatherochelate complex. In complex **2** there is a similar geometry about the Mn²⁺ center, which should create a similar zero-field splitting to first-approximation. However, we observe a markedly higher zero-field splitting, which suggests that additional effects are contributing to *D*.

Monometallic complex ²		Complex 2 (this work)		N6 Clatherochelate ⁹	
Bond Lengths					
N1-Mn	2.259(2)	N1-Mn	2.145(3)	N1-Mn	2.2721(38)
N2-Mn	2.243(2)	N2-Mn	2.175(3)	N2-Mn	2.2207(40)
N3-Mn	2.264(2)	N3-Mn	2.148(3)	N4-Mn	2.2371(37)
O1-Mn	2.1490(18)	O1-Mn	2.199(2)	N5-Mn	2.2286(42)
O2-Mn	2.117(2)	O2-Mn	2.132(2)	N7-Mn	2.2799(35)
O3-Mn	2.111(2)	O3-Mn	2.201(2)	N8-Mn	2.2112(38)
Bond Angles					
N1-Mn-N2	85.12(8)	N1-Mn-N2	84.99(12)	N1-Mn-N2	71.635(136)
N1-Mn-N3	78.94(8)	N1-Mn-N3	87.74(11)	N4-Mn-N5	71.744(143)
N2-Mn-N3	83.06(8)	N2-Mn-N3	91.24(11)	N7-Mn-N8	71.262(138)
O1-Mn-O2	89.55(7)	O1-Mn-O2	75.37(9)	N1-Mn-N7	76.124(133)
O1-Mn-O3	89.13(7)	O1-Mn-O3	75.58(9)	N1-Mn-N4	77.947(136)
O2-Mn-O3	89.35(8)	O2-Mn-O3	74.02(9)	N4-Mn-N7	78.782(141)
N1-Mn-O1	80.39(7)	N1-Mn-O1	82.90(10)	N2-Mn-N5	101.745(143)
N2-Mn-O2	82.02(8)	N2-Mn-O2	83.45(10)	N2-Mn-N8	95.255(142)
N3-Mn-O3	82.98(8)	N3-Mn-O3	82.27(10)	N5-Mn-N8	102.503(142)

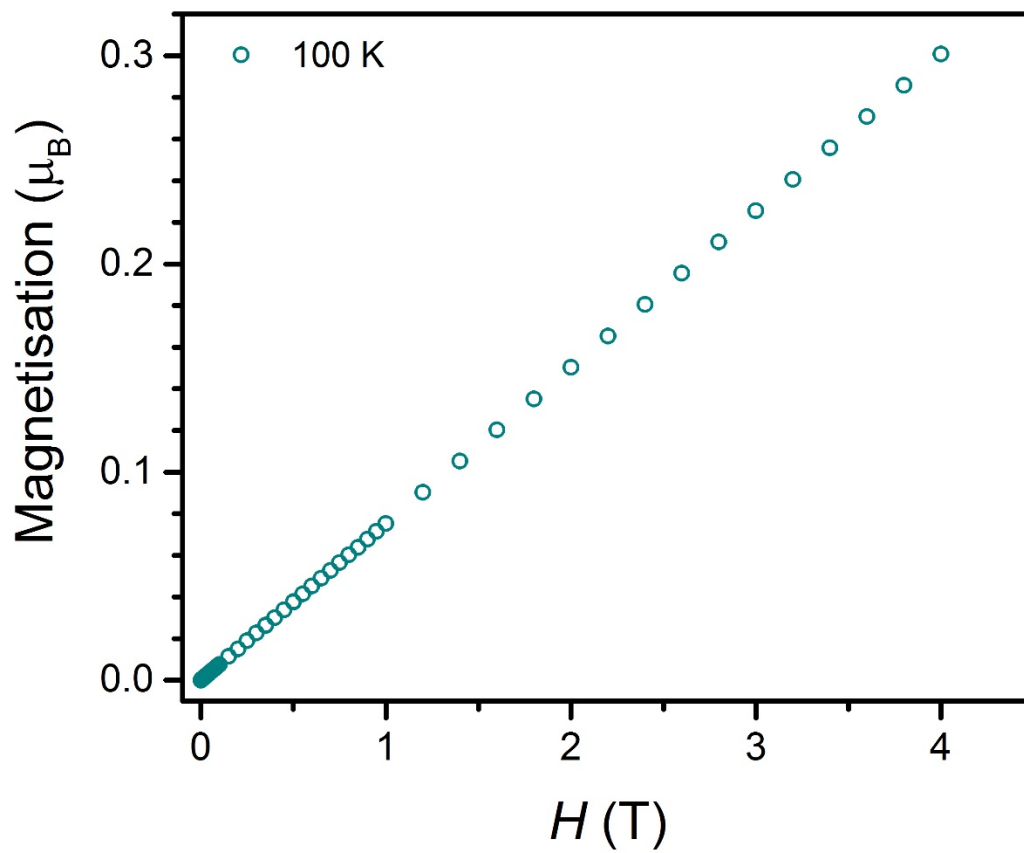


Figure S2.1: Variable field magnetization plot collected at 100 K. The linear behavior over all fields indicates the absence of ferromagnetic impurities in the sample.

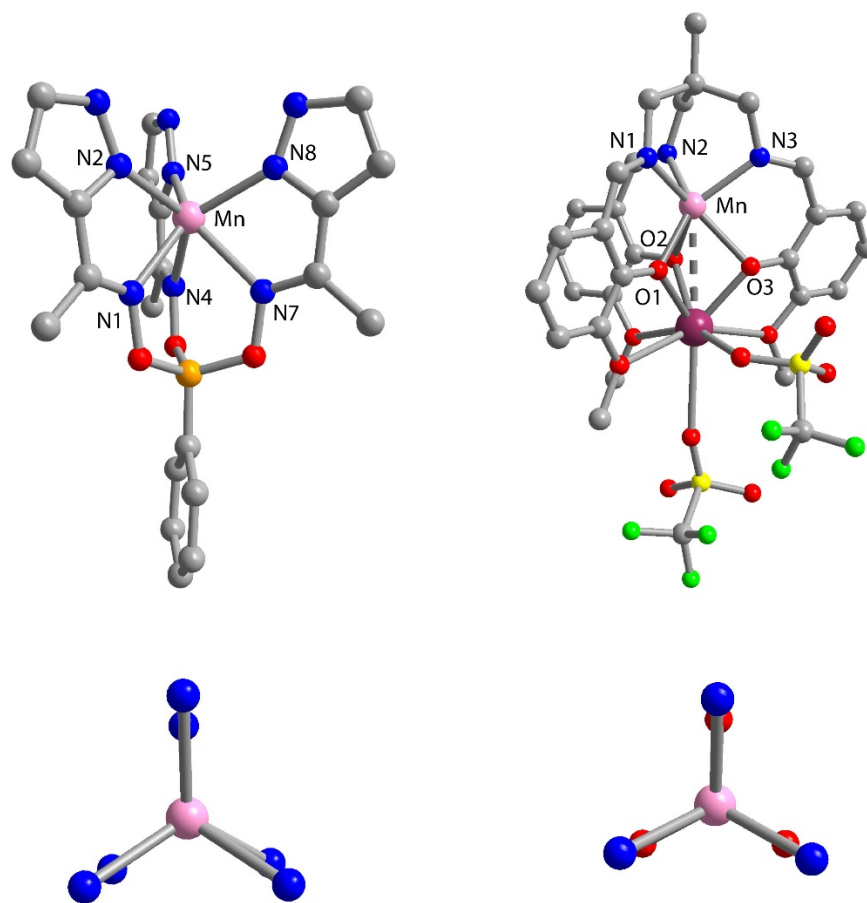


Figure S2.2: Left, a Mn²⁺ clathrochelate, which exhibits a D value of -0.32 cm^{-1} .²⁶ The metrics of the Mn²⁺ environment are tabulated in Table S2.2. The two structures both feature nearly idealized trigonal prismatic geometries, which should result in similar values for D if only ligand field effects are considered. The significant deviation in D values between the two structures indicates that additional spin-orbit effects play into the observed anisotropy in complex **2**.

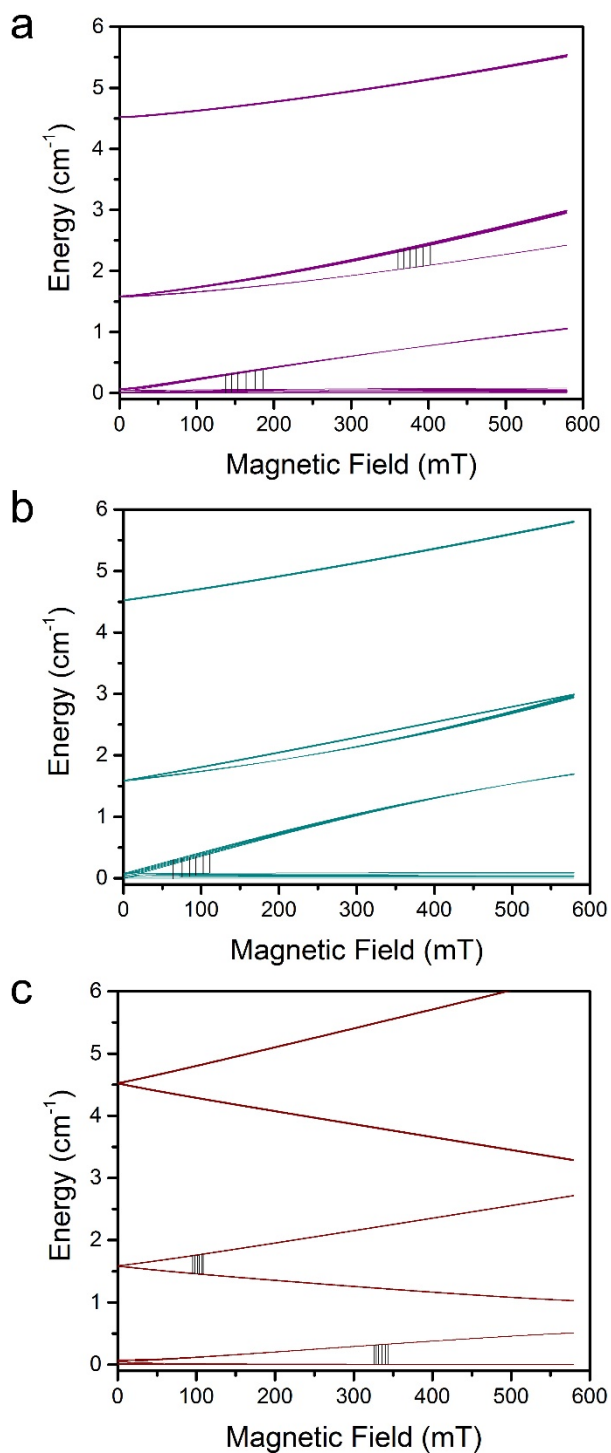


Figure S2.3: Zeeman plots for complex **2** along the (a) *x*, (b) *y*, and (c) *z* axes as calculated based on the parameters found by simulating the cw-EPR spectrum. The plots are normalized to the ground state. The observed transitions are shown as black lines. Hyperfine states are included in each plot and every hyperfine transition is shown separately. The hyperfine transitions are extremely close together in the *z*-direction but are distinct. These plots were calculated by EasySpin using the parameters outlined in the main text.⁴

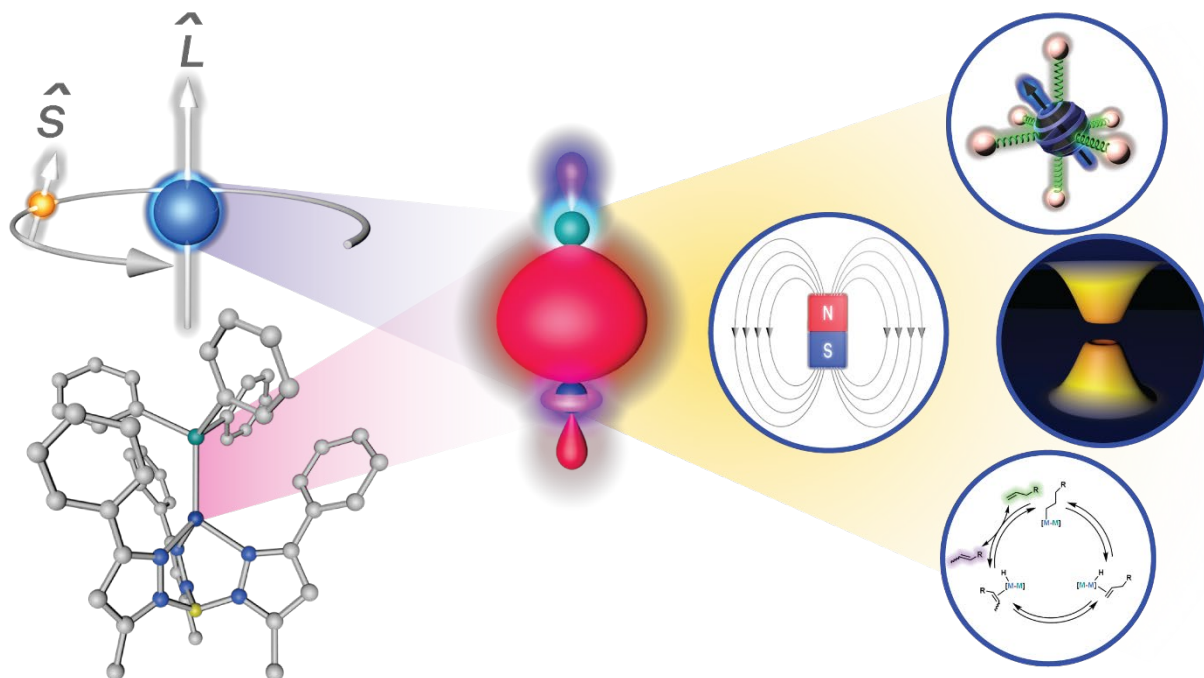
Chapter Three: Magnetic Anisotropy in Heterobimetallic Complexes

Reprinted with permission from:

Coste, S. C.; Pearson, T. J.; Freedman, D. E. *Inorganic Chemistry* **2019**, *58*, 11893–11902.

Copyright 2019 Royal Society of Chemistry

This section was written in collaboration with the co-authors listed above



Introduction

Spin-orbit coupling (SOC) is a powerful phenomenon which impacts the character and relative energy of atomic orbitals, with more significant effects manifesting in the heavier elements. Fundamentally, SOC can be defined as the interaction between the two key components of a magnetic moment: an electron's spin (S) and orbital angular momentum (L). SOC is responsible for many effects across a myriad of fields. In core electron-based spectroscopy experiments, for example, spin-orbit coupling is a vital element to describe the electronic structure of orbitals (e.g. $4d_{3/2}$ and $4d_{5/2}$ in gold as found in X-ray photoelectron spectroscopy)¹ and the splitting of yellow sodium D-lines lying at the intersection of astronomy and magnetism.^{2,3} Similarly, in condensed matter physics, SOC is crucial in enabling the electronic structure which creates topological insulators by providing an internal magnetic field.^{4,5,6}

Closer to inorganic chemistry, SOC is an essential component of the d-orbital manifold description, but is frequently relegated to lower energy scale interactions. Despite its relatively small energetic contribution, SOC impacts crucial properties such as magnetism,^{7,8} excited state dynamics,^{9,10,11} quantum coherence,¹² and catalytic pathway determination.^{13,14,15} Within catalysis, SOC enhances intersystem crossing rates, thereby promoting spin-forbidden pathways along a reaction coordinate, accelerating the sluggish cleavage of strong bonds.^{16,17} SOC also generates magnetic anisotropy essential for single molecule magnets by mediating coupling to excited states, providing molecules with preferred orientation of the magnetization.^{18,19,20} Developing new approaches to tune SOC would propel our fundamental understanding of electronic structure in coordination complexes and guide the tailoring of complexes towards such applications.

Transition metal complexes provide an excellent platform to probe the fundamental nature of SOC, especially through the lens of bimetallic complexes. Here, we can isolate a first-row transition metal with weak spin-orbit coupling and bind it to a heavy main-group element, thereby separating the two key components of SOC into two atoms, each of which can be varied and interrogated. The aggregate picture of electronic structure provides insight into the SOC contribution through systematic modulation of the metal-metal interaction. To understand these dynamics, we first must consider each contribution to the energies of the valence orbitals: the ligand field strength, electron-electron repulsion, and SOC. First-row transition metals are sensitive towards each of these parameters. Crucially, in first-row metal complexes, comparable ligand field and electronic repulsion energies also allow for access to high spin states. Additionally, first-row metals feature relatively low SOC due to the nominal Z_{eff}^2 dependence of SOC.^{21,22} The combination of these attributes makes them perfectly suited for an investigation of the impact of SOC from heavy elements.

Using heavy diamagnetic elements to modulate SOC has deep precedent, dating back to the well-studied heavy-atom effect, wherein heavy atoms enhance SOC-mediated processes.^{23,24} This effect dramatically impacts the photophysical properties of molecules where SOC enhances singlet to triplet transition rates underpinning its importance to luminescent materials. Using diamagnetic elements to impact SOC also has significant precedent within the solid state literature where unusually large magnetocrystalline anisotropies exist in magnetic materials such as FePt and MnBi.²⁵⁻²⁸ Our approach to tune SOC transfer between two metals could provide insight into the properties of such solid state materials through isolation of the fundamental two-atom interaction in a molecule. This model will inform the design of new magnetic materials, an approach successfully demonstrated with the designed synthesis of Fe-doped Li_3N inspired by a

linear, two coordinate iron complex.^{29,30} Within this Forum article, we will discuss the impact of heavy elements on SOC in transition metal complexes, with a focus on synthesizing bonds between transition metals and heavy main group elements in molecular species. We will consider the impact this approach can have on the targeted design of bimetallic complexes for specific applications.

Measuring spin-orbit coupling

As a fundamentally atomic phenomenon, directly measuring the SOC component in the d-orbital manifold is challenging in molecular compounds. However, SOC manifests in quantifiable properties such as intersystem crossing rates and magnetic anisotropy promoting them to effective proxies for SOC. A powerful approach to measure SOC is through EPR spectroscopy and magnetometry, which are capable of probing magnetic anisotropy through the zero-field splitting parameter (D), the second-order orbital contribution. In most first-row transition metal complexes, orbital angular momentum is quenched by the ligand field. This second-order term, however, incorporates orbital angular momentum back into the electronic structure. Zero-field splitting arises through coupling of the ground electronic states to excited states through SOC. Each excited state's contribution to D is inversely proportional to its energy separation from the ground state and proportional to the effective SOC constant squared, ζ_{eff}^2 .³¹ Therefore, SOC and ligand fields are delicately intertwined in their contributions to D , underpinning the importance of SOC in electronic structure. To understand contributions from SOC to D , a comprehensive understanding of the ligand field, electronic structure, and the excited state manifold of the complex is required. The following examples demonstrate some ways that D has seen use as a proxy for SOC and outline some of the challenges of using this parameter to measure SOC.

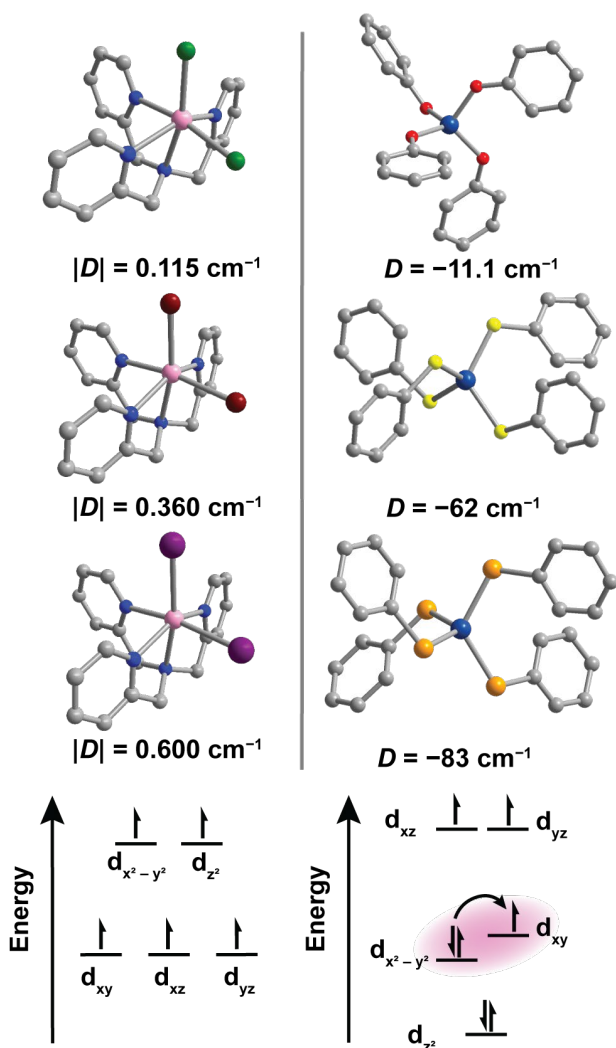


Figure 3.1. Examples of the two extremes of ligand SOC contributions to D . The isotropic, weak ligand field of Mn^{2+} allows ligand SOC to govern D whereas the ligand field dominates in the Co^{2+} complexes shown here.

Pink, cobalt blue, green, burgundy, purple, red, yellow, orange, blue, and gray spheres represent manganese, cobalt, chlorine, bromine, iodine, oxygen, sulfur, selenium, nitrogen, and carbon atoms, respectively, and hydrogen atoms have been omitted for clarity.

Trends within analogous ligand fields

The influence of SOC on D via the heavy-atom effect is best illustrated in high-spin Mn^{2+} complexes, whose electronically-isotropic ${}^6\text{A}_1$ ground states are resistant to ligand field changes. Duboc and coworkers observed that the zero-field splitting of Mn^{2+} -halide complexes generally trend as $|D_{\text{I}}| > |D_{\text{Br}}| > |D_{\text{Cl}}|$, correlating with the halide SOC.³² Using a combination of EPR spectroscopy and density functional theory (DFT), Neese and coworkers determined that D in Mn^{2+} -halide complexes is indeed proportional to the metal and halide SOC contributions, $\zeta_{\text{Mn}}\zeta_{\text{X}}$ (where $\text{X} = \text{Cl}, \text{Br}, \text{and I}$).^{33,34} The dominance of heavy-ligand SOC on magnetic anisotropy in many Mn^{2+} complexes can be attributed to multiple

opposite, but similar in magnitude, contributions to D neutralizing each other in

the symmetric electronic environment. However, stronger ligand fields can overcome ligand SOC in the isotropic ${}^6\text{A}_1$ ground state by lowering the excited quartet state energies such as in

isoelectronic Fe^{3+} porphyrin complexes.^{35,36} This implies that the weak ligand field, in conjunction with the electronic symmetry, about Mn^{2+} allows ligand SOC to dominate D in these complexes.

In many other first-row transition metal complexes, where the electronic structure is not isotropic, the ligand field can dominate contributions to D . This is particularly true for Co^{2+} complexes whose odd electron count can promote large D values by introducing energetically low-lying excited states.³⁷ Long and coworkers synthesized the series $[\text{Co}(\text{EPh})_4]^{2-}$ ($\text{E} = \text{O}, \text{S}, \text{and Se}$), and determined using SQUID magnetometry that changing the donor atom from O to Se yielded an increase in D from $-11.1(3)$ to $-83(1) \text{ cm}^{-1}$.³⁸ Thorough investigation of the electronic absorption spectra and concomitant ligand field analysis demonstrated that the trend in D correlated with a change in the Racah B parameter, reflecting the softness of the ligand donors. Neese and coworkers confirmed through *ab initio* methods that the weaker ligand field of the heavier donors indeed had a greater influence over D than the ligand SOC in this system.³⁹

In complexes with more metal-ligand covalency, both SOC and ligand field can contribute similarly to D .^{40,41,42} Experimentally quantifying the effect of ligand SOC on D then requires sufficient knowledge of its ligand field influence to deconvolute the two competing factors. Using the rich absorption spectra of $S = 1 \text{ Ni}^{2+}$, Desrochers and coworkers quantified the differing ligand field strength of axial halide donors in the series $[\text{Tp}^*\text{NiX}]$ (where Tp^{*-} = hydrotris(3,5-dimethylpyrazole)borate and $\text{X} = \text{Cl}^-, \text{Br}^-, \text{and } \Gamma^-$).⁴³ Using EPR spectroscopy, they observed $|D|$ increase from $3.93(2)$ to $23.01(4) \text{ cm}^{-1}$ between the Cl and I congeners, which correlates to the change in halide SOC constants. Through an angular overlap modal (AOM) analysis of the d-d transitions, they determined the ligand field changes throughout the halide series cannot account for the magnetic anisotropy enhancement. Consequently, they showed that the halide SOC facilitates the increase of $|D|$ in the series where the effective SOC constant, ξ_{eff} , of Ni^{2+} exceeds

its free-ion value (630 cm^{-1}) by up to 370 cm^{-1} in $[\text{Tp}^*\text{NiII}]$. Despite a clear change in ligand field affecting D throughout a series, this study illustrates how ligand SOC can still play a demonstrable role in magnetic anisotropy.

In addition to the ligand field effects, prior theoretical research supports the chemically intuitive concept that metal-ligand covalency impacts SOC transfer.^{41,44} Many experiments on the heavy-atom effect thus far have relied on using electronegative donors to change D .^{45–49} An intuitive way to engender a more covalent metal-ligand interaction is to use relatively electropositive donors. It is worth noting that several groups have begun exploring this approach using pnictogen and transition metal-based donors.^{50,51} Though to maximize the SOC of first-row transition metals, heavier ligands with more covalent interactions are necessary. Specifically, systematic analyses of bonding between heavy main group elements and high-spin paramagnetic transition metals remain scarce in the literature.

From ligand-based effects to heterobimetallic complexes

Earlier and heavier p-block metals and metalloids are ideal donors to generate covalent bonds to first-row transition metals. However, in their most common oxidation states, the p-block elements become more Lewis acidic moving down the groups due to the relativistic contraction of the s-orbitals and radial expansion of the p orbitals.⁵² It is therefore difficult to incorporate such heavy donors into the primary coordination sphere of paramagnetic first-row metals.

A successful approach to facilitate such metal-metal interactions relies on utilizing the supporting framework of scaffold ligands. In our initial attempt to overcome the challenge of stabilizing an interaction between two polycationic ions, we targeted a ligand scaffold that contains two binding pockets capable of accommodating two positively charged

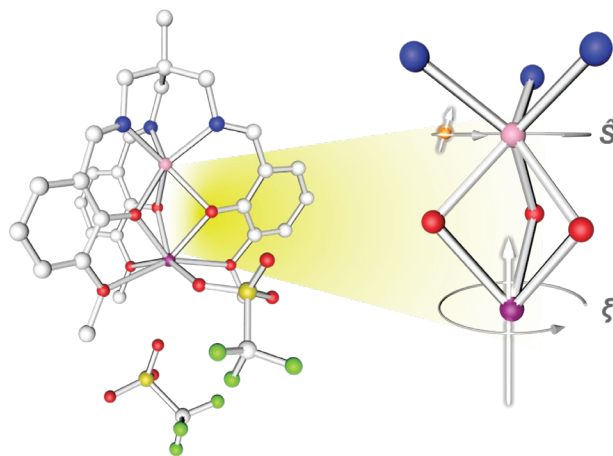


Figure 3.2. Molecular structure of $[L_1MnBi(OTf)_2]$ where purple, pink, red, blue, gray, yellow, and green represent Bi, Mn, O, N, C, S, and F atom respectively.

metal ions.⁵³ For this study we used high-spin Mn^{2+} because it has an isotropic electronic structure that is immune to ligand field distortions. This allowed us to comfortably attribute any notable deviations in the magnetic behavior expected for Mn^{2+} to the influence of Bi^{3+} . Towards this end, we used the tripodal nonadentate ligand, 1,1,1-tris[(3-methoxysalicylideneamino)methyl]ethane (H_3L_1), to stabilize an interaction between Mn^{2+} and Bi^{3+} , the heaviest ion stable to radioactive decay (Figure 3.2). The three anionic phenoxy donors provide a bridging support such that the bismuth is in the secondary coordination sphere of Mn^{2+} . Importantly, this ligand enforces the closest Mn^{2+} - Bi^{3+} distance in a paramagnetic heterobimetallic complex, 3.2163(5) Å. Given the high spin-orbit coupling of Bi^{3+} , we anticipated that the Bi^{3+} proximity would have a profound effect on the magnetic properties of this complex.

Upon characterization *via* SQUID magnetometry and EPR spectroscopy, we determined that the high-spin Mn^{2+} center exhibits a substantially larger D value than complexes with similar (six-coordinate N_xO_y) primary coordination spheres. The $|D|$ value of 0.70(2) cm^{-1} was approximately twice that of the next highest (0.32 cm^{-1})⁵⁴ for a six-coordinate complex with an

N_xO_y coordination sphere and approximately four-fold greater than that of the mono-metallated Mn^{2+} complex of the same ligand ($|D| = 0.168 \text{ cm}^{-1}$).⁵⁵ In fact, the magnetic properties of this complex most closely resemble those of Mn^{2+} compounds featuring direct bonds to heavy halide ions such as Br^- and I^- . Because the primary coordination sphere could not be reasonably implicated in the manifestation of these magnetic properties, we proposed that the heavy Bi^{3+} ion in the secondary coordination sphere was strongly influencing the magnetic properties. This hypothesis is further supported by the work of Duboc and coworkers in their observation of the highest $|D|$ measured for a manganous ion, $1.46(1) \text{ cm}^{-1}$.⁵⁶ Their system featured five-coordinate Mn^{2+} coordinated by polyoxotungstate ions which featured heavy tungsten atoms in the secondary coordination sphere. Together, these results suggest that even SOC originating from the secondary coordination sphere metal can influence magnetic anisotropy in high-spin Mn^{2+} .

SOC transfer *via* direct, covalent bonding

Theoretical investigations into heavy-atom effects suggest that inner sphere covalency would more greatly affect SOC transfer.^{57,58} Intuitively, a covalent bond in the primary coordination sphere would allow more electron density, i.e. SOC, to be shared between the two

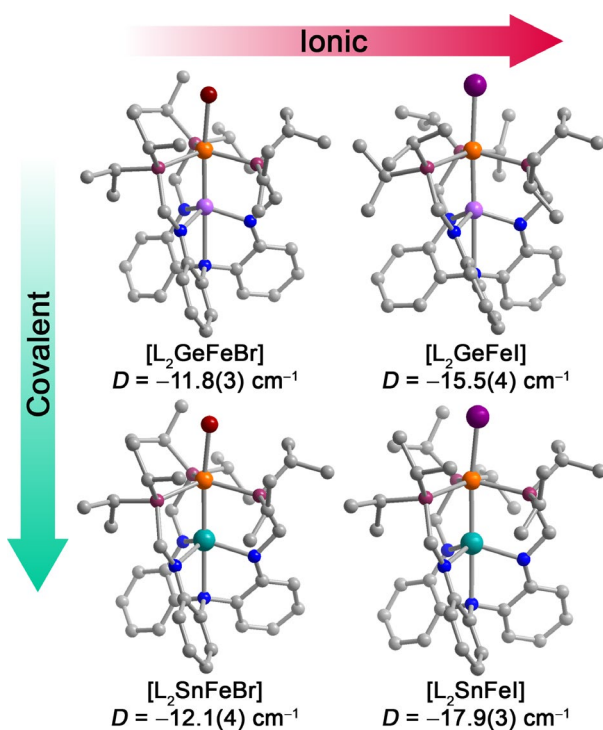


Figure 3.3. Molecular structures of series showing changes in D as a function of ionic- versus covalent-interacting ligand mass. Orange, turquoise, pink, red, violet, plum, blue, and gray spheres represent Fe, Sn, Ge, Br, I, P, N, and C atoms, respectively.

transition metals are necessary to stabilize paramagnetic ground states so that magnetic anisotropy can act as a proxy for SOC transfer.

We again targeted scaffold ligands to help determine the relative influence of ionic versus covalent interactions on magnetic anisotropy. Specifically, we drew inspiration from Lu and coworkers whose tris-phosphinoamide support has allowed isolation of numerous complexes featuring first-row transition metal-main group element bonds.^{63–69} As all the transition metal-main group complexes Lu and coworkers had synthesized to that point were diamagnetic or $S =$

metal centers than an ionic bond. Towards this end, we wanted to test how ionic and covalent interactions in the primary coordination sphere influence magnetic anisotropy. We first needed to address the challenge of creating a bonding interaction between two highly Lewis acidic metals. Many complexes bearing covalent bonds between first-row metals and main group metals feature electron rich transition metals, such as zero-valent carbonyl compounds, whose strong ligand field environment promote spin pairing.^{59–62} Less electron-rich

$^{1/2}$, we could not use D as a proxy for magnetic anisotropy in any of their previously established systems. To synthesize higher spin complexes, the polarity of the bond must be reversed where the main group element provides the electrons stabilizing the bond. Towards this goal, we utilized the lone pair of heavier group 14 elements, which can act as Lewis bases in their divalent state. We successfully synthesized the first paramagnetic complexes with crystallographically characterized Fe-Sn and Fe-Ge (shown in Figure 3.3) bonds using this approach.⁷⁰ The intermediate spin complexes featured a trigonal bipyramidal ferrous center with axially-flanking halides (Br^- , I^-) and group 14 elements (Ge^{2+} , Sn^{2+}), an ideal system to test ionic versus covalent influence on magnetic anisotropy.

Through chemical substitution of the axial donor mass, i.e. SOC, we systematically probed how both the electronegative halide and electropositive group 14 element influenced magnetic anisotropy using SQUID magnetometry. We found that increasing the mass of either group did not greatly impact $|D|$; the difference between the lightest and heaviest donors to Fe^{2+} was 6 cm^{-1} . Counterintuitively, the halides had a slightly larger influence than the group 14 elements. With the support of theoretical calculations and spectroscopy, we determined that the axial ligands only contribute 2.2% at most to the lowest-lying electronic states making D resilient to axial ligand modifications.

Inspection of the d-orbital diagram (Figure 4b) helps illustrate our conclusion. The strong ligand field about the Fe^{2+} center leaves the energetically high d_{z^2} (A_1^*) orbital unpopulated,

which has the most axial ligand character, i.e. the largest SOC. While coupling to this state contributes to D , it is much smaller in comparison to the contribution from the lower-lying E orbital set, which can interact via π -bonding with the axial donors. The halides' better ability to engage in π -bonding is reflected by the greater change to the ^{57}Fe Mössbauer quadrupole splitting parameter

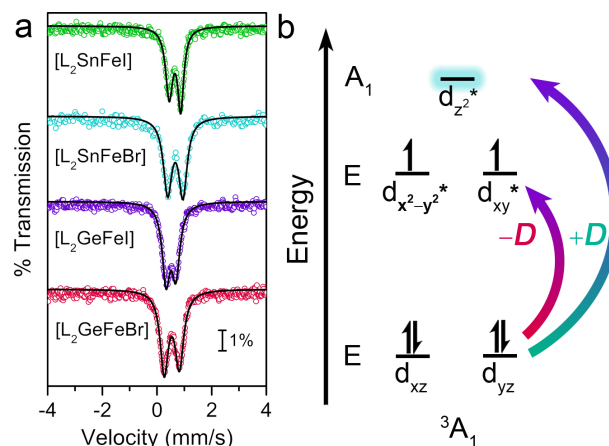
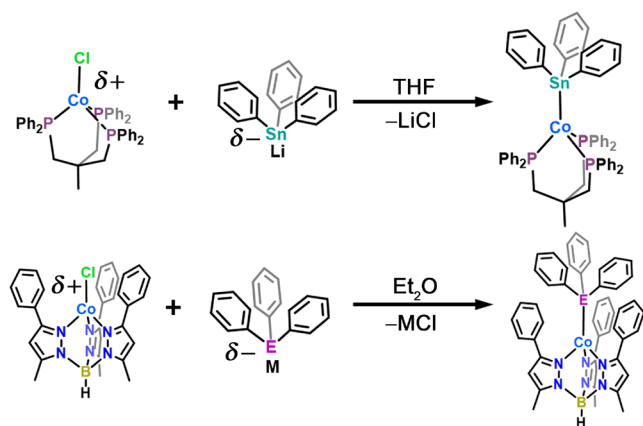


Figure 3.4. (a) ^{57}Fe Mössbauer spectra depicting the greater influence of halides on ΔE_Q and E orbital sets. (b) Qualitative d-orbital diagram of C_{3v} ($S = 1$) Fe^{2+} center highlighting the lack of unpaired spin density in the $d_{z^2^*}$ orbital.

(ΔE_Q) between the bromide and iodide complexes, underlying its correlation to the changes in D . This result highlights an important design criterion when invoking the heavy-atom effect to augment magnetic anisotropy: matching the symmetry of the lower-lying states with the heavy element bonding orbitals.

Our results thus far outline two important goals towards understanding how covalency facilitates the heavy-atom effect on magnetic anisotropy. It is essential that heavy element character be present in the electronic ground and low-lying excited states. This goal requires the overall ligand field strength to be lowered to increase coupling to the states with more ligand character, i.e. the anti-bonding orbitals. Lowering the ligand field energy simultaneously puts it on par with the SOC energy, which then requires complete understanding of the ligand field to elucidate SOC transfer from heavier elements. Therefore, it is of equal importance to quantify the

Scheme 1. Syntheses of paramagnetic complexes 1 – 3 with unsupported metal-metal bonds. (M = Li, K; E = Ge, Sn)



pedagogically approach the experimental quantification of the ligand field strength of group 14 donors, and its interplay with SOC, on influencing D .

Towards interactions between spin and heavy ligand orbitals

To study how covalency influences SOC transfer, we need to manipulate the ligand field such that there is more heavy-ligand contribution towards magnetic anisotropy. With an axially based heavy ligand, the best approach is to stabilize the d_{z^2} orbital. Starting from the previous trigonal bipyramidal geometry, this is achieved by removal of an axial ligand and pyramidalization of the equatorial donors to obtain pseudo-tetrahedral geometry. Lowering the molecular orbital with heavy element character would then allow it to contribute more to the lowest lying excited states. Additionally, an electronically isotropic ground state (i.e. an orbital singlet ground state term of A or B symmetry) is ideal

ligand field strength of the heavier p-block metals, which is also of importance for homogenous catalysis.⁷¹ Next, we will outline the synthesis of novel heterobimetallic complexes that will allow us to achieve these goals. Through analysis of the magnetic properties and electronic structure of these complexes, we hope to

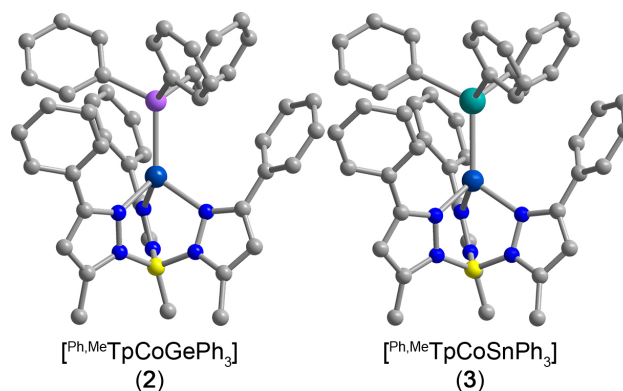


Figure 3.5. Molecular structures of 2 and 3 determined from single-crystal X-ray diffraction. Turquoise, pink, cobalt blue, gray, blue, and yellow spheres represent Sn, Ge, Co, C, N, and B, respectively; H atoms omitted for clarity.

because orbital degeneracy introduces low-lying excited states, and this convolutes analysis of the magnetic anisotropy. The foregoing analysis prompted us to engineer a new system with a weaker, symmetric ligand field to stabilize high-spin ground states. However, high-spin complexes with metal-metal bonds are uncommon due to the covalent metal-metal interaction. To significantly weaken the ligand field, it is necessary to employ lower-coordinate complexes with the help of unsupported metal-metal bonds. Relying on unsupported bonds would diminish secondary influences on magnetic anisotropy from ancillary ligands while weakening the ligand field. Using these design criteria, we seek to illustrate our synthetic approach to stabilize high-spin complexes to study how covalency affects SOC transfer.

We can access high-spin complexes featuring unsupported metal-metal bonds through precise synthetic design. Without the support of a scaffold ligand, an unsupported covalent bond requires a favorable electrostatic interaction for stabilization. Additionally, it is essential that the first-row transition metal is Lewis acidic to stabilize high-spin ground states, as opposed to the Lewis basic transition metals in most carbonyl-based main group metal-bonded complexes. In this scheme, we can stabilize a covalent bond by fusing a negatively charged heavy main group metal fragment with a positively charged transition metal moiety. An example of suitable capping ligands to promote a low-coordinate environment would be neutral or anionic tripodal ligands, which would leave an open axial site for heavy element coordination. A high-spin complex with an isotropic ground state is then acquired through judicious choice of the transition metal ion. Thus, we will initially target divalent or monovalent first-row transition metals in pseudo-tetrahedral geometry; e.g. V^{2+} , Mn^{2+} , Co^{2+} , Co^+ , and Ni^{2+} fit the outlined electronic structure criteria.

Huttner and coworkers demonstrated an initial success with this strategy in isolating [(triphos)CoSnPh₃] (**1**), a paramagnetic ($S = 1$) Co⁺ complex with an unsupported bond to tin.⁷² We note this was one of the few crystallographically-characterized paramagnetic complexes featuring first-row metal-tin bonds until recently. The complex was electrostatically-stabilized by the metathesis reaction of a monocationic [(triphos)Co]⁺ fragment with an anionic triphenyl stannide (Ph₃Sn⁻) reagent. The scarcity of paramagnetic complexes with first-row metal-heavy main group metal bonds prompted us to investigate the magnetic properties of **1**. Simulation of the magnetization data (Figure S3) with the Hamiltonian, $\hat{H} = D[\hat{S}_Z^2 - \frac{1}{3}S(S + 1)] + g_{\text{iso}}\mu_B\mathbf{SH}$, yields values of 2.0(3) cm⁻¹ and 2.06(4) for $|D|$ and g_{iso} , respectively. The low $|D|$ value is evident by the overlaying of isofield lines and is a consequence of the strong ligand field raising the energies of the lowest-lying excited states. This provides further impetus to stabilize the anti-bonding orbitals lowering the excited state energies.

To further weaken the ligand field, we targeted complexes with weaker donors such as nitrogen-based ligands. We chose to use the tetrahedrally-directing tris(pyrazolyl)borate ligand (Tp⁻) to cap divalent transition metals serving as a cationic foundation for our system. The anionic ligand also provides extra stability to the transition metal fragment over neutral ligands that may dissociate in solution. For our initial studies, we will use Co²⁺ because its rich absorption spectrum in pseudo-tetrahedral complexes is well-studied providing a strong basis to quantify heavy donor ligand field influence. Drawing inspiration from Huttner and coworkers, we utilized the triphenyl group 14 anions as simple heavy donors to the Co²⁺ center. We synthesized the desired complexes via metathesis reactions of LiGePh₃ or KSnPh₃ with [Ph₃MeTpCoCl]⁷³ in Et₂O. The molecular structures of [Ph₃MeTpCoGePh₃] (**2**) and [Ph₃MeTpCoSnPh₃] (**3**), determined by single crystal X-ray diffraction, are shown in Figure 5. Both complexes exhibit approximate C_{3v} symmetry and feature

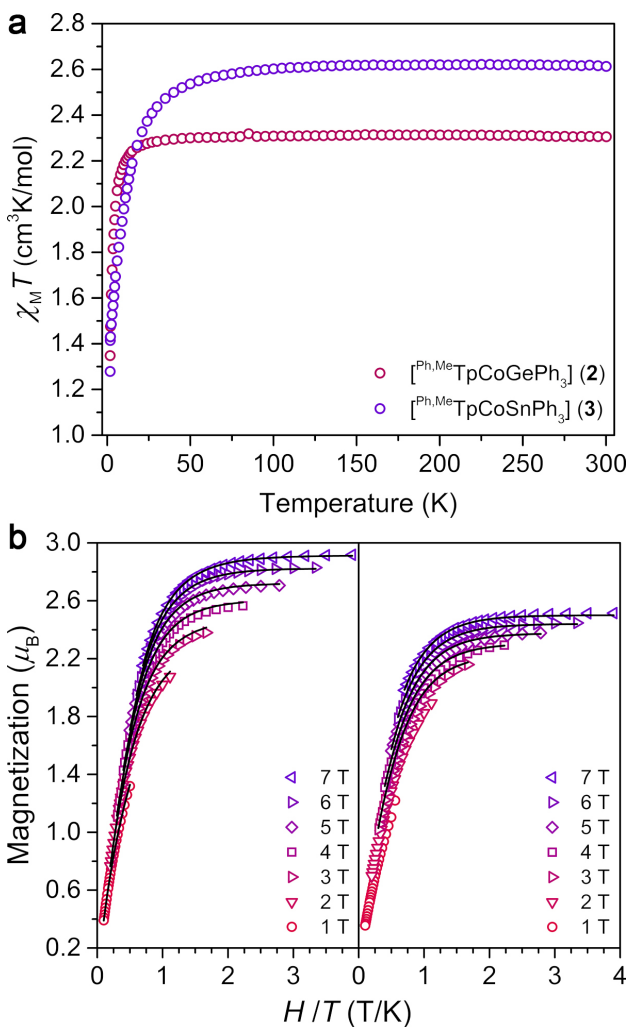


Figure 3.6. (a) Variable-temperature dc susceptibility data for **2** and **3** with $H_{dc} = 0.1$ T. (b) Variable-temperature, variable-field magnetization for **2** (left) and **3** (right), with black lines representing the best fit. The parameters for the fit are given in Table S3.4 in the Supporting Information.

towards D . The downturn in the susceptibility data is attributable to the presence of D which we can more accurately quantify through simulation of magnetization data. Starting with parameters obtained from X-band EPR spectra (Figure S3.4), we simulated magnetization data using the Hamiltonian, $\hat{H} = D[\hat{S}_Z^2 - \frac{1}{3}S(S+1)] + E(\hat{S}_x^2 - \hat{S}_y^2) + g\mu_B\mathbf{S}\mathbf{H}$ to yield D values of 3.9(3) and

unsupported metal-metal bond lengths (2.503(1) Å in **2** and 2.654(1) Å in **3**) shorter than the sum of their covalent radii (Co-Ge: 2.70 Å; Co-Sn: 2.89 Å). Importantly, the Co-N distances in **2** and **3** suggest that the complexes are high spin.

To confirm the spin-state and probe the magnetic properties of **2** and **3**, we turned to EPR spectroscopy and SQUID magnetometry (Figure 3.6). Variable-temperature dc magnetic susceptibility data shows room temperature χ_{MT} values of 2.32 and 2.62 $\text{cm}^3\text{Kmol}^{-1}$ corroborating an $S = 3/2$ ground state in **2** and **3**, respectively. Therefore, these are the first high-spin Co^{2+} complexes featuring Co-Ge and Co-Sn bonds, providing an ideal system to study the interplay of the ligand field and SOC

11.9(1) cm^{-1} for complexes **2** and **3**, respectively. The high-spin nature of the complexes enables observation of a clear increase in D with heavier donors owing to more axial ligand contribution.

Experimentally deconvoluting the influences of ligand geometry and SOC

The impact of SOC is more apparent with a weaker ligand field, however, we now need to thoroughly analyze the ligand field to better quantify SOC influence on D . Each excited state contribution to D is indirectly proportional to the energy separation and proportional to ζ_{eff}^2 , where ζ_{eff} represents a combination of each donor atom's inherent SOC weighted by their contribution to the relevant molecular orbital.^{41,44} In other words, the ligand SOC is anisotropic and states with more d_{z^2} character will contribute more to D in our series. The sign of a contribution is then determined by the symmetry relation between the two states: a negative contribution if related by the L_z operator, and conversely positive if the states are related via $L_{x,y}$.⁷⁴ We note that orbital mixing in 3-fold symmetric systems induces a negative contribution to D when coupling between two E orbital sets ($d_{x^2-y^2}$, d_{xy} and d_{xz} , d_{yz}).⁷⁵ Therefore, there are competing contributions between states with d_{z^2} character (positive) and states with more E orbital character (negative). Maintaining an isostructural series is therefore vital where the identical pyrazole donors maintain control of the E orbital set energies. This allows any changes to the axial ligand to be our independent variable towards D . Understanding this axial influence is then the last piece of the puzzle.

Previous studies into the donor ability of group 14 elements toward transition metals relied on vibrational spectroscopy and trans- effects of ligand substitution. They demonstrated that the σ -donating ability of the group 14 elements ranked as $\text{Ge} < \text{Si} < \text{Sn}$ towards Ir^+ and Rh^+ centers, differing from the halides and chalcogenides whose ligand fields weaken moving down the group.^{76,77} A similar trend was observed in first-row transition metal complexes, such as $\text{LMn}(\text{CO})_5$ ($L = \text{group 14 donor}$) complexes, where the relative σ -donating and pi-accepting ability

of numerous group 14 donors were compared using carbonyl stretching frequencies. This implies that the lowest-lying excited state is higher in energy in **3** rendering it a less positive D value, the opposite of what we observe.

We probed the ligand field strength of Ph_3Ge^- and Ph_3Sn^- using an angular overlap model (AOM) analysis of the electronic absorption spectra shown in Figure 3.7a.⁷⁸ While we do not observe the two lowest transitions (the transition to the ^4E is in the mid-IR and $^4\text{A}_1$ band is symmetry forbidden in C_{3v} symmetry), we can fit the four higher lying transitions to estimate the energy of the low energy states. We fit the diffuse reflectance spectra using the program `ddnfit` starting with parameters derived by Telsler and coworkers;^{79,80} a detailed discussion of the fits is in the SI. The parameters from the best fit (Table S3.5) suggest a σ -donating ability of both tin ($\epsilon_\sigma = 2363 \text{ cm}^{-1}$) and germanium ($\epsilon_\sigma = 2145 \text{ cm}^{-1}$) similar to that of a chloride in a similar environment ($\epsilon_\sigma(\text{Cl}) = 2270 - 2290 \text{ cm}^{-1}$).⁸¹ We note that the differences in ϵ_σ between tin and germanium corroborate the trend in Ir^+ and Rh^+ complexes, however, the parameter values are much smaller than we hypothesized. This may be due to mismatch between tin valence orbitals and metal 3d orbitals. As a consequence of the overall ligand field, the energy of the ^4E state in **2** is simulated to be higher than **3**. While this undoubtedly contributes to a more positive value of D observed in **3**, we can account for other low-lying states by simulating D with the inclusion of ζ_{eff} using the AOM. By systematic variation, we found that ζ_{eff} was much lower in **2** than **3**, 357 cm^{-1} versus 531 cm^{-1} , to replicate the measured D values. This suggests that SOC from the heavier tin donor is in fact contributing to the magnetic anisotropy of the Co center where the free-ion ζ value in Co^{2+} is 515 cm^{-1} .⁷⁸ The lower ζ_{eff} in **2** is likely a result of the orbital reduction from the covalent bond that is uncompensated by the SOC constant of the germanium donor.

The preceding ligand field analysis provides a framework to experimentally probe how covalency affects SOC conferral through metal-metal bonds. While covalency is a complex, and sometimes intangible concept to quantify experimentally, the AOM provides parameters that together can paint an accurate picture of molecular orbitals. The ϵ_σ parameter represents orbital overlap and energy matching between two atomic orbitals by quantifying the destabilization of metal-ligand antibonding orbitals. Based on this description, we infer that the metal-metal bonding

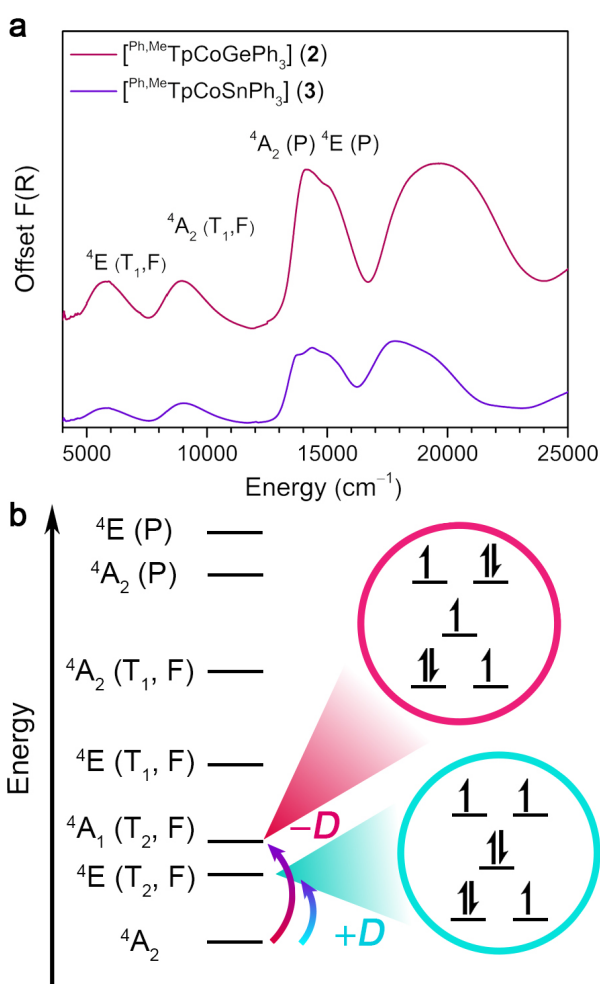


Figure 3.7. (a) Diffuse reflectance spectra of **2** and **3** measured at room temperature. (b) Energy level diagram of Co²⁺ in pseudo-tetrahedral C_{3v} symmetry (⁴A₂ ground state) depicting most influential states towards *D* with the largest contributing electronic configuration to those states.

in **2** and **3** is similar in covalency to that of a chloride. Further, the Racah *B* parameters in **2** (677) and **3** (678) suggest a similar nephelauxetic effect compared to Tp-based Co²⁺ complexes. We presumed that tin, like iodide, would reduce the interelectronic repulsion further owing to its large polarizable 5s and 5p orbitals. We will not speculate further about the implication because many factors contribute to the Racah *B* parameter. These ligand field parameters, however, do provide a starting point to analyze the covalency, and its influence on SOC transfer in high-spin complexes.

The outlined synthetic criteria and subsequent analysis establish a foundation to begin studying the influences of covalency on

SOC transfer to first-row transition metal centers. Beyond the measurements discussed here, direct measurements of SOC and covalency is accessible using synchrotron-based techniques such as X-ray absorption spectroscopy (XAS) and X-ray magnetic circular dichroism (XMCD). Future experiments will rely on these direct experimental probes, in addition to those used in this work, to better understand the metal-metal bond's influence on magnetic anisotropy. Concurrent theoretical calculations are also vital to support the experimental data due to shortcomings of the AOM. While the AOM provides chemically intuitive parameters to inform synthetic direction, it does not accurately depict the complexity of molecular orbitals and electronic structure such as anisotropic SOC ligand contributions. Future studies will explore covalent bonds between first-row metals and heavier group 13 and 15 elements with the goal of exploiting the large SOC of the 6p elements to engender large magnetic anisotropy. The synthesis of the latter may, however, require more research towards a better fundamental understanding of the reactivity of 6p elements.

Conclusions and Outlook

The foregoing results and analysis underline the importance of appropriately considering molecular geometry, spin-orbit coupling, and metal-ligand covalency in molecular design. Specifically, we have shown that spin-orbit coupling can powerfully modulate the magnetic properties of transition metals even in the absence of direct bonding in electronically isotropic systems. We note, however, that use of high-spin complexes with electron density in the molecular orbitals with ligand character is crucial to observing this heavy-atom effect. Further, we have demonstrated that the covalency of the metal-metal interaction is critical in considering the spectral and magnetic properties of transition metal-main group heterobimetallics and has strong implications for the transfer of spin-orbit coupling from the ligand sphere to the transition metal.

These results provide a framework for synthetically controlling SOC in transition metal complexes and materials. This and subsequent research will enable the manipulation of SOC in transition metal complexes and will support advancements in fields as diverse as molecular magnetism, topological materials, and two-state reactivity in catalysis. Specific molecular targets to further this research are paramagnetic species featuring direct bonds 6p elements such as lead and bismuth. Further, we plan to pursue X-ray measurements to directly probe SOC and covalency to help deconvolute the influences of ligand field geometry and the heavy atom effect on the magnetic properties of these compounds.

Supplementary Information

Experimental Details.

General Considerations. All compounds were manipulated and handled under a dinitrogen atmosphere in an MBraun Unilab Pro glovebox. All glassware was either oven-dried at 150 °C for at least four hours or flame-dried prior to use. Diethyl ether (Et₂O), benzene, and n-hexane were dried using a commercial solvent purification system from Pure Process Technology and stored over 3 or 4 Å sieves for a minimum of one day prior to use. CDCl₃ and C₆D₆ were purchased from Cambridge Isotope Labs, deoxygenated by three successive freeze-pump-thaw cycles, filtered through a pad of activated alumina, and stored over 3 or 4 Å sieves prior to use. [(triphos)CoSnPh₃](**1**) and [Ph₃MeTpCoCl] were prepared according to literature procedures.^{82,83} HSnPh₃ and HGePh₃ were purchased from MilliporeSigma and vacuum distilled prior to use. All other chemicals were used as received. Silylated Celite (Si-Celite) was prepared by stirring 25 g activated, dried Celite 545 in 100 mL toluene with 14 mL trimethylsilylchloride and 14 mL of triethylamine under N₂ overnight at 40 °C, followed by filtration, washing with 80 mL MeOH and 200 mL toluene, and drying for 24 hours at 100 °C.

[Ph₃MeTpCoGePh₃]·benzene(**2**). LiGePh₃ was generated by the deprotonation of HGePh₃ (264.1 mg, 0.866 mmol) with ⁿBuLi (0.54 mL, 0.866 mmol) in 5 mL of Et₂O at room temperature to generate a clear, slightly yellow solution. This was added dropwise at room temperature to a fine suspension of [Ph₃MeTpCoCl] (401.1 mg, 0.694 mmol) in 10 mL of Et₂O to precipitate a purple micro-crystalline solid. After allowing the reaction mixture to stir overnight, the solid was filtered out and washed with 5 mL Et₂O then dried *in vacuo*. The solid was dissolved in 40 mL benzene, filtered over Si-Celite on a fritted funnel, then layered under 100 mL n-hexane. Purple, hexagonal

plates of **2** were obtained (Yield: 375.5 mg, 58.5 %). IR (ATR, cm^{-1}): 3055 (w), 3045 (w), 3034 (w), 2982 (w), 2933 (w), 2863 (w), 2529 (w), 1545 (m), 1507 (w), 1478 (m), 1452 (m), 1436 (s), 1425 (s), 1378 (w), 1362 (m), 1341 (m), 1332 (w), 1302 (w), 1288 (w), 1259 (w), 1221 (w), 1212 (w), 1183 (s), 1166 (m), 1113 (m), 1094 (m), 1074 (m), 1094 (m), 1074 (m), 1056 (s), 1030 (m), 1024 (m), 998 (w), 986 (w), 979 (m), 912 (m), 852 (w), 843 (w), 831 (w), 802 (m), 789 (w), 777 (s), 769 (s), 764 (s), 739 (s), 708 (s), 700 (s), 696 (s), 684 (m), 668 (vs), 661 (m), 656 (m), 636 (m), 617 (m), 603 (w) UV-Vis-NIR (CDCl_3) λ_{max} , nm (ϵ): 514 (1767), 655 (1058), 682 (1199), 703 (sh, 991), 1096 (94), 1679 (67). ^1H NMR (600 MHz, C_6D_6 , 298 K): δ 58.22 (3H), 18.95 (9H), 18.43 (br, 6H), 14.54 (6H), 8.16 (3H), 6.63 (6H), 5.12 (br, 6H), 2.94 (3H), -10.15 (br, 1H) ppm. Anal. Calcd. for $\text{GeCoN}_6\text{C}_{48}\text{BH}_4\cdot(\text{C}_6\text{H}_6)$: 70.16 %C; 5.34 %H; 9.09 %N. Found: 67.51 %C; 5.32 %H; 9.12 %N; carbon analysis consistently gave lower values that would could not be accounted for by loss of solvent, we attribute this is to incomplete combustion of the organogermanium species.

[^{Ph,Me}TpCoSnPh₃]·benzene(3). Yellow KSnPh_3 was generated by stirring HSnPh_3 (222.2 mg, 0.633 mmol) and KH (25.3 mg, 0.633 mmol) in 5 mL of Et_2O for 4 hours at room temperature. To this, a suspension of [^{Ph,Me}TpCoCl] (241.6 mg, 0.418 mmol) in 15 mL Et_2O was added at room temperature, a white precipitate formed and the reaction was allowed to stir overnight at room temperature. The precipitate was filtered out and washed with 4 x 5 mL Et_2O and dried. Then, it was taken up in 80 mL benzene, filtered through Si-Celite on a fritted funnel, then layered under 100 mL n-hexane. Purple, hexagonal platelets of **3** were obtained (Yield: 142.7 mg, 35.2 %). IR (ATR, cm^{-1}): 3049 (w), 3025 (w), 2995 (w), 2975 (w), 2965 (w), 2932 (w), 2530 (w), 1543 (m), 1507 (w), 1475 (m), 1452 (m), 1435 (s), 1423 (s), 1376 (w), 1361 (m), 1341 (m), 1302 (w), 1286 (w), 1254 (w), 1215 (w), 1180 (s), 1094 (m), 1056 (s), 1031 (m), 996 (w), 977 (m), 912 (w), 842

(w), 802 (w), 777 (m), 764 (s), 731 (s), 697 (s), 677 (vs), 650 (s), 637 (s), 533 (m), 526 (m), 490 (m), 451 (s), 443 (s), 407 (w). UV-Vis-NIR (CDCl₃) λ_{max} , nm (ϵ): 516 (sh, 716), 554 (1202), 650 (1221), 683 (1015), 715 (644), 1069 (101), 1678 (60). ¹H NMR (600 MHz, C₆D₆, 298 K): δ 63.93 (3H), 28.49 (6H), 18.63 (9H), 13.34 (6H), 8.82 (3H), 7.99 (6H), 7.06, 4.88 (3H), -22.41 (1H) ppm. Anal. Calcd. for SnCoN₆C₄₈BH₄₃·(C₆H₆): 66.83 %C; 5.09 %H; 8.66 %N. Found: 66.68 %C; 4.96 %H; 8.30 %N.

Magnetic Measurements. Magnetic data were collected using a Quantum Design MPMS-XL SQUID magnetometer. Measurements for all compounds were obtained on finely ground microcrystalline powders. The compounds were restrained in a frozen eicosane matrix and flame sealed in a quartz tube under vacuum. Dc magnetic susceptibility measurements were performed in the temperature range 1.8–300 K under dc fields of 0.1, 0.5 and 1 T. Dc magnetization measurements were performed under applied magnetic fields of 1, 2, 3, 4, 5, 6 and 7 T in the temperature range of 1.8–10 K. Dc magnetic susceptibility data were corrected for diamagnetic contributions from the sample holder and eicosane as well as for the core diamagnetism of each sample, estimated using Pascal's constants.⁸⁴³ A temperature-independent paramagnetism (TIP) correction was applied for both **2** and **3** with values of $1.3 \times 10^{-3} \text{ cm}^3 \text{ mol}^{-1}$ and $1.1 \times 10^{-3} \text{ cm}^3 \text{ mol}^{-1}$, respectively. Prior to full characterization, variable dc field magnetization data was collected from 0 to 4 T at 100 K to ensure the absence of curvature associated with ferromagnetic impurities.

Electron Paramagnetic Resonance (EPR) Spectroscopy. Polycrystalline samples of **2** and **3** were loaded into a 4 mm OD quartz EPR tube under a dinitrogen atmosphere and restrained with eicosane. Continuous-wave EPR spectra were measured at the University of Chicago EPR facility using a Bruker Elexsys 500 X-band EPR spectrometer. Samples were cooled using an Oxford Systems continuous-flow He cryostat coupled with a 10 K He stinger from Bruker. Spectra were

acquired with the Bruker Win-EPR software suite. Spectral simulations were carried out using Easyspin.⁴

X-ray Diffraction. Single crystal diffraction data collections were performed on single crystals coated with Paratone-N oil and mounted on a MicroMountsTM rod. The crystals were frozen while coated in Paratone-N oil under a stream of N₂ during the measurement. Structures for **2** and **3** were collected with CuK α ($\lambda = 1.54178 \text{ \AA}$) and MoK α ($\lambda = 0.71073 \text{ \AA}$) sealed tube diffraction sources respectively. Both sources were equipped with a graphite monochromator and a Bruker APEX2 CCD detector. Raw data were integrated and corrected for Lorentz and polarization effects using Bruker Apex3 v. 2013.⁵ Absorption corrections were applied using SADABS.⁶ Space group assignments were determined by examination of systematic absences, *E*-statistics, and successive refinement of the structures. The crystal structure was solved by direct methods with the aid of successive difference Fourier maps in SHELXS⁷ operated with the OLEX2 interface.⁸ The crystals showed no significant decay during data collection. Thermal parameters were refined anisotropically for all non-hydrogen atoms. Hydrogen atoms were placed in ideal positions and refined using a riding model for all structures. Compounds **2** and **3** crystallized with a benzene molecule that was disordered over a special position, so a solvent mask was used.

Powder X-ray Diffraction Measurements. Polycrystalline samples of **2** and **3** were loaded in a hollow metallic sample holder and both sides sealed with Kapton tape inside the glovebox. The powder X-ray diffraction (PXRD) patterns were measured in transmission geometry (with sample spinning) using a STOE STADI P instrument equipped with a CuK α 1 sealed tube source and a 1D strip detector covering 2 θ range of 6°. All patterns were collected at room temperature.

All Other Physical Measurements. Combustion analysis of all complexes was performed by Midwest Microlabs (Indianapolis, IN). Infrared spectra were recorded on a Bruker Alpha FTIR

spectrometer equipped with an attenuated total reflectance accessory. Solution-phase NMR spectra were collected with a Bruker Avance III 600 MHz spectrometer. Proton NMR spectra are referenced to d_6 -benzene at 7.16 ppm. UV-vis-NIR and diffuse reflectance spectra were collected on a Varian Cary 5000 spectrometer at room temperature in $CDCl_3$ for the solutions or over KBr for solid measurements.

Ligand Field Theory (LFT) Analysis. LFT analysis of the electronic structures of **2** and **3** were performed with use of the angular overlap model (AOM).⁹ The computer program DDN, which is available from J. Telsler, was employed to perform the analysis. The program used the complete d^7 (equivalent to d^3) weak-field basis including interelectronic repulsion (Racah parameters: B , C), spin-orbit coupling (ζ_{eff}), and AOM ligand-field bonding parameters (ϵ_{σ} , ϵ_{π}). DDN allows use of a non-linear least-squares fitting subroutine (DSTEPIT, from QCPE, Bloomington, IN) to match observed electronic transition energies to those calculated by user-defined variable parameters. The general AOM procedure involved an initial fit of spin-allowed optical transitions with variation of B and AOM bonding parameters without ζ_{eff} ; C was set to $4.7B$. The geometric parameters used for the analysis were taken from the single-crystal X-ray diffraction data, and the bonding parameters for the three pyrazole N donors were set to be identical as they are crystallographically symmetric. In order to reduce overparameterization, the $\epsilon_{\sigma}(\text{N})$ parameter was calculated using the $1/r^6$ dependence on bond distance from known $\epsilon_{\sigma}(\text{N})$ parameters in similar Tp-based Co^{2+} complexes and held constant throughout the analysis.¹⁰ The analysis was performed assuming C_{3v} symmetry of the complexes; therefore we set $\epsilon_{\pi c}(\text{Sn}) = \epsilon_{\pi s}(\text{Sn})$. From this initial fit, ζ_{eff} was varied until a reasonable match for $|D|$ was obtained. The resulting electronic structures were then checked to ensure that they were still in agreement with experiment.

Discussion of discrepancy between EPR and magnetometry g-values. We simulated the magnetization data from SQUID magnetometry with slightly lower g-values than what were used to simulate X-band EPR spectroscopy. We attribute this discrepancy to slight structural distortions that occur at lower temperatures. Structural distortions upon cooling is corroborated by the PXRD in Figure S3.6 which show deviations in the room temperature patterns from simulations of the single crystal data measured at 100 K.

Table S3.1 | Crystallographic information for the structural refinement of **2**.

Empirical Formula	GeCoN ₆ C ₅₄ BH ₄₉
Formula weight	924.32 g/mol
Temperature	100.0 K
Wavelength	1.54178 Å
Crystal System	Trigonal
Space Group	<i>R</i> -3
Unit Cell Dimensions	<i>a</i> = 12.4224(6) Å, α = 90.0° <i>b</i> = 12.4224(6) Å, β = 120.0° <i>c</i> = 48.074(4) Å, γ = 90.0°
Volume	6424.7(8) Å ³
<i>Z</i>	6
Density (calculated)	1.433 g/cm ³
Absorption coefficient	4.254 mm ⁻¹
<i>F</i> ₀₀₀	2874.0
Crystal color	Purple
Crystal size	0.398 × 0.384 × 0.110 mm ³
2 θ range	2.757 to 68.026°
Index ranges	-14 ≤ <i>h</i> ≤ 9 -14 ≤ <i>k</i> ≤ 14 -57 ≤ <i>l</i> ≤ 56
Reflections collected	27268
Independent reflections	2606 [<i>R</i> _{int} = 0.0228]
Completeness to θ = 60.128°	99.92 %
Absorption correction	Multi-scan
Maximum and minimum transmission	0.3824 and 0.2160
Refinement method	Full-matrix least-squares on <i>F</i> ²
Data / restraints / parameters	2606 / 0 / 173
Goodness-of-fit on <i>F</i> ^{2a}	1.075
Final <i>R</i> indices [<i>I</i> > 2 σ (<i>I</i>) = 10408 data] ^b	<i>R</i> ₁ = 3.37 %, <i>wR</i> ₂ = 8.62 %
<i>R</i> indices (all data, 0.80 Å)	<i>R</i> ₁ = 3.40 %, <i>wR</i> ₂ = 8.64 %
Largest diff. peak and hole	0.54 and -0.34 e.Å ⁻³

^a GooF = $[\sum[w(F_o^2 - F_c^2)^2] / (n-p)]^{1/2}$ where *n* is the number of reflections and *p* is the total number of parameters refined. ^b*R*₁ = $\sum||F_o| - |F_c|| / \sum|F_o|$; *wR*₂ = $[\sum[w(F_o^2 - F_c^2)^2] / \sum[w(F_o^2)^2]]^{1/2}$

Table S3.2 | Crystallographic information for the structural refinement of **3**.

Empirical Formula	SnCoN ₆ C ₅₄ BH ₄₉
Formula weight	970.42 g/mol
Temperature	100.0 K
Wavelength	0.71073 Å
Crystal System	Monoclinic
Space Group	<i>R</i> -3
Unit Cell Dimensions	<i>a</i> = 12.373(2) Å, α = 90.0° <i>b</i> = 12.373(2) Å, β = 120.0° <i>c</i> = 48.707(8) Å, γ = 90.0°
Volume	6458(2) Å ³
<i>Z</i>	6
Density (calculated)	1.497 g/cm ³
Absorption coefficient	1.012 mm ⁻¹
<i>F</i> ₀₀₀	2982.0
Crystal color	Purple
Crystal size	0.516 × 0.344 × 0.050 mm ³
2 θ range	3.892 to 64.18°
Index ranges	-17 ≤ <i>h</i> ≤ 17 -17 ≤ <i>k</i> ≤ 17 -70 ≤ <i>l</i> ≤ 70
Reflections collected	51077
Independent reflections	4682 [<i>R</i> _{int} = 0.0371]
Completeness to θ = 64.18°	100.0 %
Absorption correction	Multi-scan
Maximum and minimum transmission	0.2679 and 0.2211
Refinement method	Full-matrix least-squares on <i>F</i> ²
Data / restraints / parameters	4682 / 0 / 173
Goodness-of-fit on <i>F</i> ^{2a}	1.055
Final <i>R</i> indices [<i>I</i> > 2 σ (<i>I</i>) = 10408 data] ^b	<i>R</i> ₁ = 5.35 %, <i>wR</i> ₂ = 14.83 %
<i>R</i> indices (all data, 0.80 Å)	<i>R</i> ₁ = 6.87 %, <i>wR</i> ₂ = 16.01 %
Largest diff. peak and hole	4.87 and -0.98 e.Å ⁻³

^a GooF = $[\sum[w(F_o^2 - F_c^2)^2] / (n-p)]^{1/2}$ where *n* is the number of reflections and *p* is the total number of parameters refined. ^b*R*₁ = $\sum||F_o| - |F_c|| / \sum|F_o|$; *wR*₂ = $[\sum[w(F_o^2 - F_c^2)^2] / \sum[w(F_o^2)^2]]^{1/2}$

Table S3.3 | Simulation parameters for X-band EPR spectra of **2** and **3**.

Compound	D (cm ⁻¹)	E (cm ⁻¹)	g_{\parallel}	g_{\perp}
2	3.9	0.52	2.28	2.26
3	12.0	0.70	2.25	2.31

Table S3.4 | Fit parameters to the variable-temperature, variable-field magnetization curves for **1 – 3**.

Compound	D (cm ⁻¹)	E (cm ⁻¹)	g_{\parallel}	g_{\perp}
1	2.0(3)	--	2.06(4)	2.06(4)
2	3.9(3)	0.52(3)	2.20(2)	2.20(2)
3	11.9(1)	0.7(1)	2.28(2)	2.28(2)

Table S3.5 | Fitted AOM parameters for **2** and **3**. (E = Ge, Sn)

Compound	$\xi_{\text{eff}} (\text{cm}^{-1})$	B	$\epsilon_{\sigma}(\text{N}) (\text{cm}^{-1})$	$\epsilon_{\pi\text{s}}(\text{N}) (\text{cm}^{-1})$	$\epsilon_{\sigma}(\text{E}) (\text{cm}^{-1})$	$\epsilon_{\pi}(\text{E}) (\text{cm}^{-1})$
2	357	677	3235	1	2145	-934
3	531	678	3401	129	2363	-633

Table S3.6 | Tabulated experimental and calculated band energies from the AOM analysis from a ${}^4\text{A}_2$ ground state, assignments in $\text{C}_{3\text{v}}$ symmetry with T_d origins in parentheses. All values are given in units of cm^{-1} .

Compound	${}^4\text{E} (\text{T}_2, \text{F})$	${}^4\text{A}_1 (\text{T}_2, \text{F})$	${}^4\text{E} (\text{T}_1, \text{F})$	${}^4\text{A}_2 (\text{T}_1, \text{F})$	${}^4\text{A}_2 (\text{T}_1, \text{P})^*$	${}^4\text{E} (\text{T}_1, \text{P})$
2						
observed	not obsd	forbidden	5956	9124	14225 14663	15267
calculated	2988	4500	5915	8966	14628	15303
3						
observed	not obsd	forbidden	5959	9355	14641	15384
calculated	2906	4628	5992	9308	14572	15452

*Multiple transitions observed to this spin-allowed state due to coupling to states arising from ${}^2\text{G}$ free-ion term.

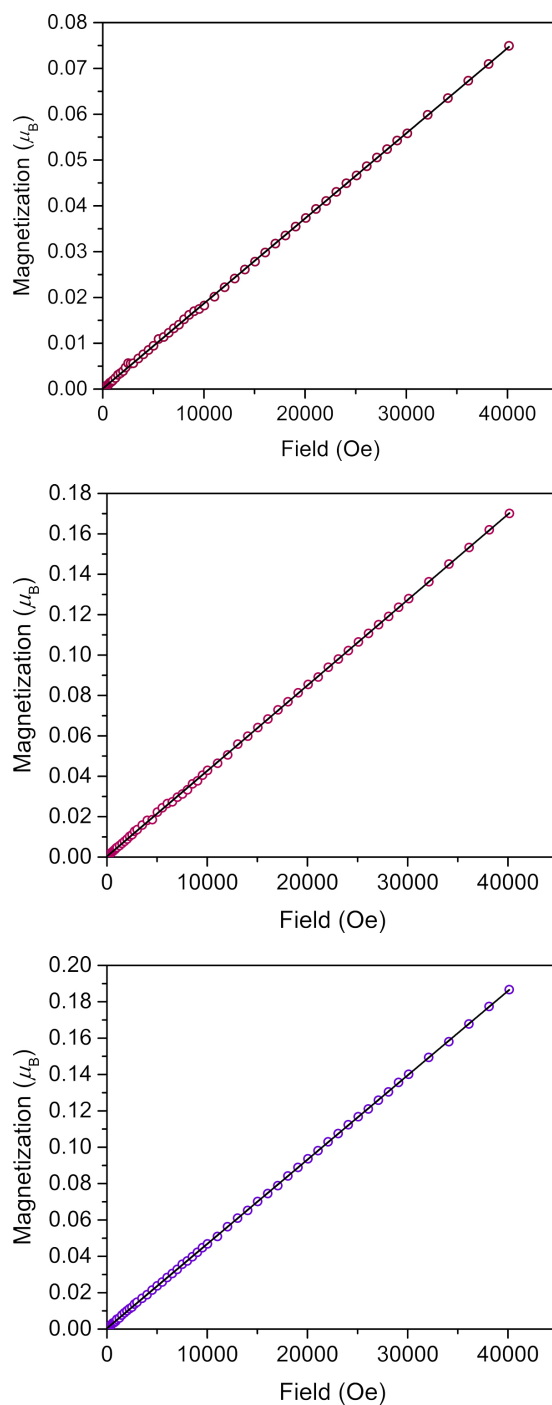


Figure S3.1 | Variable-field magnetization data for **1** (top), **2** (middle), and **3** (bottom) collected restrained under eicosane acquired at 100 K. The black line is a linear fit to the data illustrating the absence of ferromagnetic impurities.

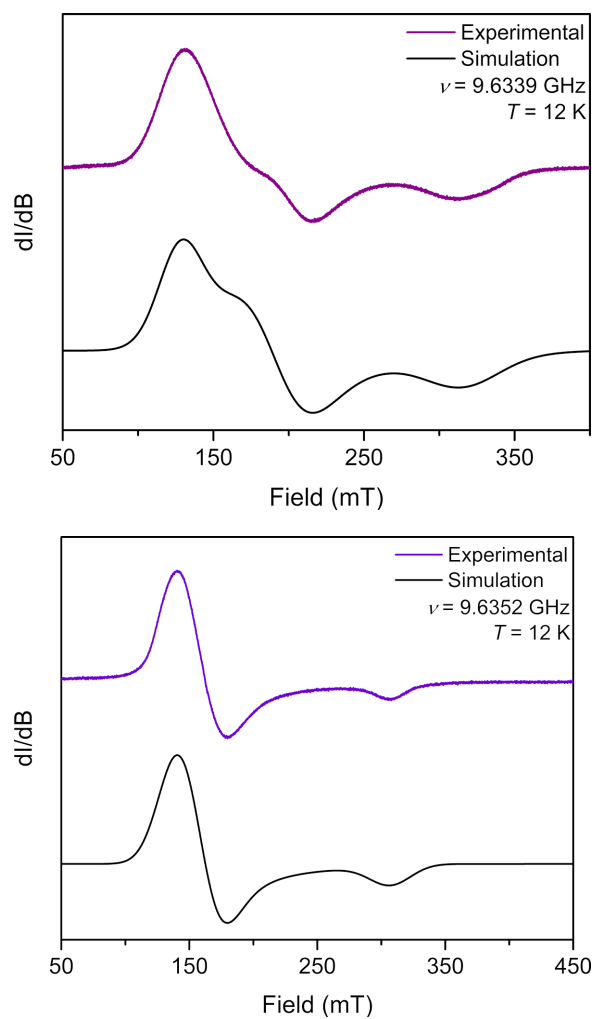


Figure S3.4 | X-band EPR spectra of **2** (top) and **3** (bottom) measured at 12 K encased in eicosane. Parameters for the simulation are given in Table S3.3.

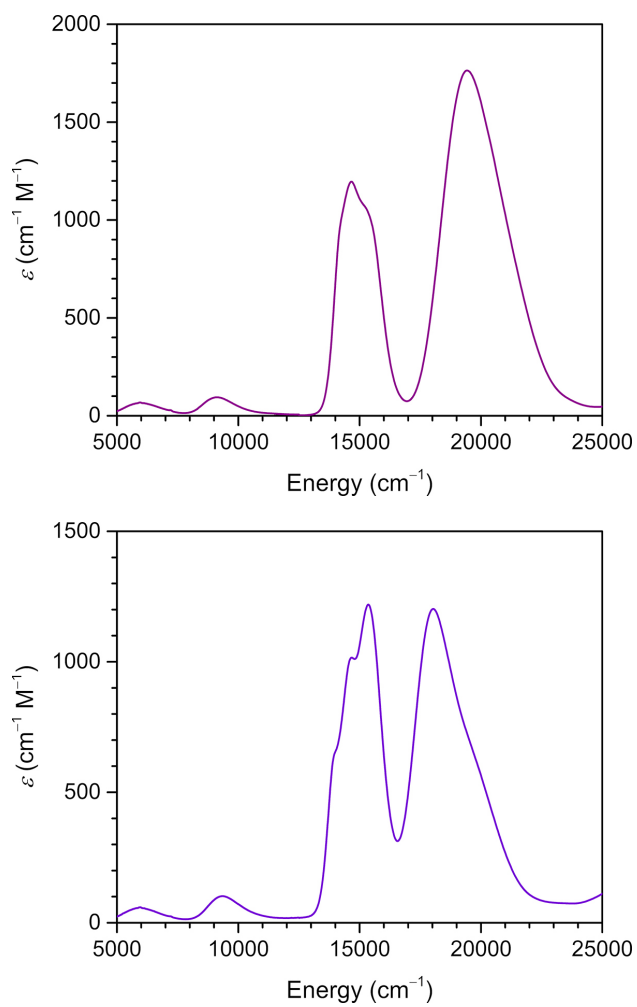


Figure S3.5 | Electronic absorption spectra of **2** (top) and **3** (bottom) measured at room temperature in CDCl_3 .

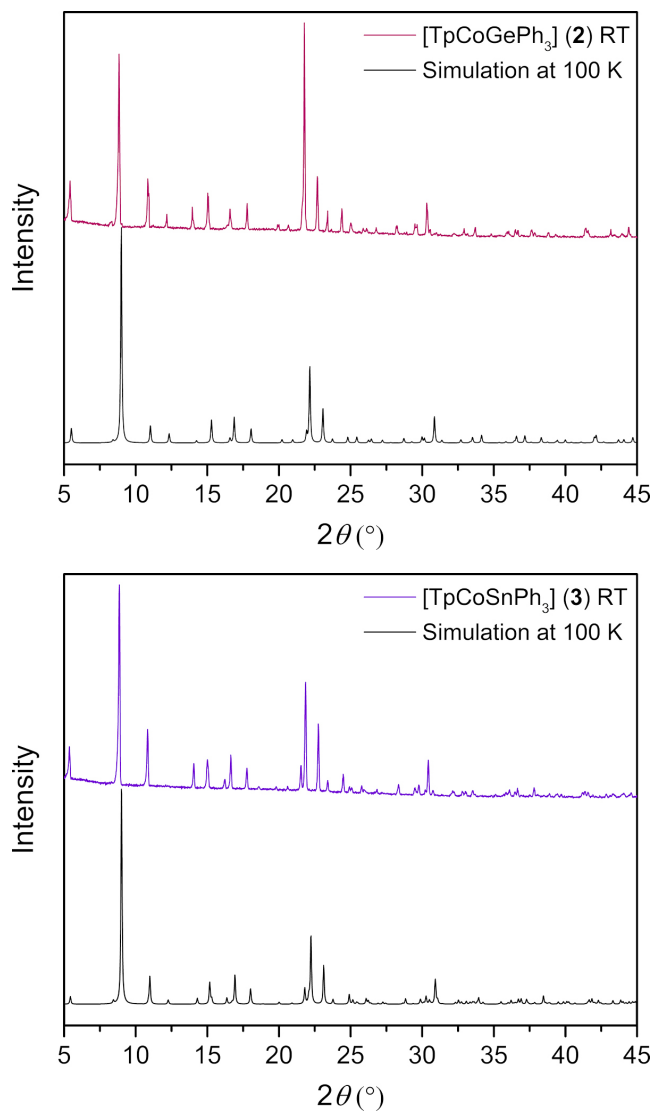


Figure S3.6 | Powder X-ray diffraction patterns for **2** (top) and **3** (bottom) measured at room temperature with CuK α radiation. The bottom patterns are simulations from the single crystal X-ray diffraction data measured at 100K.

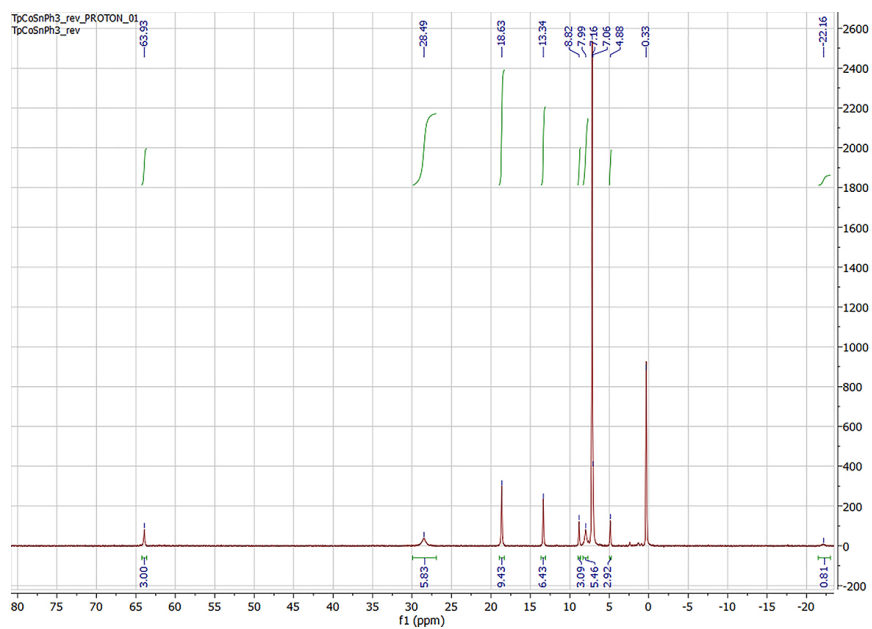
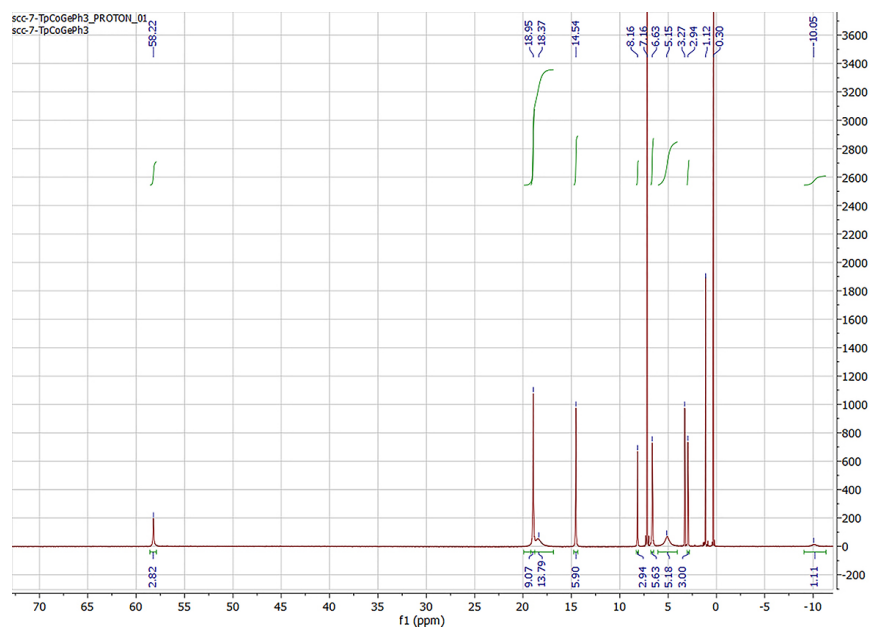


Figure S3.7 | ^1H nuclear magnetic resonance spectrum of **2** (top) and **3** (bottom) measured in C_6D_6 at room temperature.

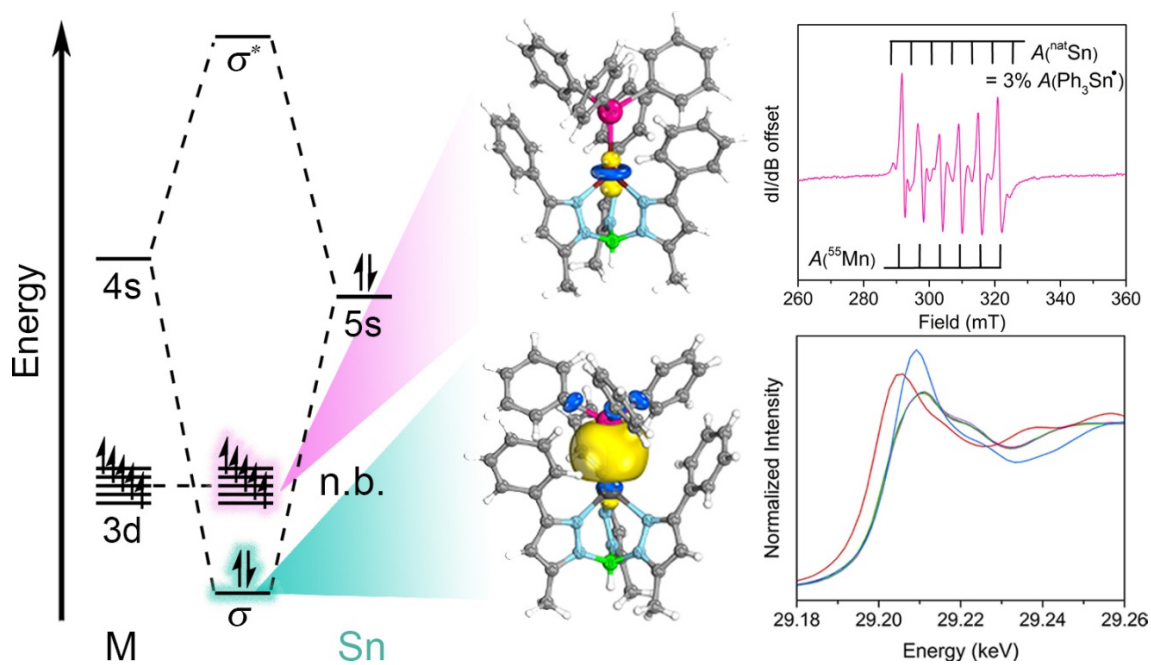
Chapter Four: Orbital Energy Mismatch Engenders High-Spin Ground States in Heterobimetallic Complexes

Reprinted with permission from:

Coste, S. C.; Pearson, T. J.; Altman, A. B.; Klein, R. A.; Finney, B. A.; Hu, M. Y.; Alp, E. E.; Vlaisavljevich, B.; Freedman, D. E. *Chem. Sci.* **2020**, *11*, 9971-9977.

Copyright 2020 Royal Society of Chemistry

This section was written in collaboration with the co-authors listed above



Introduction

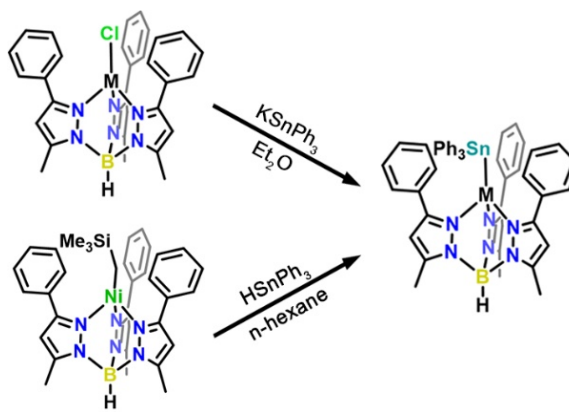
Synthetic control over spin state in transition metal complexes is crucial for tuning magnetic properties¹ and reactivity.^{2□7} An intriguing method for creating high-spin bimetallic complexes is inspired by lanthanide complexes, in which the f orbitals are spatially contracted and thus do not interact with the ligand field. In transition metal complexes we can engineer an energetic mismatch between the frontier orbitals of the ligands and the 3d orbitals of the metal to afford a similar orbital depiction. From a molecular orbital (MO) perspective, poor energetic alignment between ligand donor and metal d orbitals would yield highly localized d orbitals exhibiting minimal interaction with the ligand field. We hypothesize using a heavy main group metal donor, such as Sn, could facilitate this energy mismatch as its electropositivity and larger principal quantum number theoretically render higher energy frontier orbitals.⁸ This approach will also provide key insight into the electronic structure of transition metal-Sn complexes which are of interest for cooperative catalysis^{9□12} and radical-based transformations.^{13□16}

Herein, we report an isostructural series of transition metal-Sn complexes, $[\text{Ph}_3\text{MeTp}^-\text{M}(\text{SnPh}_3)]$ ($\text{Ph}_3\text{MeTp}^- = \text{hydrotris}(3\text{-phenyl-5-methylpyrazolyl})\text{borate}$; $\text{M} = \text{Mn}$ (**3**), Fe (**4**), Co (**5**), Ni (**6**), Zn (**7**)), in which high spin ground states are stabilized by an unusual bonding interaction. Using a series of first row transition metals allows us to probe the ligand field from various techniques while controlling metal-metal covalency to understand bonding. Despite a covalent interaction between the Sn and the transition metals, i.e. a similar atomic contribution to a bonding MO, Sn minimally interacts with the 3d manifold of the transition metal. This yields highly localized d orbitals on the transition metal exhibiting a weak field electronic structure. We attribute this observation to energetic mismatch between the 5s/5p donor orbitals of Sn and the 3d orbitals of the transition metal.

Results and Discussion

We targeted unsupported metal-metal bonds to diminish the impact of ancillary ligands on the electronic structure. A divalent metal (Mn^{2+} , Fe^{2+} , Co^{2+} , Ni^{2+} , Zn^{2+}) is capped with hydrotris(3-phenyl-5-methylpyrazolyl) borate ($^{\text{Ph,Me}}\text{Tp}^-$) leaving an open axial site for Sn coordination. Reacting this fragment with the organometallic anion, triphenyl stannide (Ph_3Sn^-), yielded the desired four-coordinate complexes featuring unsupported metal-metal bonds between these transition metals and Sn. We accessed complexes **3** – **7** via two routes as shown in Scheme 1. Compounds **3**, **4**, **5**, and **7** form by metathesis of $^{\text{Ph,Me}}\text{TpMCl}$ ($\text{M} = \text{Mn}^{2+}$ (**1**), Fe^{2+} , Co^{2+} , Zn^{2+} (**2**))^{17,18} with KSnPh_3 in diethyl ether.¹⁹ To access **6**, we reacted a trimethylsilyl Ni complex with HSnPh_3 in n-hexane to eliminate trimethylsilane as **6** was unstable towards metathesis reaction conditions. Further synthetic details are available in the supporting information.

The molecular structures of **3** – **6** were determined from single crystal X-ray diffraction. The structures (Fig. 4.1) show that both metals exist in a pseudo-tetrahedral environment connected by an unsupported metal-metal bond. These complexes crystallize isostructurally in $R\bar{3}$, as corroborated by PXRD (Fig. S4.1), with the metal-metal bond coinciding with the 3-fold rotation axis. The M–Sn bond distances in complexes **3**, **4**, **5**, **6**, and **7** (2.757(1), 2.698(1), 2.654(1), 2.668(1), and 2.603(1) Å respectively) are similar to or shorter than the sum of their covalent radii suggesting the presence of covalent bonding.²⁰ Analysis of the bonding via Cotton's formal shortness ratio (FSR) yields values of 1.040, 1.018, 1.010, 1.017, and 0.962, respectively.^{21,22} The similar



Scheme 4.1. Synthetic pathways to **3** – **7**. $\text{M} = \text{Mn}$, Fe , Co , Ni , Zn .

values demonstrate that the metal-metal bonds have comparable bond order but that the Zn-Sn bond in **7** is the strongest. The vibrational Raman spectra (Fig. S4.2) support this analysis where the metal-metal stretching frequencies of **3** – **6** are between 170 – 173 cm^{-1} but the stretching mode in **7** is 180 cm^{-1} .

We probed the spin ground state in complexes **3** – **6** using SQUID magnetometry. Variable-temperature dc magnetic susceptibility data (shown in Fig. 4.2) on polycrystalline samples of **3**, **4**, **5**, and **6** display room-temperature χ_{MT} values of 4.32, 3.58, 2.11, and 1.36 $\text{cm}^3 \text{K mol}^{-1}$ in accordance with $S = 5/2$, $S = 2$, $S = 3/2$, and $S = 1$ ground states, respectively. The room-temperature values persist down until ~ 15 K in **3** and **6** or ~ 100 K in **4** and **5**, which we attribute to the presence of zero-field splitting, D , a parameter for magnetic anisotropy. The high-spin state in the M–Sn bonded complexes here is rare as many such compounds feature low-valent strong-field environments.^{23,24} The high-spin nature here provides a unique opportunity to probe the ligand field influence of Sn to assess the metal-metal bonding.

We began our assessment of the ligand field in **3** – **6** with electronic absorption and ^{57}Fe Mössbauer spectroscopy. Diffuse reflectance spectra of **3** – **6** (Fig. 4.3) show charge transfers in the UV-visible region and d-d transitions at lower energies. We assign the former as $\text{Ph}_3\text{Sn} \rightarrow \text{M}$

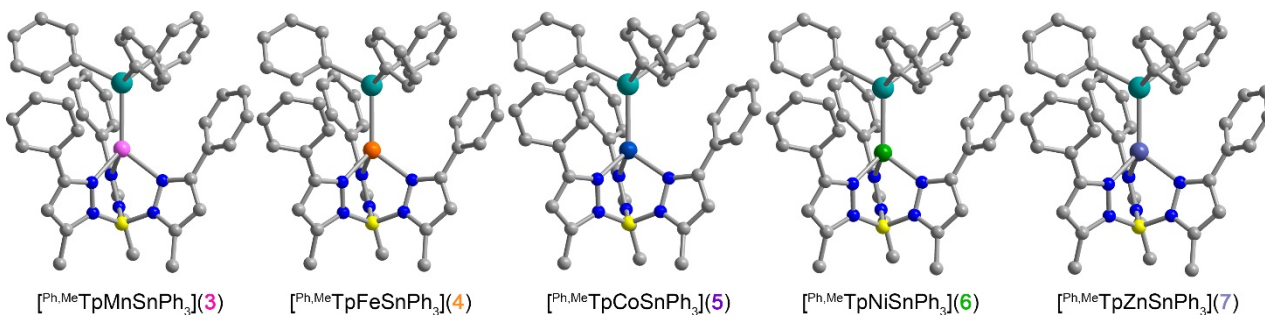


Figure 4.2 Molecular structures of the $[\text{Ph,MeTpMSnPh}_3]$ series determined by X-ray crystallography where $\text{M} = \text{Mn}$ (**3**), Fe (**4**), Co (**5**), Ni (**6**), and Zn (**7**). The blue, grey, yellow, turquoise, pink, orange, cobalt blue, green, and purple spheres represent nitrogen, carbon, boron, tin, manganese, iron, cobalt, nickel, and zinc atoms respectively. The hydrogens are omitted for clarity.

(M = Mn, Fe, Co, Ni) metal-to-metal charge transfer (MMCT) reflecting the stability of Sn's higher oxidation states. This assignment is supported by the lack of comparable CT bands in the parent chloride compounds and by the similar intensity between the CT ($\sim 10^3 \text{ L mol}^{-1} \text{ cm}^{-1}$) and higher energy d-d transitions.^{25,26} The MMCT band red-shifts linearly with increasing transition metal electronegativity (Fig. S4.5), implying the energetic stabilization of the acceptor d orbitals with increasing electronegativity.^{27,28} The d-d transition energies and intensities in **5** and **6** are characteristic of 4A_2 and 3A_2 ground states, implying the following frontier orbital energy ordering: $e(d_{xz}, d_{yz}) > a_1(d_{z^2}) > e(d_{xy}, d_{x^2-y^2})$.^{39,29,30} The ^{57}Fe Mössbauer spectrum of **4** at 80 K (Fig. 4.3b) corroborates a similar d orbital ordering where the isomer shift ($\delta = 0.742(1) \text{ mm s}^{-1}$) and ΔE_Q values ($1.061(3) \text{ mm s}^{-1}$) are similar to other C_{3v} -symmetric ferrous complexes with a 5E ground state (tabulated in Table S4.7).^{31,32} Importantly, the d-d transition energies of **4** – **6** are lower than that of structurally similar Tp^- metal halide complexes suggesting a weak ligand field environment. This contrasts with previous studies of Sn ligands, which characterize it as a relatively strong σ -donor.^{33–36} This discrepancy prompted us to investigate the degree of Sn character in the 3d-based MOs.

To probe the contribution of Sn towards the d orbitals, we used the zero-field splitting and hyperfine parameters from magnetometry and electron paramagnetic resonance (EPR) spectroscopy. As magnetic anisotropy stems from spin-orbit coupling (SOC), we would expect a high degree of covalency between 3d orbitals and the heavy Sn donor to yield larger axial zero field splitting (D) values compared to lighter ligands with smaller SOC constants.³⁷ We quantified the magnetic anisotropy in **4** – **6** using SQUID magnetometry, specifically through variable-field, variable-temperature magnetization data (Fig. S4.7); the magnetic properties of **5** were reported previously.¹⁹ Using the program DAVE 2.0,³⁸ we simulated the magnetization data with the spin

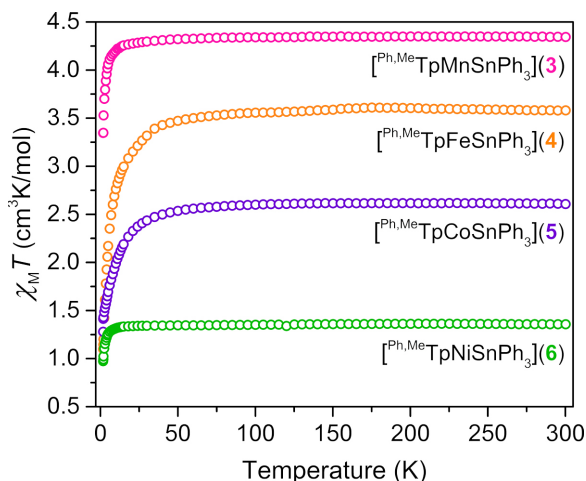


Figure 4.2 (a) Temperature dependent magnetic susceptibility of polycrystalline powders of **3** – **6** collected under an applied field of 0.1 T.

and $-3.0(2) \text{ cm}^{-1}$ ($E/D = 0$), respectively. These values are both surprisingly small relative to isoelectronic C_{3v} symmetric complexes regardless of donor SOC.^{39–41,42–45}

The D value and hyperfine analysis of **3** were determined through X-band EPR spectroscopy. A spectrum of a solid state dilution of **3** in **7** (1:20 Mn:Zn) is shown in Fig. 4.4 where Sn hyperfine is prevalent in the intra-Kramers ($M_S = \pm 1/2$) transition (inset). We modelled the spectrum using EASYSPIN⁴⁶ with the following spin Hamiltonian, $\hat{H} = g_{\text{iso}}\mu_B\mathbf{S}\mathbf{H} + \mathbf{A}\mathbf{I}\mathbf{S} + D[\hat{S}_z^2 - S(S+1)/3]$ where all parameters hold their previous definitions and A is the hyperfine coupling tensor and I is the nuclear spin. The best simulation to the EPR spectrum of **3** at 12 K (shown in Fig. S4.9) reveals a D value of

Hamiltonian $\hat{H} = g_{\text{iso}}\mu_B\mathbf{S}\mathbf{H} + D[\hat{S}_z^2 - S(S+1)/3] + E(\hat{S}_x^2 - \hat{S}_y^2)$ where g_{iso} is the isotropic g -value, μ_B is the Bohr magneton, S is the spin quantum number, H is the applied magnetic field, D is the axial zero-field splitting parameter, and E is the transverse zero-field splitting parameter. The D values extracted for **4**, **5**, and **6** from the simulations are $12.9(3) \text{ cm}^{-1}$ ($E/D = 0.26$), $11.9(1) \text{ cm}^{-1}$ ($E/D = 0.06$)

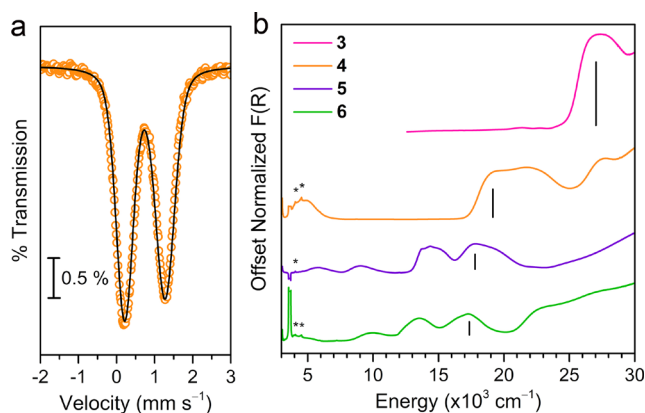


Figure 4.3 (a) ^{57}Fe Mossbauer spectra for a powder sample of **4** collected at 80 K. Open circles represent the experimental data, and the black line represents the fit to the spectrum. (b) Diffuse reflectance of **3** – **6** measured in KBr at room temperature where the black bars mark the MMCTs. The asterisks mark absorbances from the ligand, and the water absorbance at $\sim 3,300 \text{ cm}^{-1}$ has been manually removed from the data.

0.1015(6) cm^{-1} at 12 K, which is much smaller in comparison to D values with heavy atom donors such as iodide.^{47,48} Remarkably, the D value of **1**, with the notably ionic axial Cl donor to Mn replacing Sn, is almost twice that of **3** corroborating the relatively small D values from magnetometry in **4** – **6**. The D values reported here broadly suggest there is little SOC contribution from the heavy Sn donor towards magnetic anisotropy.

Analysis of the metal hyperfine parameters in Fig. 4.4 yields a $^{\text{nat}}\text{Sn}$ hyperfine coupling ($I = 1/2$ for ^{115}Sn , ^{117}Sn , and ^{119}Sn) of 141(3) MHz and a ^{55}Mn hyperfine coupling ($I = 5/2$) of 164(2) MHz. The ^{55}Mn hyperfine coupling parameter is low relative to other Mn^{2+} species, which can be attributed to the presence of covalent bonding based on previous observations.⁴⁹ Despite the comparable metal hyperfine magnitude, the $^{\text{nat}}\text{Sn}$ hyperfine in **3** is only ~3% as large as Sn-centered radicals, such as $\text{Ph}_3\text{Sn}\cdot$ (5230 MHz) where the spin density is completely localized at the Sn nucleus.⁵⁰ This suggests there is little covalency between the $3d_z^2$ based orbital and the Sn donor orbitals. The foregoing analyses indicate a lack of Sn character in the d-based MOs suggesting an ionic interaction.

To assess the covalency of the metal-metal bonds in **3** – **7**, we used X-ray spectroscopic techniques to probe the electron distribution about the Sn nucleus. The X-ray absorption near-edge spectra (XANES) at the Sn K-edge are shown in Fig. 4.5a. The XANES region are similar in **3** – **7** where the intensities and onset energy overlay well. The onset energy, defined by the energy of the inflection point (better illustrated by plotting the first derivative shown in Fig. S4.9), for each compound is 29201.7 eV. This indicates that the Sn valency does not change between **3** – **7** within the resolution limit of the Sn K-edge.^{51–54} Importantly, the onset energies of **3** – **7** are between that of the SnO and SnO₂ references, 29200.1 and 29203.4 eV respectively, alluding to a Sn valency between +2 and +4. Comparison of the onset energy between **3** – **7** with structurally similar

organometallic controls, ~ 29201.1 eV for Ph_3SnX ($X = \text{SnPh}_3, \text{Ph}, \text{Cl}, \text{and F}$), further corroborates the apparent Sn valency (Fig. S4.9). This observation matches the valence trends in ^{119}Sn Mossbauer spectra of transition metal- Sn^{2+} complexes where the isomer shift values are closer to those of Sn^{4+} than Sn^{2+} .⁹ We attribute these observations to significant donation of s-electron density from the Sn nucleus towards the transition metal. The apparent Sn valency from XAS therefore suggests covalent M–Sn bonding throughout the series with high Sn character.

We examined covalency changes more precisely by determining the ^{119}Sn quadrupole splitting parameter, ΔE_Q , using synchrotron Mössbauer spectroscopy (SMS) of the ^{119}Sn nucleus. The SMS data at 60 K are shown in Fig. 4.5b with fits to the data yielding ΔE_Q values of 0.623(3), 1.198(2), 1.204(4), 1.134(2), and 0.896(2) mm s^{-1} for complexes **3**, **4**, **5**, **6**, and **7**, respectively.

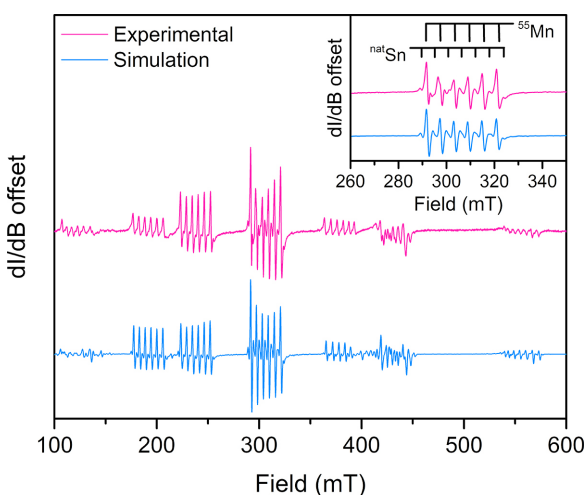


Figure 4.4 Overlay of the experimental (pink) cw-EPR spectrum of **3** diluted in a polycrystalline sample of **7** (Mn:Zn 1:20) and the simulation (light blue) at room temperature collected at X-band ($\nu = 9.6328$ GHz). Inset: A zoomed image of the intra-Kramers ($M_S = \pm 1/2$) transition. The light blue spectrum was simulated using the following parameters: $g_{\text{iso}} = 1.9933(2)$, $S = 5/2$, $A_{\text{iso}}(^{55}\text{Mn}, I = 5/2) = 164(2)$ MHz, $A_{\text{iso}}(\text{natSn}, I = 1/2) = 141(3)$ MHz, $D = 0.0939(4)$ cm^{-1} .

We find a linear correlation of the ^{119}Sn ΔE_Q values here with the Pauling electronegativities of the transition metal (shown in Fig. S4.10) where higher electronegativities engender larger ΔE_Q values. This trend can be extended towards formally tetravalent Ph_3SnX species ($X = \text{I}, \text{Br}, \text{Cl}, \text{OH}, \text{F}$) indicating the ΔE_Q values correlate with the polarity of the axial bond to Ph_3Sn . We interpret this trend in our bimetallic series as a change in the M–Sn bond polarity with electron density shifting towards M in more electronegative transition metals.

To complement the spectroscopic analysis of the bonding interaction, we turned to theoretical calculations (details in supporting information). We employed both density functional theory (DFT) and complete active space self-consistent field calculations with corrections from second-order perturbation theory (CASSCF/CASPT2) to analyse the bonding in the ground state. The Mayer bond orders (MBOs) from DFT and CASSCF (Table S4.14) both confirm a single M–Sn bond with **7** having the strongest bond (MBO of ~ 0.8 in **7** versus ~ 0.6 for **3** – **6**) corroborating analysis of the Raman spectra. Hirshfeld charge decomposition analysis (Tables S4.17 – S18) of the sigma bond, which divides the atomic contribution of each element towards a molecular orbital (MO), corroborates that the bond is a polar-covalent interaction with a majority of Sn character. Furthermore, the decomposition agrees with the ^{119}Sn ΔE_Q values where the ratio of % atomic contribution (M:Sn) to the bond changes from 0.57 in **3** to 0.75 in **6**. The X-ray spectroscopy and CASSCF

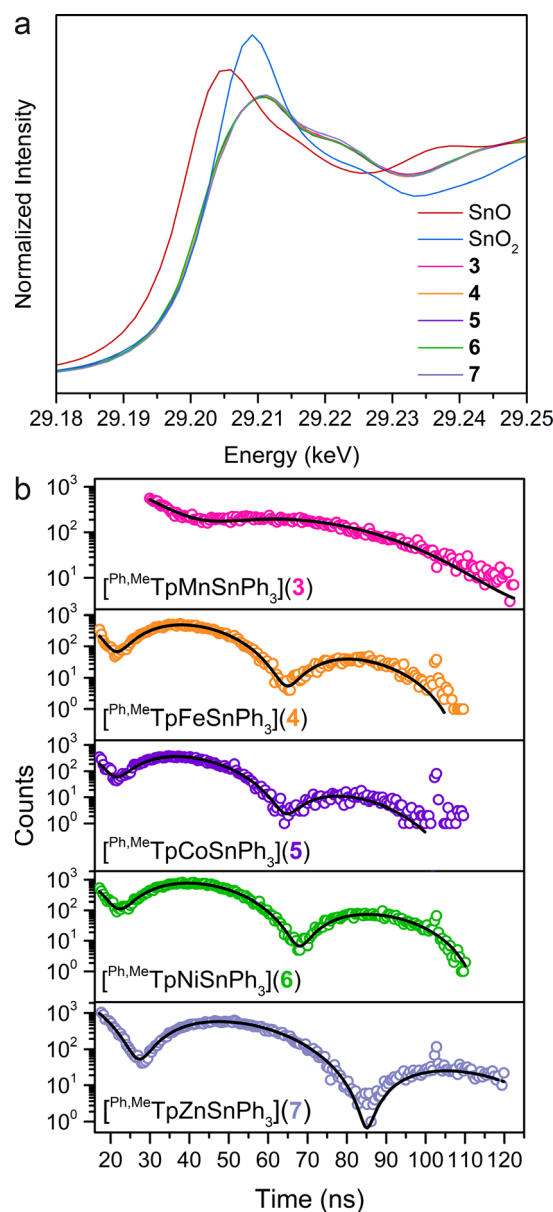


Figure 4.5 (a) The XANES spectra at the Sn K-edge for polycrystalline samples of **3** – **7** (29200.4 eV for Sn metal reference), including SnO and SnO₂ standards, measured at 25 K. (b) ^{119}Sn synchrotron Mössbauer spectra of **3** – **7** collected at 60 K. Open circles represent the experimental data, and the black lines represent fits to the spectra.

calculations both support a polar-covalent metal-metal interaction which is more polar with less electronegative transition metals.

Computational investigation of the d-based orbitals in **3** – **6** corroborate a lack of Sn character despite the covalent bond. The calculations confirm the ground states of complexes **3** – **6** in accordance with the magnetometry, EPR, and electronic absorption data; some of the natural orbitals for **3** are shown in Fig. 4.6 for illustration. The calculated D values (Table S4.20) and electronic excited states (Table S4.21) agree with the experimental magnetic data and absorption spectra supporting an accurate description of the electronic structure. Close inspection of the natural orbital with $3d_{z^2}$ character reveals the weak ligand field is attributable to a lack of M–Sn antibonding character. This analysis demonstrates that we cannot treat Sn as a ligand in a traditional sense, since the d-orbitals do not mix appreciably with the Sn orbitals. This is best illustrated by Hirshfeld charge decomposition analysis of the frontier molecular orbitals where the $3d_{z^2}$ orbital has ~2.4% average Sn character for **3** – **6**. Interestingly, the 4d orbitals have much more Sn character where the $4d_{z^2}$ orbital has ~11.7% average Sn contribution. The MOs with M–Sn antibonding character are much higher in energy as evidenced by natural orbital occupation numbers (Figs. S11 – S14). Therefore, the 3d orbitals are essentially localized on the transition metal and non-bonding with respect to Sn in **3** – **6**.

The aggregate data here allow us to construct a qualitative MO picture (shown in Fig. 4.6) which describes the M–Sn bonding interaction. A foundational aspect of ligand field theory towards describing metal-ligand interactions is the introduction of covalency which implies d orbital-based MOs have metal-ligand antibonding character. Indeed, crystallographic, spectroscopic, and theoretical data shows that the Sn donor forms a polar-covalent bond in which electron density shifts away from Sn with more electronegative transition metals. However, we

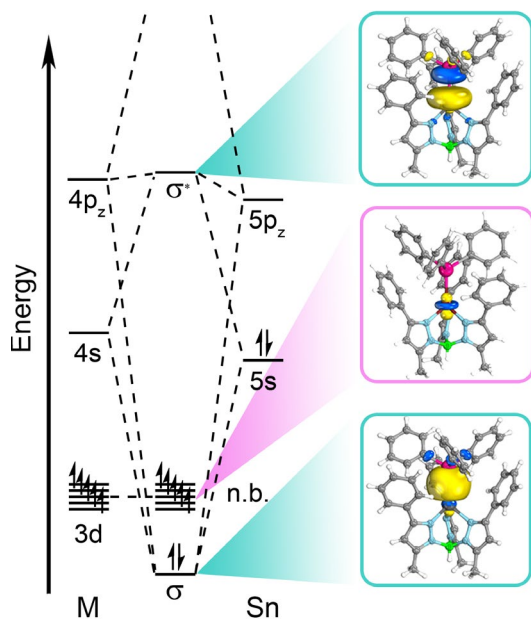


Figure 4.6. Qualitative molecular orbital diagram depicting the natural orbitals of the σ -bonding and -antibonding orbitals and the orbital with primarily $3d_{z^2}$ orbital character for compound **3**.

is energetic mismatch between the M 3d orbitals and the electropositive Sn donor orbitals. The Hirshfeld charge decomposition analysis supports this as the higher lying M 4s, 4p, and 4d orbitals have more atomic Sn contribution than the 3d-based MOs. This suggests that the localization of the M 3d orbitals are due to the higher energy of the Ph_3Sn donor orbitals relative to the 3d orbitals. This energetic mismatch is supported by atomic ionization potentials and energies of the hydrogen-like atomic orbitals.⁵⁵

Conclusions

The comprehensive study reported herein illuminates the importance of energetic alignment in governing orbital interactions and spin ground states. Specifically, the better alignment of Sn donor orbitals with transition metal 4s and 4p orbitals yield highly localized, non-bonding 3d orbitals. This engenders a weak ligand field about the transition metal stabilizing a high-spin ground state, unusual to bimetallic complexes. Understanding such factors governing

find that the 3d-based MOs have no M-Sn antibonding character, countering the classical MO description of coordination complexes. Consequently, the electronic and magnetic properties in **3** – **6** are more like a free ion description with respect to the M 3d orbitals despite the covalent M-Sn interaction. This is surprising as the Sn 5s/5p_z and M 3d_{z²} orbitals have appropriate symmetry and orbital overlap to form a bonding interaction.

We argue that the origin for this observation

metal-metal interactions will be crucial in cooperative catalysis and targeting spin-selective reactivity. This demonstrates the potential use of electropositive main group metals in stabilizing unusual electronic structures. Furthermore, the bonding analysis here represents an advancement in the fundamental understanding of metal-metal interactions, particularly with Sn which has been proposed to promote inverted ligand fields.⁵⁶

Supplementary Information

Experimental Details.

General Considerations. All compounds were manipulated and handled under a dinitrogen atmosphere in an MBraun Unilab Pro glovebox. All glassware was either oven-dried at 150 °C for at least four hours or flame-dried prior to use. Dichloromethane (DCM), methanol (MeOH), Diethylether (Et₂O), benzene, toluene, and n-hexane were dried using a commercial solvent purification system from Pure Process Technology and stored over 3 or 4 Å sieves for a minimum of one day prior to use. CDCl₃ and C₆D₆ were purchased from Cambridge Isotope Labs, deoxygenated by three successive freeze-pump-thaw cycles, filtered through a pad of activated alumina, and stored over 3 or 4 Å sieves prior to use. KTp^{Ph,Me}, ^{Ph,Me}TpFeCl, ^{Ph,Me}TpCoCl, and [^{Ph,Me}TpNiCH₂SiMe₃]^{1/2} hexane, and [^{Ph,Me}TpCoSnPh₃] were prepared according to literature procedures.^{57–61} HSnPh₃ was purchased from MilliporeSigma and vacuum distilled prior to use. All other chemicals were used as received. Silylated Celite was prepared by stirring 25 g activated, dried Celite 545 in 100 mL toluene with 14 mL trimethylsilylchloride and 14 mL of triethylamine under N₂ overnight at 40 °C, followed by filtration, washing with 80 mL MeOH and 200 mL toluene, and drying for 24 hours at 100 °C.

[^{Ph,Me}TpMnCl](1). A solution of KTp (1.0463 g, 2.00 mmol) in 15 mL DCM was added to a stirring solution of MnCl₂ (0.2573 g, 2.04 mmol) in 3 mL MeOH at room temperature. The white, cloudy solution was allowed to stir overnight at room temperature. The reaction mixture was subsequently pumped down to dryness. The product was extracted into 20 mL DCM, filtered through a Celite pad on a fritted filter, and then concentrated to about 4 mL. Crystalline product suitable for X-ray diffraction was obtained by adding 15 mL of n-hexane and allowing it to sit at

room temperature overnight. The white needles were then isolated by decanting the mother liquor, washing with 3 x 5 mL n-hexane, and drying *in vacuo*. Yield: 0.4563 g (39.7%). IR (ATR, cm^{-1}): 3131 (w), 3057 (w), 2968 (w), 2927 (w), 2909 (w), 2570 (w), 1577 (w), 1570 (w), 1558 (w), 1541 (m), 1521 (w), 1507 (m), 1497 (w), 1486 (m), 1478 (m), 1464 (w), 1456 (w), 1450 (m), 1431 (m), 1410 (m), 1400 (w), 1387 (w), 1379 (w), 1357 (m), 1341 (m), 1323 (m), 1304 (m), 1282 (w), 1188 (m), 1172 (m), 1156 (m), 1106 (m), 1096 (m), 1067 (s), 1041 (m), 1030 (w), 999 (w), 993 (w), 977 (m), 913 (m), 842 (w), 827 (w), 799 (m), 778 (s), 761 (vs), 690 (vs), 679 (vs), 668 (s), 658 (m), 640 (s), 619 (m), 603 (m). Anal. Calcd. for $\text{MnClN}_6\text{C}_{30}\text{BH}_{28}$: 62.80 %C; 4.92 %H; 14.65 %N. Found: 62.70 %C; 4.83 %H; 14.53 %N.

[^{Ph,Me}TpZnCl](2). A solution of KTp (1.3216 g, 2.53 mmol) in 15 mL DCM was added to a stirring solution of ZnCl_2 (0.3483 g, 2.56 mmol) in 3 mL MeOH at room temperature. The white, cloudy solution was allowed to stir overnight at room temperature. The reaction mixture was subsequently pumped down to dryness. The product was extracted into 20 mL DCM, filtered through a Celite pad on a fritted filter, and then concentrated to about 4 mL. Crystalline product suitable for X-ray diffraction was obtained by adding 15 mL of n-hexane and allowing it to sit at room temperature overnight. The white needles were then isolated by decanting the mother liquor, washing with 3 x 5 mL n-hexane, and drying *in vacuo*. Yield: 0.6667g (45.1%) IR (ATR, cm^{-1}): 3139 (w), 3122 (w), 3089 (w), 3061 (w), 3046 (w), 3027 (w), 2988 (w), 2961 (w), 2930 (w), 2916 (w), 2546 (m), 1574 (w), 1568 (w), 1545 (m), 1508 (w), 1474 (m), 1438 (m), 1414 (m), 1385 (m), 1370 (m), 1342 (m), 1310 (w), 1282 (w), 1216 (w), 1186 (m), 1171 (s), 1129 (w), 1094 (m), 1064 (s), 1028 (w), 998 (w), 984 (m), 917 (w), 909 (w), 858 (w), 836 (w), 810 (m), 804 (m), 781 (m), 772 (m), 759 (vs), 721 (w), 704 (m), 691 (vs), 668 (m), 655 (m), 636 (s), 623 (w), 616 (w), 612 (w), 604 (w). ¹H NMR (500 MHz, CDCl_3 , 298 K): δ 7.72 (d, 6H), 7.41 (t, 6H), 7.36 (t, 3H), 6.26 (s, 3H), 5.00 (br

d, 1H), 2.57 (s, 9H) ppm. Anal. Calcd. for $\text{ZnClN}_6\text{C}_{30}\text{BH}_{28}$: 61.68 %C; 4.83 %H; 14.38 %N. Found: 61.46 %C; 4.91 %H; 14.17 %N.

[^{Ph,Me}TpMnSnPh₃]·benzene(3). Yellow KSnPh_3 was generated by stirring HSnPh_3 (482.0 mg, 1.373 mmol) and KH (55.1 mg, 1.374 mmol) in 5 mL of Et_2O for 4 hours at room temperature. To this, a suspension of **1** (504.0 mg, 0.8784 mmol) in 15 mL Et_2O was added at room temperature, a white precipitate formed and the reaction was allowed to stir overnight at room temperature. The precipitate was filtered out and washed with 4 x 5 mL Et_2O and dried. Then, it was taken up in 80 mL benzene, filtered through silylated Celite on a fritted funnel, then layered under 100 mL n-hexane. Colorless hexagonal platelets of **3** were obtained (Yield: 410.5 mg, 48.4%). The IR (ATR, cm^{-1}): 3048 (w), 3023 (w), 3001 (w), 2975 (w), 2964 (w), 2928 (w), 2527 (w), 1542 (m), 1506 (w), 1474 (m), 1450 (m), 1432 (s), 1423 (s), 1376 (w), 1358 (m), 1341 (m), 1303 (w), 1283 (w), 1254 (w), 1215 (w), 1178 (s), 1092 (m), 1060 (s), 1030 (m), 995 (w), 975 (m), 912 (w), 841 (w), 802 (w), 777 (m), 763 (s), 730 (s), 695 (s), 677 (vs), 656 (s), 638 (s), 531 (m), 522 (m), 489 (m), 451 (s), 442 (s), 409 (w). UV-Vis-NIR (C_6D_6) λ_{max} , nm (ϵ): 360 (2595). Anal. Calcd. for $\text{SnMnN}_6\text{C}_{48}\text{BH}_{43} \cdot \frac{1}{2}(\text{C}_6\text{H}_6)$: 66.04 %C; 5.00 %H; 9.06 %N. Found: 66.34 %C; 5.01 %H; 8.83 %N.

[^{Ph,Me}TpFeSnPh₃]·benzene(4). **4** was synthesized in a similar fashion to **3**, except that [^{Ph,Me}TpFeCl] (510.3 mg, 0.8879 mmol) was reacted with KSnPh_3 (1.373 mmol). Orange, hexagonal platelets of **4** were obtained with a benzene/n-hexane layering (Yield: 295.9 mg, 34.4 %). IR (ATR, cm^{-1}): 3048 (w), 3024 (w), 2995 (w), 2975 (w), 2965 (w), 2919 (w), 2527 (w), 1541 (m), 1506 (w), 1474 (m), 1451 (m), 1433 (s), 1423 (s), 1376 (w), 1359 (m), 1342 (m), 1300 (w), 1285 (w), 1254 (w), 1214 (w), 1180 (s), 1093 (m), 1058 (s), 1030 (m), 995 (w), 976 (m), 912 (w), 841 (w), 802 (w), 776 (m), 763 (s), 730 (s), 696 (s), 677 (vs), 656 (s), 637 (s), 532 (m), 524 (m), 488 (m), 451 (s), 442 (s), 417 (w). UV-Vis-NIR (C_6D_6) λ_{max} , nm (ϵ): 356 (1331), 462 (1510), 513

(sh, 727). ^1H NMR (500 MHz, C_6D_6 , 298 K): δ 59.90 (3H), 32.59 (6H), 29.33 (9H), 10.20 (6H), 8.86 (3H), 7.67 (6H), 6.29 (3H), 5.85 (6H), -15.79 (1H) ppm. Anal. Calcd. for $\text{SnFeN}_6\text{C}_{48}\text{BH}_{43}\cdot(\text{C}_6\text{H}_6)$: 67.05 %C; 5.11 %H; 8.69 %N. Found: 66.76 %C; 5.07 %H; 8.41 %N.

[Ph,MeTpNiSnPh_3] \cdot benzene(6). A solution of HSnPh_3 (107.0 mg, 0.3048 mmol) in 2 mL of n-hexane was added to a stirring solution of [$\text{Ph,MeTpNiCH}_2\text{SiMe}_3$] $\cdot\frac{1}{2}$ hexane (151.6 mg, 0.2261 mmol) in 15 mL of n-hexane at room temperature. After allowing the reaction mixture to stir for 5 hours at room temperature, the turquoise precipitate was filtered out and washed with 3 x 5 mL hexanes then dried *in vacuo*. Turquoise, hexagonal platelets of **6** were obtained by dissolving the product in 8 mL benzene, filtering through silylated Celite, and layering under 30 mL of n-hexane. (Yield: 107.9 mg, 49.2%) IR (ATR, cm^{-1}): 3048 (w), 3024 (w), 2995 (w), 2975 (w), 2965 (w), 2931 (w), 2521(w), 1543 (m), 1506 (w), 1475(m), 1451 (m), 1435 (s), 1423 (s), 1377 (w), 1361 (m), 1344 (m), 1300 (w), 1285 (w), 1253 (w), 1218 (w), 1186 (s), 1094 (m), 1057 (s), 1031 (m), 996 (w), 979 (m), 912(w), 838 (w), 803 (w), 779 (m), 763 (s), 730 (s), 697 (s), 676 (vs), 656 (s), 637 (s), 535 (m), 528 (m), 488 (m), 452 (s), 443 (s), 404 (w). UV-Vis-NIR (C_6D_6) λ_{max} , nm (ϵ): 367 (1975), 576 (1511), 709 (1191), 975 (348). ^1H NMR (500 MHz, C_6D_6 , 298 K): δ 73.93, 14.39, 9.99, 9.55, 8.90, 8.01, 7.47, 7.08, -9.24 ppm. Anal. Calcd. for $\text{SnNiN}_6\text{C}_{48}\text{BH}_{43}\cdot(\text{C}_6\text{H}_6)$: 66.85 %C; 5.09 %H; 8.66 %N. Found: 66.54 %C; 5.09 %H; 8.82 %N.

[Ph,MeTpZnSnPh_3] \cdot benzene (7). **7** was synthesized in a similar fashion to **3**, except that **2** (559.0 mg, 0.9578 mmol) was reacted with KSnPh_3 (1.437 mmol). Colorless, hexagonal platelets of **7** were obtained with a benzene/n-hexane layering (Yield: 451.0 mg, 48.3 %). IR (ATR, cm^{-1}): 3050 (w), 3026 (w), 2996 (w), 2977 (w), 2966 (w), 2931 (w), 2513 (w), 1544 (m), 1507 (w), 1476 (m), 1451 (m), 1435 (s), 1424 (s), 1376 (w), 1362 (m), 1343 (m), 1301 (w), 1286 (w) 1255 (w), 1219 (w), 1186 (s), 1093 (m), 1059 (s), 1031 (m), 996 (w), 976 (m), 913 (w), 834 (w), 803 (w), 780 (m),

764 (s), 731 (s), 697 (s), 676 (vs), 656 (s), 637 (s), 532 (m), 527 (m), 489 (m), 451 (s), 443 (s), 410 (w). ^1H NMR (600 MHz, C_6D_6 , 298 K): δ 7.50 (d, 6H), 7.14 (t, 3H), 7.09 (t, 6H), 7.04 (d, 6H), 6.75 (t, 3H), 6.50 (t, 6H), 5.93 (s, 3H), 5.00 (br s, 1H), 2.24 (s, 9H) ppm. ^{119}Sn NMR (223.8 MHz, C_6D_6 , 298 K) -118.45 ppm. Anal. Calcd. for $\text{SnZnN}_6\text{C}_{48}\text{BH}_{43}\cdot\frac{1}{2}(\text{C}_6\text{H}_6)$: 65.31 %C; 4.94 %H; 8.96 %N. Found: 65.39 %C; 4.82 %H; 9.15 %N.

Magnetic Measurements. Magnetic data were collected using a Quantum Design MPMS-XL SQUID magnetometer. Measurements for all compounds were obtained on finely ground microcrystalline powders. The compounds were restrained in a frozen eicosane matrix and flame sealed in a quartz tube under vacuum. Dc susceptibility measurements were collected in the temperature range 1.8–300 K under dc fields of 0.1, 0.5 and 1 T. Dc magnetization measurements were performed under applied magnetic fields of 1, 2, 3, 4, 5, 6 and 7 T in the temperature range of 1.8–10 K. Dc magnetic susceptibility data were corrected for diamagnetic contributions from the sample holder and eicosane as well as for the core diamagnetism of each sample, estimated using Pascal's constants.⁶² Prior to full characterization, variable dc field magnetization data was collected from 0 to 4 T at 100 K to ensure the absence of curvature associated with ferromagnetic impurities.

X-ray Diffraction. Single crystal diffraction data collections were performed on single crystals coated with Paratone-N oil and mounted on a MicroMountsTM rod. The crystals were frozen while coated in Paratone-N oil under a stream of N_2 during the measurement. Structures for **1** - **7** were collected with a Mo $\text{K}\alpha$ ($\lambda = 0.71073$ Å) sealed tube diffraction source with a graphite monochromator, and a Bruker APEX2 CCD detector. Raw data were integrated and corrected for Lorentz and polarization effects using Bruker Apex3 v. 2013.⁶³ Absorption corrections were applied using SADABS.⁶⁴ Space group assignments were determined by examination of

systematic absences, *E*-statistics, and successive refinement of the structures. The crystal structure was solved by direct methods with the aid of successive difference Fourier maps in SHELXS⁶⁵ operated with the OLEX2 interface.⁶⁶ The crystals showed no significant decay during data collection. Thermal parameters were refined anisotropically for all non-hydrogen atoms. Hydrogen atoms were placed in ideal positions and refined using a riding model for all structures. Compounds **3** – **7** crystallized with a benzene molecule that was disordered over a special position, so a solvent mask was used.

Zero-field ⁵⁷Fe Mössbauer Spectroscopic Measurements. Measurement of **4** was performed under zero applied magnetic field and at 80 K on ca. 70 mg of ground, microcrystalline product. The sample was loaded into a circular plastic cap of 1 cm² area under an inert atmosphere covered in Paratone-N oil and transferred quickly to the cryostat to avoid sample decomposition. The spectrum was collected with a constant acceleration spectrometer and a ⁵⁷Co/Rh source. Prior to measurements, the spectrometer was calibrated at 295 K with α -Fe foil. Spectra were analyzed using the WMOSS Mössbauer Spectral Analysis Software (www.wmoss.org).

Raman Spectroscopy Measurements. Crystals of **3** – **7** were sealed in 0.7 mm capillaries with Illumabond UV Curable Epoxy in the glovebox. Raman spectra were collected using a Horiba LabRam HR Evolution confocal microscope. Individual crystals were excited with 633 nm (compounds **3** and **4**) and 532 nm (compounds **5** – **7**) continuous-wave diode lasers equipped with a long working distance 50 \times microscope objective (NA = 0.50; Nikon) and 1800 grooves/mm grating at 0.95 mW (633 nm) and 2.5 mW (532 nm) power at room temperature. The spectra were collected for 10 minutes.

Powder X-ray Diffraction Measurements. Polycrystalline samples of **3 – 7** were loaded in a hollow metallic sample holder and both sides sealed with Kapton tape inside the glovebox. The powder X-ray diffraction (PXRD) patterns were measured in transmission geometry (with sample spinning) using a STOE STADI P instrument equipped with a CuK α 1 sealed tube source and a 1D strip detector covering 2θ range of 6° . All patterns were collected at room temperature.

Electron Paramagnetic Resonance (EPR) Spectroscopy. Polycrystalline samples were loaded into a 4 mm OD quartz EPR tube under a dinitrogen atmosphere and restrained with eicosane. Continuous-wave EPR spectra were measured at the University of Chicago EPR facility using a Bruker Elexsys 500 X-band EPR spectrometer. Samples were cooled using an Oxford Systems continuous-flow He cryostat coupled with a 10 K He stinger from Bruker. Spectra were acquired with the Bruker Win-EPR software suite. Spectral simulations were carried out using Easyspin.⁶⁷

X-Ray Absorption Spectroscopy (XAS). Transmission XAS measurements at the Sn K-edge (29.2 keV) were acquired at sector 20-BM at the Advanced Photon Source of Argonne National Laboratory. Samples were prepared by sealing layers of polycrystalline or amorphous powders between pieces of Kapton tape inside a dinitrogen glovebox and adhering the layers to Teflon sample holders. The sample holders were then mounted onto a sample rod and placed under vacuum. Samples were measured at 25 K using a Displex closed-cycle He refrigerator. All measurements at the Sn K-edge were run concurrently with Sn foil for energy calibration. The spectra were normalized and analyzed using the software Athena.⁶⁸

¹¹⁹Sn Synchrotron Mössbauer Spectroscopy. Spectra for **3 – 7** were measured at Sector 30-ID at the Advanced Photon Source of Argonne National Laboratory. Samples were prepared by mixing unenriched polycrystalline powders with oil, to improve thermal conductivity, and placing inside a custom-made 9-well copper sample holder in a dinitrogen-filled glovebox. Kapton tape

was used to seal the samples and protect from dioxygen. Measurements were done under vacuum and cooled used a closed-loop He refrigerator equipped with a Be window. The spectra were fit iteratively with the Newton method using the CONUSS-2.2.0 software. The agreement between data and the fits were parameterized by a normalized χ^2 value which are displayed for each fit in Table S4.11. The natural abundance of ^{119}Sn was used for fitting with a fixed Lamb-Mössbauer factor of 0.05. The density of each compound was fixed to the value obtained from single crystal X-Ray diffraction measurements. We fit the spectra using a single Sn site and allowed the following parameters to freely refine: ΔE_Q , texture coefficient, sample thickness, and the scaling factor. We used the density obtained from single crystal X-ray diffraction and used a Lamb-Mössbauer factor of 0.05 for the fits. A distribution of electric quadrupole splitting was also used in the fit and allowed to refine freely.

All Other Physical Measurements. Combustion analysis of all complexes was performed by Midwest Microlabs (Indianapolis, IN). Infrared spectra were recorded on a Bruker Alpha FTIR spectrometer equipped with an attenuated total reflectance accessory. Solution-phase NMR spectra were collected with a Bruker Avance III 600 MHz spectrometer. Proton NMR spectra are referenced to CDCl_3 or d_6 -benzene at 7.26 and 7.16 ppm, respectively. UV-vis-NIR and diffuse reflectance spectra were collected on a Varian Cary 5000 spectrometer at room temperature in C_6D_6 for the solutions or over KBr for solid measurements.

Computational Details.

Analysis of bonding in the ground state. Single point energy calculations were performed for molecular geometries obtained from experiment using density functional theory (DFT) to analyze the bonding in **3-7** and compare with the CASPT2 results. All calculations were performed in the

Turbomole program package.⁶⁹ The TPSSh^{70,71} functional and def2-TZVP basis set⁷² was used. The resolution of the identity (RI) approximation was used as well.^{73–75} Atomic charges, spin densities, and the charge decomposition of the σ bonding orbital computed using intrinsic bond orbital (IBO) analysis as implemented in IboView.⁷⁶ Mayer bond orders were computed using the MultiWFN program.^{77,78} The occupation numbers for the lowest CI Root from the CASSCF calculation described above (for the ground state spin) were used to calculate the so-called effective bond order (EBO) which is the occupation number of the bonding orbital minus the occupation number of the antibonding orbital, divided by two.

Calculated Magnetic Properties. All complete active space self-consistent field level of theory (CASSCF) with corrections to the energy from second order perturbation theory (CASPT2) were performed on geometries obtained by diffraction experiments for **3-6**.^{79–81} The active space includes the 3d and 4d orbitals from the transition metal (Mn, Fe, Co, or Ni) along with the bonding and antibonding orbitals between Sn and transition metal. The corresponding number of electrons to maintain a neutral charge were included. Specifically, the active spaces were ($7e$, $12o$), ($8e$, $12o$), ($9e$, $12o$), and ($10e$, $12o$), for Mn, Fe, Co, and Ni, respectively. All calculations were performed with the OpenMolcas 8.0 software package.⁸² An imaginary shift of 0.2 and an IPEA shift of 0.25 were used in all CASPT2 calculations. ANO-RCC basis sets was used for all atoms with the following contractions: 6s5p3d2f1g for Mn, Fe, Co and Ni; 6s5p3e1f for Sn; 3s2p1d for N; 2s1p for B and C; and 1s for H.^{83–86} CASPT2 calculations were performed for the lowest energy state of the ground state spins ($S=3/2$ for Co, $S=1$ for Ni, and $S=2$ for Fe) to analyze the bonding. The natural orbitals and their occupation in the spin-free ground state are shown in Figures S11 to S14. The orbitals were state-averaged and all excitations within the 3d manifold were computed. This corresponds to the following number of states: Mn (1 sextet, 24 quartets, and 75 doublets),

Fe (5 quintets, 45 triplets, and 50 singlets), Co (10 quartets and 40 doublets), and Ni (10 triplets and 15 singlets). Spin-orbit coupling effects were included *a posteriori* using the restricted active space state interaction approach (RASSI). The diagonal elements of the effective Hamiltonian were replaced with the single state CASPT2 energies. The obtained RASSI spin-orbit states were introduced into the SINGLE-ANISO module to calculate the magnetic properties (D and E).⁸⁷ Additional information regarding the excited state electron configurations can be found at the University of South Dakota's library database via this link: <https://red.library.usd.edu/data/1/>.

Table S4.1 | Crystallographic information for the structural refinement of **1**.

Empirical Formula	MnClN ₆ C ₃₀ BH ₂₈
Formula weight	573.78 g/mol
Temperature	100.07 K
Wavelength	0.71073 Å
Crystal System	Trigonal
Space Group	<i>R</i> 3c
Unit Cell Dimensions	$a = 12.0230(1)$ Å, $\alpha = 90.0^\circ$ $b = 12.0230(1)$ Å, $\beta = 90.0^\circ$ $c = 32.558(3)$ Å, $\gamma = 120.0^\circ$
Volume	4075.8(1) Å ³
<i>Z</i>	6
Density (calculated)	1.403 g/cm ³
Absorption coefficient	0.616 mm ⁻¹
<i>F</i> ₀₀₀	1782.0
Crystal color	Colorless
Crystal size	0.342 × 0.150 × 0.084 mm ³
2 θ range	4.644 to 68.426°
Index ranges	-19 ≤ <i>h</i> ≤ 18 -19 ≤ <i>k</i> ≤ 18 -21 ≤ <i>l</i> ≤ 51
Reflections collected	41720
Independent reflections	7916 [<i>R</i> _{int} = 0.0371]
Completeness to 2 θ = 68.426°	81.1 %
Absorption correction	Multi-scan
Maximum and minimum transmission	0.4853 and 0.4292
Refinement method	Full-matrix least-squares on <i>F</i> ²
Data / restraints / parameters	2860 / 1 / 119
Goodness-of-fit on <i>F</i> ^{2a}	1.061
Final <i>R</i> indices [<i>I</i> > 2 σ (<i>I</i>)] ^b	<i>R</i> ₁ = 3.10 %, <i>wR</i> ₂ = 6.80 %
<i>R</i> indices (all data)	<i>R</i> ₁ = 4.15 %, <i>wR</i> ₂ = 7.18 %
Largest diff. peak and hole	0.31 and -0.36 e.Å ⁻³

^a GooF = $[\sum[w(F_o^2 - F_c^2)^2] / (n-p)]^{1/2}$ where *n* is the number of reflections and *p* is the total number of parameters refined. ^b*R*₁ = $\sum||F_o| - |F_c|| / \sum|F_o|$; *wR*₂ = $[\sum[w(F_o^2 - F_c^2)^2] / \sum[w(F_o^2)^2]]^{1/2}$

Table S4.2 | Crystallographic information for the structural refinement of **2**.

Empirical Formula	ZnClN ₆ C ₃₀ BH ₂₈
Formula weight	584.21 g/mol
Temperature	100.11 K
Wavelength	0.71073 Å
Crystal System	Monoclinic
Space Group	<i>P</i> 2 ₁ / <i>n</i>
Unit Cell Dimensions	<i>a</i> = 11.0364(8) Å, α = 90.0° <i>b</i> = 15.2242(1) Å, β = 94.548(2)° <i>c</i> = 16.1001(1) Å, γ = 90.0°
Volume	2696.6(4) Å ³
<i>Z</i>	4
Density (calculated)	1.439 g/cm ³
Absorption coefficient	1.04 mm ⁻¹
<i>F</i> ₀₀₀	1208.0
Crystal color	Colorless
Crystal size	0.348 × 0.122 × 0.040 mm ³
2 θ range	3.688 to 60.42°
Index ranges	-15 ≤ <i>h</i> ≤ 15 -21 ≤ <i>k</i> ≤ 21 -22 ≤ <i>l</i> ≤ 22
Reflections collected	44426
Independent reflections	7978 [<i>R</i> _{int} = 0.0855]
Completeness to 2 θ = 60.42°	100.0 %
Absorption correction	Multi-scan
Maximum and minimum transmission	0.4932 and 0.4028
Refinement method	Full-matrix least-squares on <i>F</i> ²
Data / restraints / parameters	7978 / 0 / 355
Goodness-of-fit on <i>F</i> ^{2a}	1.010
Final <i>R</i> indices [<i>I</i> > 2 σ (<i>I</i>)] ^b	<i>R</i> ₁ = 4.69 %, <i>wR</i> ₂ = 9.00 %
<i>R</i> indices (all data)	<i>R</i> ₁ = 9.26 %, <i>wR</i> ₂ = 10.48 %
Largest diff. peak and hole	0.72 and -0.69 e.Å ⁻³

^a GooF = $[\sum[w(F_o^2 - F_c^2)^2] / (n-p)]^{1/2}$ where *n* is the number of reflections and *p* is the total number of parameters refined. ^b*R*₁ = $\sum||F_o| - |F_c|| / \sum|F_o|$; *wR*₂ = $[\sum[w(F_o^2 - F_c^2)^2] / \sum[w(F_o^2)^2]]^{1/2}$

Table S4.3 | Crystallographic information for the structural refinement of **3**.

Empirical Formula	SnMnN ₆ C ₅₄ BH ₄₉
Formula weight	966.43 g/mol
Temperature	100.0 K
Wavelength	0.71073 Å
Crystal System	Trigonal
Space Group	<i>R</i> -3
Unit Cell Dimensions	<i>a</i> = 12.3824(6) Å, α = 90.0° <i>b</i> = 12.3824(6) Å, β = 120.0° <i>c</i> = 49.104(2) Å, γ = 90.0°
Volume	6520.2(7) Å ³
<i>Z</i>	6
Density (calculated)	1.477 g/cm ³
Absorption coefficient	0.912 mm ⁻¹
<i>F</i> ₀₀₀	2970.0
Crystal color	Colorless
Crystal size	0.456 × 0.419 × 0.110 mm ³
2 θ range	3.888 to 60.114°
Index ranges	-17 ≤ <i>h</i> ≤ 17 -17 ≤ <i>k</i> ≤ 16 -69 ≤ <i>l</i> ≤ 69
Reflections collected	55305
Independent reflections	4263 [<i>R</i> _{int} = 0.0425]
Completeness to 2 θ = 60.114°	100.0 %
Absorption correction	Multi-scan
Maximum and minimum transmission	0.9927 and 0.7230
Refinement method	Full-matrix least-squares on <i>F</i> ²
Data / restraints / parameters	4263 / 0 / 173
Goodness-of-fit on <i>F</i> ^{2a}	1.048
Final <i>R</i> indices [<i>I</i> > 2 σ (<i>I</i>)] ^b	<i>R</i> ₁ = 5.33 %, <i>wR</i> ₂ = 14.90 %
<i>R</i> indices (all data)	<i>R</i> ₁ = 6.53 %, <i>wR</i> ₂ = 16.47 %
Largest diff. peak and hole	5.01 and -1.62 e.Å ⁻³

^a GooF = $[\sum[w(F_o^2 - F_c^2)^2] / (n-p)]^{1/2}$ where *n* is the number of reflections and *p* is the total number of parameters refined. ^b*R*₁ = $\sum||F_o| - |F_c|| / \sum|F_o|$; *wR*₂ = $[\sum[w(F_o^2 - F_c^2)^2] / \sum[w(F_o^2)^2]]^{1/2}$

Table S4.4 | Crystallographic information for the structural refinement of **4**.

Empirical Formula	SnFeN ₆ C ₅₄ BH ₄₉
Formula weight	967.34 g/mol
Temperature	100.0 K
Wavelength	0.71073 Å
Crystal System	Trigonal
Space Group	<i>R</i> -3
Unit Cell Dimensions	<i>a</i> = 12.3722(2) Å, α = 90.0° <i>b</i> = 12.3722(2) Å, β = 120.0° <i>c</i> = 48.796(1) Å, γ = 90.0°
Volume	6468.6(2) Å ³
<i>Z</i>	6
Density (calculated)	1.490 g/cm ³
Absorption coefficient	0.962 mm ⁻¹
<i>F</i> ₀₀₀	2976.0
Crystal color	Orange
Crystal size	0.127 × 0.056 × 0.025 mm ³
2 θ range	2.504 to 60.128°
Index ranges	-16 ≤ <i>h</i> ≤ 15 -17 ≤ <i>k</i> ≤ 17 -68 ≤ <i>l</i> ≤ 68
Reflections collected	37148
Independent reflections	4228 [<i>R</i> _{int} = 0.0295]
Completeness to θ = 60.128°	100.0 %
Absorption correction	Multi-scan
Maximum and minimum transmission	0.9879 and 0.8782
Refinement method	Full-matrix least-squares on <i>F</i> ²
Data / restraints / parameters	4228 / 0 / 173
Goodness-of-fit on <i>F</i> ^{2a}	1.049
Final <i>R</i> indices [<i>I</i> > 2 σ (<i>I</i>) = 10408 data] ^b	<i>R</i> ₁ = 3.03 %, <i>wR</i> ₂ = 7.06 %
<i>R</i> indices (all data, 0.80 Å)	<i>R</i> ₁ = 4.15 %, <i>wR</i> ₂ = 7.71 %
Largest diff. peak and hole	0.39 and -0.91 e.Å ⁻³

^a GooF = $[\sum[w(F_o^2 - F_c^2)^2] / (n-p)]^{1/2}$ where *n* is the number of reflections and *p* is the total number of parameters refined. ^b*R*₁ = $\sum||F_o| - |F_c|| / \sum|F_o|$; *wR*₂ = $[\sum[w(F_o^2 - F_c^2)^2] / \sum[w(F_o^2)^2]]^{1/2}$

Table S4.5 | Crystallographic information for the structural refinement of **6**.

Empirical Formula	SnNiN ₆ C ₅₄ BH ₄₉
Formula weight	970.20 g/mol
Temperature	100.0 K
Wavelength	0.71073 Å
Crystal System	Trigonal
Space Group	<i>R</i> -3
Unit Cell Dimensions	$a = 12.3186(4)$ Å, $\alpha = 90.0^\circ$ $b = 12.3186(4)$ Å, $\beta = 120.0^\circ$ $c = 49.082(2)$ Å, $\gamma = 90.0^\circ$
Volume	6450.4(5) Å ³
<i>Z</i>	6
Density (calculated)	1.499 g/cm ³
Absorption coefficient	1.066 mm ⁻¹
<i>F</i> ₀₀₀	2988.0
Crystal color	Turquoise
Crystal size	0.443 × 0.380 × 0.044 mm ³
2 θ range	2.49 to 61.21°
Index ranges	-17 ≤ <i>h</i> ≤ 17 -17 ≤ <i>k</i> ≤ 17 -70 ≤ <i>l</i> ≤ 69
Reflections collected	65036
Independent reflections	4430 [<i>R</i> _{int} = 0.0329]
Completeness to $\theta = 52.48^\circ$	100.0 %
Absorption correction	Multi-scan
Maximum and minimum transmission	0.8872 and 0.6505
Refinement method	Full-matrix least-squares on <i>F</i> ²
Data / restraints / parameters	4430 / 0 / 173
Goodness-of-fit on <i>F</i> ^{2a}	1.050
Final <i>R</i> indices [<i>I</i> > 2 σ (<i>I</i>) = 10408 data] ^b	<i>R</i> ₁ = 3.27 %, <i>wR</i> ₂ = 8.23 %
<i>R</i> indices (all data, 0.80 Å)	<i>R</i> ₁ = 4.15 %, <i>wR</i> ₂ = 8.71 %
Largest diff. peak and hole	0.60 and -0.90 e.Å ⁻³

^a GooF = $[\sum[w(F_o^2 - F_c^2)^2] / (n-p)]^{1/2}$ where *n* is the number of reflections and *p* is the total number of parameters refined. ^b*R*₁ = $\sum||F_o| - |F_c|| / \sum|F_o|$; *wR*₂ = $[\sum[w(F_o^2 - F_c^2)^2] / \sum[w(F_o^2)^2]]^{1/2}$

Table S4.6 | Crystallographic information for the structural refinement of 7.

Empirical Formula	SnZnN ₆ C ₅₄ BH ₄₉
Formula weight	976.86 g/mol
Temperature	100.0 K
Wavelength	0.71073 Å
Crystal System	Monoclinic
Space Group	<i>R</i> -3
Unit Cell Dimensions	$a = 12.3859(4)$ Å, $\alpha = 90.0^\circ$ $b = 12.3859(4)$ Å, $\beta = 120.0^\circ$ $c = 48.738(2)$ Å, $\gamma = 90.0^\circ$
Volume	6475.2(5) Å ³
<i>Z</i>	6
Density (calculated)	1.503 g/cm ³
Absorption coefficient	1.181 mm ⁻¹
<i>F</i> ₀₀₀	3000.0
Crystal color	Colorless
Crystal size	0.470 × 0.260 × 0.044 mm ³
2 θ range	3.888 to 58.378°
Index ranges	-16 ≤ <i>h</i> ≤ 16 -16 ≤ <i>k</i> ≤ 16 -66 ≤ <i>l</i> ≤ 66
Reflections collected	54021
Independent reflections	3891 [<i>R</i> _{int} = 0.0448]
Completeness to $\theta = 58.378^\circ$	99.96 %
Absorption correction	Multi-scan
Maximum and minimum transmission	0.9514 and 0.7101
Refinement method	Full-matrix least-squares on <i>F</i> ²
Data / restraints / parameters	3891 / 0 / 173
Goodness-of-fit on <i>F</i> ^{2a}	1.088
Final <i>R</i> indices [<i>I</i> > 2 σ (<i>I</i>) = 10408 data] ^b	<i>R</i> ₁ = 4.22 %, <i>wR</i> ₂ = 10.96 %
<i>R</i> indices (all data, 0.80 Å)	<i>R</i> ₁ = 5.01 %, <i>wR</i> ₂ = 11.72 %
Largest diff. peak and hole	2.48 and -1.62 e.Å ⁻³

^a GooF = $[\sum[w(F_o^2 - F_c^2)^2] / (n-p)]^{1/2}$ where *n* is the number of reflections and *p* is the total number of parameters refined. ^b*R*₁ = $\sum||F_o| - |F_c|| / \sum|F_o|$; *wR*₂ = $[\sum[w(F_o^2 - F_c^2)^2] / \sum[w(F_o^2)^2]]^{1/2}$

Table S4.7 | Comparison of ^{57}Fe Mössbauer parameters between compound **4** and known values of similar compounds.

Compound	δ (mm s $^{-1}$)	ΔE_Q (mm s $^{-1}$)
$^{\text{Ph,Me}}\text{TpFeSnPh}_3$ (4)	0.742(1)	1.061(3)
$\text{PhB}(\text{MesIm})_3\text{Fe-N=PPh}_3$ ³²	0.44(1)	0.78(1)
$[\text{PhBP}_3^{\text{CH}_2\text{Cy}}]\text{Fe-N=PPh}_3$ ³³	0.820	1.449
$[\text{PhBP}_3^{i\text{Pr}_3}]\text{Fe-N=PPh}_3$ ³³	0.617	1.373

Table S4.8 | Fit parameters to the variable-temperature, variable field magnetization data of **3**, **4**, **5**, **6**. Parameters for **4** were reported previously⁵, but are displayed here for easier comparison.

Compound	D (cm $^{-1}$)	E (cm $^{-1}$)	g_{iso}
3	-0.2(1)	0	1.99(2)
4	12.9(3)	3.3(2)	2.14(1)
5	11.9(1)	0.7(1)	2.28(2)
6	-3.0(2)	0	2.28(2)

Table S4.9 | Fit parameters to the cw-EPR spectra of samples of **1** and **3** diluted in a polycrystalline sample of **7** in a 1:20 (Mn:Zn) ratio.

Compound	Temperature (K)	g_{iso}	D (cm $^{-1}$)	A_{iso} (^{55}Mn , MHz)	A_{iso} ($^{\text{nat}}\text{Sn}$, MHz)
1	298	1.999(2)	0.230(1)	-	-
	10	1.999(2)	0.236(1)	-	-
3	298	1.9933(2)	0.0939(4)	164(2)	141(3)
	12	1.9933(3)	0.1015(6)	164(3)	-

Table S4.10 | Results from peak-fitting XANES data at Sn K-edge for **3** – **7**, and SnO, SnO₂, Ph₆Sn₂, Ph₄Sn, Ph₃SnCl, and Ph₃SnF references. The step was fit with an arctangent function and the peaks were fit with pseudo-Voigt functions with $\gamma = 0.5$ for all compounds. Peak and step positions are reported in eV.

Compound	Step			Peak 1			Peak 2			Reduced χ^2
	Height	Center	Width	Height	Center	σ	Height	Center	σ	
3	0.847	29201.7	3.5	9.72	29209.1	18.09	0.701	29223.7	7.97	0.0047
4	0.829	29201.7	3.53	10.117	29209.1	18.24	0.828	29223.7	8.29	0.0049
5	0.830	29201.7	3.52	10.404	29208.7	18.84	0.779	29223.5	7.81	0.0055
6	0.829	29201.8	3.51	10.473	29208.7	18.85	0.85	29223.7	8.49	0.0056
7	0.771	29201.7	3.64	10.469	29209.1	17.20	2.62	29223.8	13.92	0.0051
Ph ₆ Sn ₂	0.718	29201.0	1.59	9.272	29204.1	12.22	7.26	29224.5	22.58	0.0052
Ph ₄ Sn	0.719	29201.1	1.68	9.303	29204.1	12.10	7.29	29224.8	22.72	0.0057
Ph ₃ SnCl	0.749	29201.2	1.74	9.319	29204.1	12.02	7.27	29224.2	22.86	0.0099
Ph ₃ SnF	0.759	29202.1	2.21	9.704	29203.3	10.83	6.80	29225.0	24.30	0.0081
SnO	0.895	29200.1	4.73	10.796	29203.8	13.69	0.71	29215.4	7.66	0.0026
SnO ₂	0.682	29203.4	5.18	14.65	29208.7	13.15	3.39	29224.6	13.16	0.0099

Table S4.11 | Fit parameters to the ¹¹⁹Sn synchrotron Mössbauer spectra of polycrystalline samples of **4** – **7** at 60 K.

Compound	ΔE_Q (mm s ⁻¹)	χ^2
3	0.623(3)	2.54
4	1.198(2)	2.08
5	1.204(4)	2.11
6	1.134(2)	1.99
7	0.896(2)	2.58

Table S4.12 | Charges computed using the intrinsic bond orbital (IBO) charge localization from the TPSSh calculation. Note that N1 refers to nitrogen coordinated to the transition metal (TM) while N2 refers to the nitrogen coordination to boron.

Atom	3	4	5	6	7
Sn	0.266	0.320	0.365	0.263	-0.530
TM	1.154	1.077	1.017	1.042	3.755
B	0.081	0.082	0.071	0.088	-0.046
N1 _{avg}	-0.352	-0.343	-0.339	-0.232	-0.472
N2 _{avg}	-0.054	-0.051	-0.060	-0.050	-0.113

Table S4.13 | Atomic spin densities computed using the intrinsic bond orbital (IBO) charge localization from the TPSSh calculation. No spin density is included for Zn, since it is a closed shell singlet. The N atom designation is the same as in Table S4.12.

Atom	3	4	5	6
Sn	-0.006	0.060	0.130	-0.025
TM	4.764	3.672	2.583	1.688
B	0.001	0.001	0.002	0.000
N1 _{avg}	0.041	0.058	0.064	0.066
N2 _{avg}	0.002	-0.001	0.000	-0.004

Table S4.14 | Mayer and bond orders from the TPSSh and CASSCF calculations, respectively, analyzed using MultiWFN.

Compound	TPSSh	CASSCF
3	0.613	0.794
4	0.561	0.796
5	0.530	0.670
6	0.645	0.822
7	0.808	

Table S4.15 | Natural orbital occupation numbers for the σ bonding and antibonding orbitals from the CASSCF calculations. The effective bond order (EBO) computed using these occupation numbers is also reported.

Compound	Bonding	Antibonding	EBO
3	1.981	0.017	0.982
4	1.982	0.016	0.983
5	1.982	0.014	0.984
6	1.985	0.014	0.986

Table S4.16 | Contributions from Sn and the transition metal to the covalent sigma bond using IboView from the TPSSh calculation.

Compound	Sn	TM	Other Atoms
3	0.773	0.203	0.024
4	0.786	0.191	0.023
5	0.803	0.173	0.024
6	0.790	0.197	0.023
7	1.630	0.239	0.132

Table S4.17 | Percent contributions from Sn to each active space orbital using Hirshfeld method in MultiWFN from the CASSCF calculation.

	3	4	5	6
σ	54.58	52.54	50.59	49.27
$3d_{xy}$	0.48	0.46	0.43	0.36
$3d_{x^2-y^2}$	0.50	0.47	0.44	0.36
$3d_{z^2}$	1.45	1.77	2.96	3.40
$3d_{xz}$	1.67	1.66	1.57	1.27
$3d_{yz}$	1.67	1.67	1.57	1.27
σ^*	34.38	32.11	26.38	30.06
$4d_{xy}$	1.95	2.08	2.80	1.87
$4d_{x^2-y^2}$	1.95	2.10	2.78	1.88
$4d_{z^2}$	8.48	10.94	16.32	11.19
$4d_{xz}$	9.31	9.17	9.06	5.85
$4d_{yz}$	9.31	9.17	9.05	5.85

Table S4.18 | Percent contributions from the transition metal to each active space orbital using Hirshfeld method in MultiWFN from the CASSCF calculation.

	3	4	5	6
σ	30.88	33.26	35.28	36.85
$3d_{xy}$	95.61	95.45	95.28	96.00
$3d_{x^2-y^2}$	95.61	95.45	95.28	96.00
$3d_{z^2}$	93.75	93.06	91.17	91.15
$3d_{xz}$	94.49	94.46	94.58	95.20
$3d_{yz}$	94.49	94.46	94.58	95.20
σ^*	50.72	51.87	55.56	54.18
$4d_{xy}$	85.17	84.04	81.83	87.17
$4d_{x^2-y^2}$	85.17	84.04	81.83	87.17
$4d_{z^2}$	78.11	75.65	70.91	78.43
$4d_{xz}$	79.99	79.74	78.91	84.72
$4d_{yz}$	79.99	79.74	78.91	84.72

Table S4.19 | s/p/d orbital contributions from Sn and the transition metal (TM) to the σ bonding orbital from the CASSCF calculations.

Element	Orbital	3	4	5	6
Sn	s	20.37	17.99	19.25	16.74
	p	39.02	38.06	38.39	35.62
	d	0.68	0.78	0.79	0.8
TM	s	15.76	17.9	14.6	17.79
	p	14.74	15.32	14.9	15.21
	d	4.66	6.05	7.92	9.45

Table S4.20 | Calculated zero-field splitting parameters for **3** – **6** given in cm^{-1} from SO-CASPT2.

Compound	Transition Metal	D	E
3	Mn (SS-CASPT2)	0.08	0.0
4	Fe (SS-CASPT2)	34.3	1.1
5	Co (SS-CASPT2)	13.5	2.6
6	Ni (SS-CASPT2)	-11.4	0.4
	Ni (MS-CASPT2)	-12.9	2.3

Table S4.21 | Relative energies (cm^{-1}) of the lowest lying high spin states at the CASPT2 level of theory using an (10e, 12o), (9e, 12o), and (8e, 12o) active space at the CASPT2 level of theory for **4**, **5**, and **6** respectively. Dashes represent excitations not observed within the energy limits of the spectrometer.

TpFeSnPh ₃ (4)		TpCoSnPh ₃ (5)		TpNiSnPh ₃ (6)	
CASPT2	Experiment	CASPT2	Experiment	CASPT2	Experiment
0		0		0	
5	-	1858	-	3788	-
396	-	1861	-	3797	-
4669	4871	3936	-	4059	4333
4669		4964	5959	6848	Not allowed
		4979		6866	
		9008	9308	9011	10256
		15758	14572	17868	14104
		15774		17871	
		16986	15452	19005	17261

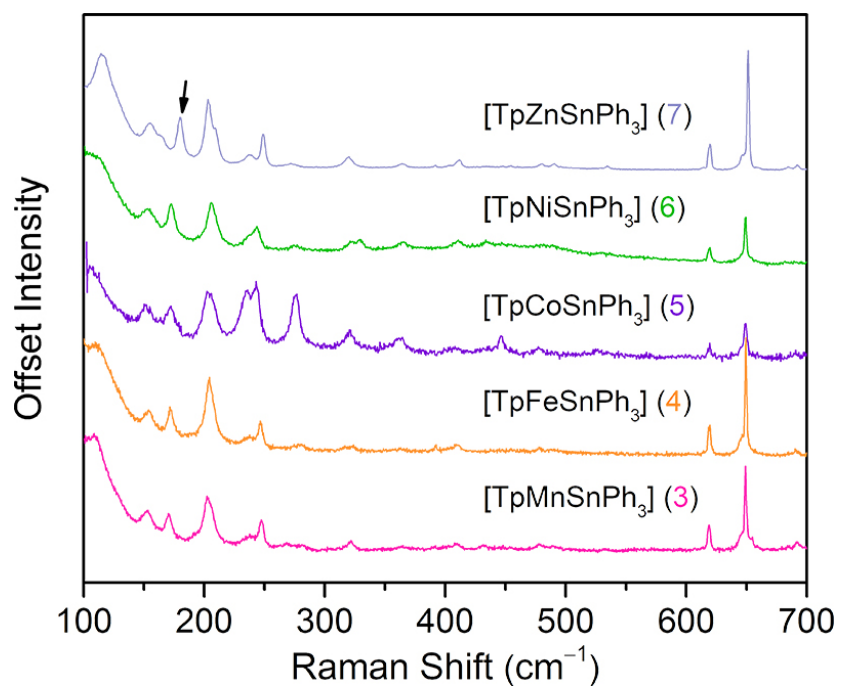


Figure S4.2 | Overlay of Raman spectra for **3** – **7** collected at room temperature under N₂. The black arrow highlights the TM-Sn bond stretching frequency.

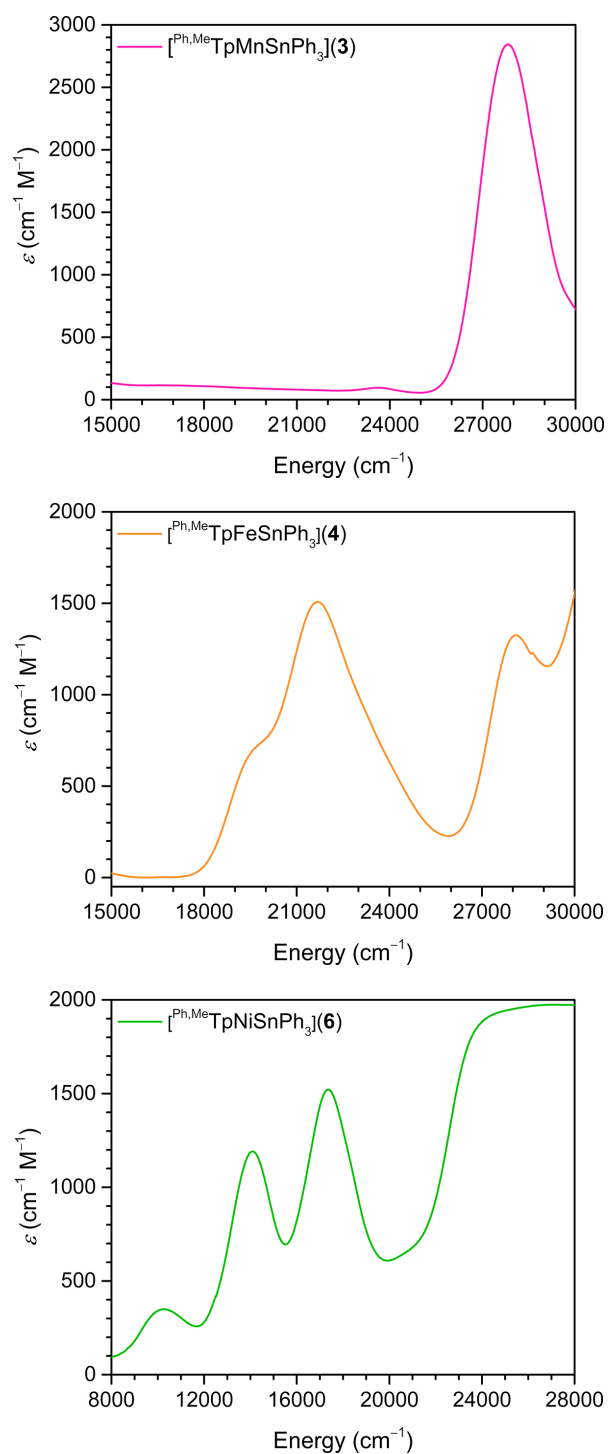


Figure S4.3 | Electronic absorption spectra of **3** (top), **4** (middle), and **6** (bottom) measured at room temperature in C_6D_6 . Note: the peak at $\sim 23,600 \text{ cm}^{-1}$ in the spectrum of **3** is an artifact from background subtraction.

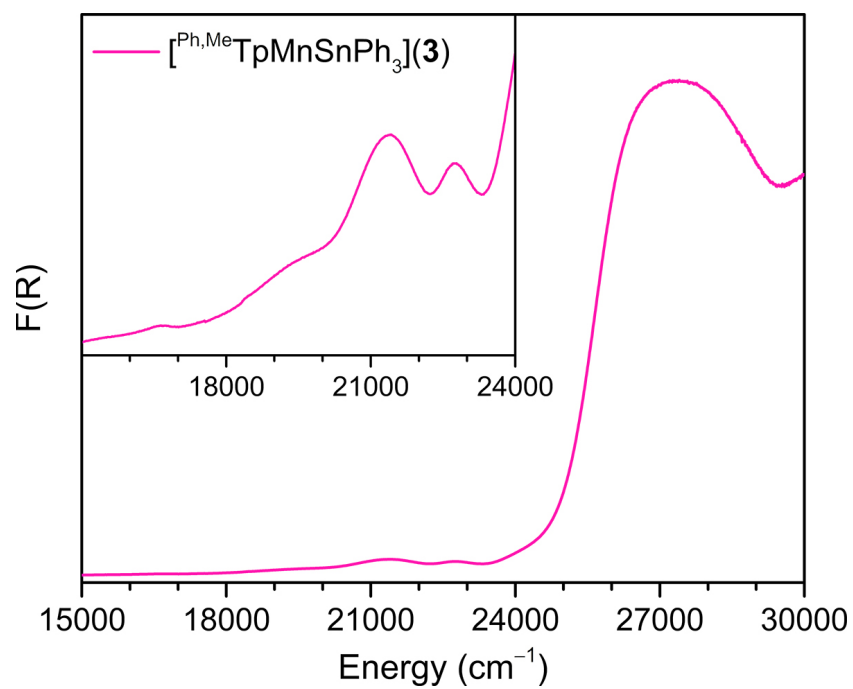


Figure S4.4 | Electronic absorption spectra of **3** measured at room temperature over KBr with an inset of the spectra magnified for easier visualization of the spin-forbidden transitions.

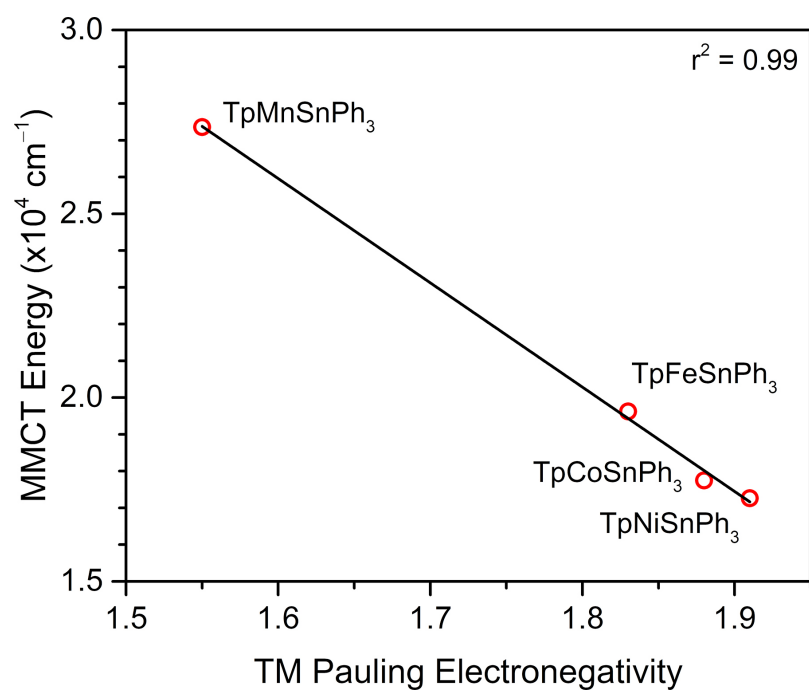


Figure S4.5 | Plot of metal-to-metal charge transfer band energy of **3** – **6** against transition metal (TM) Pauling electronegativity.

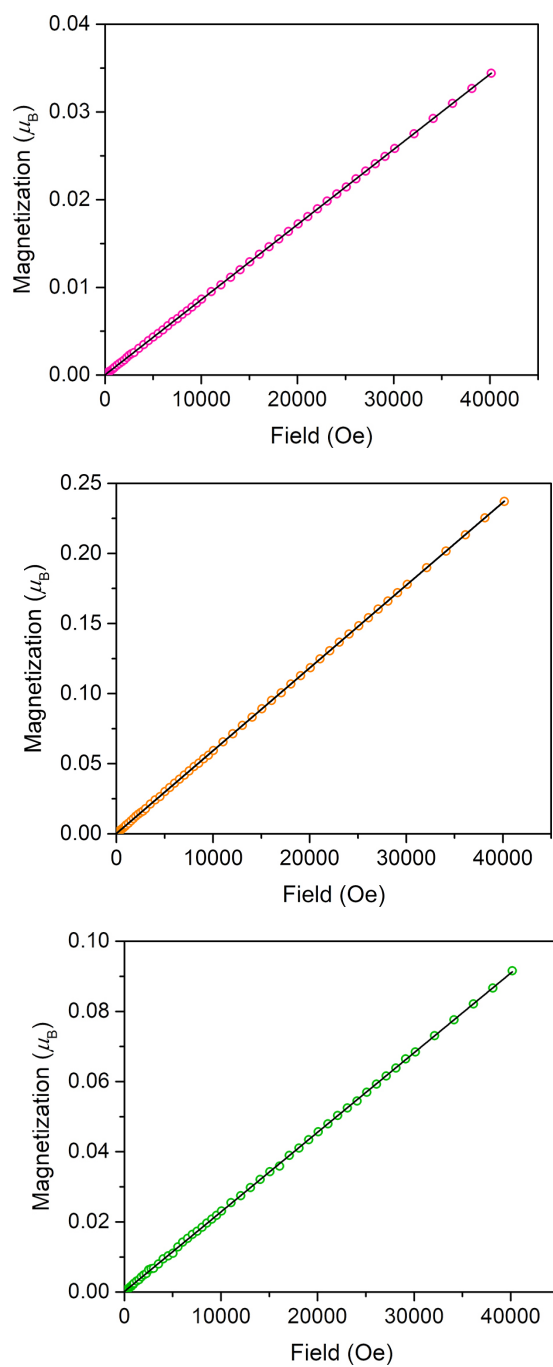


Figure S4.6 | Variable-field magnetization of polycrystalline samples of **3** (top), **4** (middle), **6** (bottom) restrained under eicosane acquired at 100 K. The black line is a linear fit to the data.

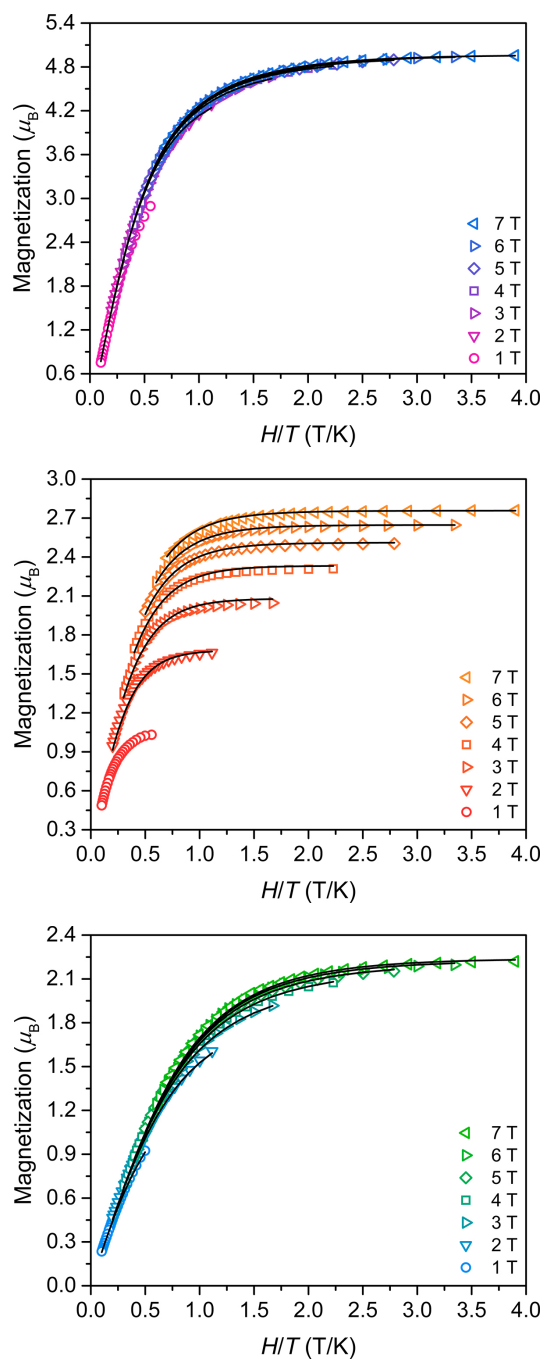


Figure S4.7 | Variable-temperature, variable-field magnetization data for **3**, **4**, and **5** collected between 1.8 and 10 K from 1 to 7 T in 1 T increments. Black lines are simulations of the data obtained from fits using DAVE 2.0 and the spin Hamiltonian, $\hat{H} = g_{\text{iso}}\mu_B\mathbf{S}\mathbf{H} + D[\hat{S}_z^2 - 1/3S(S+1)]$. The parameters for the simulation are given in Table S4.8.

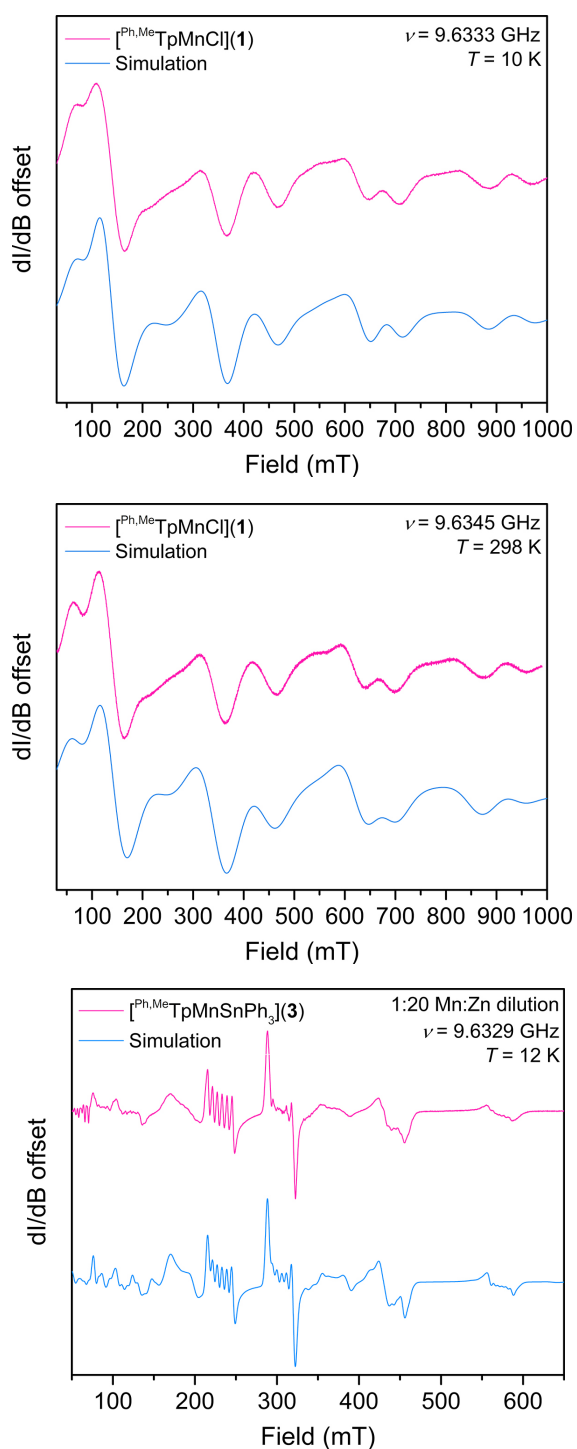


Figure S4.8 | X-band cw-EPR spectrum of **1** (top and middle) and **3** (bottom) diluted in a polycrystalline sample of **7** in a 1:20 (Mn:Zn) ratio encased in eicosane. Simulations of the data were obtained from fits using Easyspin with the spin Hamiltonian, $\hat{H} = g_{\text{iso}}\mu_{\text{B}}\mathbf{S}\mathbf{H} + A\mathbf{I}\mathbf{S} + D[\hat{S}_z^2 - \frac{1}{3}S(S+1)]$. Parameters for the simulations are given in Table S4.9.

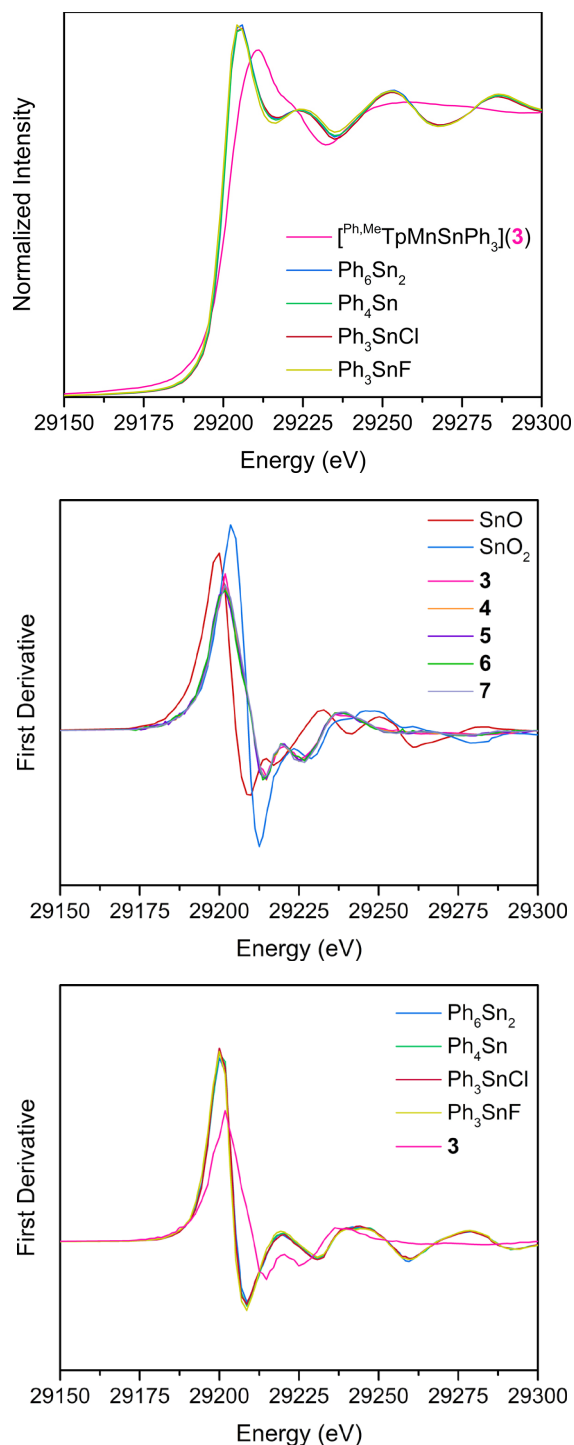


Figure S4.9 | (top) Overlay of XANES data at the Sn K-edge for powder samples of Ph_6Sn_2 , Ph_4Sn , Ph_3SnCl , and Ph_3SnF , shown with the spectrum of **3** for reference, measured at 25 K. (middle) First derivative of XANES data for **3** – **7** with oxide references. (bottom) First derivative of XANES data for **3** and organometallic references.

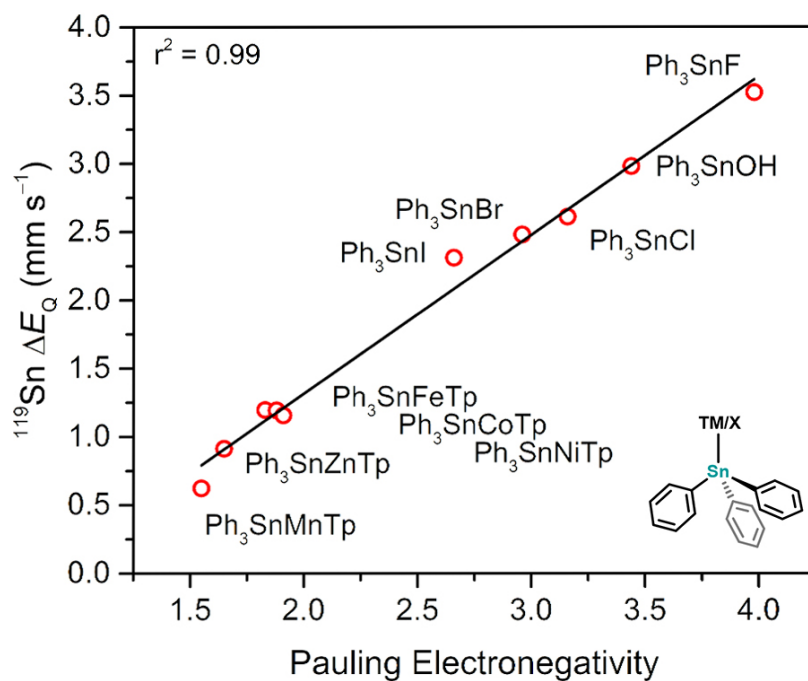


Figure S4.10 | Plot of ^{119}Sn ΔE_Q values of **3** – **7** (transition metal axial ligand, TM) and other triphenyl tin compounds (anionic axial ligand, X) against axial ligand Pauling electronegativity. ΔE_Q values for Ph_3SnX compounds taken from ref. 34.

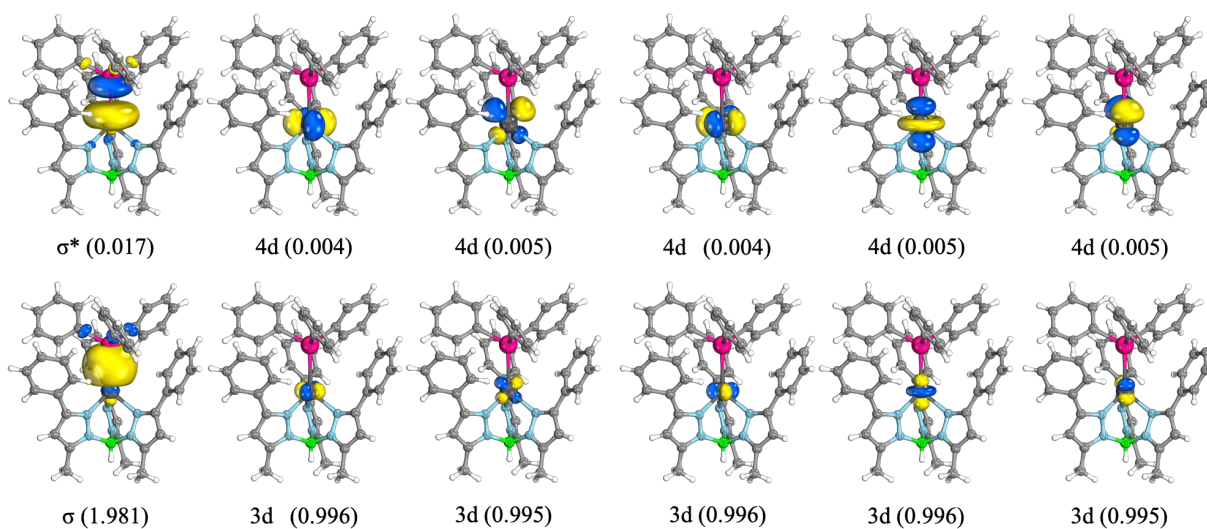


Figure S4.11 | Active natural orbitals from the SA1-CASSCF calculation of **3** in the sextet spin state. The corresponding occupation numbers from lowest CI Root are given in parentheses. An 80% threshold was used for plotting the orbitals.

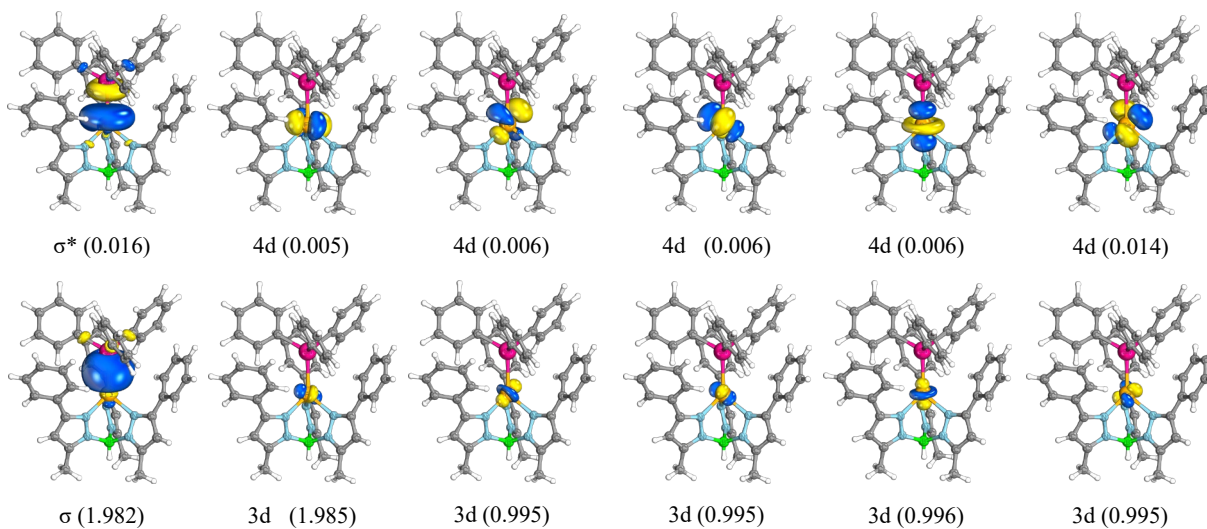


Figure S4.12 | Active natural orbitals from the SA5-CASSCF calculation of **4** in the quintet spin state. The corresponding occupation numbers from lowest CI Root are given in parentheses. An 80% threshold was used for plotting the orbitals.

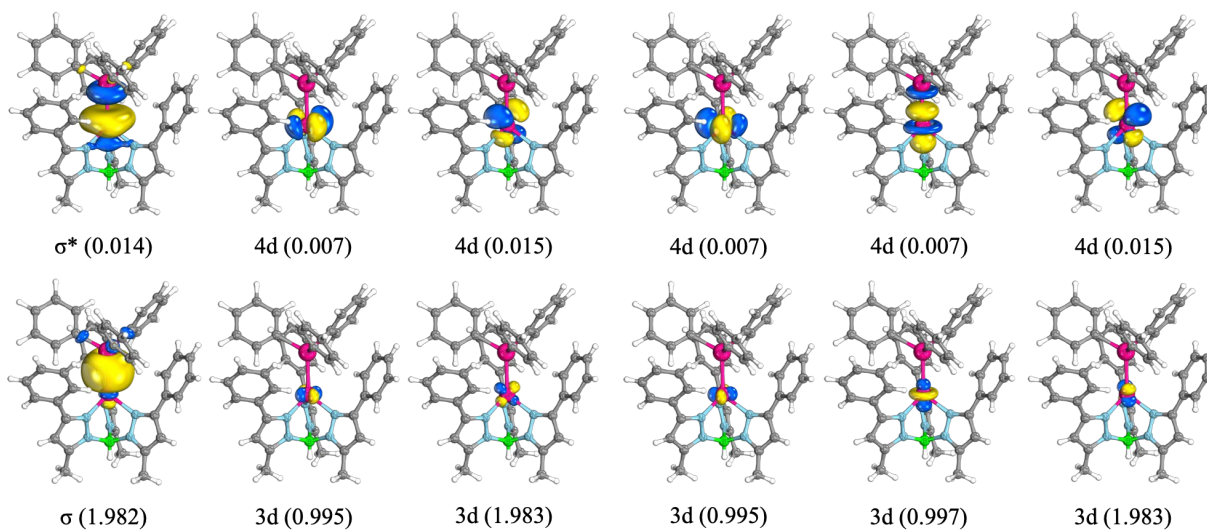


Figure S4.13 | Active natural orbitals from the SA10-CASSCF calculation of **5** in the quartet spin state. The corresponding occupation numbers from lowest CI Root are given in parentheses. An 80% threshold was used for plotting the orbitals.

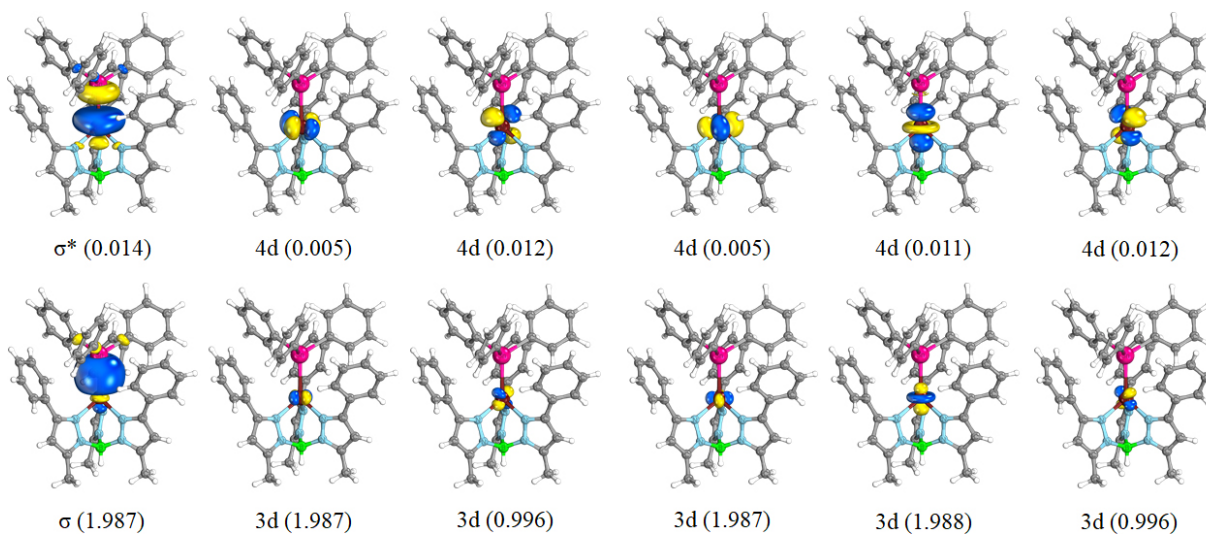


Figure S4.14 | Active natural orbitals from the SA10-CASSCF calculation of **6** in the triplet spin state. The corresponding occupation numbers from lowest CI Root are given in parentheses. An 80% threshold was used for plotting the orbitals.

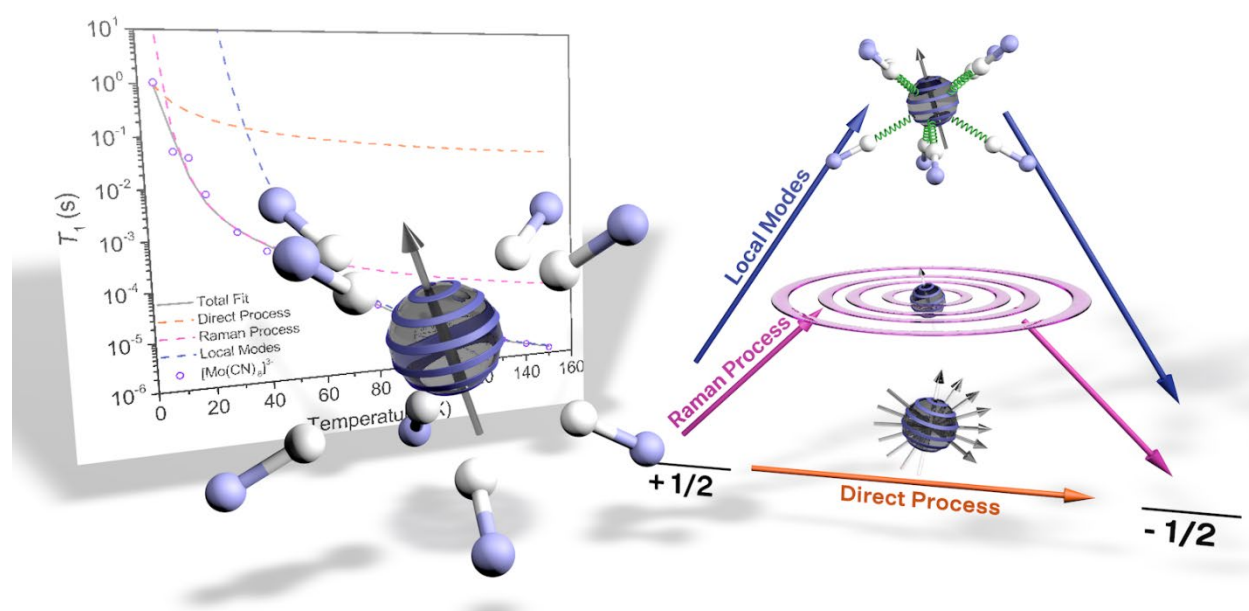
Chapter Five: Octacyanomethylate Qubit Candidates

Reprinted with permission from:

Pearson, T. J.; Laorenza, D.; Krzyaniak, M.; Wasielewski M. R.; Freedman, D. E.
Dalton Transactions **2018**, 47, 11744–11748.

Copyright 2018 Royal Society of Chemistry

This section was written in collaboration with the co-authors listed above



Introduction

Quantum information processing (QIP) promises to fundamentally transform our approach to computation, enabling advances in fields ranging from biochemistry to physics to cryptography.^{1,2} Creation of viable quantum bits, or qubits necessitates the development of systems wherein long-lived superpositions of quantum states are possible. Electron spins, both in molecules and solid-state systems, offer considerable advantages as candidate qubits, including their facility of manipulation with pulsed microwaves.³⁻¹² Magnetic molecules are extremely promising species with which to study the variables that influence coherence time, T_2 , as synthetic chemistry offers a means to tune factors contributing to decoherence. Indeed, through such experimentation, our laboratory and others have developed design principles for increasing coherence times and have implemented them to achieve millisecond coherence times.¹³⁻¹⁶ These and other related advances have allowed the demonstration of gate operations, the proof of concept implementation of Grover's quantum search algorithm, and a theoretical demonstration of adiabatic quantum computation using electron spin qubits.^{17-19,20,21} To further enhance our understanding of spin dynamics in coordination compounds and to propel the field past single- or few-qubit systems, it is vital to understand the factors contributing to spin-lattice relaxation, T_1 , which represents the maximum information storage time as well as the upper limit to T_2 . Indeed, the study of T_1 has recently seen renewed interest for these reasons.^{22,23} By understanding the impact of chemical properties on the specific relaxation mechanisms operative in these compounds, we can implement new design principles to create the next generation of molecular qubits and larger multi-qubit architectures.

Homoleptic cyanometallate complexes and cyanometallate frameworks provide a convenient platform upon which to study fundamental spin relaxation processes. Cyanometallate

complexes have been foundational in the development of modern transition metal chemistry; the study of cyanometallates dates back hundreds of years with the discovery of Prussian Blue.^{24,25} Over the past several decades, the study of magnetism using cyanometallate chemistry has flourished, with emphasis on the structurally predictable networks generated from cyanometallate building units.²⁶⁻³⁰ Such networks allow for the convenient construction of spatially well-defined arrays of paramagnetic metal ions, a highly appealing prospect for qubits.^{31,32} Indeed, if cyanometallate complexes can be established as viable candidate qubits, they would offer significant promise for the creation of spatially controlled qubit arrays.

Results and Discussion

To initiate our studies of cyanometallates, we probed the coherence properties of two structurally analogous homoleptic cyanometallate complexes, $[\text{Mo}(\text{CN})_8][\text{HNBu}_3]_3$ and $[\text{W}(\text{CN})_8][\text{HNBu}_3]_3$.³³ These two species feature within many reported frameworks,³⁴⁻⁴⁰ yet their

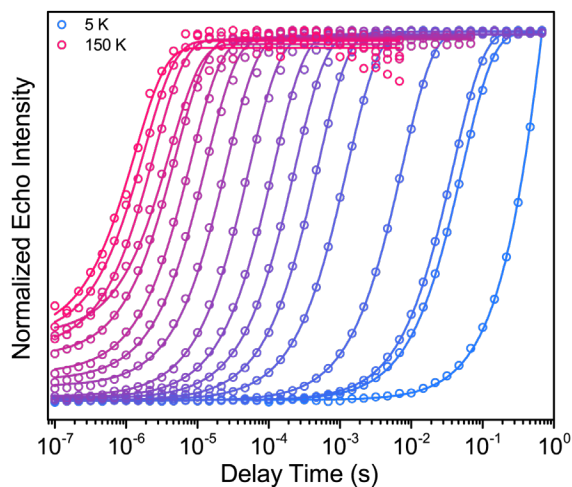


Figure 5.1: Saturation recovery curves as observed upon application of the described saturation recovery pulse sequence (see ESI for detail) on a 0.5 mM solution of **1** in a butyronitrile glass. The solid lines are fits to the data utilizing a monoexponential function.

coherence properties remain unknown.

$[\text{Mo}(\text{CN})_8][\text{HNBu}_3]_3$ (1) and

$[\text{W}(\text{CN})_8][\text{HNBu}_3]_3$ (2) offer two primary

advantages which led to their selection for

this study. First, since both complexes are $S =$

$\frac{1}{2}$, their transitions are easily addressable,

owing to the absence of zero-field splitting,

which could disrupt electron paramagnetic

resonance (EPR) addressability and thereby

convolute the analysis of observed relaxation

rates. Second, these eight-coordinate

compounds are isostructural in solution.^{41,42} This structural similarity allows us to directly compare the influence of spin-orbit coupling on the processes that contribute to the spin-lattice relaxation time, T_1 .

To investigate the viability of these two complexes as candidate qubits, we acquired pulsed electron paramagnetic resonance (EPR) data for each complex in both a butyronitrile glass and a 40 vol % dimethylformamide/toluene glass over a wide temperature range. We observed a spin echo up to 150 K for **1** and 90 K for **2**. This overall relaxation behaviour largely persisted across samples and in different solvent conditions. Here, we were interested in two parameters: T_1 , the spin-lattice relaxation time, and T_2 , the coherence time. Understanding these variables is crucial to evaluating qubit performance, as T_2 represents the operational time of the qubit, and T_1 is both the upper bound to T_2 and is the maximum information storage time.⁴³

We initiated our experiments by determining T_1 through a saturation recovery experiment. In this experiment, a train of picket fence pulses saturates the transition. The return of the peak is then monitored as a function of time after the saturation pulse train with a Hahn-echo detection sequence. The echo intensity is then plotted as a function of the delay time between the end of the picket fence pulse train and the detection sequence. We extracted T_1 values by fitting the resulting

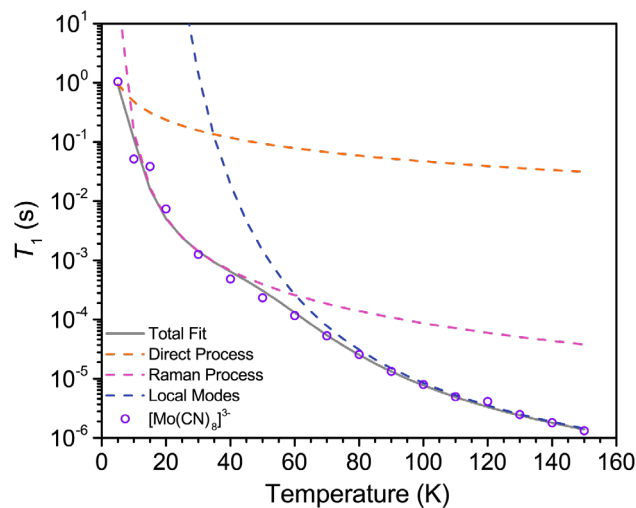


Figure 5.2: Plot of the spin-lattice relaxation time, T_1 vs. temperature from 5 K to 150 K in a 0.5 mM solution of **1** in a butyronitrile glass. The solid line is a fit to the data using the model given in the main text incorporating the direct process, the Raman process, and contributions from local modes (shown as dashed lines).

saturation recovery curves (Figure 5.1) to a monoexponential function. The full details of the data fitting can be found in the ESI.

To determine which processes mediate the spin lattice relaxation of these compounds, we fit the temperature dependence of T_1 to the model

$$\frac{1}{T_1} = A_{dir}T + A_{ram} \left(\frac{T}{\theta_D}\right)^9 J_8 \left(\frac{\theta_D}{T}\right) + A_{loc} \frac{e^{\Delta_{loc}/T}}{(e^{\Delta_{loc}/T} - 1)^2}$$

wherein we accounted for the influence of three different relaxation processes: the direct process, the Raman process and local modes. In the model above, A_{dir} , A_{ram} , and A_{loc} are the direct, Raman, and local mode coefficients respectively, θ_D is the Debye temperature, J_8 is the transport integral

$$J_8 \left(\frac{\theta_D}{T}\right) = \int_0^{\theta_D/T} x^8 \frac{e^x}{(e^x - 1)^2} dx$$

and Δ_{loc} is the energy of the local mode vibrations.⁴⁴ Understanding each of these processes is vital to understanding the manifestation of chemical principles operative in the temperature dependence of the spin-lattice relaxation. At temperatures below 10 K, the direct process, wherein the excited state relaxes through a single phonon-induced spin flip, is frequently significant.⁴⁵ Given that this is formally a spin-forbidden process requiring the breaking of time reversal symmetry, the influence of a hyperfine field typically mediates this process.⁴⁶ In the intermediate temperature regime (20 – 60 K), the Raman process is most prominent. This process is a two-phonon event analogous to Raman scattering of photons. Above 60 K, the Raman process gives way to local mode relaxation, in which more localised vibrational modes dominate relaxation, in contrast to the long-range phonons contributing to relaxation *via* the Raman process. These localised vibrational modes have become a subject of much interest in QIP, and scientists have recently achieved computational insight into them.^{47,48}

Notably, at 5 K, we observe unusually large values of T_1 for both **1** and **2** of 1.05 s, and 0.63 s in butyronitrile respectively. These values offer significant promise for the use of compounds such as **1** and **2** as qubits. We attribute the marked increase in T_1 relative to other coordination compounds to the relatively small contribution of the direct process to the relaxation in these systems. A fit to the data yielded a direct constant (A_{dir}) of less than $1.0 \text{ K}^{-1}\text{s}^{-1}$ for both compounds, which falls significantly outside of the range of $A_{\text{dir}} = 10 - 50 \text{ K}^{-1}\text{s}^{-1}$ found for most

transition metal complexes.⁴⁰ We hypothesise that the small contribution of the direct process arises from the low natural abundance of spin-active nuclei with which the spin is directly interacting ($^{95}\text{Mo} = 15.92\%$, $^{97}\text{Mo} = 9.55\%$, $^{183}\text{W} = 14.31\%$).⁴⁶ More in-depth discussion of this phenomenon can be found in the ESI.

With increasing temperature, the Raman process begins to dominate, and the T_1 values of **1** and **2** diverge, consistent with the difference in spin-orbit coupling between the two complexes ($\zeta = 900 \text{ cm}^{-1}$ and $\zeta = 2700 \text{ cm}^{-1}$ for Mo^{5+} and W^{5+} respectively).⁴⁹ As spin-orbit coupling of the complex increases, the interaction between the spin and the phonon bath strengthens. Therefore, we expect ions containing heavier metals to display more rapid spin-lattice relaxation.⁵⁰ We find

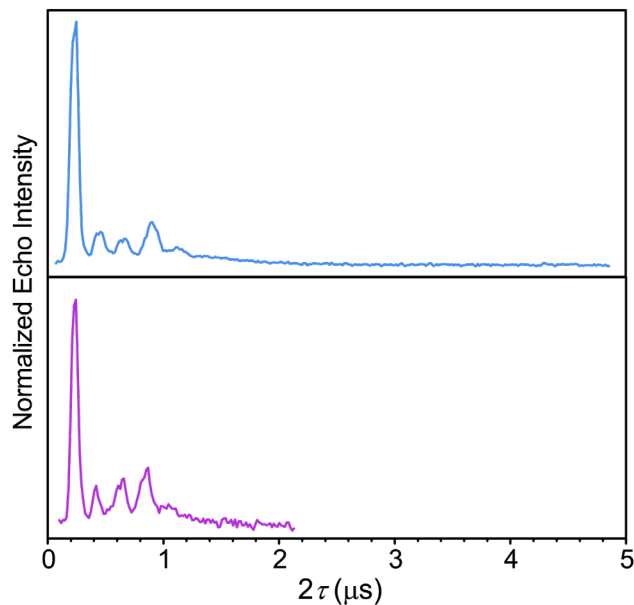


Figure 5.3: Two-pulse Hahn-echo decay curves of a 0.5 mM solution of **1** (top) and a 0.5 mM solution of **2** (bottom) collected at 40 K in butyronitrile. These curves are representative of the data across all temperatures sampled for both **1** and **2**. The extremely deep ESEEM modulation was composed of three frequencies, a result of the ^{14}N nuclei of the cyanide ions experiencing exact cancellation, resulting in a splitting of the nuclear sublevels.

that **2** displays an order of magnitude larger Raman coefficient (A_{ram}) (0.86 MHz vs. 0.053 MHz) and slightly larger local mode coefficient (A_{loc}) (90 MHz vs. 20 MHz) than **1**. In addition to a smaller local mode coefficient, we observe lower characteristic local mode energies for **2** than for **1** (416.1 K for **2** and 514.0 for **1**). We suggest that the strong interaction between the spin and the electronic energy levels resulting from spin-orbit coupling in **2** increases the susceptibility of this complex to relax as a result of vibrational distortions to its ligand sphere. This, in turn, lowers the energy at which vibrational relaxation processes become operative in **2**.⁴⁵ The increase in the contributions of these vibrational relaxation processes leads to the loss of a measurable spin echo by 90 K in **2**, in contrast to the persistence of the echo in **1** until 150 K. In this case, the influence of specific local modes on the relaxation of these complexes cannot be deconvoluted from the spin-orbit contribution which powerfully impacts T_1 . Future studies on other cyanometallate series will probe this effect.

The second key figure of merit for a qubit is T_2 , which we investigated by performing two-pulse Hahn echo experiments. Intriguingly, upon inspection of the T_2 data, we observed deep electron spin echo envelope modulation (ESEEM) within the decay curves of both **1** and **2** (Figure 5.3). A Fourier transform of the data reveals that three distinct frequencies and a broad unresolved feature comprise the ESEEM (Figure 5.4). We attribute the

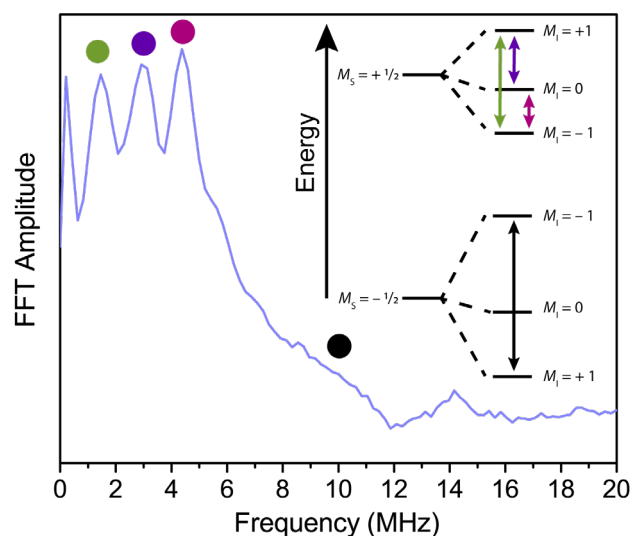


Figure 5.4: Fourier transform of the ESEEM modulation of a 0.5 mM solution of **1** at 40 K in butyronitrile. The three frequencies arise from nullification of the external field at the ^{14}N nuclei, which results in the splitting of the M_1 states shown in the inset. The ^{14}N frequencies are marked with a colour corresponding to the transition to which they correspond.

unusually strong ESEEM in this case to a coincidental, but well preceded exact cancellation condition, wherein $A_{\text{iso}} = 2\nu_1$, where A_{iso} is the isotropic hyperfine parameter and ν_1 is the nuclear Larmor frequency.⁵¹ This condition is met when the hyperfine field cancels out the external field, leaving the nuclear spin sublevels to split from the influence of the electric quadrupole interaction. As illustrated in Figure 5.4, we observe the diagnostic three-line pattern (green, purple, and red dots) followed by a broad higher frequency feature (black dot) in the Fourier transform of the data.

To interpret our T_2 data and extract information regarding the temperature dependence of T_2 for **1** and **2** without overparameterization, we normalised the data collected at each temperature to the 5 K data and subsequently fit the resulting curve to the exponential function:

$$N(\tau) = Ae^{-2\tau/T_R}$$

where N is the curve resulting from the division of a higher temperature curve by the 5 K curve, A is a y-axis scalar term, and T_R in this case is the ratio of the T_2 at the higher temperature to the T_2 at 5 K. This approach enabled us to obtain the temperature dependence of T_2 relative to the T_2 value at 5 K. We have included further details of this fitting in the ESI. For both compounds, we observe a decrease in T_2 as temperature increases – likely influenced by a decrease in T_1 and by fluctuations of methyl groups in the solvent molecules.^{45,52} This behaviour is expected, as in other studies, we and others have observed that T_2 generally remains constant as a function of temperature until approximately 30 K, and then decreases resulting from environmental interference.⁵³⁻⁵⁵ These data demonstrate, however, that we can measure T_2 out to the same temperature we can measure T_1 , thus indicating that these complexes are likely T_1 limited, meaning that the spin-lattice relaxation process indeed serves as the limiting factor to coherence. Future measurements at higher field will enable exact determination of T_2 values as we will have moved away from the exact cancellation condition.

Conclusions

We demonstrate that two cyanometallate complexes are viable qubit candidates, and indeed comprise two of the paucity of examples of second and third row transition metal complexes. At 5 K, these compounds exhibit exceptionally long spin-lattice relaxation times of approximately 1 s. We attribute this observation to the relatively small contribution from the direct process to spin-lattice relaxation resulting from the weak hyperfine field exerted by the transition metal nucleus on the electron spin. In accordance with the smaller spin-orbit coupling constant of **1**, we observe a smaller change in relaxation time with increasing temperature relative to **2**, implicating the stronger influence of spin-orbit coupling in the higher temperature vibrational relaxation processes than in the direct process. This reflects that changes in spin-orbit coupling can be used as a handle to control spin-lattice relaxation by tuning the Raman and local mode contributions but that the direct process is more strongly influenced by other factors.

We propose that these compounds and similar cyanometallates will continue to be valuable platforms upon which to perform these well-controlled studies into fundamental relaxation behaviours – particularly local mode relaxation processes, given the relative simplicity of the ligand field. We also suggest that cyanide frameworks incorporating these ions are worthy of study as potential solid-state qubit arrays given the exceptionally long spin-lattice relaxation times of their constituent parts.

Supporting Information

Experimental Details

General Considerations. Unless otherwise noted, all compounds were purchased from commercial sources and used without further purification. We synthesised both **1** and **2** via literature methods.⁵⁶ All samples were prepared under anaerobic conditions in a dinitrogen glovebox to prevent contamination by dioxygen.

EPR Measurements. We acquired solution phase data on multiple samples of both **1** and **2** to ensure reproducibility. We measured samples in two solvent systems: dry, deoxygenated butyronitrile, or 40 vol% dimethylformamide/toluene. We ensured that all samples had concentrations below 1 mM to limit dipolar contributions.⁵⁷ Here, we report a sample of **1** in 0.5 mM in PrCN and 0.5 mM in 40 vol% DMF/toluene, and a sample of **2** in 0.5 mM in DMF/toluene and 0.5 mM butyronitrile. All samples were prepared in 4 mm OD quartz EPR tubes (Wilmad Labglass) and, depending on the time between preparation and measurement, either flame sealed under high vacuum or flash frozen in liquid nitrogen under an atmosphere of N₂ to prevent contamination of the solvent glass by O₂. For data collection on the same sample over multiple days, samples were stored in liquid N₂ between measurements to prevent decomposition. We acquired EPR data at X-band (~9.5 GHz) on all samples using a Bruker E580 X-band spectrometer equipped with a 5 mm split ring resonator (Bruker ER4118X-MS5) and a 1 kW TWT amplifier (Applied Systems Engineering) at Northwestern University. For all pulsed measurements, the resonator was overcoupled to prevent ringdown following the application of the microwave pulses. Temperature was controlled using an Oxford Instruments Mercury iTC cryostat. *T*₁ data were collected on the most intense central resonance in the echo-detected EPR spectrum (Figure S5.1) using a saturation recovery sequence with a 4- or 8-step phase cycle. This sequence consisted of

eight 20 ns picket fence pulses to saturate the transition followed by a delay (T), and a detection sequence $\pi/2 - \tau - \pi - \tau - \text{echo}$ in which $\pi/2 = 16$ ns, $\pi = 32$ ns, and $\tau = 240$ ns. T was incremented from a starting value of 100 ns.

We phased the T_1 data by maximization of the sum of squares of the data points in the real component of the spectrum, normalised them such that the data spanned the intensity range between 0 and 1, and then fit the data using a monoexponential function of the form

$$\mathbf{I}(t) = -\mathbf{A}(e^{-t/T_1} - \mathbf{d} - \mathbf{1})$$

where I is the normalised echo intensity, A and d are normalization coefficients (approximately 1 and 0 respectively), and t is the delay time (s). Data were also fit using the exponential function

$$\mathbf{I}(t) = -\mathbf{A}(e^{-t/T_1 - \sqrt{t}/c} - \mathbf{d} - \mathbf{1})$$

where all terms retain their original definitions, and c is a spectral diffusion parameter.⁵⁸ Use of one function over another did not appreciably change the T_1 values extracted, a fact reflected in the direct comparison of the monoexponential T_1 values to the T_1 values extracted using the function including a spectral diffusion term. Both sets of fitting parameters are included in Tables S5.2-5.9 and are plotted in Figure S5.6.

We simulated the temperature dependence of T_1 using MatLab R2017b. The function utilised was

$$\log\left(\frac{1}{T_1}\right) = \log\left(A_{dir}T + A_{ram}\left(\frac{T}{\theta_D}\right)^9 J_8\left(\frac{\theta_D}{T}\right) + A_{loc}\frac{e^{\Delta_{loc}/T}}{(e^{\Delta_{loc}/T} - 1)^2}\right)$$

where A corresponds to the coefficients associated with the direct process (dir), Raman process (ram), and local mode contributions (loc) respectively, θ_D is the Debye temperature, and Δ_{loc} is the energy (in K) of the local mode vibrations. J_8 is the transport integral

$$J_8\left(\frac{\theta_D}{T}\right) = \int_0^{\theta_D/T} x^8 \frac{e^x}{(e^x - 1)^2} dx$$

which can be expressed in the form of MatLab code as

`function y = J8(x)`

```

y = real(-(x.^8./(-1+exp(x)))+8.*(-(x.^8./8)+x.^7.* ...
log(1-exp(x))+7.*x.^6.*polylog(2,exp(x))-42.*x.^5.* ...
polylog(3,exp(x))+210.*x.^4.*polylog(4,exp(x))-840.* ...
x.^3.*polylog(5,exp(x))+2520.*x.^2.*polylog(6,exp(x))-5040.* ...
x.*polylog(7,exp(x))+5040.*polylog(8,exp(x)))-8.*(5040.* ...
polylog(8,1)));

```

`end`

We utilised this function rather than the function $\frac{1}{T_1} = A_{\text{dir}}T + A_{\text{ram}}\left(\frac{T}{\theta_D}\right)^9 J_8\left(\frac{\theta_D}{T}\right) + A_{\text{loc}}\frac{e^{\Delta_{\text{loc}}/T}}{(e^{\Delta_{\text{loc}}/T}-1)^2}$ to avoid overweighting the high-temperature data.⁵⁹ See Tables S5.10-5.11 for detailed fit parameters.

As with the T_1 data, we collected T_2 data on the highest-intensity central resonance. We utilised a Hahn echo sequence ($\pi/2 - \tau - \pi - \tau - \text{echo}$) with a 4-step phase cycle, in which $\pi/2 = 16$ ns, $\pi = 32$ ns, and τ was varied from 80 ns for each complex. We set the acquisition trigger to capture the top one-third of the spin echo, and then integrated the acquired portion of the spin echo to obtain the data. We subsequently phased the data by maximizing the sum of the data points in the real component of the spectrum. Extremely deep electron spin echo envelope modulations (ESEEM) resulting from interaction of the spin with different nitrogen centers precluded the fitting of T_2 data without substantial overparameterization. To be more specific, this deep, multifrequency

modulation arose from exact cancellation at the nitrogen atoms.⁶⁰ This arises when the hyperfine field at a quadrupolar nucleus (such as $I = 1$ for ^{14}N) cancels out the external field, resulting in quadrupole splitting in one M_S level. We did model these data to extract a ratio of the T_2 value at a given temperature to the T_2 value at 5 K, and the temperature dependence of T_2 could be observed. This was accomplished by normalizing the data at a given temperature to the data at 5 K to eliminate the ESEEM (assumed to be temperature independent) following the method outlined by Vennam *et al.*⁶¹ The resulting curve was fit using the exponential function

$$N(\tau) = A * e^{2\tau/T_R}$$

where N is the curve normalised to the 5 K data, A is a scale factor, τ is delay time, and T_R in this case is the ratio of T_2 at the given temperature to the T_2 at 5 K.

Brief discussion of direct process suppression: For a complex to relax through the direct process, time reversal symmetry must be violated. One way for this symmetry to break is through the interaction of the spin with a magnetic hyperfine field.⁶² The interaction between the spin and the hyperfine field in this system, however, is weak owing to the the relatively low natural abundance ($\sim 20\%$ for Mo and $\sim 15\%$ for W) of the nuclear spin-active isotopes of the transition metal on which the spin is localised. This reduces the overall influence of the hyperfine field across the sample and, we hypothesise, reduces the likelihood that the spin can relax through the direct process. This manifests in the low direct process contribution to relaxation, and in turn allows for the long T_1 times observed at 5 K.

Table S5.1 | Fit parameters for echo-detected EPR spectra of **1** and **2** in 0.5 mM solutions of butyronitrile. The spectra are shown in Figure S5.1. Natural abundances of all spin-active nuclei were used to model the hyperfine interactions. Simulations of the spectra were performed using EasySpin.⁶³

Complex	g_{iso}	A_{iso} (MHz)	Linewidth (FWHM) (mT)
1	1.973	103	1.5
2	1.963	185	1.7

Table S5.2 | T_1 fit parameters for a 0.5 mM solution of **1** in a butyronitrile glass using the fit function

$$I(t) = -A \left(e^{-t/T_1 - \sqrt{t/c}} - d - 1 \right)$$

The standard error for each fit is reported in parentheses. The inclusion of the spectral diffusion term $\sqrt{t/c}$ throughout the fitting process proved to have minimal impact on the T_1 values extracted. This is reflected in Figure S5.6.

Temperature (K)	A	T_1 (s)	c (s)**	d
5*	2.48(9)	1.39(7)	1000(200)	0.0005(2)
10	0.99491)	0.0550(4)	27(7)	0.0010(5)
15	0.9960(9)	0.0396(2)	100(40)	0.0018(4)
20	0.9977(8)	0.00758(4)	30(20)	0.0006(5)
30	0.9932(10)	0.00127(1)	0(10000)	0.0037(7)
40	0.994(1)	0.000484(2)	0(7E33)	0.0030(9)
50	0.986(3)	0.000244(5)	0.1(1)	0.003(2)
60	0.995(4)	0.000134(5)	0.008(3)	-0.004(4)
70	0.988(7)	0.000061(3)	0.004(3)	-0.001(6)
80	0.979(6)	0.000033(1)	0.0005(2)	0.010(6)
90	0.965(8)	0.0000174(8)	0.00022(7)	0.020(8)
100	0.94(1)	0.0000098(7)	0.0002(1)	0.04(1)
110	0.90(1)	0.0000060(4)	0.00013(9)	0.09(2)
120	0.88(3)	0.000008(1)	0.000015(7)	0.10(3)
130	0.85(3)	0.0000026(4)	0.000(2)	0.15(4)
140	0.84(5)	0.0000021(4)	0.0000(1)	0.16(6)
150	0.77(3)	0.0000013(1)	1.42E+27	0.23(4)

* The echo at 5 K did not fully recover during the experiment, meaning that the estimate for T_1 is less reliable than the ESDs from the fitting reflect. **Spectral diffusion terms could be changed over a wide range with no observable effect on the shape of the fit curve. This is reflected in the large errors associated with these values.

Table S5.3 | T_1 fit parameters for a 0.5 mM solution of **1** in a butyronitrile glass using the fit function

$$I(t) = -A(e^{-t/T_1} - d - 1)$$

The standard error for each fit is reported in parentheses.

Temperature (K)	A	T_1 (s)	d
5*	2.07(5)	1.05(3)	0.0016(3)
10	0.989(1)	0.0520(3)	0.0034(7)
15	0.994(1)	0.0386(1)	0.0029(4)
20	0.9963(7)	0.00745(2)	0.0017(4)
30	0.9931(8)	0.001270(4)	0.0038(5)
40	0.994(1)	0.000484(2)	0.0029(8)
50	0.981(2)	0.000233(2)	0.008(2)
60	0.980(4)	0.000116(2)	0.010(3)
70	0.971(5)	0.000053(1)	0.014(4)
80	0.945(5)	0.0000257(5)	0.043(5)
90	0.924(5)	0.0000133(3)	0.062(5)
100	0.901(6)	0.0000080(2)	0.084(7)
110	0.860(6)	0.0000050(1)	0.140(7)
120	0.78(1)	0.0000041(2)	0.23(2)
130	0.84(1)	0.00000249(9)	0.17(1)
140	0.80(1)	0.00000181(9)	0.21(2)
150	0.77(2)	0.0000013(1)	0.23(4)

* The echo at 5 K did not fully recover during the experiment, meaning that the estimate for T_1 is less reliable than the ESDs from the fitting reflect.

Table S5.4 | T_1 fit parameters for a 0.5 mM solution of **1** in a 40 vol% DMF/toluene glass using the fit function

$$I(t) = -A \left(e^{-t/T_1 - \sqrt{t/c}} - d - 1 \right)$$

The standard error for each fit is reported in parentheses. The inclusion of the spectral diffusion term $\sqrt{t/c}$ proved to have minimal impact on the T_1 values extracted. This is reflected in Figure S5.6.

Temperature (K)	A	T_1 (s)	c (s)**	d
5	0.975(5)	1.48(5)	34(8)	0.003(1)
10	0.990(3)	0.139(3)	4.7(6)	0.0060(9)
15	0.982(3)	0.0275(6)	3(1)	0.010(2)
20	0.983(3)	0.0068(1)	3(1)	0.006(2)
30	0.983(3)	0.00134(3)	0(20)	0.009(2)
40	0.988(3)	0.000492(5)	0(1E37)	0.009(2)
50	0.981(3)	0.000214(3)	0(3E35)	0.010(2)
60	0.978(4)	0.000103(1)	5 E 24	0.012(3)
70	0.979(6)	0.000051(2)	0.006(4)	0.009(5)
80	0.96(1)	0.000030(2)	0.002(3)	0.00(1)
90	0.99(1)	0.000019(1)	0.0003(2)	0.00(1)
100	0.97(2)	0.000011(1)	0.0002(2)	0.0(2)
110	0.97(2)	0.000009(1)	0.00004(2)	0.00(2)
120	0.99(2)	0.000007(1)	0.000015(5)	0.00(2)

**Spectral diffusion terms could be changed over a wide range with no observable effect on the shape of the fit curve. This is reflected in the large errors associated with these values.

Table S5.5 | T_1 fit parameters for a 0.5 mM solution of **1** in a 40 vol% DMF/toluene glass using the monoexponential fit function

$$I(t) = -A(e^{-t/T_1} - d - 1)$$

The standard error for each fit is reported in parentheses.

Temperature (K)	A	T_1 (s)	d
5	0.957(7)	1.13(3)	0.010(2)
10	0.964(7)	0.110(2)	0.014(2)
15	0.973(3)	0.0245(3)	0.015(2)
20	0.978(2)	0.00638(6)	0.009(1)
30	0.982(3)	0.00132(1)	0.011(2)
40	0.988(3)	0.000492(5)	0.009(2)
50	0.982(3)	0.000214(2)	0.010(1)
60	0.979(4)	0.000103(1)	0.012(3)
70	0.966(4)	0.0000552(9)	-0.021(3)
80	0.948(6)	0.0000267(7)	0.025(5)
90	0.949(7)	0.0000151(4)	0.034(6)
100	0.91(1)	0.0000091(4)	0.05(1)
110	0.90(1)	0.0000060(2)	-0.08(1)
120	0.88(1)	0.0000040(2)	0.10(1)

Table S5.6 | T_1 fit parameters for a 0.5 mM solution of **2** in a butyronitrile glass using the fit function

$$I(t) = -A \left(e^{-t/T_1 - \sqrt{t/c}} - d - 1 \right)$$

The standard error for each fit is reported in parentheses. The inclusion of the spectral diffusion term $\sqrt{t/c}$ proved to have minimal impact on the T_1 values extracted. This is reflected in Figure S5.6.

Temperature (K)	A	T_1 (s)	c (s)*	d
5	0.95(1)	1.8(4)	1.9(4)	0.000(5)
10	0.989(2)	0.0713(5)	22(4)	0.0009(5)
15	0.991(1)	0.0120(1)	12(5)	0.0012(8)
20	0.993(2)	0.00133(2)	6(10)	-0.002(1)
30	0.988(4)	0.00030(1)	0.02(1)	-0.000(3)
40	0.989(5)	0.000095(3)	0.006(2)	0.000(3)
50	0.973(8)	0.000027(1)	0.003(2)	-0.015(6)
60	0.939(6)	0.0000100(3)	0.0006(2)	0.060(6)
70	0.888(9)	0.0000043(2)	0.00017(9)	-0.12(1)
80	0.79(2)	0.0000020(2)	0.00004(3)	-0.26(3)
90	0.83(3)	0.0000021(3)	0.0000018(5)	-0.19(4)

*Spectral diffusion terms could be changed over a wide range with no observable effect on the shape of the fit curve. This is reflected in the large errors associated with these values.

Table S5.7 | T_1 fit parameters for a 0.5 mM solution of **2** in a butyronitrile glass using the fit function

$$\mathbf{I(t)} = -\mathbf{A}(e^{-t/T_1} - \mathbf{d} - \mathbf{1})$$

The standard error for each fit is reported in parentheses.

Temperature (K)	A	T_1 (s)	d
5	1.0	0.63(5)	0.003(9)
10	0.991(2)	0.0664(5)	0.0038(8)
15	0.988(2)	0.01157(7)	0.0031(7)
20	0.991(2)	0.001310(8)	0.0034(9)
30	0.975(4)	0.000268(4)	0.011(3)
40	0.973(4)	0.000083(1)	0.015(3)
50	0.965(5)	0.0000249(4)	0.029(3)
60	0.912(4)	0.0000087(1)	-0.084(3)
70	0.858(4)	0.00000371(6)	0.160(5)
80	0.742(6)	0.00000167(4)	0.330(9)
90	0.66(1)	0.00000097(4)	0.48(2)

Table S5.8 | T_1 fit parameters for a 0.5 mM solution of **2** in a 40 vol% DMF/toluene glass using the fit function

$$I(t) = -A \left(e^{-t/T_1 - \sqrt{t/c}} - d - 1 \right)$$

The standard error for each fit is reported in parentheses. The inclusion of the spectral diffusion term $\sqrt{t/c}$ proved to have minimal impact on the T_1 values extracted. This is reflected in Figure S5.6.

Temperature (K)	A	T_1 (s)	c (s)*	d
5	0.989(3)	0.469(9)	21(3)	0.002(1)
10	0.991(3)	0.0304(7)	1.5(3)	0.003(1)
15	0.984(2)	0.00393(8)	1×10^3 (2)	0.005(2)
20	0.971(3)	0.00131(1)	-3×10^{33} (0)	-0.011(2)
30	0.95(1)	0.00031(3)	0.011(8)	-0.022(9)
40	0.930(5)	0.000062(1)	-3×10^{25} (0)	-0.057(4)
50	0.859(9)	0.0000215(6)	9×10^{26} (0)	0.115(6)
60	0.77(1)	0.0000075(2)	8×10^{25} (0)	0.242(8)
70	0.64(1)	0.0000029(1)	2×10^{24} (0)	0.52(2)
80	0.50(1)	0.0000018(1)	2×10^{30} (0)	0.95(4)
90	0.40(2)	0.0000009(1)	-1×10^{29} (3)	1.4(1)

*Spectral diffusion terms could be changed over a wide range with no observable effect on the shape of the fit curve. This is reflected in the large errors associated with these values.

Table S5.9 | T_1 fit parameters for a 0.5 mM solution of **2** in a 40 vol% DMF/toluene glass using the fit function.

$$I(t) = -A(e^{-t/T_1} - d - 1)$$

The standard error for each fit is reported in parentheses.

Temperature (K)	A	T_1 (s)	d
5	0.973(5)	0.388(6)	0.008(2)
10	0.978(5)	0.0255(4)	0.011(2)
15	0.983(2)	0.00392(4)	0.006(1)
20	0.971(3)	0.00131(1)	0.012(2)
30	0.929(8)	0.000256(9)	0.038(6)
40	0.930(5)	0.000062(1)	0.057(4)
50	0.882(7)	0.0000218(6)	0.115(6)
60	0.796(6)	0.0000076(2)	0.241(7)
70	0.650(9)	0.0000031(1)	0.51(2)
80	0.50(2)	0.0000018(1)	0.95(4)
90	0.41(2)	0.0000009(1)	1.4(1)

Table S5.10 | Parameters from fitting the temperature dependence of T_1 using the fit function

$$\log\left(\frac{1}{T_1}\right) = \log\left(A_{dir}T + A_{ram}\left(\frac{T}{\theta_D}\right)^9 J_8\left(\frac{\theta_D}{T}\right) + A_{loc}\frac{e^{\Delta_{loc}/T}}{(e^{\Delta_{loc}/T} - 1)^2}\right)$$

while using T_1 values extracted using the fit function including a spectral diffusion term

$$I(t) = -A\left(e^{-t/T_1 - \sqrt{t/c}} - d - 1\right)$$

Errors from fitting are presented as 95% confidence bounds.

Sample	A_{dir} ($s^{-1} K^{-1}$)	A_{loc} ($s^{-1} \times 10^8$)	A_{ram} ($s^{-1} \times 10^5$)	Δ_{loc} (K)	θ_D (K)
1 (0.5 mM in PrCN)	0.149 (-0.001, 0.299)	0.129 (-0.066, 0.325)	0.462 (-0.171, 1.095)	494.1 (338.1, 649.8)	76.73 (49.2, 104.3)
2 (0.5 mM in PrCN)	0.107 (0.02353, 0.1905)	0.2407 (-0.2037, 0.6851)	4.318 (-2.376, 11.01)	339.6 (213.1, 466.1)	102.1 (73.03, 131.2)
1 (0.5 mM in DMF/Tol)	0.138 (0.08674, 0.1893)	0.072 (0.0022, 0.141)	0.67 (0.215, 1.12)	350 (279.1, 420.8)	88.32 (74.99, 101.7)
2 (0.5 mM in DMF/Tol)	0.3986 (0.2934, 0.5038)	0.3911 (-0.1933, 0.589)	2.039 (0.9617, 3.11)	339.8 (306.9, 372.6)	78.36 (69.13, 87.58)

Table S5.11 | Parameters from fitting the temperature dependence of T_1 using the fit function

$$\log\left(\frac{1}{T_1}\right) = \log\left(A_{dir}T + A_{ram}\left(\frac{T}{\theta_D}\right)^9 J_8\left(\frac{\theta_D}{T}\right) + A_{loc}\frac{e^{\Delta_{loc}/T}}{(e^{\Delta_{loc}/T} - 1)^2}\right)$$

while using T_1 values extracted using the fit function

$$I(t) = -A(e^{-t/T_1} - d - 1)$$

Errors from fitting are presented as 95% confidence bounds.

Sample	A_{dir} ($s^{-1} K^{-1}$)	A_{local} ($s^{-1} \times 10^8$)	A_{ram} ($s^{-1} \times 10^5$)	Δ_{loc} (K)	θ_D (K)
1 (0.5 mM in PrCN)	0.213 (0.027, 0.399)	0.2 (-0.06, 0.46)	0.53(-0.12, 0.12)	514 (380.2, 648.2)	79.5 (53.8, 105)
2 (0.5 mM in PrCN)	0.3428 (0.1367, 0.549)	0.9424 (-.7458, 2.631)	8.569 (-1.679, 18.82)	416.1 (287, 545.3)	115.8 (89.91, 141.6)
1 (0.5 mM in DMF/Tol)	0.209 (0.120, 0.300)	0.072 (0.0022, 0.141)	0.67 (0.21, 1.15)	432.5 (345.1, 519.8)	85.6 (71.2, 100)
2 (0.5 mM in DMF/Tol)	0.4915 (0.3102, 0.6728)	0.4349 (0.1038, 0.7649)	2.353 (0.6501, 4.056)	350 (299.6, 400.4)	79.23 (66.38, 92.07)

Table S5.12 | Temperature dependence of T_2 for a 0.5 mM solution of **1** in butyronitrile relative to the T_2 at 5 K extracted using the equation

$$N(\tau) = A * e^{2\tau/T_R}$$

These data are plotted in Figure S5.9.

Temperature (K)	Change in T_2 ratio (T_R) (compared to 5K T_2)	A
10	0.0000190	1.0192
20	-0.000217	0.9564
30	0.0000860	1.0184
40	0.0001170	1.0245
50	0.0001360	1.0248
60	0.0001120	1.0253
70	-0.0000157	0.9821
80	-0.0000703	0.9677
90	0.0002010	1.0758
100	0.0011300	1.3392
110	0.0026500	1.9293
120	0.0050700	3.3190
130	0.0081000	6.6383
140	0.0098000	9.6361
150	0.0112000	13.0688

Table S5.13 | Temperature dependence of T_2 for a 0.5 mM solution of **1** in 40 vol% DMF/toluene relative to the T_2 at 5 K extracted using the equation

$$N(\tau) = A * e^{2\tau/T_R}$$

These data are plotted in Figure S5.9.

Temperature (K)	Change in T_2 ratio (T_R) (compared to 5K T_2)	A
10	0.0000501	1.0122
15	0.0000696	1.0179
20	0.0000772	1.0128
30	0.000148	1.0438
40	0.000183	1.0401
50	0.000301	1.0739
60	0.000738	1.1939
70	0.000651	1.1779
80	0.000324	1.0963
90	0.000217	1.0529
100	0.000129	1.0587
110	0.000108	1.0439
120	0.000292	1.0808

Table S5.14 | Temperature dependence of T_2 for a 0.5 mM solution of **2** in butyronitrile relative to the T_2 at 5 K extracted using the equation

$$N(\tau) = A * e^{2\tau/T_R}$$

These data are plotted in Figure S5.10.

Temperature (K)	Change in T_2 ratio (T_R) (compared to 5K T_2)	A
10	0.000117	1.0478
15	0.000136	1.0432
20	0.000112	1.0455
30	-0.0000157	1.0528
40	-0.0000703	1.0480
50	0.000201	1.0825
60	0.00113	1.0963
70	0.00265	1.1779
80	0.00507	1.4256
90	0.00810	1.8171

Table S5.15 | Temperature dependence of T_2 for a 0.5 mM solution of **2** in 40 vol% DMF/toluene relative to the T_2 at 5 K using the equation

$$N(\tau) = A * e^{2\tau/T_R}$$

These data are plotted in Figure S5.10.

Temperature (K)	Change in T_2 ratio (T_R) (compared to 5K T_2)	A
10	0.000809	1.0053
15	0.000116	1.0161
20	0.000167	1.0186
30	0.000200	1.0365
40	0.000258	1.0281
50	0.00116	1.2502
60	0.00221	1.5453
70	0.00244	1.6784
80	0.00334	1.9737
90	0.00360	1.9010

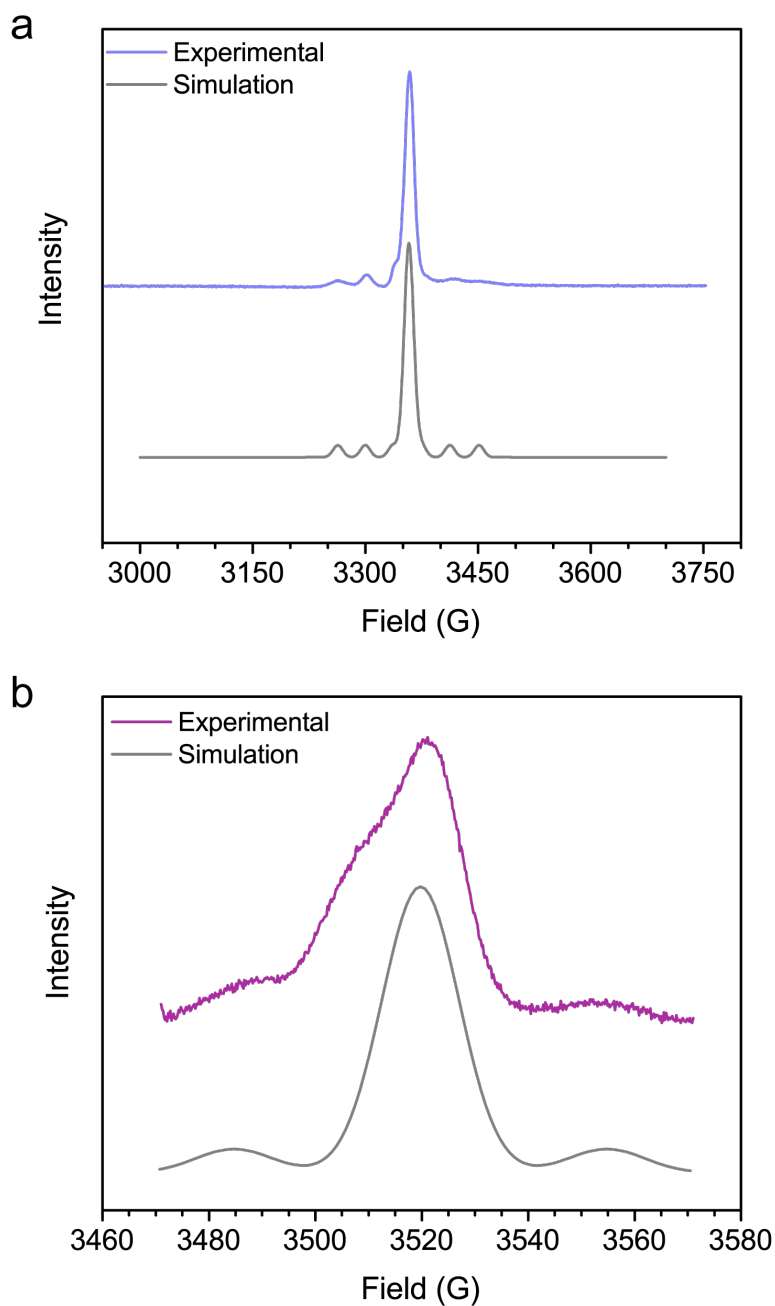


Figure S5.1 | Echo-detected EPR spectrum of (a) **1** and (b) **2** in a 0.5 mM butyronitrile glass at 20 K. T_1 and T_2 data were collected at the highest central resonance at approximately 3370 G (**1**) and 3520 G (**2**). Fit parameters can be found in Table S5.1.

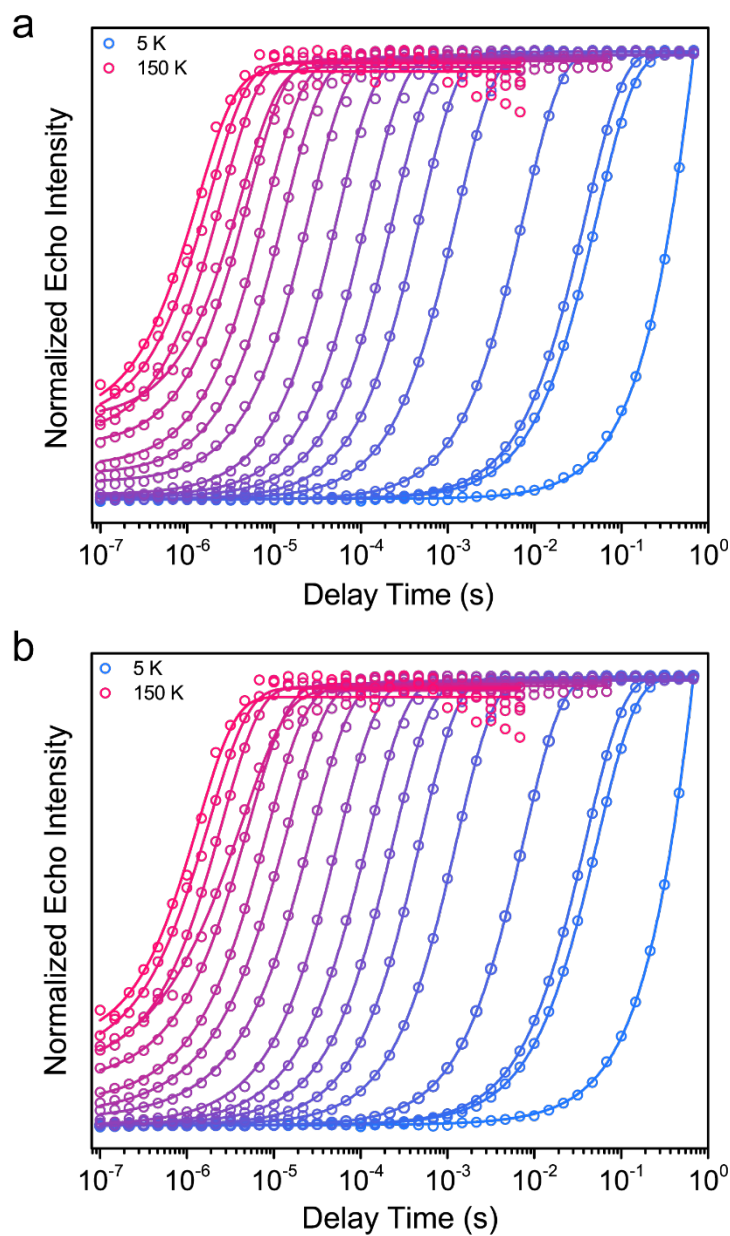


Figure S5.2 | Saturation recovery curves collected on a 0.5 mM solution of **1** in butyronitrile. Solid lines are fits to the data using an (a) monoexponential function, and (b) a function incorporating a term including spectral diffusion. As was noted earlier, using one fit over another did not appreciably change T_1 values extracted.

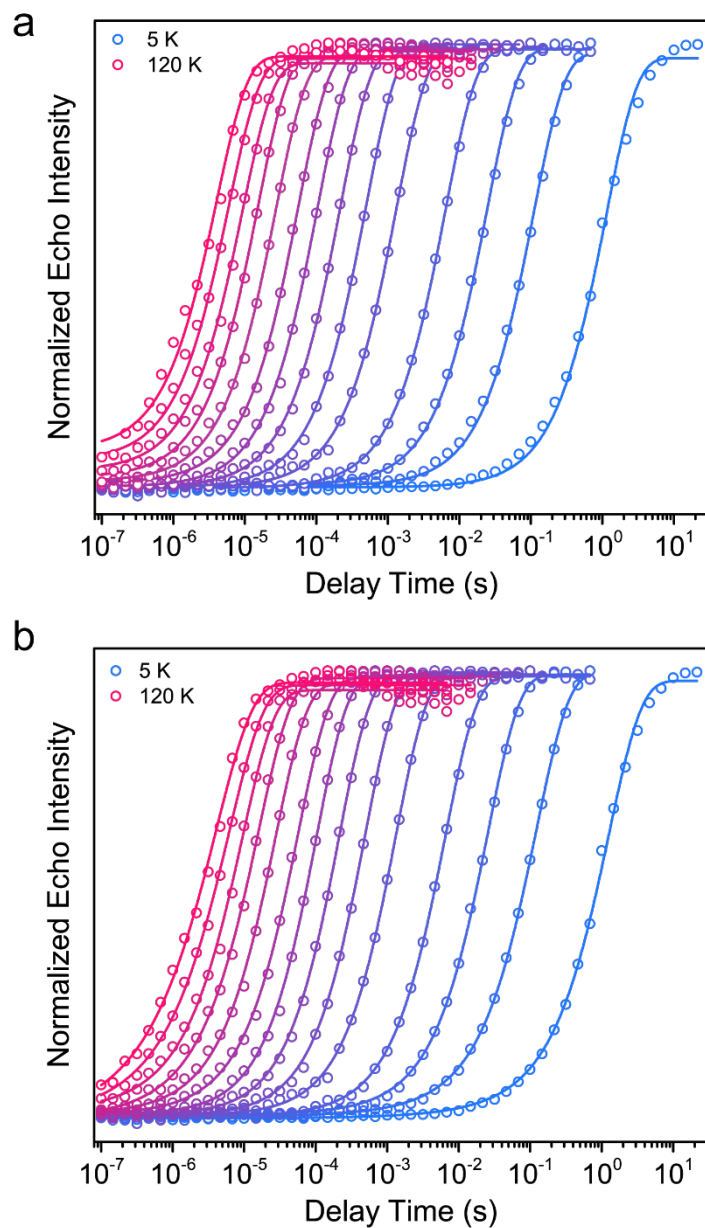


Figure S5.3 | Saturation recovery curves collected on a 0.5 mM solution of **1** in 40 vol% DMF/toluene. Solid lines are fits to the data using an (a) monoexponential function, and (b) a function incorporating a term including spectral diffusion. As was noted earlier, using one fit over another did not appreciably change T_1 values extracted.

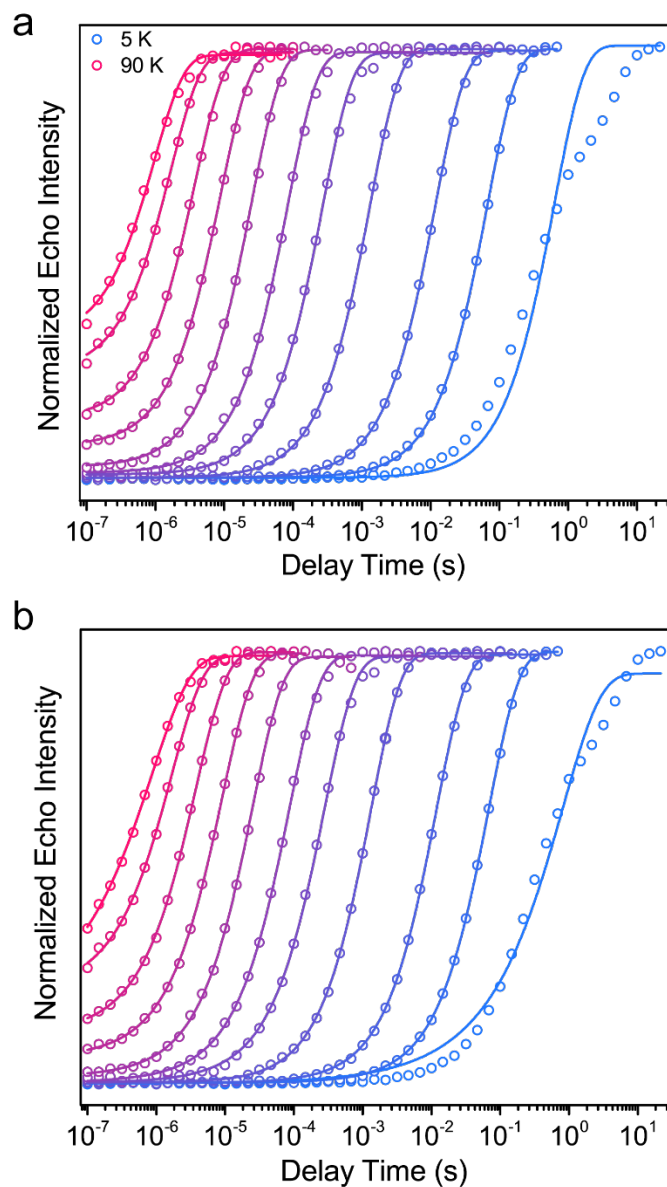


Figure S5.4 | Saturation recovery curves collected on a 0.5 mM solution of **2** in butyronitrile. Solid lines are fits to the data using an (a) monoexponential function, and (b) a function incorporating a term including spectral diffusion. As was noted earlier, using one fit over another did not appreciably change T_1 values extracted.

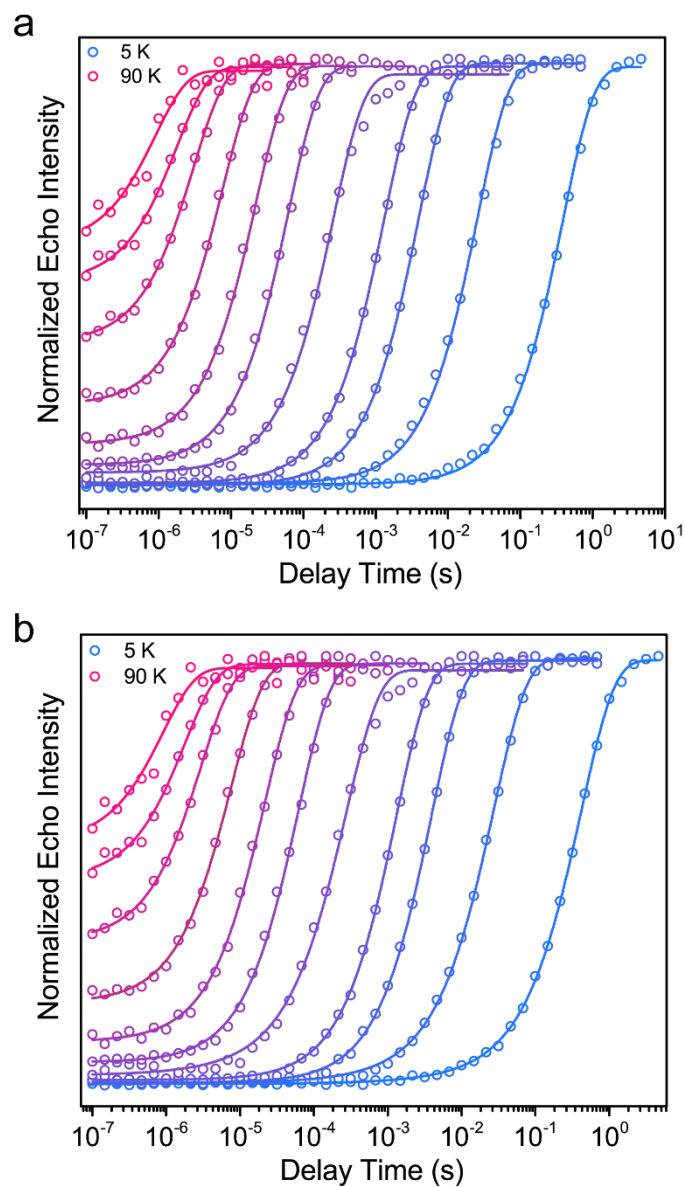


Figure S5.5 | Saturation recovery curves collected on a 0.5 mM solution of **2** in 40 vol% DMF/toluene. Solid lines are fits to the data using an (a) monoexponential function, and (b) a function incorporating a term including spectral diffusion. As was noted earlier, using one fit over another did not appreciably change T_1 values extracted.

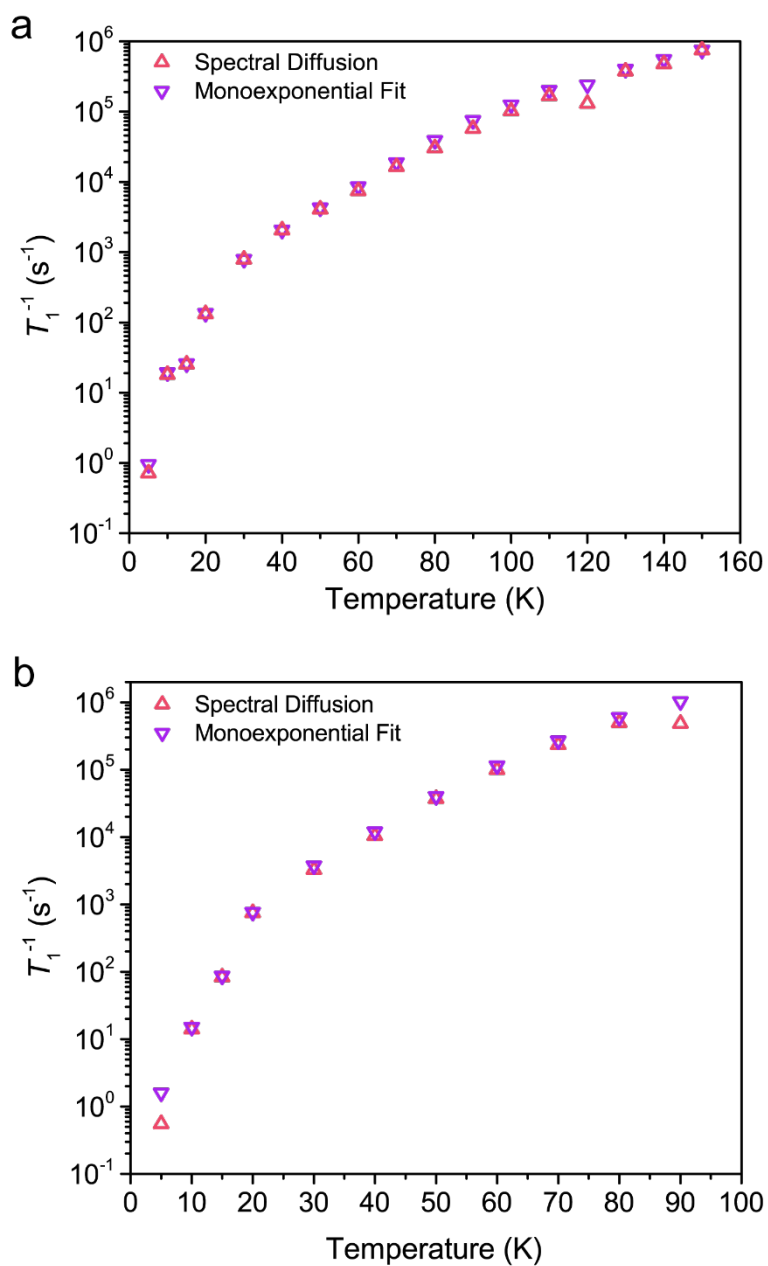


Figure S5.6 | Comparison of T_1 values of **1** (0.5 mM) and **2** (0.5 mM) in butyronitrile extracted using a monoexponential fit vs. using a fit including a spectral diffusion term for (a) $[\text{Mo}(\text{CN})_8]^{3-}$ and (b) $[\text{W}(\text{CN})_8]^{3-}$. The T_1 values only diverge slightly and remain within experimental error, so spectral diffusion was determined to have a minimal influence on T_1 . This is expected for data collected through a saturation recovery experiment.

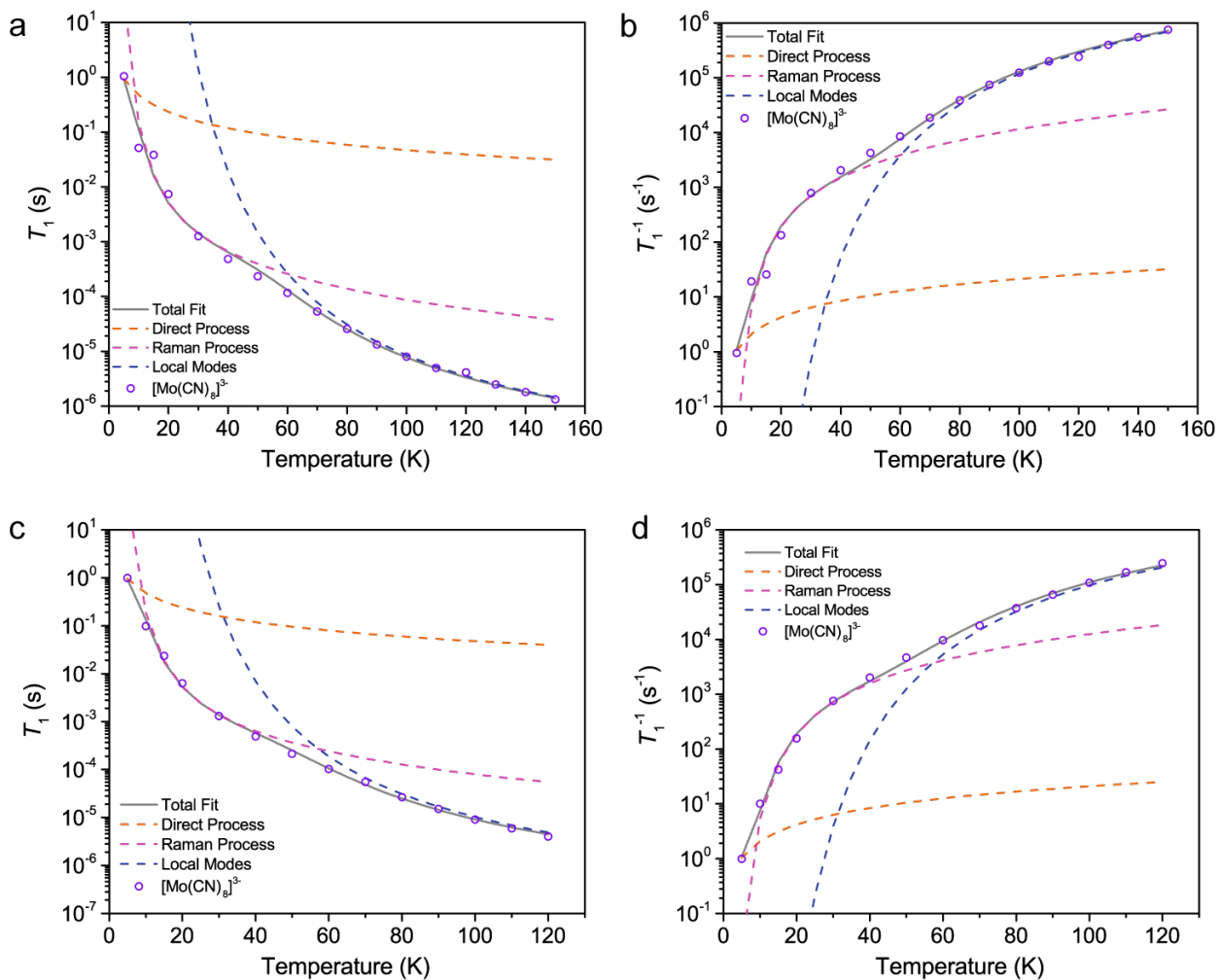


Figure S5.7 | Temperature dependence of T_1 for 0.5 mM solutions of **1** in (a,b) PrCN and (c,d) 40 vol% DMF/toluene. T_1 values were extracted using a monoexponential function. We also included the same data plotted as the rate of relaxation (T_1^{-1}) (b, d). Fit parameters are included in Tables S5.10 and S5.11.

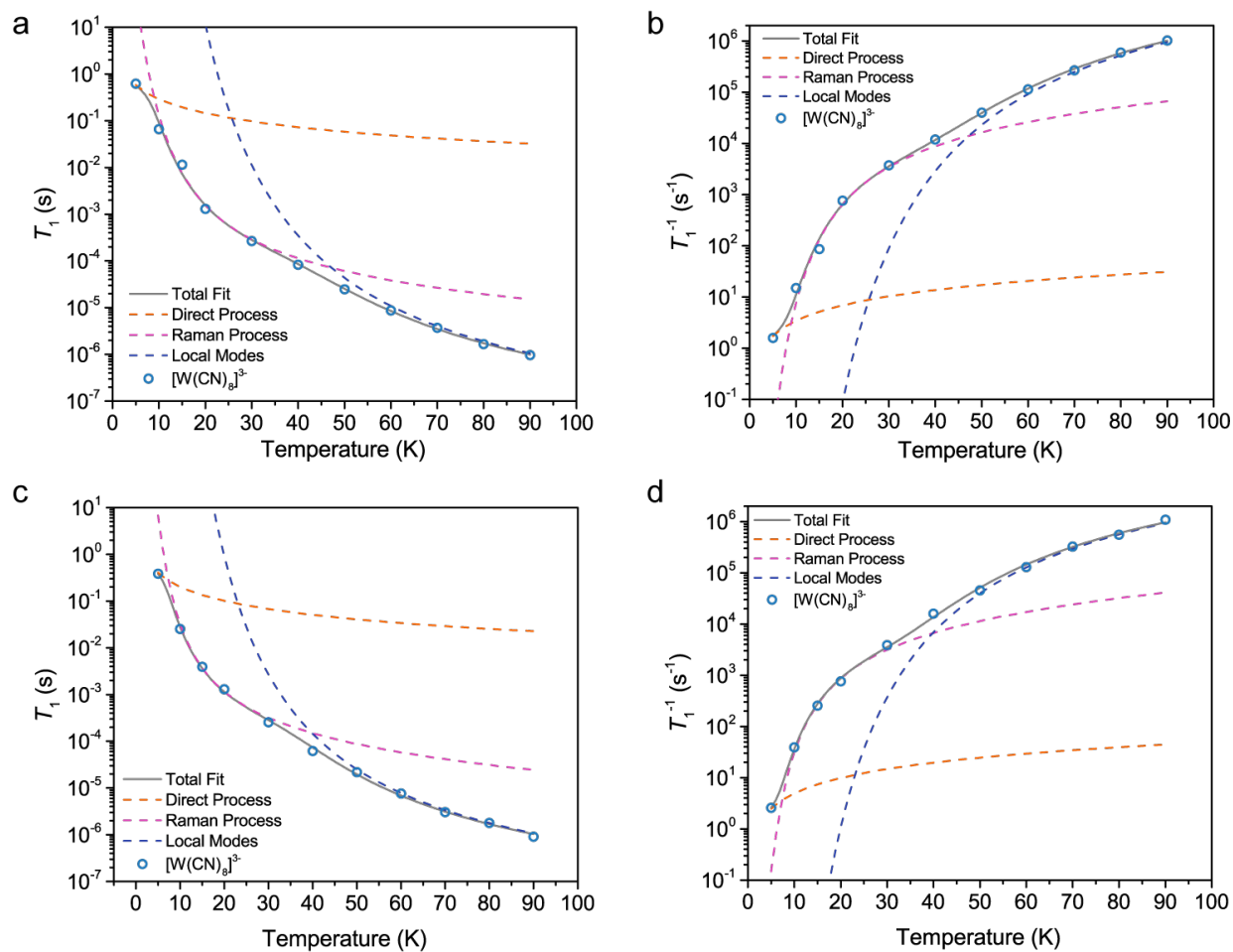


Figure S5.8 | Temperature dependence of T_1 for 0.5 mM solutions of **2** in (a,b) PrCN and (c,d) 40 vol% DMF/toluene. T_1 values were extracted using a monoexponential function. We also included the same data plotted as the rate of relaxation (T_1^{-1}) (b, d). Fit parameters are included in Tables S5.10 and S5.11.

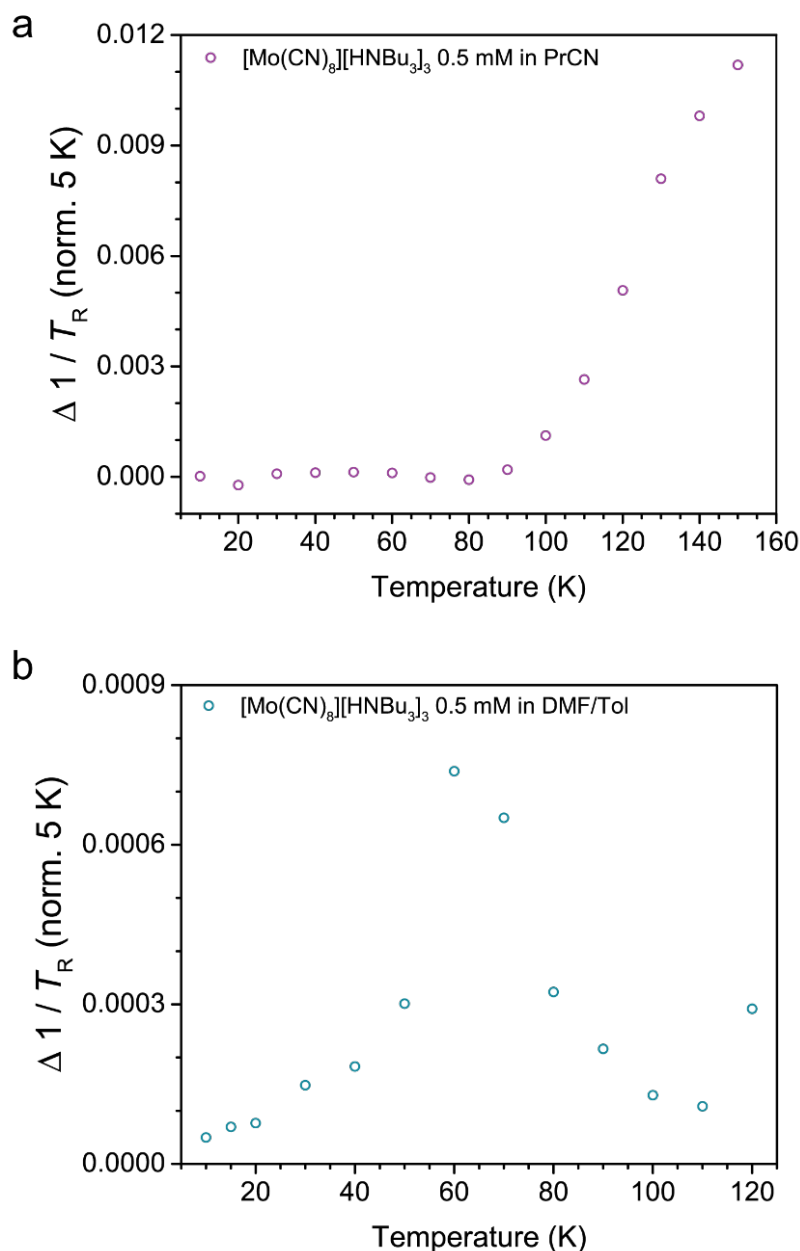


Figure S5.9 | Temperature dependence of T_2 normalised to the T_2 value at 5 K for 0.5 mM solutions of **1** in a) butyronitrile, and b) 40 vol% DMF/toluene. As temperature increases, the spin-spin relaxation rate generally increases. This trend is commensurate with T_2 studies on other transition metal systems. Absolute values of T_2 could not be determined at X-band because of exact cancellation, but the temperature dependence was determined *via* normalization of the data to the 5 K decay curve to remove ESEEM modulation and extraction of relative T_2 from the resulting normalised decay curve.

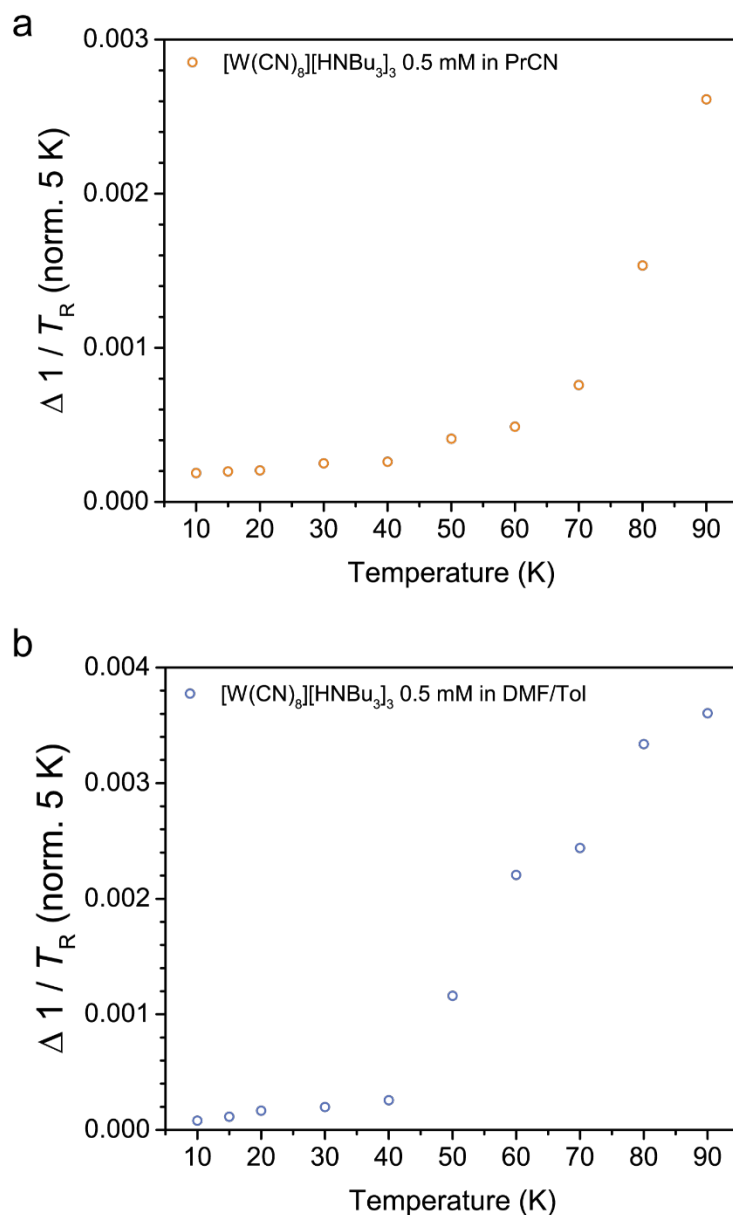


Figure S5.10 | Temperature dependence of T_2 normalised to the T_2 value at 5 K for 0.5 mM solutions of **2** in (a) butyronitrile, and (b) 40 vol% DMF/toluene. As temperature increases, the spin-spin relaxation rate generally increases. This trend is commensurate with T_2 studies on other transition metal systems. Absolute values of T_2 could not be determined at X-band because of exact cancellation, but the temperature dependence was determined *via* normalization of the data to the 5 K decay curve to remove ESEEM modulation and extraction of relative T_2 from the resulting normalised decay curve.

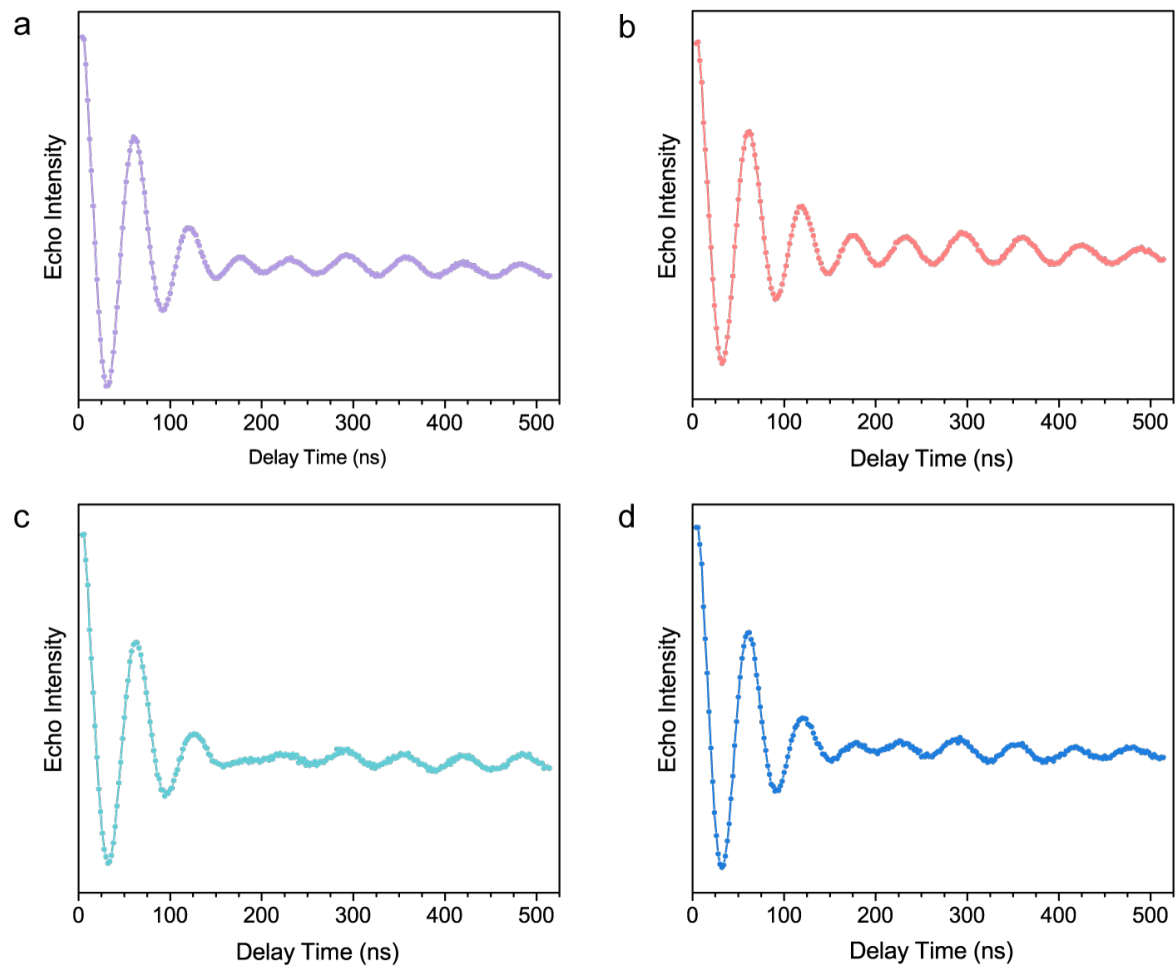


Figure S5.11 | Nutation data for **1** (a)(b), and **2** (c)(d), as 0.5 mM solutions in PrCN (a)(c), and 40 vol% DMF/toluene (b)(d) collected at 20 K. Solid line is a guide for the eyes.

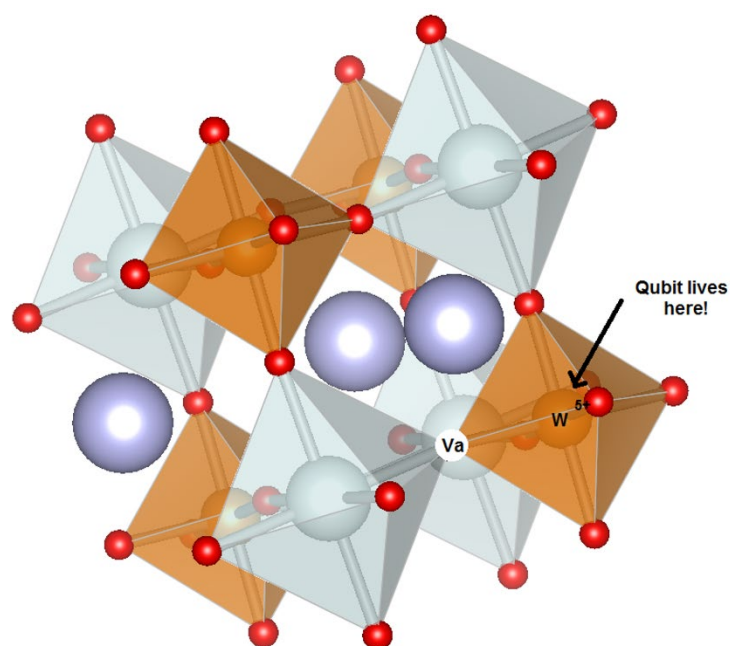
Chapter Six: Introduction of Spin Centers in Single Crystals of Ba_2CaWO_6

Reprinted with permission from:

Mekhola Sinha, Tyler J. Pearson, Tim R. Reeder, Hector K. Vivanco, Danna E. Freedman, W. Adam Phelan, and Tyrel M. McQueen *Physical Review Materials* **2019**, 3, 125002.

Copyright 2019 American Physical Society

This section was written in collaboration with the co-authors listed above



Introduction

The advent of quantum information science (QIS) will fundamentally change our approach to computation, allowing us to answer currently intractable questions in a myriad of fields including biochemistry, physics, and cryptography.^{1,2} QIS is an aggregate term comprising quantum sensing, quantum computing, and quantum metrology amongst other fields. Of these areas, the most advanced is quantum computing which relies on a computing paradigm wherein information is processed using quantum bits, or qubits, which can be placed into an arbitrary superposition of two states. A wide range of systems from photons to superconducting devices have been studied as candidates for QIS.³

A highly promising area of research is harnessing electronic spins as qubits. As inherently quantum systems, electronic spins are ideal qubit candidates both for their modularity and their ease of manipulation with microwave radiation.^{4,5,6,7,8,9,10,11} Electronic defect sites, in particular nitrogen-vacancy sites in diamond,¹² phosphorus defects in silicon,⁵ and double-vacancy sites in silicon carbide are prominent examples.^{13-14,15} However, to create systems with the longest possible coherence times, we must continue to glean new insights into what drives decoherence and develop new materials design principles for qubit hosts. T_1 , the longitudinal electronic spin relaxation time constant, relates to the spin-lattice relaxation time of the electronic spin. This parameter represents the maximum data storage time of an electronic spin. T_2 is the spin echo dephasing time constant in the xy -plane and relates to the spin-spin relaxation time. T_2 also represents the coherence time, the maximum operation time of a qubit.¹⁶ The factors which influence these parameters are different, so to maximize the coherence time in a system, one must carefully design around both T_1 and T_2 . Recent studies of T_2 both in molecular and in solid-state systems have found that nuclear spins play a significant role in promoting decoherence.^{7,9-10,11,15,17,18} As such, removal of nuclear

spin has become one of the most widely adopted design parameters for electronic spin qubit systems [6,19,20,21,22].^{6,19-20,21,22} While fundamentally, T_2 represents the functional operating time of a qubit, we often find that T_1 is the most restrictive parameter in practice, as T_1 represents the theoretical upper limit to T_2 . The chemical properties leading to maximization of T_1 remain an open question and indeed many recent studies have focused heavily on questions related to T_1 [23,24,25].^{23,24,25} Recent advances in pulse decoupling techniques have demonstrated that a short T_2 can be overcome [26,27,28,29],^{26,27,28,29} but T_1 remains a limiting factor. Since the longitudinal relaxation time, T_1 , represents the upper limit to the phase memory time, we must find ways to control the processes leading to T_1 relaxation.

In this manuscript, we test a design strategy to avoid electronic excitations and destruction of spin information by utilizing a wide band gap insulating oxide as a host material. In the case of a wide band gap material, the difference between the ground and excited states is large enough to avoid band-to-band and defect-to-band transitions, thereby causing native defects to produce trap states known as deep traps far away from the band edges. This allows certain defects, such as nitrogen vacancy centers, to be initialized and measured at room temperature [30].³⁰ Further, for the materials system used, it is possible to systematically introduce single-spin isolated paramagnetic centers by controlled defect chemistry.

We report the single crystal synthesis and structure of $\text{Ba}_2\text{CaWO}_{6-\delta}$, an insulating double perovskite with a large band gap (3.6 eV) [31].³¹ The primary naturally occurring isotopes of Ba, Ca, W and O have zero nuclear spin, largely eliminating spin-bath effects from the lattice. Furthermore, the oxide framework itself is rigid, helping suppress local vibrationally mediated decoherence mechanisms. The introduction of oxygen vacancies creates nominally W^{5+} (d^1), $S = \frac{1}{2}$, $I = 0$ point defects in the single crystals of $\text{Ba}_2\text{CaWO}_{6-\delta}$. Coherence studies of $\text{Ba}_2\text{CaWO}_{6-\delta}$

show promising longitudinal relaxation time T_1 and relatively constant transverse relaxation time T_2 over a temperature range of $T = 20$ to 60 K, lending credence to our design strategy.

Experimental Section

A. Single crystal growth

Ba_2CaWO_6 powder was purchased from Sigma Aldrich (99.9%). The purchased powder was sealed in a rubber tube, evacuated, and compacted into a rod (typically 5 mm in diameter and 60 mm long for the feed and 25 mm long for the seed) using a hydraulic press under an isostatic pressure of 70 MPa. After removal from the rubber tube, the rods were sintered at $T = 1000$ °C for 24 hours in air. A Laser Diode Floating Zone (LDFZ) furnace (Crystal Systems Inc FD-FZ-5-200-VPO-PC) with 5×200 W GaAs lasers (976 nm) was used as the heating source. During all of the growths, the molten zone was moved upwards with the seed crystal being at the bottom and the feed rod above it. This was accomplished by holding the lasers in a fixed position at an angle of 4° to the horizontal axis and translating both the seed and feed rods downwards. Successive optimizations yielded final parameters of 15 mm/hr feeding rate, 10 mm/hr growing rate and 20 rpm rotation rate for counter-rotating rods.

B. Characterization

Synchrotron X-ray powder diffraction data (XRPD) were obtained from 11-BM-B at Argonne National Laboratory using a Bending Magnet (BM) of critical energy 19.5 keV as the source. Twelve independent analyzers each separated by $\sim 2^\circ$ in 2θ and consisting of a Si (111) crystal and a LaCl_3 scintillator were used for detection. Backscattered X-ray Laue diffraction (with the X-ray beam of about 1 mm in diameter) was utilized to check the orientations of the crystals. The microstructural homogeneity of sample surfaces cut directly from the cross sections

of the as-grown crystals was probed using a JEOL JSM IT100 scanning electron microscope (SEM) at 20 keV operating in backscatter mode. Laboratory-based X-ray diffraction patterns were collected using a Bruker D8 Focus diffractometer with CuK_α radiation and a Bruker D8 Advance with an Oxford Cryosystem PheniX cryocontroller with CuK_α radiation from $T = 80 - 300$ K. Phase identification and unit cell determinations were carried out using the Bruker TOPAS software (Bruker AXS). A Quantum Design Physical Properties Measurement System (PPMS) was used for the heat capacity measurements from $T = 1.9$ to 300 K at $\mu_o H = 0$ T using the semi-adiabatic method. Electron paramagnetic resonance (EPR) spectroscopy was performed on crushed microcrystalline powders contained within a 4 mm OD quartz EPR tube. EPR data were obtained at $T = 297$ K at X-band frequency (~ 0.3 T, 9.5 GHz) on a Bruker E580 X-band spectrometer equipped with a 1 kW TWT amplifier (Applied Systems Engineering) and on a Bruker E580 X-band spectrometer at the National Biomedical EPR Center at the Medical College of Wisconsin (Milwaukee, WI) equipped with a 1 kW TWT amplifier. Temperature was controlled using an Oxford Instruments CF935 helium cryostat and an Oxford Instruments ITC503 temperature controller (UIUC), and an Oxford Instruments ITC503S temperature controller (MCW). All data were processed using a combination of Xepr, Python 2.7, Origin Pro 2015, and MatLab R2018b. EasySpin [32]³² was used to simulate the CW (continuous wave) EPR spectra of the $\text{W } 5d$ ions.

III. Results and Discussion

A. Single crystal growth

Ba_2CaWO_6 is a B-site ordered double perovskite with a twelve coordinate Ba cation site and octahedrally coordinated smaller cation Ca/W sites consisting of alternate large and small octahedra of Ca and W, respectively, see Fig. 6.1(a). The high vapor pressures of BaO and CaO at

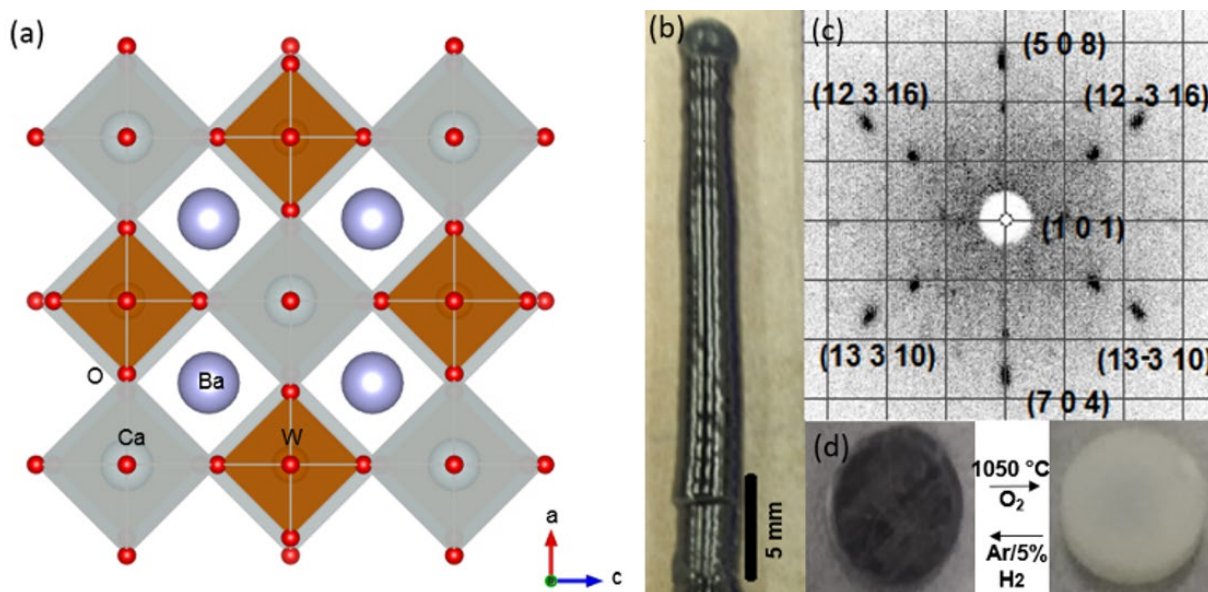


Figure 6.1. (a) Double perovskite structure of Ba_2CaWO_6 ($\delta = 0$) containing alternate octahedra of WO_6 (orange) and CaO_6 (grey) and twelve coordinate Ba atom in the A site. The isolated WO_6 octahedra are primed to become spin centers upon introduction of electrons by removal of oxygen (red spheres). (b) A typical Ba_2CaWO_6 single crystal. (c) Representative Laue diffraction along the (101) direction, perpendicular to the growth axis. (d) Oxygen vacancy concentration can be tuned by sintering under controlled oxygen partial pressure.

the melting temperature of Ba_2CaWO_6 ($T \approx 1450^\circ\text{C}$ as determined from thermogravimetric analysis) makes it difficult to grow crystals via direct melting at atmospheric pressure [33].³³ Initial floating zone crystal growth attempts in oxygen, air, carbon dioxide, and static argon atmospheres at atmospheric pressure led to significant vaporization of calcium (in the form of oxides), and, as a result, produced samples containing a BaWO_4 impurity phase, leading to cracks. The optimum growth conditions were found to be a 7 bar high-purity argon atmosphere flowing at the rate of 2.5 mL/min and 40% of laser power. These conditions significantly reduce the vaporization of calcium oxide, which allowed us to obtain blue tinted single crystals. A typical $\text{Ba}_2\text{CaWO}_{6-\delta}$ crystal (45 mm in length and 5 mm in diameter) grown using optimal conditions is shown in Fig. 6.1(a). X-ray Laue photographs along the cross section of the grown crystals show no detectable variation in orientation and no evidence of twinning, see Fig. 6.1(b).

A back-scattered SEM micrograph taken from a cross section of a crystal (Fig. S6.1.) complements our Laue data showing a uniform microstructure with no evidence of domain formation or any inclusions on the micrometer length scale, see Fig. 6.1(c). The as-grown crystals are blue (a signature of W^{5+}) and oxygen deficient, a result of the reducing atmosphere. The precise oxygen vacancy concentration is controllable via post-annealing; single crystals were sintered in flowing oxygen for one month at $T = 1050\text{ }^{\circ}\text{C}$ to obtain colorless single crystals of Ba_2CaWO_6 , demonstrating tunability of the oxygen vacancy concentration, and hence the number of spin centers, see Fig. 6.1(d).

B. Crystal structure

To understand the origin and behavior of the relaxation rates, we analyzed the structure of the grown crystals and the thermal properties of the material in more detail. The structures of as grown $\text{Ba}_2\text{CaWO}_{6-\delta}$ single crystal were solved in space group $I2/m$ at $T = 295\text{ K}$ and at 100 K via Rietveld refinement to synchrotron XRPD (Fig. S6.7, Table S6V). We find that introduction of Ba site disorder and replacement of about 14% Ba atoms with Ca into the structural model result in significant improvement of the Rietveld fit (Fig. S6.2). No temperature dependent structural phase transition was observed

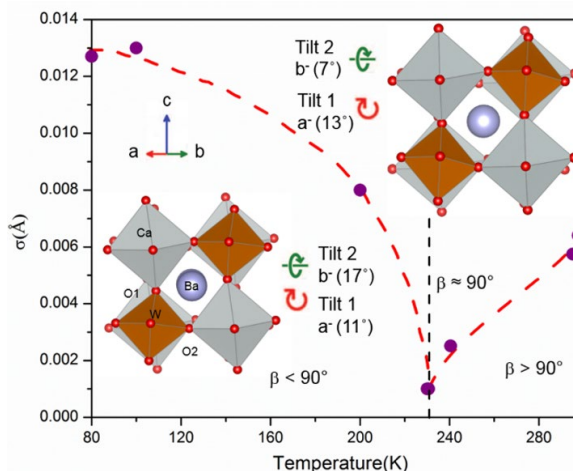


Figure 6.2. Standard deviations from the pseudo-cubic lattice parameters (distortion index) for single crystal of $\text{Ba}_2\text{CaWO}_{6-\delta}$ with increasing temperature where β is the angle between a and c axes. A line to guide the eye (red) shows the distortion index starts decreasing around $T = 140\text{ K}$, it reaches closest to the pseudo-cubic structure at $T = 230\text{ K}$ (black line) before going up again. Crystal structure of $\text{Ba}_2\text{CaWO}_{6-\delta}$ obtained from refined synchrotron XRPD data collected at $T = 295\text{ K}$ and $T = 100\text{ K}$ shows the double perovskite structure containing alternate octahedra of CaO_6 (grey) and WO_6 (orange). The structure shows an octahedral tilt pattern of $(a'b'c^0)$ at each temperature. This octahedral distortion is expected to activate low lying phonon modes in the structure resulting in faster relaxation of the spin.

within measurement resolution. The structural model obtained shows that at $T = 295$ K the structure consists of an octahedral tilt pattern ($a^-b^+c^0$) with a W-O1-Ca angle of 173° (a- axis tilt) and a W-O2-Ca angle of 167° (b- axis tilt) [34].³⁴ At $T = 100$ K W-O1-Ca angle becomes 163° and W-O2-Ca angle is 169° . The deviations from pseudo-cubic structure (distortion index i.e. standard deviations of the monoclinic lattice parameters from the pseudo-cubic lattice parameters) were calculated using cell parameters obtained from Le Bail fits to laboratory XRPD data collected at different temperatures with high purity Si as standard. Fig. 6.2 shows that the average structure is closest to pseudo-cubic at $T = 230$ K and deviates further from cubic with increasing or decreasing temperature due to in-plane rotations of the Ca/WO₆ octahedra. Such structural flexibility is expected to give rise to low-lying optical phonon modes that may increase spin-lattice relaxation *via* phonon-mediated processes.

Specific heat capacity measurements support this hypothesis. Figure 6.3 shows the heat capacity for a single crystal of Ba₂CaWO_{6- δ} as C_p/T^3 vs log T. These data approximate the one-dimensional phonon density of states. Modeling the data illustrates the various contributions to the phonon density of states [35].³⁵ In the model we used, a Debye (acoustic) contribution is

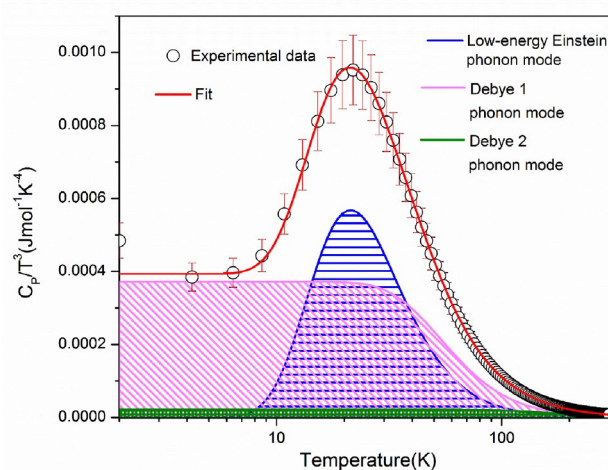


Figure 6.3. Heat capacity (C_p) divided by temperature cubed (T^3) versus log of temperature (T) for a single crystal piece of Ba₂CaWO_{6- δ} . The red line shows a fit to the experimental data including the Einstein and Debye terms. Contributions of individual components are plotted below: pink – Debye 1 phonon mode heat capacity, green – Debye 2 phonon mode heat capacity, blue – low energy Einstein phonon mode. The low-lying Einstein peak describes the distortion in the local modes while the high temperature Debye mode is associated with higher energy vibrations due to atoms having lower masses and the lower temperature Debye mode is associated with lower energy vibrations of atoms having higher atomic masses. The small upturn at $T \approx 2$ K is due to helium condensation around this temperature.

represented by a constant up to θ_D , whereas an Einstein (optical) mode is represented by a peak, resulting from activated low T behavior. The most striking feature of the plot is a large low temperature peak at $T = 21$ K with $\theta_E = 105$ K, indicating the data cannot be described by any combination of Debye terms. We observed that this low-lying Einstein phonon mode becomes operative above $T = 10$ K, resulting in a higher phonon density of states above $T = 15$ K. This corresponds to the onset of the local process as determined by modeling the temperature dependence of T_1 . Low energy optical modes can usually be attributed to a specific structural feature. It is likely the low energy vibrational states are

associated with large amplitude motion of the oxygen atoms in the Ca/WO_6 octahedra resulting in distortion of the structure from the pseudo-cubic lattice. Two-thirds (0.67) of the entropy of the Einstein mode is recovered by $T = 230$ K where the soft phonon modes are excited such that the average becomes pseudo-cubic. While the low-lying Einstein peak can be described by the distortion in the local modes, the high temperature Debye mode is associated with higher

energy vibrations of atoms having lower masses. Inversely, the lower temperature Debye mode is associated with lower energy vibrations of atoms having higher atomic masses. The high energy part of the spectrum was fitted with

Table 6.I: Characteristic temperatures and number of oscillators used in fitting Einstein and Debye modes to the specific heat for single crystal of $\text{Ba}_2\text{CaWO}_{6-\delta}$.

Mode	Temperature (K)	Oscillator strength /formula unit
Einstein	$\theta_E = 104.97(26)$	1.23(1)
Debye 1	$\theta_{D1} = 263(3)$	3.5(1)
Debye 2	$\theta_{D2} = 793(63)$	5.5(6)

two Debye contributions having $\theta_{D1} = 263$ K and $\theta_{D2} = 793$ K, a reasonable value for high energy modes in oxides. The total number of oscillators sums to 10.23(6) (the number of atoms per formula unit) which compares well to the theoretical value of 10. The values of the oscillator strengths and characteristic temperatures are given in Table 6.I.

C. Determination of the spin-state of the defect center

To characterize the spin state of the magnetic W ions resulting from oxygen deficiencies ($\text{Ba}_2\text{CaWO}_{6-\delta}$), we utilized continuous wave and pulse EPR techniques. To determine the spin state of the system, we performed transient nutation experiments (see SI discussion for details) calibrated against a 2,2-diphenyl-1-picrylhydrazyl (dpph) radical standard (Fig. S6.3,S6.4). These allowed us to confirm that the spin state which we observed was a doublet and that the transition we observed was between the $M_S = \pm 1/2$ sublevels. With this information in hand, we could easily simulate the experimental cw spectrum using EasySpin [32]³² to a spin doublet (Figure 6.4) with $g = 1.96$, which is in line with similar observations in oxygen-deficient tungsten oxides[36].³⁶ Taken together, this information leads us to conclude that the spin centers introduced by defect generation are W^{5+} ions. The weakness of this transition likely arises from low spin concentration across the sample. The spectrum in this case was measured at $T = 297$ K. We attempted to utilize a model developed according to theory outlined by *Salikhov et al.* [37]³⁷ to attempt to approximate spin concentration. However, the model cannot account for spin-spin interactions of more than approximately 50 Å. Therefore, we cannot absolutely say the concentration of spins in the sample, only that they are more than 50 Å apart (i.e. < 0.02%).

D. Pulse EPR measurements

To investigate the feasibility of the grown crystals as qubit candidates and to learn more about how the electrons interact with the material, we performed pulse EPR spectroscopy on finely ground single crystals of $\text{Ba}_2\text{CaWO}_{6-\delta}$. The immediate aim of these measurements was to determine the parameters most relevant to understanding the coherence properties of the electronic spin: T_1 and T_2 .

We determined T_1 across the temperature range $T = 5$ K to 150 K. We accomplished this using an inversion recovery pulse sequence ($\pi - T - \pi/2 - \tau - \pi - \tau - \text{echo}$). We fit the resulting inversion recovery curves using an exponential function of the form

$$I(\tau) = -A \left(e^{-(\tau/T_1 + \sqrt{\tau/c})} - b - 1 \right)$$

where I is the normalized echo intensity, A and b are normalization factors (1 and 0 approximately), and c is a factor related to spectral diffusion, which is relevant at low temperatures in this system (see SI) (Fig. 6.5a). We found that at $T = 5$ K, T_1 is 310(30) ms in this material, which provides a

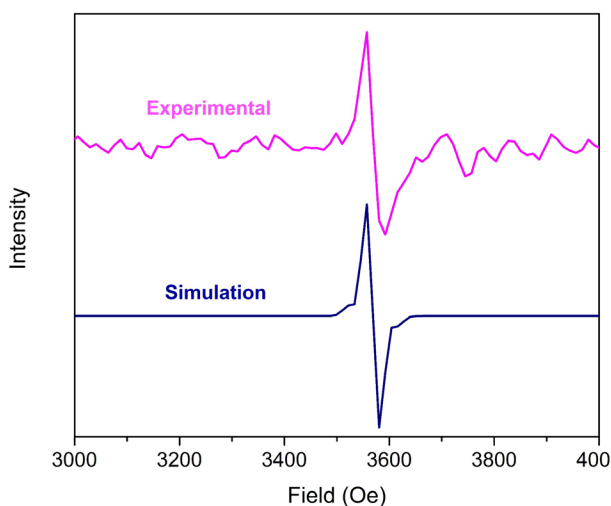


Figure 6.4. Comparison between the resonance peak obtained from experimental continuous wave spectra and the simulated fit to the experimental data to a spin doublet with $g = 1.96$ using EasySpin.

high ceiling to the coherence time of the system (Table S6.I). The T_1 of W^{5+} centers in $\text{Ba}_2\text{CaWO}_{6-\delta}$ compares very well to some of the best qubit candidates known (Table S6.II).

To investigate the spin-lattice relaxation in more detail, we examined and modelled the temperature dependence of T_1 , see Fig. 6.5(b). Modelling this dependence is useful for determining which processes

mediate spin-lattice relaxation as each process has a unique and well-defined temperature dependence. The model we utilized to fit the data was

$$\frac{1}{T_1} = A_{dir}T + A_{ram1} \left(\frac{T}{\theta_{D1}}\right)^9 J_8\left(\frac{\theta_{D1}}{T}\right) + A_{ram2} \left(\frac{T}{\theta_{D2}}\right)^9 J_8\left(\frac{\theta_{D2}}{T}\right) + A_{loc} \frac{e^{\theta_E/T}}{(e^{\theta_E/T} - 1)^2}$$

where A_{dir} , A_{ram1} , A_{ram2} and A_{loc} are coefficients reflecting the influence of the direct, Raman and the local processes respectively. Each Raman process is associated with a characteristic Debye temperature (θ_{D1} and θ_{D2}), the local mode an Einstein temperature (θ_E), fixed to values obtained from quantitative analysis of the heat capacity, and J_8 is the transport integral describing the joint phonon density of states assumed by the Debye model. This integral takes the form

$$J_8\left(\frac{\theta_D}{T}\right) = \int_0^{\theta_D/T} x^8 \frac{e^x}{(e^x - 1)^2} dx$$

This overall model for T_1 includes terms for the direct relaxation process, two Raman relaxation processes, and a term describing additional relaxation due to local modes. The direct process proceeds via a spin flip mechanism and is typically relevant only at approximately $T = 10$ K or below. The Raman and local processes are two-phonon processes analogous to Raman photon scattering and become operative at temperatures where there is substantial thermal phonon population. Examination of the temperature dependence of T_1 hints at why T_1 is long at $T = 5$ K in this system: the influence of the direct process is very small in this material, with $A_{dir} = 0.49(09)$ $\text{K}^{-1}\text{s}^{-1}$. Typical values for A_{dir} fall within the approximate range of $10\text{-}50$ $\text{K}^{-1}\text{s}^{-1}$ [38]. With minimal thermal population of the phonon modes, the only means by which the spin can relax is through the direct process. However, at X-band (~ 0.3 T) and in the absence of a strong hyperfine field – a result of the mostly nuclear spin-free nature of this material in which the spin resides – the direct process is slow [35].³⁵ However, with the onset of the two-phonon processes between $T = 15\text{-}20$

K, the spin-lattice relaxation time begins to precipitously decrease. Generally, this decrease most likely arises from the presence of heavy elements with high spin-orbit coupling in the lattice. With increasing spin-orbit coupling, the strength of spin-phonon coupling also increases, leading to enhanced relaxation rates [38].³⁸

We can gain quantitative information about the relative strength of spin-phonon coupling to the different phonon contributions by utilizing knowledge of the oscillator strength from heat capacity combined with the coefficients from the fits to $1/T_1$. The coefficient for a two-phonon process will have the general form [39]:³⁹

$$\frac{1}{T_1} = \frac{4\pi\hbar^2}{\rho_{cryst}^2 v_s^4} \frac{\langle b|V^{(1)}|a\rangle^4}{\Delta_{cryst}^4} \int_0^{\omega_{max}} \bar{n}(\bar{n} + 1) \omega^4 \rho^2(\omega) d\omega$$

where v_s is the average sound velocity, ρ_{cryst} is the crystal density and Δ_{cryst} is the orbital splitting. The $\langle b|V^{(1)}|a\rangle \equiv G$ is the matrix element called spin-phonon coupling parameter where $V^{(1)}$ is the crystal field potential produced by phonons generating strain ε and taken from the expansion of the potential into power series $V = V_0 + \varepsilon V^{(1)} + \varepsilon^2 V^{(2)} + \dots$. For Debye (Raman)-type phonon process, $\rho(\omega) = \frac{3N_D \omega^2}{2\pi^2 v_s^3}$, where N_D is the number of oscillators related to the Debye

mode, $v_s = \frac{k_B \theta_D}{\hbar \left(6\pi^2 \frac{N}{V}\right)^{\frac{1}{3}}}$ where N is the number of atoms in a crystal of volume V , resulting in:

$$\frac{1}{T_1} = A_{ram} \left(\frac{T}{\theta_D}\right)^9 J_8 \left(\frac{\theta_D}{T}\right)$$

where $A_{ram} = \frac{9 \cdot \frac{10}{6} \frac{11}{3} \pi^{\frac{11}{3}} \hbar^3 N_D^2 \left(\frac{N}{V}\right)^{\frac{10}{3}} G_{ram}^4}{\rho_{cryst}^2 k_B \theta_D \Delta_{cryst}^4}$ (derivation in the SI discussion).

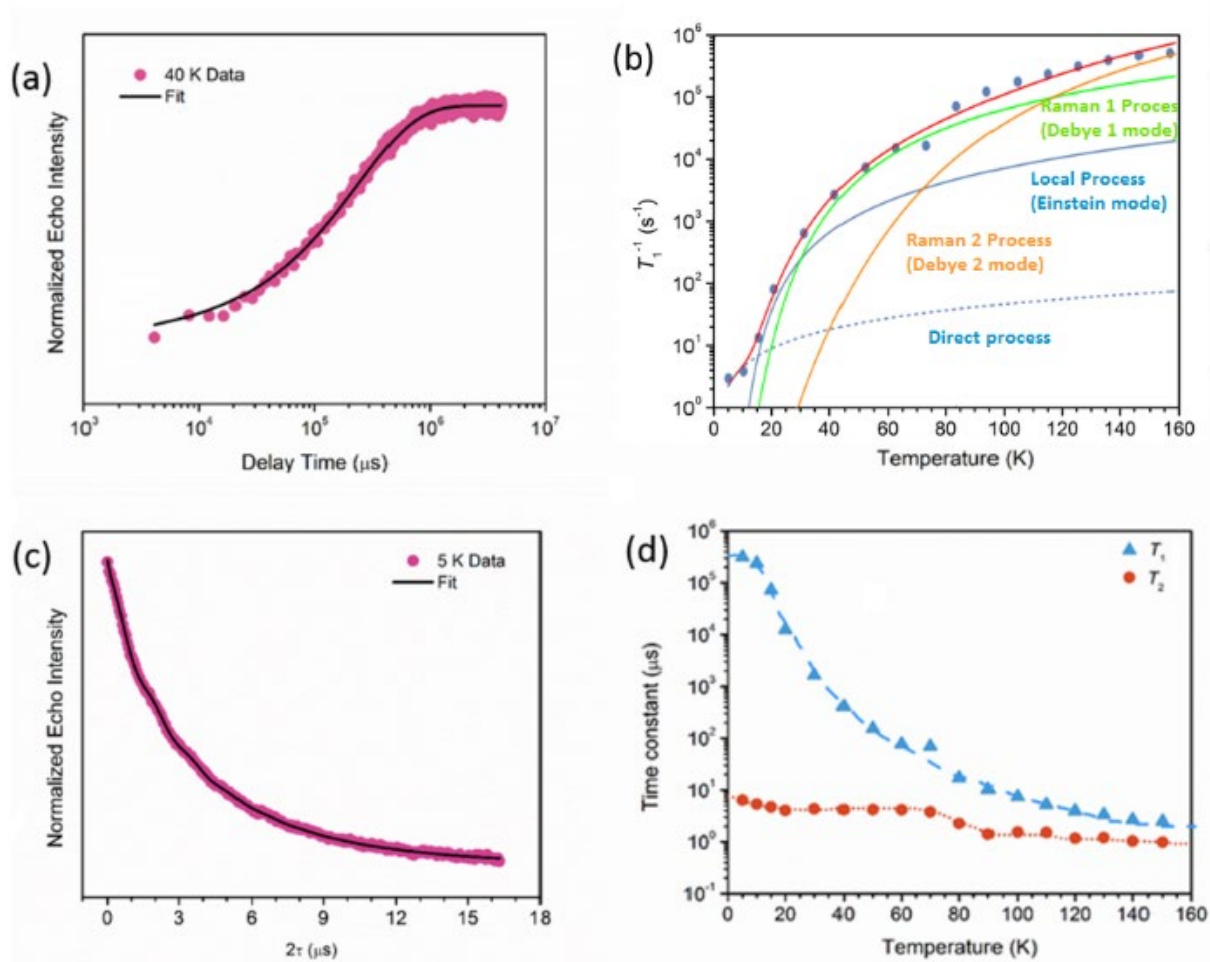


Figure 6.5. Pulse electron paramagnetic resonance spectroscopic data. (a) Inversion recovery curve used for calculating the spin-lattice relaxation time, T_1 at $T = 40$ K. (b) Temperature dependence plot of the rate of longitudinal relaxation T_1^{-1} with a quantitative fit to a combination of a Direct, two “Raman” (Debye-phonon), and one “local” (Einstein-phonon) contributions. Parameters obtained from the fit (red line) are $A_{dir} = 0.49(09) \text{ K}^{-1} \text{ s}^{-1}$, $A_{ram1} = 4.4(8) \cdot 10^6 \text{ s}^{-1}$, $A_{ram2} = 3.2(8) \cdot 10^8 \text{ s}^{-1}$, and $A_{loc} = 8(2) \cdot 10^3 \text{ s}^{-1}$. The associated Debye and Einstein temperatures were fixed at the values obtained from heat capacity measurements. (c) Hahn-echo decay curve used to calculate spin-spin relaxation time T_2 . (d) Temperature dependence plot of T_2 and T_1 . (Lines to guide the eye shows the trend followed by T_1 and T_2 with temperature).

Similarly, for an Einstein (Local)-type phonon process, $\rho(\omega) = 3 \cdot N_E \left(\frac{N}{V}\right) \delta(\omega - \omega_e)$, $v_s = \frac{k_B \theta_E}{\hbar \left(\pi^3 \frac{N}{V}\right)^{\frac{1}{3}}}$, where N_E is the number of oscillators related to the Einstein mode, resulting in:

$$\frac{1}{T_1} = A_{loc} \frac{e^{\theta_E/T}}{(e^{\theta_E/T} - 1)^2}$$

where $A_{loc} = \frac{36 \pi^5 \hbar^3 N_E^2 \left(\frac{N}{V}\right)^{\frac{10}{3}} G_{loc}^4}{\rho_{cryst}^2 k_B \theta_E \Delta_{cryst}^4}$ (derivation in the SI discussion). Using these, the ratio of coefficients for two Raman-type processes is:

$$\frac{A_{ram2}}{A_{ram1}} = \left(\frac{N_{D2}}{N_{D1}}\right)^2 \left(\frac{\theta_{D1}}{\theta_{D2}}\right) \left(\frac{G_{ram2}}{G_{ram1}}\right)^4$$

Whereas the ratio of coefficient for a Raman and Local process is:

$$\frac{A_{loc}}{A_{ram}} = \frac{36 \pi^5}{9 \cdot 6^{\frac{10}{3}} \pi^{\frac{11}{3}}} \left(\frac{N_E}{N_D}\right)^2 \left(\frac{\theta_D}{\theta_E}\right) \left(\frac{G_{loc}}{G_{ram}}\right)^4$$

We find that the spin-phonon coupling to the Debye mode with $\theta_{D2} = 793(63)$ K (Debye 2) is 3.2(4) times greater than to the one with $\theta_{D1} = 263(3)$ (Debye 1). Similarly, the coupling to the Einstein mode is 1.1(7) relative to Debye 1. These provide evidence that the spin-phonon coupling is stronger for higher frequency oscillators in this material.

Next, we examined T_2 over the same temperature range (Table S6.III). We utilized a two-pulse Hahn-echo sequence to monitor the stability of the superposition as a function of the inter-pulse delay time. We then fit the decay curves with a stretched exponential function of the form

$$I(\tau) = A(1 - B \cos(\omega\tau + d)) e^{-\tau/T_{osc}} e^{-(2\tau/T_2)^q} + f$$

see Fig. 6.3(c). The function includes two parts, the first of which describes the electron spin-echo envelope modulation (ESEEM) within the decay curve and the second of which describes the spin-echo decay itself. Within the function as written, A is a normalization factor (approximately 1), B is the ESEEM modulation amplitude, ω is the ESEEM frequency in MHz, d is the modulation phase, T_{osc} is the ESEEM decay time, q is the stretch factor, and f is an offset term to assist in fitting (approximately 0). The inclusion of the ESEEM term was necessary to model the small oscillations within the decay curve resulting from the interaction between the electronic spin and the 14.3% abundant $I = 1/2$ ^{183}W nucleus. However, the data above $T = 70$ K was fitted to the equation

$$I(\tau) = Ae^{-(2\tau/T_2)^q} + f$$

without the ESEEM term as the data was too noisy at higher temperatures to see the ESEEM. We discovered that T_2 in this material is largely invariant across the temperature range apart from a decrease from 6.35 to 4.71 μs between $T = 5$ K and $T = 15$ K. T_2 remains at approximately 4 μs until $T = 60$ K before it decreases to approximately 1 μs at $T = 90$ K and remains roughly constant until $T = 150$ K, Fig. 6.5(d). The temperature invariance of T_2 across the temperature range could be a result of the relative lack of nuclear spins and methyl groups within the lattice which can easily promote decoherence in electronic spin-based systems [38].³⁸ The low value of T_2 across the temperature range could, however, stem from the non-zero natural abundance (14.31%) of ^{183}W . Phase memory times are extremely sensitive to even incremental changes in nuclear spin concentration, as has been observed in studies examining the isotopic enrichment of diamond hosts for nitrogen vacancy centers [40].⁴⁰

IV. Conclusions

We have grown single crystals of $\text{Ba}_2\text{CaWO}_{6-\delta}$ for the first time. Continuous wave and pulse EPR measurements confirm the presence of oxygen vacancies that create W^{5+} defect centers in the system. Coherence studies indicate that these defects in $\text{Ba}_2\text{CaWO}_{6-\delta}$ are viable quantum bit candidates. Without significant optimization, the longitudinal relaxation time, T_1 in this material rivals that of top quantum bit candidates, and the transverse relaxation time, T_2 shows relative insensitivity to temperature across the measurement range. Remarkably, $T_1 = 310$ ms at $T = 5$ K, only decreasing upon population of low-lying phonon modes at 15 K and with the onset of local vibrational modes above 60 K. Work towards reducing the influence of these modes is ongoing. Specifically, we plan to slow phonon-mediated relaxation by designing systems with lighter elements with less spin-orbit coupling and systems with less susceptibility to octahedral tilting. Further we calculate the spin-phonon coupling of the higher frequency Debye 2 mode to be ~ 3 times as strong as the Einstein or the Debye 1 modes. The fact that all coupling strengths are not equal is chemically intuitive; our results show how to gain access to such information in a general, broadly applicable way. It also suggests that simply pushing all vibrational spectral weight to high frequencies is not the only way to design a high T_1 lifetime – instead, reducing the spin-phonon coupling to only the modes present at low energy (e.g. by making such coupling symmetry-forbidden), is the key. In short, complex oxides are viable hosts for quantum bit centers and the chemical control of oxygen vacancies can be used to introduce spin centers in the lattice. We further find that systematic materials design principles can be used to create qubits with long longitudinal relaxation times.

Supporting Information:

I. EXPERIMENTAL DETAILS

A. Electron Paramagnetic Resonance Spectroscopy

T_1 data were collected on the most intense central resonance in the echo-detected EPR spectrum using an inversion recovery sequence ($\pi - T - \pi/2 - \tau - \pi - \text{echo}$) with a 2-step phase cycle. This sequence consisted of a π pulse to invert the spin followed by a delay time (T) followed by a Hahn-echo detection sequence ($\pi/2 - \tau - \pi - \tau - \text{echo}$) in which $\pi/2 = 16$ ns, $\pi = 32$ ns, and $\tau = 140$ ns. T was incremented from a starting value of 300 ns.

We phased the inversion recovery data by maximizing the sum of squares of the data points in the real component of the spectrum, normalized them such that the data spanned the range 0 to 1, and fit the data using the exponential function

$$I(\tau) = -A \left(e^{-(\tau/T_1 + \sqrt{\tau/q})} - b - 1 \right)$$

where I is the normalized echo intensity, A and b are normalization factors (1 and 0 approximately), and q is a factor related to spectral diffusion, which is relevant at low temperatures in this system. Fitting with the spectral diffusion term included becomes unnecessary as temperature increases. Therefore, above 100 K, a monoexponential function

$$I(\tau) = -A \left(e^{-(\tau/T_1)} - b - 1 \right)$$

was used to fit the data.

As with the T_1 data, T_2 data were collected on the highest-intensity central resonance in the EDFS spectrum. We utilized a Hahn-echo sequence ($\pi/2 - \tau - \pi - \tau - \text{echo}$) with a 2-step phase cycle in which $\pi/2 = 16$ ns and $\pi = 32$ ns, and τ was varied from 160 ns. We set the acquisition trigger to capture the spin echo and integrated over the entire echo to obtain the data. We

subsequently phased the data by maximizing the sum of the squares of the data points in the real component of the spectrum. The decay curves were fit using the function

$$I(\tau) = A(1 - b * \cos(\omega\tau + c)e^{-\tau/T_{osc}})e^{-(2\tau/T_2)^q} + f$$

where A is a normalization factor (usually 1), b is the ESEEM modulation amplitude, ω is the modulation frequency, c is the modulation phase, T_{osc} is the ESEEM decay time, q is a stretch factor, and f is an offset term to assist in fitting (usually 0). Fitting the decay curves required the inclusion of a term to account for ESEEM modulations, as faint ESEEM modulations are observable within the curves. These oscillations result from the interaction of the electron spin with the $I = 1/2$ ^{183}W nucleus. Above $T = 60$ K, the ESEEM term was not used, as the data became too noisy to observe ESEEM. The resulting equation was a stretched exponential function of the form

$$I(\tau) = Ae^{-(2\tau/T_2)^q} + f$$

Transient nutations were collected on the most intense central resonance in the EDFS spectrum. The sequence used to collect these data consisted of a tipping pulse of varying length (4 ns increments), followed by a Hahn echo detection sequence ($\pi/2 - \tau - \pi - \tau - \text{echo}$) where τ was kept constant at 200 ns. After performing a Fourier transform of the Rabi oscillations, we were able to extract a nutation frequency. Comparison of the nutation frequency as a function of B_1 field to a dilute sample of a known $S = 1/2$ species, 2, 2-diphenyl-1-picrylhydrazyl radical (dpph), allowed us to determine the spin state of the spin center in $\text{Ba}_2\text{CaWO}_{6-\delta}$. Through this analysis, we determined that the electronic structure was a Kramers doublet ($S = 1/2$), commensurate with the electronic structure simulations. B_1 field was calculated from the following formula under the assumption that the DPPH $S = 1/2$ radical has a g value of 2.0037 and that the transition observed is between the $M_S = \pm 1/2$ sublevels.

$$\omega_{nut}(m_S, m_S + 1) = \frac{g_1 \beta_e B_1}{\hbar} [S(S + 1) - m_S(m_S + 1)]^{1/2}$$

β_e is the Bohr magneton, ω_{nut} is the nutation frequency, $S = 1/2$, $m_S = -1/2$. Comparison of the Rabi frequency at a given B_1 power to that observed in the sample gave that the spin state was indeed $S = 1/2$.

We used PyCrystalField to simulate the EPR spectrum of the W^{5+} ions by simulating the Zeeman splitting for an ion for a given magnetic field

$$\Delta E = -\vec{\mu} \cdot \vec{B} = -\frac{\mu_B(\vec{L} + g_S \vec{S})}{\hbar} \cdot \vec{B}$$

for a given field direction. Then we solved for the value of magnetic field required to achieve resonance at a given energy difference (determined by the microwave frequency = 9.440 GHz), and generated a Lorentzian derivative at the resonance field. We did this 2×10^7 times for randomly chosen field directions, and summed up the spectra to produce the powder-averaged EPR signal shown in Fig. 6.2. This yielded a resonance curve like in Fig. 6.2, but with the resonance peak at 3600 Oe. This small discrepancy could arise from three possible sources: (i) the point charge crystal field model is an approximation: the oxygen atoms are not point charges but have extended electron orbitals, (ii) the ligand positions used to simulate the spectrum were from a 100 K refinement while the experimental spectrum was taken at 77 K, and we expect the ligands to have shifted slightly between these two temperatures, and (iii) oxygen positions are difficult to precisely determine from X-rays because of the small X-ray cross section of oxygen. We found that small adjustment ($\pm 3\%$) to the oxygen positions yielded a W^{5+} resonance peak at 3600 Oe which agrees with the data very well, showing that the first principles point charge approximation is close to the true W^{5+} single ion Hamiltonian.

We simulated and fit the temperature dependence of T_1 using parameters obtained from the heat capacity analysis in Wolfram Mathematica 12.0 Student Version. For the derivation of the dependence of A_{loc} we used the following equation [41]⁴¹

$$\frac{1}{T_1} = \frac{4\pi \hbar^2}{\rho_{cryst}^2 v_s^4} \frac{\langle b|V^{(1)}|a \rangle^4}{\Delta_{cryst}^4} \int_0^{\omega_{max}} \bar{n}(\bar{n} + 1) \omega^4 \rho^2(\omega) d\omega$$

where v_s is the average sound velocity, ρ_{cryst} is the crystal density and Δ_{cryst} is the orbital splitting. The $\langle b|V^{(1)}|a \rangle \equiv G$ is the matrix element called spin-phonon coupling parameter where $V^{(1)}$ is the crystal field potential produced by phonons generating strain ε and taken from the expansion of the potential into power series $V = V_0 + \varepsilon V^{(1)} + \varepsilon^2 V^{(2)} + \dots$

Taking $\bar{n}(\bar{n} + 1) = \frac{e^{\frac{\hbar\omega}{k_B T}}}{\left(e^{\frac{\hbar\omega}{k_B T}} - 1\right)^2}$ and $\rho(\omega) = 3 \cdot N_E \left(\frac{N}{V}\right) \delta(\omega - \omega_e)$ where N_E is the number of

oscillators related to the Einstein mode, where N is the number of atoms in a crystal of volume V , we get,

$$\frac{1}{T_1} = c_1 \cdot \int_0^{\infty} \frac{e^{\frac{\hbar\omega}{k_B T}}}{\left(e^{\frac{\hbar\omega}{k_B T}} - 1\right)^2} \cdot 9 \cdot N_E^2 \left(\frac{N}{V}\right)^2 \delta^2(\omega - \omega_e) d\omega$$

Using $\int_0^{\infty} f(x) \delta(x - x_0) dx = f(x_0)$ this becomes

$$\frac{1}{T_1} = c_1 \cdot 9 \cdot N_E^2 \left(\frac{N}{V}\right)^2 \frac{e^{\frac{\hbar\omega}{k_B T}}}{\left(e^{\frac{\hbar\omega}{k_B T}} - 1\right)^2} \omega_e^4 \cdot \delta(\omega - \omega_e)|_{\omega=\omega_e}$$

Using $\delta(\alpha x) = \frac{1}{\alpha} \delta(x)$ and $\delta(x) = 1$ if $x = 0$ gives

$\delta(\omega - \omega_e)|_{\omega=\omega_e} = \frac{1}{\omega_e}$; so we get:

$$\frac{1}{T_1} = \frac{36 \pi \hbar^2 N_E^2 \omega_e^3 G^4 \left(\frac{N}{V}\right)^2 e^{\frac{\hbar\omega}{k_B T}}}{\rho_{cryst}^2 \Delta_{cryst}^4 v_s^4 \left(e^{\frac{\hbar\omega}{k_B T}} - 1\right)^2};$$

Since for an Einstein mode $v_s = \frac{k_B \theta_E}{\hbar \left(\pi^3 \frac{N}{V}\right)^{\frac{1}{3}}}$ and $\hbar\omega = k_B \theta_E$, we get

$$\frac{1}{T_1} = A_{loc} \frac{e^{\theta_E/T}}{(e^{\theta_E/T} - 1)^2}$$

where $A_{loc} = \frac{36 \pi^5 \hbar^3 N_E^2 \left(\frac{N}{V}\right)^{\frac{10}{3}} G_{loc}^4}{\rho_{cryst}^2 k_B \theta_E \Delta_{cryst}^4}$.

For the derivation of the dependence of A_{ram} we used the same equation [1]

$$\frac{1}{T_1} = \frac{4\pi \hbar^2}{\rho_{cryst}^2 v_s^4} \frac{\langle b|V^{(1)}|a \rangle^4}{\Delta_{cryst}^4} \int_0^{\omega_{max}} \bar{n}(\bar{n} + 1) \omega^4 \rho^2(\omega) d\omega$$

Since $\rho(\omega) = \frac{3 N_D \omega^2}{2 \pi^2 v_s^3}$ for a Debye mode where N_D is the number of oscillators related to the

Debye mode, we get

$$\frac{1}{T_1} = \frac{9 \cdot \hbar^2 N_D^2 G_{ram}^4}{\rho_{cryst}^2 \pi^3 v_s^{10} \Delta_{cryst}^4} \left(\frac{k_B T}{\theta_D}\right)^9 J_8\left(\frac{\theta_D}{T}\right)$$

Substituting $v_s = \frac{k_B \theta_D}{\hbar \left(6\pi^2 \frac{N}{V}\right)^{\frac{1}{3}}}$ we get:

$$\frac{1}{T_1} = A_{ram} \left(\frac{T}{\theta_D} \right)^9 J_8 \left(\frac{\theta_D}{T} \right)$$

$$\text{where } A_{ram} = \frac{9 \cdot 6^{\frac{10}{3}} \pi^{\frac{11}{3}} \hbar^3 N_D^2 \left(\frac{N}{V} \right)^{\frac{10}{3}} G_{ram}^4}{\rho_{cryst}^2 k_B \theta_D \Delta_{cryst}^4}.$$

B. Thermogravimetric analysis

A thermogravimetric analyzer (TGA) & differential scanning calorimeter (DSC) (TA Instruments SDT Q600) was used for the thermogravimetric analysis. On heating a single crystal of $\text{Ba}_2\text{CaWO}_{6.8}$ under high-purity argon at the rate of $10^\circ\text{C}/\text{min}$ a broad endothermic peak was observed in the heat profile at $T = 1450^\circ\text{C}$ indicating the melting transition in the material.

II. TABLES

Table S6.I. Fit parameters for fitting inversion recovery curves from the temperature range $T = 5 - 150$ K. From $T = 5 - 100$ K, the function utilized was $I(\tau) = -A \left(e^{-(\tau/T_1 + \sqrt{\tau/q})} - b - 1 \right)$ where I is the normalized echo intensity, A and b are normalization factors (1 and 0 approximately), and q is a factor related to spectral diffusion. At elevated temperatures, spectral diffusion becomes less important, and so the fit function $I(\tau) = -A \left(e^{-\tau/T_1} - b - 1 \right)$ was used instead.

Temperature (K)	A	T_1 (μs)	q (μs)	b
5	1.025(4)	310000(30000)	18000 (200)	0.015(2)
10	1.049(7)	240000(50000)	11100 (200)	0.012(3)
15	1.012(6)	72000(7000)	7600 (200)	0.000(5)
20	0.984(6)	12500(500)	4700 (200)	0.000(6)
30	0.972(6)	1650(40)	1470 (70)	0.000(6)
40	0.960(9)	410(10)	890 (90)	0.000(9)
50	0.942(8)	154(4)	420 (40)	0.000(9)
60	0.92(1)	77(3)	340(70)	0.00(1)
70	0.973(7)	70(1)	390 (50)	0.000(7)
80	0.83(7)	17(4)	100 (200)	0.00(9)
90	0.93(4)	10(1)	300 (400)	0.00(4)
100	0.92(5)	7(1)	200(500)	0.00(6)
110	0.92(2)	5.3(2)	--	0.00(2)
120	0.89(3)	4.0(2)	--	0.00(3)
130	0.90(3)	3.2(2)	--	0.00(4)
140	0.89(4)	2.7(2)	--	0.00(4)
150	0.86(5)	2.5(2)	--	0.00(6)

Table S6.II. Comparison of T_1 for some known qubit candidates.

Compound	Temp, T_1
Ba₂CaWO_{6-δ} (this work)	5 K, 310 ms
[V(C₈S₈)₃]²⁻a	10 K, 20.4 ms
[VO(C₃S₄O)₂]²⁻b	10 K, 20.7 ms
[Mo(CN)₈]³⁻c	5 K, 1050 ms
[W(CN)₈]³⁻d	5 K, 630 ms
N@C₆₀/C₆₀^e	4 K, >1000 ms
[Cu(S₂C₄N₂)₂]²⁻f	7 K, 87 ms
CuPc^g	5 K, 59 ms
NV center in diamond^h	40 K, >10 s
Ga donor qubits in ZnOⁱ	1.5 K, >100 ms
Ce³⁺ ion in YAG^j	3.5 K, 4.5 ms

J. M. Zadrozny, J. Niklas, O. G. Poluektov, D. E. Freedman, *ACS Cent. Sci.* **1** (9), 488–492 (2015).

C.-J. Yu, M. J. Graham, J. M. Zadrozny, J. Niklas, M. D. Krzyaniak, M. R. Wasielewski, O. G. Poluektov, D. E. Freedman, *J. Am. Chem. Soc.* **138** (44), 14678–14685 (2016).

T. J. Pearson, D. W. Laorenza, M. D. Krzyaniak, M. R. Wasielewski, D. E. Freedman, *Dalton Trans.* **47** (34), 11744–11748 (2018).

M. Atzori, S. Benci, E. Morra, L. Tesi, M. Chiesa, R. Torre, L. Sorace, R. Sessoli, *Inorg. Chem.* **57** (2), 731–740 (2017).

W. Harneit, *Phys. Rev. A* **65** (3), 32322 (2002).

K. Bader, D. Dengler, S. Lenz, B. Endeward, S.D. Jiang, P. Neugebauer, J. van Slageren, *Nat. Comm.* **5**, 5304 (2014).

M. Warner, S. Din, I. S. Tupitsyn, G. W. Morley, A. M. Stoneham, J. A. Gardener, Z. Wu, A. J. Fisher, S. Heutz, C. W. Kay, G. Aeppli, *Nature* **503** (7477), 504 (2013).

S. Takahashi, R. Hanson, J. van Tol, M. S. Sherwin, D. D. Awschalom, *Phys. Rev. Lett.* **101** (4), 47601 (2008).

X. Linpeng, M.L.K. Viitaniemi, A. Vishnuradhan, Y. Kozuka, C. Johnson, M. Kawasaki, K.M.C. Fu, *Phys. Rev. Applied* **10**, 064061-9 (2018).

j. P. Siyushev, K. Xia, R. Reuter, M. Jamali, N. Zhao, N. Yang, C. Duan, N. Kukharchyk, A.D. Wieck, R. Kolesov & J. Wrachtrup, *Nature Comm.* **5**, 3895 (2014)

Table S6.III. T_2 values over a range of $T = 5$ K to 150 K fit to the Hahn echo decay curves according to the equation

$$I(\tau) = Ae^{-(2\tau/T_2)^q} + f$$

where A is a normalization factor, q is a stretch factor, and f is a linear offset term used to assist in fitting.

Temperature (K)	A	T_2 (μ s)	q	f
5	1.018(4)	6.35(3)	0.832(6)	0.007(2)
10	1.012(5)	5.35(4)	0.762(6)	0.001(2)
15	1.004(5)	4.71(3)	0.757(6)	0.002(1)
20	0.994(5)	4.05(3)	0.735(6)	0.008(1)
30	1.030(6)	4.33(4)	0.741(7)	0.022(1)
40	1.026(6)	4.17(3)	0.714(6)	0.024(1)
50	1.049(7)	4.18(4)	0.701(7)	0.017(2)
60	1.022(8)	4.15(5)	0.726(8)	0.016(2)
70	0.997(8)	3.77(3)	0.750(9)	0.045(4)
80	0.84(6)	2.3(2)	1.2(1)	0.014(8)
90	1.20(8)	1.4(1)	1.04(9)	0.021(5)
100	1.09(6)	1.5(1)	1.2(1)	0.011(5)
110	1.06(7)	1.5(1)	1.1(1)	0.001(6)
120	1.2(1)	1.2(1)	1.0(1)	-0.001(6)
130	1.09(9)	1.2(1)	1.3(2)	-0.004(6)
140	1.1(1)	1.0(1)	1.2(2)	0.004(6)
150	0.92(9)	0.99(7)	2.1(4)	0.005(7)

Table S6.IV: T_2 values over a range of $T = 5$ K to 70 K fit to the Hahn echo decay curves according to the equation

$$I(\tau) = A(1 - b * \cos(\omega\tau + c))e^{-\tau/T_{osc}}e^{-(2\tau/T_2)^q} + f$$

where A is a normalization factor (usually 1), b is the ESEEM modulation amplitude, ω is the modulation frequency, c is the modulation phase, T_{osc} is the ESEEM decay time, q is a stretch factor, and f is an offset term to assist in fitting (usually 0).

Temperature (K)	Amplitude (A)	Modulation amplitude (B)	ESEEM Frequency (ω) (MHz)	Modulation Phase (d)	ESEEM decay time (T_{osc}) (μ s)	T_2 (μ s)	Stretch Factor (q)	Offset (e)
5	1.005(4)	0.030(3)	4.00(6)	1.35(9)	5(1)	6.46(3)	0.841(5)	0.008(1)
10	1.03(1)	0.03(1)	10(3)	-0.0(7)	0.2(2)	5.25(7)	0.74(1)	-0.002(2)
15	0.976(6)	0.029(4)	3.82(9)	2.1(1)	5(2)	4.88(4)	0.779(7)	0.004(1)
20	0.978(8)	0.021(5)	4.0(2)	1.7(2)	5(4)	4.14(5)	0.744(8)	0.008(1)
30	1.06(3)	0.11(3)	5(1)	0.9(3)	0.35(7)	4.2(1)	0.71(2)	0.017(2)
40	1.06(3)	0.11(3)	4(1)	0.9(3)	0.35(7)	4.0(1)	0.67(2)	0.018(2)
50	1.07(4)	0.13(4)	4(1)	1.1(3)	0.33(7)	4.1(2)	0.67(2)	0.011(3)
60	1.03(2)	0.04(1)	4.6(4)	0.9(3)	1.3(6)	4.13(9)	0.71(1)	0.013(2)
70	0.97(1)	0.047(5)	4.0(1)	1.7(1)	3.1(9)	3.99(4)	0.76(1)	0.042(4)

Table S6.V. Unit cell parameters and atomic coordinates for single crystal of $\text{Ba}_2\text{CaWO}_{6-\delta}$ as obtained from Rietveld fits to a high-resolution synchrotron XRPD data. All isotropic thermal displacement parameters (B_{iso}) were refined.

Synchrotron XRPD (11-BM-B), $\lambda = 0.4127\text{\AA}$					
T = 295 K			T = 100 K		
$R_{\text{exp}}(\%)$:	4.48	$R_{\text{wp}}(\%)$:	7.56		
$R_p(\%)$:	5.93	GOF :	1.69		
Step size	0.001	Step size	0.001		
Z	2	Z	2		
Molecular weight	567.34 g/mol	Molecular weight	573.17 g/mol		
Chemical formula	$\text{Ba}_{1.72}\text{Ca}_{1.28}\text{WO}_6$	Chemical formula	$\text{Ba}_{1.78}\text{Ca}_{1.22}\text{WO}_6$		
Number of Reflections	1466	Number of Reflections	1424		
Atomic Position			Atomic Position		
Ba	x	0.4949(7)	Ba	x	0.5016(2)
	y	0.5		y	0.5
	z	0.2455(4)		z	0.2497(2)
	Occ	0.86(1) (Ba), 0.14(1) (Ca)		Occ	0.89(1) (Ba), 0.11(1) (Ca)
	B_{iso}	0.62(20)		B_{iso}	0.291(6)
Ca	x	0.5	Ca	x	0.5
	y	0.0		y	0.0
	z	0.0		z	0.0
	Occ	1		Occ	1
	B_{iso}	0.35(20)		B_{iso}	0.303(39)
W	x	0.0	W	x	0.0
	y	0.5		y	0.5
	z	0.0		z	0.0
	Occ	1		Occ	1
	B_{iso}	0.50(20)		B_{iso}	0.203(15)
O1	x	0.5212(27)	O1	x	0.5525(12)
	y	0.0		y	0.0
	z	0.2749(6)		z	0.2831(8)
	Occ	1		Occ	1
	B_{iso}	0.84(21)		B_{iso}	0.721(75)
O2	x	0.22177(11)	O2	x	0.2409(7)
	y	0.722(12)		y	0.7176(5)
	z	0.02868(30)		z	0.0212(6)
	Occ	1		Occ	1
	B_{iso}	0.84(21)		B_{iso}	0.721(75)

Table S6.VI. Selected bond lengths and angles for single crystal of Ba₂CaWO_{6-δ} as obtained from Rietveld fits to a high-resolution synchrotron XRPD data.

T = 295 K		T = 100 K	
Atoms	Bond lengths (Å)	Atoms	Bond lengths (Å)
Ba1 O1	2.868(17)	Ba1 O1	2.644(8)
Ba1 O1	3.058(17)	Ba1 O1	3.283(8)
2 x Ba1 O1	2.9723(11)	2 x Ba1 O1	2.9854(10)
2 x Ba1 O2	3.13(4)	2 x Ba1 O2	2.774(5)
2 x Ba1 O2	2.82(5)	2 x Ba1 O2	2.913(5)
2 x Ba1 O2	2.76(4)	2 x Ba1 O2	3.010(5)
2 x Ba1 O2	3.18(4)	2 x Ba1 O2	3.155(5)
2 x Ca2 O1	2.307(5)	2 x Ca2 O1	2.387(7)
4 x Ca2 O2	2.34(5)	4 x Ca2 O2	2.271(4)
2 x W1 O1	1.890(5)	2 x W1 O1	1.838(7)
4 x W1 O2	1.87(5)	4 x W1 O2	1.927(4)
Atoms	Bond angles(°)	Atoms	Bond angles(°)
W1 O1 Ca2	173.1(5)	W1 O1 Ca2	162.8(3)
W1 O2 Ca2	166.73(4)	W1 O2 Ca2	168.9(3)

III. FIGURES

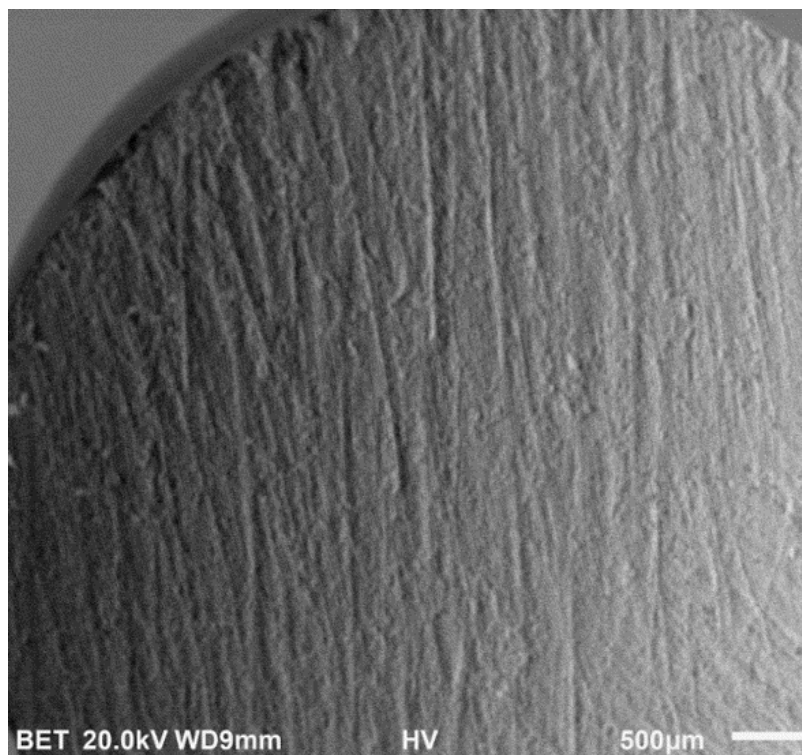


Figure S6.1. SEM backscattered micrograph showing the uniform homogeneous microstructure of a crystal after being cut perpendicular to growth direction.

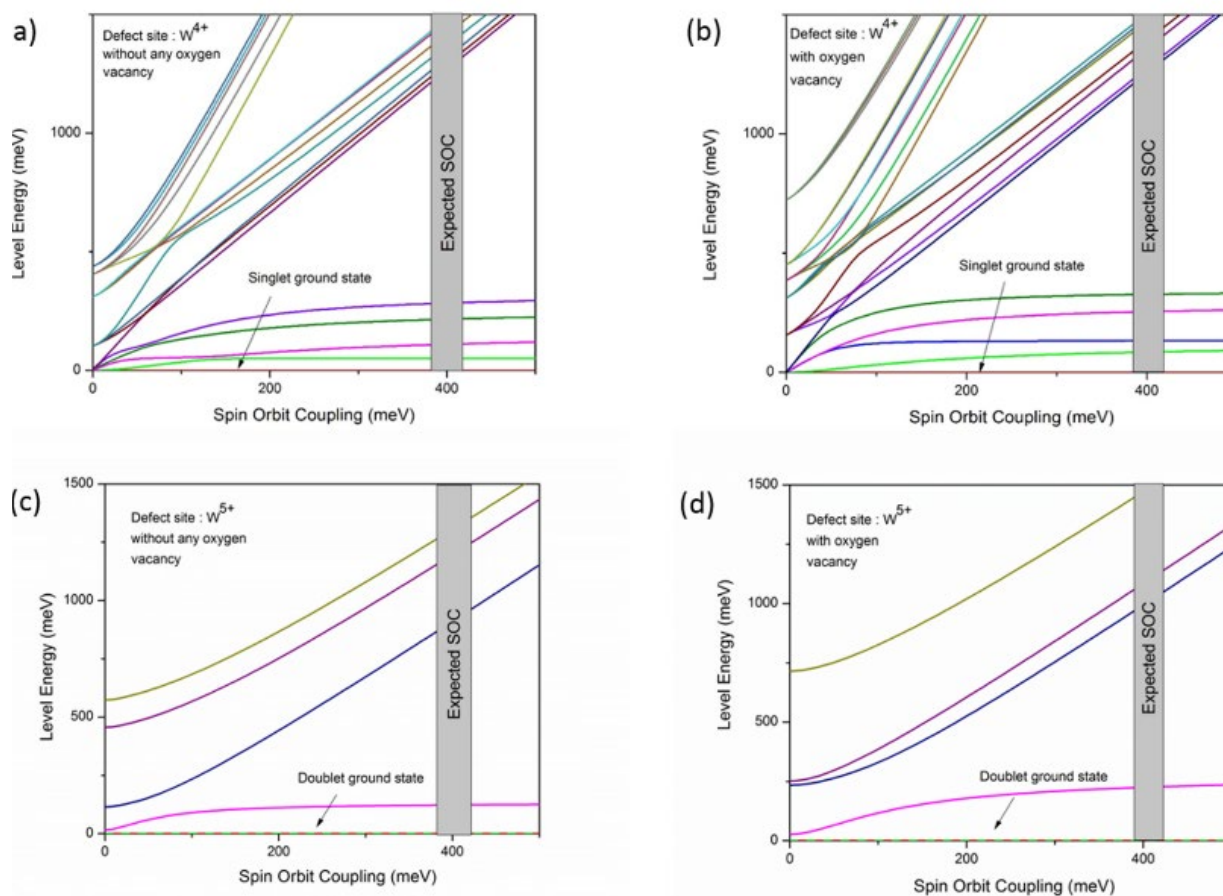


Figure S6.2. Resulting energy level along with spin orbit coupling from the point charge calculations to the oxygen ligand obtained from the PXRD refinement to the $Ba_2CaWO_{6-\delta}$ pulverized single crystals. a) Assuming the structure contains W^{4+} octahedra as the defect site without any oxygen vacancy, b) with one oxygen atom missing in the WO_6 octahedra, c) W^{5+} without oxygen vacancy and d) with one oxygen atom missing in the WO_6 octahedra at $T = 100$ K.

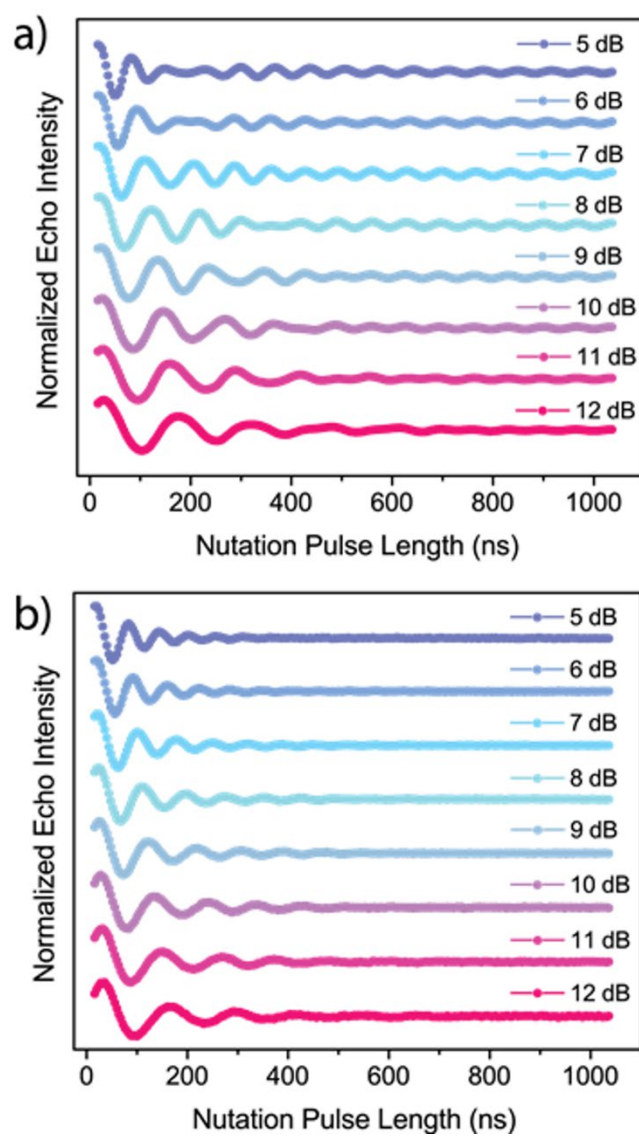


Figure S6.3. Transient nutations collected on a) a glassy solution of dpph in PrCN, and b) a powdered sample of $\text{Ba}_2\text{CaWO}_{6-\delta}$ at $T = 80$ K. The dpph radical was used to calibrate the power of the tipping pulse to assist in determination of the spin state of the paramagnetic sites in the sample.

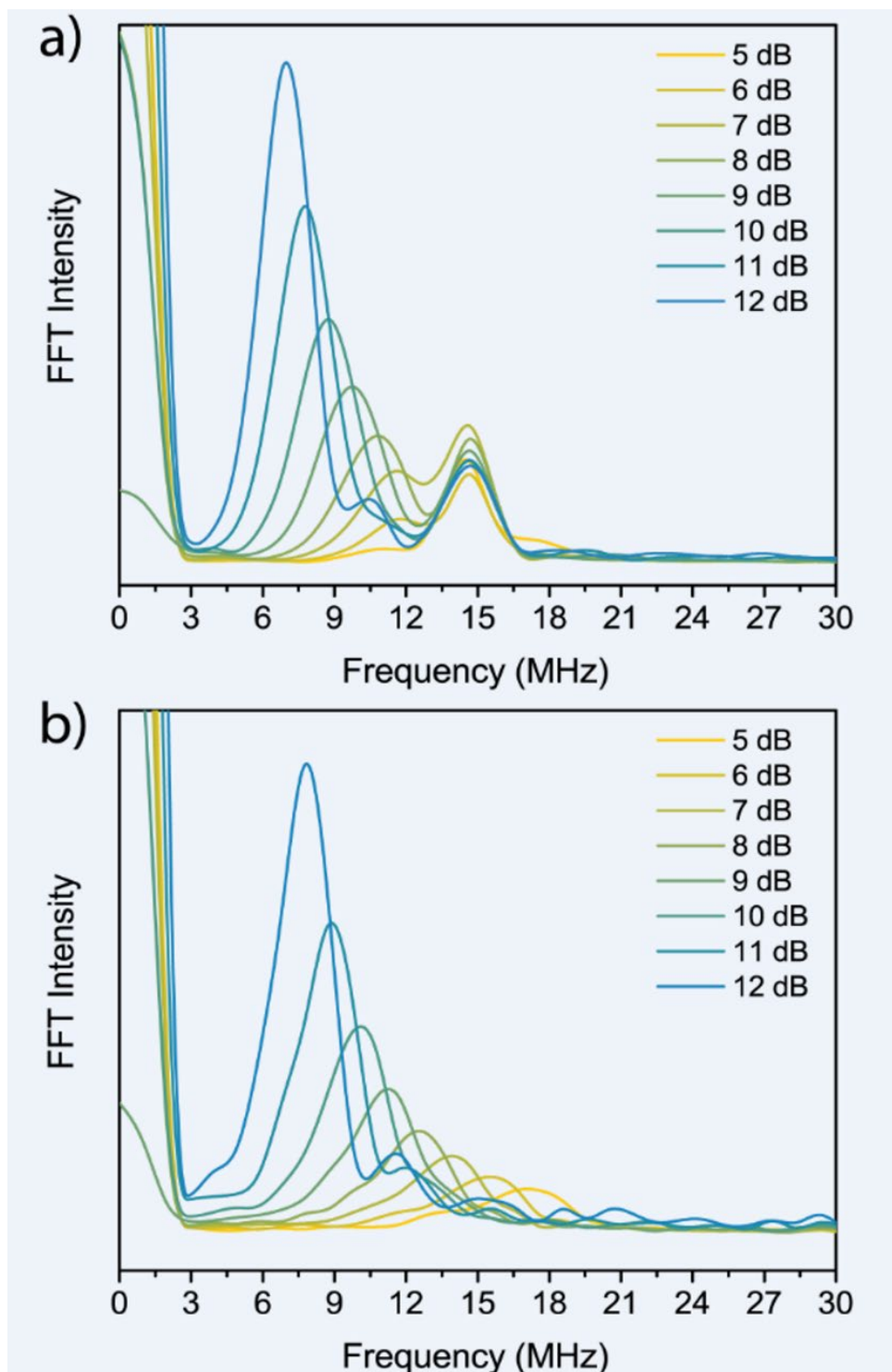


Figure S6.4. Fourier transforms of transient nutations of a) a dpph in a PrCN glass and b) powdered $\text{Ba}_2\text{CaWO}_{6-\delta}$. The transient nutations are shown in Figure S6.3. Fourier transforms were performed using a Hamming window. The second, power-independent frequency peak observed at 14.6 MHz in a) is a result of protons in the solvent coupling to the electron spin – a manifestation

of the Hartmann-Hahn effect. The power-dependent peak of the dpph standard, a well-established $S = \frac{1}{2}$ system, was used to calibrate the power of the tipping field to determine the spin state of the paramagnetic sites in the perovskite system.

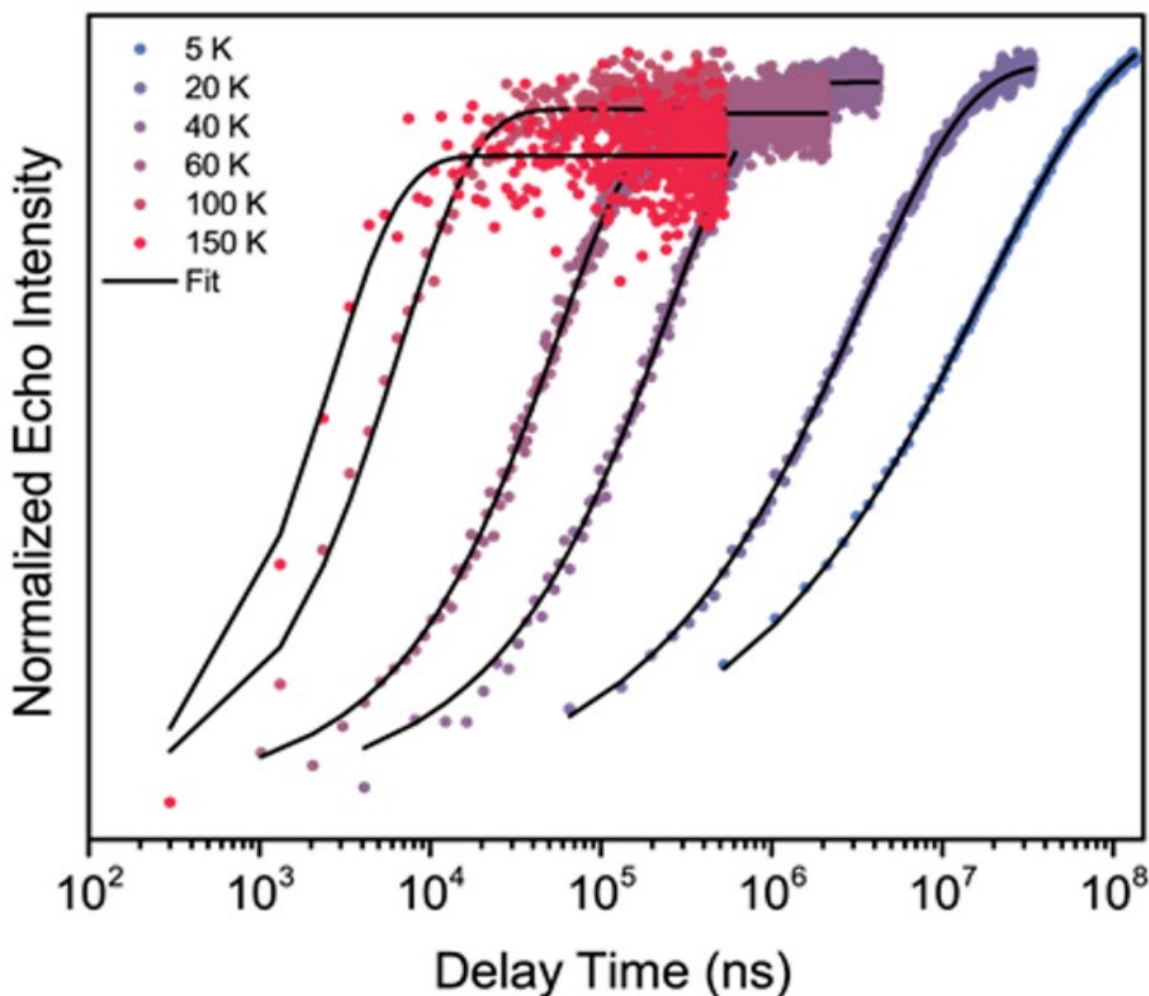


Figure S6.5. Selected inversion recovery curves collected on a powdered sample of $\text{Ba}_2\text{CaWO}_{6-\delta}$ and fit using the equation $I(\tau) = -A \left(e^{-(\tau/T_1 + \sqrt{\tau/q})} - b - 1 \right)$ where I is the normalized echo intensity, A and b are normalization factors (1 and 0 approximately), and q is a factor related to spectral diffusion, which is relevant at low temperatures in this system. Fit parameters can be found in Table S6.I.

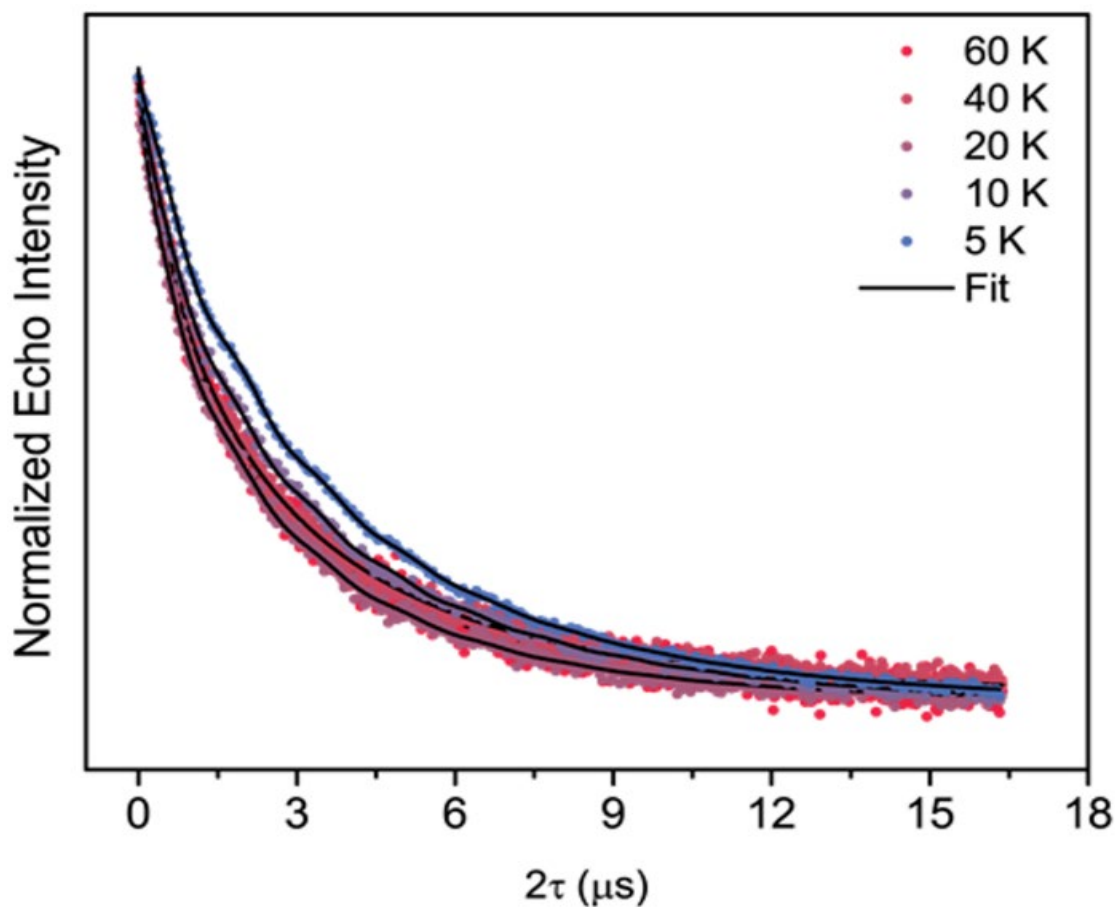


Figure S6.6. Selected Hahn echo decay curves collected on a powdered sample of $\text{Ba}_2\text{CaWO}_{6-\delta}$ and fit using the equation $I(\tau) = A(1 - b * \cos(\omega\tau + c))e^{-\tau/T_{osc}}e^{-(2\tau/T_2)^q} + f$ where A is a normalization factor (usually 1), b is the ESEEM modulation amplitude, ω is the modulation frequency, c is the modulation phase, T_{osc} is the ESEEM decay time, q is a stretch factor, and f is a term to assist in fitting (usually 0). In these curves, ESEEM arising from the interaction between the electronic spin and an $I = 1/2$ ^{183}W nucleus (Larmor frequency = 0.6258 MHz at the measurement field) is evident and able to be modeled. Past $T = 60$ K, a stretched exponential function $I(\tau) = Ae^{-(2\tau/T_2)^q} + f$ without the term for ESEEM was used. Use of one equation over the other did not influence the value of T_2 extracted.

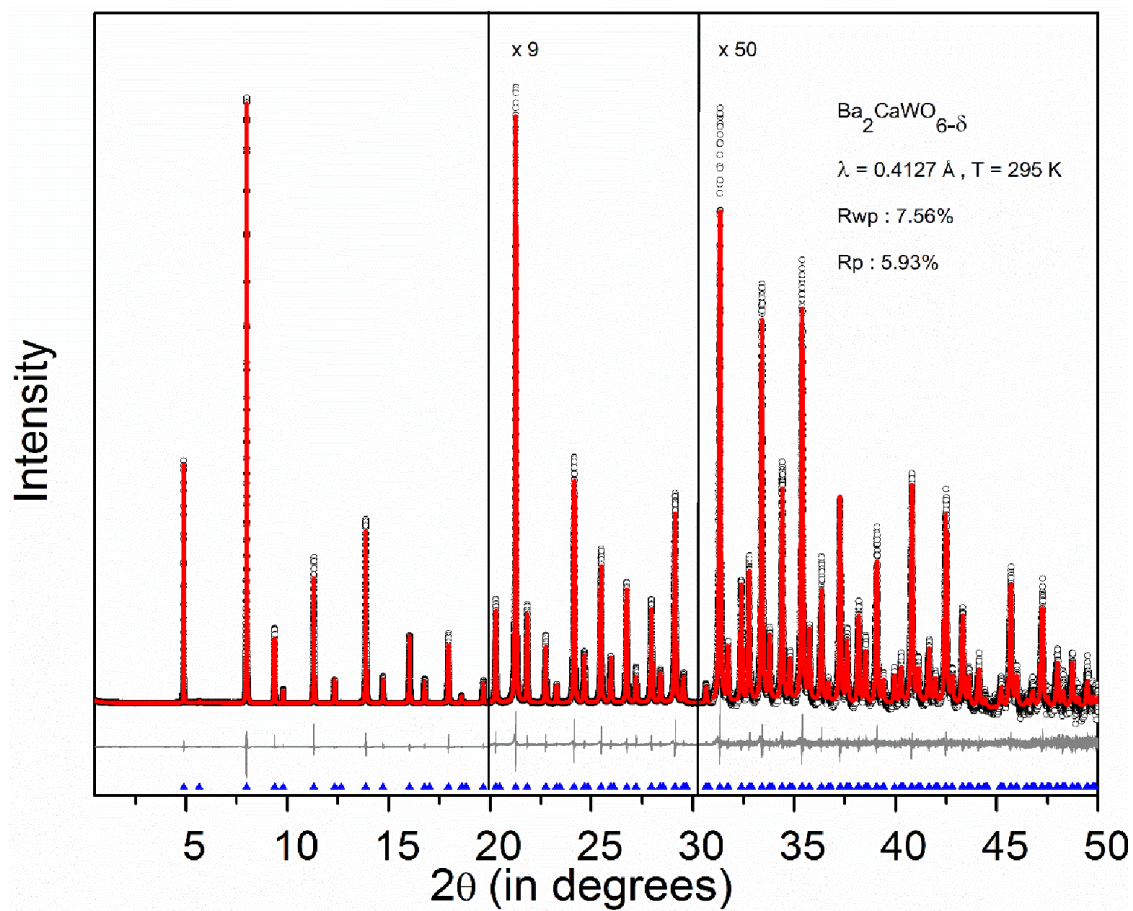


Figure S6.7. Rietveld fit (red line) to synchrotron XRPD data (black points) for pulverized single crystals of $\text{Ba}_2\text{CaWO}_{6-\delta}$ collected at $T = 295 \text{ K}$. Grey line shows the difference between observed and calculated intensity. Blue ticks mark are the expected positions of reflections for the fitted monoclinic (Spacegroup: $I2/m$) phase.

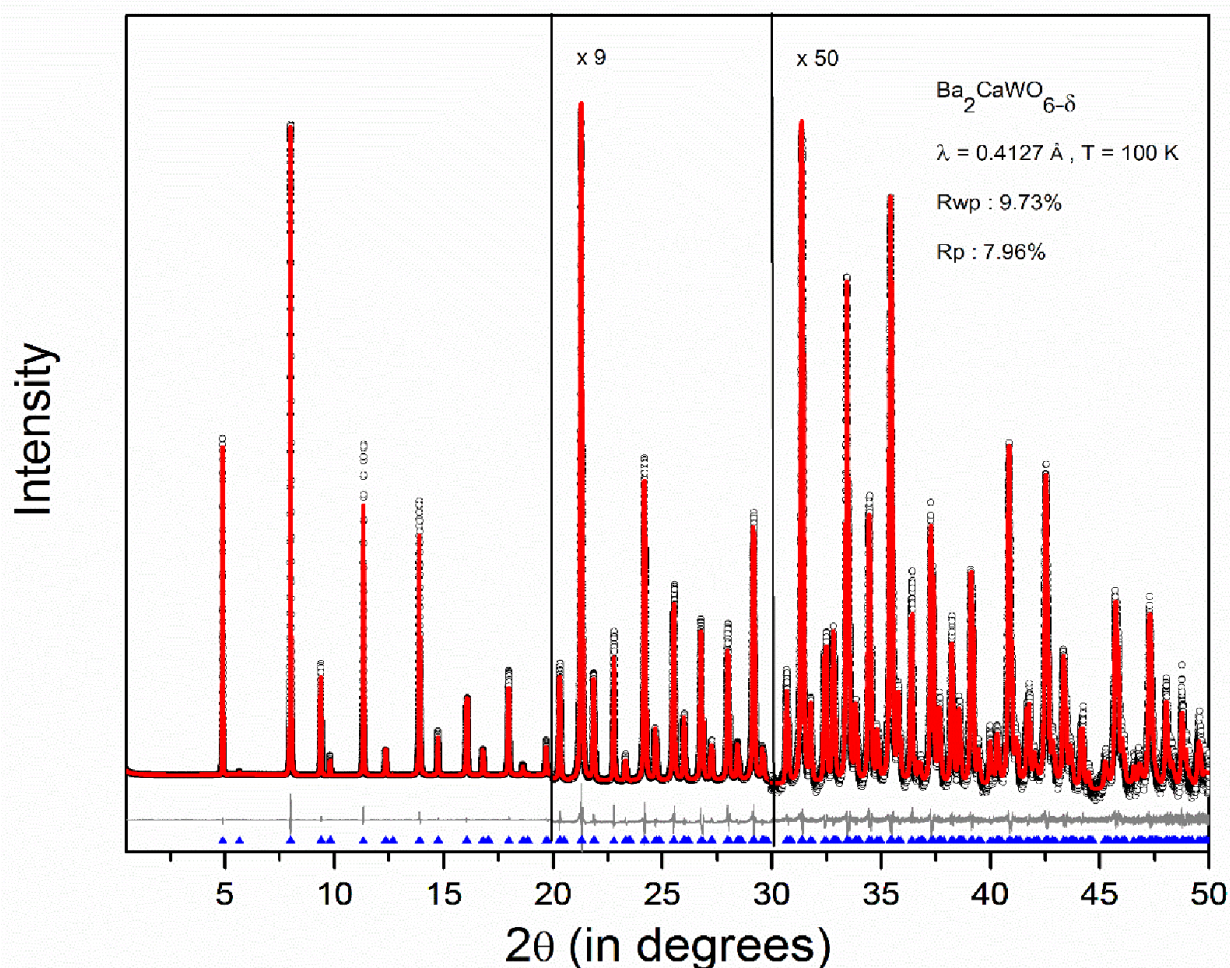


Figure S6.8. Rietveld fit (red line) to synchrotron XRPD data (black points) for pulverized single crystals of $\text{Ba}_2\text{CaWO}_{6-\delta}$ collected at $T = 100 \text{ K}$. Grey line shows the difference between observed and calculated intensity. Blue ticks mark are the expected positions of reflections for the fitted monoclinic (Spacegroup: $I2/m$) phase.

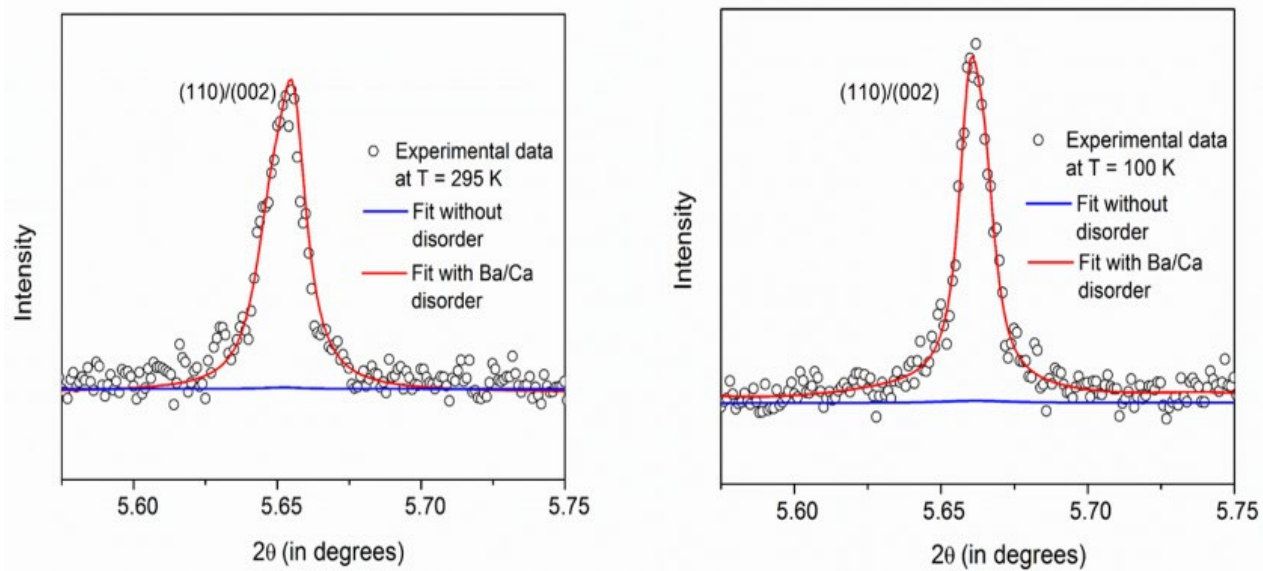


Figure S6.9. Rietveld fit to synchrotron XRD data (black points) for pulverized single crystals of $\text{Ba}_2\text{CaWO}_{6-\delta}$ with (red line) and without (blue line) Ba site disorder in the double perovskite structure.

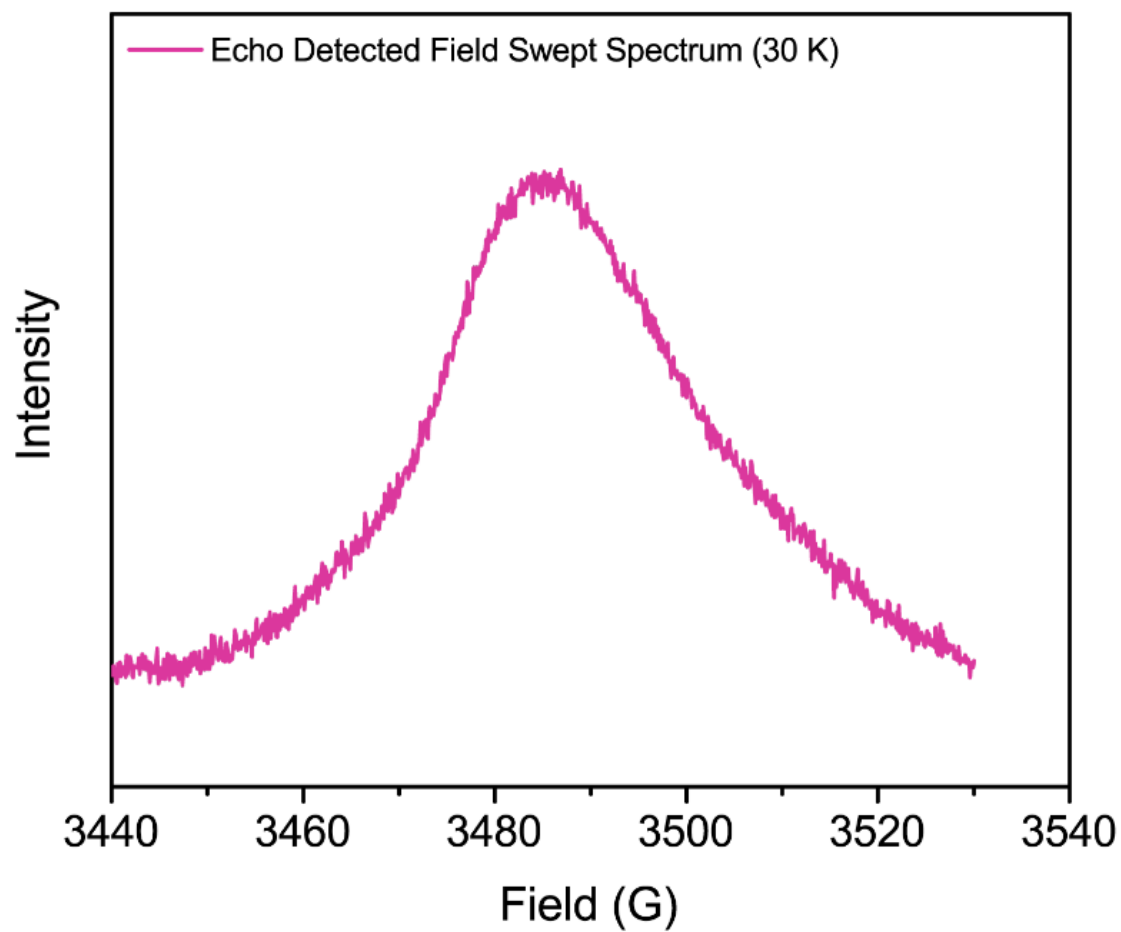


Figure S10. The echo-detected pulse ESR spectra collected at $T = 30$ K.

References for Chapter One

- (1) Condon, E.; Shortley, G. *The Theory of Atomic Spectra*; Cambridge University Press, 1957.
- (2) (a) Gatteschi, D.; Kahn, O.; Miller, J. S.; Palacio, F. *Magnetic Molecular Materials*; Springer Science & Business Media, 2012; Vol. 198. (b) Kahn, O. *Molecular Magnetism*; VCH: Weinheim, Germany, 1993.
- (3) Eaton, S. S.; Eaton, G. R. In *Biological Magnetic Resonance*; Berliner, L. J., Eaton, S. S., Eaton, G. R., Eds.; Kluwer Academic/Plenum Publishers: New York, 2000; Vol. 19, Distance Measurements in Biological Systems by EPR, pp 29–154.
- (4) Kong, D.; Cui, Y. Opportunities in Chemistry and Materials Science for Topological Insulators and their Nanostructures. *Nat. Chem.* **2011**, 3, 845–849. (b) Mückler, L.; Zhang, H.; Chadov, S.; Yan, B.; Casper, F.; Kübler, J.; Zhang, S.-C.; Felser, C. Topological Insulators from a Chemist's Perspective. *Angew. Chem. Int. Ed.* **2012**, 51, 7221–7225. (c) Cava, R. J.; Ji, H.; Fucillo, M. K.; Gibson, Q. D.; Hor, Y. S. Crystal Structure and Chemistry of Topological Insulators. *J. Mater. Chem. C* **2013**, 1, 3176–3189.
- (5) Marian, C. M. Spin-orbit coupling and intersystem crossing in molecules. *WIREs Comput Mol Sci* **2011**, 2 (2), 187–203.
- (6) Sun, Y.; Tang, H.; Chen, K.; Hu, L.; Yao, J.; Shaik, S.; Chen, H. Two-state Reactivity in Low-Valent Iron-Mediated C-H Activation and the Implications for Other First-Row Transition metals. *J. Am. Chem. Soc.* **2016**, 138, 3715–3730. (b) Bellows, S. M.; Cundari, T. R.; Holland, P. L. Spin-Crossover During α -Hydride Elimination in High-Spin Fe(II)- and Co(II)-Alkyl Complexes. *Organometallics*, **2013**, 32, 4741–4751. (c) Danovich, D.; Shaik, S. Spin-Orbit Coupling in the Oxidative Activation of H-H by FeO^+ . Selection Rules and Reactivity Effects.

- J. Am. Chem. Soc.* **1997**, 119, 1773–1786. (d) Schröder, D.; Shaik, S.; Schwarz, H. Two-State Reactivity as a New Concept in Organometallic Chemistry. *Acc. Chem. Res.* **2000**, 33, 139–145. (e) Poli, R.; Harvey, J. N. Spin Forbidden Chemical Reactions of Transition Metal Compounds. New Ideas and New Computational Challenges. *Chem. Soc. Rev.* **2003**, 32, 1–8.
- (7) Rau, I. G.; Baumann, S.; Rusponi, S.; Donati, F.; Stepanow, S.; Gragnaniello, L.; Dreiser, J.; Piamonteze, C.; Nolting, F.; Gangopadhyay, S.; Albertini, O. R.; Macfarlane, R. M.; Lutz, C. P.; Jones, B. A.; Gambardella, P.; Heinrich, A. J.; Brune, H. Reaching the magnetic anisotropy limit of a 3d metal atom. *Science* **2014**, 344 (6187), 988–992.
- (8) (a) Bunting, P. C.; Atanasov, M.; Damgaard-Møller, E.; Perfetti, M.; Crassee, I.; Orlita, M.; Overgaard, J.; van Slageren, J.; Neese, F.; Long, J. R. A Linear Cobalt(II) Complex with Maximal Orbital Angular Momentum from a Non-Aufbau Ground State. *Science* **2018**, 362, eaat7319. (b) Guo, F.-S.; Day, B. M.; Chen, Y.-C.; Tong, M.-L.; Mansikkamäki, A.; Layfield, R. A. Magnetic Hysteresis Up to 80 Kelvin in a Dysprosium Metallocene Single-Molecule Magnet. *Science* **2018**, 362, 1400–1403. (c) Thiele, S.; Balestro, F.; Ballou, R.; Klyatskaya, S.; Ruben, M.; Wernsdorfer, W. Electrically Driven Nuclear Spin Resonance in Single-Molecule Magnets. *Science* **2014**, 344, 1135–1138. (d) Zadrozny, J. M.; Xiao, D. J.; Atanasov, M.; Long, G. J.; Grandjean, F.; Neese, F.; Long, J. R. Magnetic blocking in a linear iron (I) complex. *Nat. Chem.* **2013**, 5 (7), 577–581.
- (9) (a) Craig, G. A.; Murrie, M. 3d single-ion magnets. *Chem. Soc. Rev.* **2015**, 44 (8), 2135–2147. (b) Meng, Y.-S.; Jiang, S.-D.; Wang, B.-W.; Gao, S. Understanding the magnetic anisotropy toward single-ion magnets. *Acc. Chem. Res.* **2016**, 49 (11), 2381–2389.

- (10) (a) Pyykkö, P. Relativistic Effects in Chemistry: More Common Than You Thought. *Annu. Rev. Phys. Chem.* **2012**, 63, 45–64. (b) Pyykkö, P. The Physics Behind Chemistry and the Periodic Table. *Chem. Rev.* **2012**, 112, 371–384.
- (11) (a) Nielsen, M. A.; Chuang, I.; Grover, L. K. Quantum Computation and Quantum Information. *Am. J. Phys.* **2002**, 70 (5), 558–559. (b) Feynman, R. P. Simulating physics with computers. *Int. J. Theor. Phys.* **1982**, 21 (6-7), 467–488.
- (12) (a) Zadrozny, J. M.; Niklas, J.; Poluektov, O. G.; Freedman, D. E. Millisecond Coherence Time in a Tunable Molecular Electronic Spin Qubit. *ACS Cent. Sci.* **2015**, 1 (9), 488–492. (b) Aromí, G.; Aguilà, D.; Gamez, P.; Luis, F.; Roubeau, O. Design of magnetic coordination complexes for quantum computing. *Chem. Soc. Rev.* **2012**, 41 (2), 537–546. (c) Troiani, F.; Affronte, M. Molecular spins for quantum information technologies. *Chem. Soc. Rev.* **2011**, 40(6), 3119. (d) Stamp, P. C. E.; Gaita-Ariño, A. Spin-based quantum computers made by chemistry: hows and whys. *J. Mater. Chem.* **2009**, 19 (12), 1718–1730.
- (13) Abragam, A.; Bleaney, B. *Electron Paramagnetic Resonance of Transition Ions*; OUP Oxford, 2012.

References for Chapter Two

- (1) (a) Chen, Y. L.; Analytis, J. G.; Chu, J.-H.; Liu, Z. K.; Mo, S.-K.; Qi, X. L.; Zhang, H. J.; Lu, D. H.; Dai, X.; Fang, Z.; Zhang, S. C.; Fisher, I. R.; Hussain, Z.; Shen, Z.-X. Experimental Realization of a Three-Dimensional Topological Insulator, Bi₂Te₃. *Science* **2009**, 325 (5937), 178–181. (b) Xia, Y.; Qian, D.; Hsieh, D.; Wray, L.; Pal, A.; Lin, H.; Bansil, A.; Grauer, D.; Hor, Y. S.; Cava, R. J.; Hasan, M. Z. Observation of a large-gap topological-insulator class with a single Dirac cone on the surface. *Nat. Phys.* **2009**, 5 (6), 398–402. (c) Hsieh, D.; Xia,

- Y.; Qian, D.; Wray, L.; Meier, F.; Dil, J. H.; Osterwalder, J.; Patthey, L.; Fedorov, A. V.; Lin, H.; Bansil, A.; Grauer, D.; Hor, Y. S.; Cava, R. J.; Hasan, M. Z. Observation of Time-Reversal-Protected Single-Dirac-Cone Topological-Insulator States in Bi_2Te_3 and Sb_2Te_3 . *Phys. Rev. Lett.* **2009**, *103* (14). (d) Kuroda, K.; Miyahara, H.; Ye, M.; Ereemeev, S. V.; Koroteev, Y. M.; Krasovskii, E. E.; Chulkov, E. V.; Hiramoto, S.; Moriyoshi, C.; Kuroiwa, Y.; Miyamoto, K.; Okuda, T.; Arita, M.; Shimada, K.; Namatame, H.; Taniguchi, M.; Ueda, Y.; Kimura, A. Experimental Verification of PbBi_2Te_4 as a 3D Topological Insulator. *Phys. Rev. Lett.* **2012**, *108* (20). (e) Kirchmayr, H. R. Permanent magnets and hard magnetic materials. *J. Phys. D: Appl. Phys.* **1996**, *29* (11), 2763–2778.
- (2) Marian, C. M. Spin-orbit coupling and intersystem crossing in molecules. *WIREs Comput Mol Sci* **2011**, *2* (2), 187–203.
- (3) (a) Desrochers, P. J.; Telsler, J.; Zvyagin, S. A.; Ozarowski, A.; Krzystek, J.; Vicic, D. A. Electronic Structure of Four-Coordinate C_3v Nickel(II) Scorpionate Complexes: Investigation by High-Frequency and -Field Electron Paramagnetic Resonance and Electronic Absorption Spectroscopies. *Inorg. Chem.* **2006**, *45* (22), 8930–8941. (b) Karunadasa, H. I.; Arquero, K. D.; Berben, L. A.; Long, J. R. Enhancing the Magnetic Anisotropy of Cyano-Ligated Chromium(II) and Chromium(III) Complexes via Heavy Halide Ligand Effects. *Inorg. Chem.* **2010**, *49* (11), 4738–4740. (c) Mantel, C.; Baffert, C.; Romero, I.; Deronzier, A.; Pécaut, J.; Collomb, M.-N.; Duboc, C. Structural Characterization and Electronic Properties Determination by High-Field and High-Frequency EPR of a Series of Five-Coordinated Mn(II) Complexes. *Inorg. Chem.* **2004**, *43* (20), 6455–6463. (d) Zein, S.; Duboc, C.; Lubitz, W.;

- Neese, F. A Systematic Density Functional Study of the Zero-Field Splitting in Mn(II) Coordination Compounds. *Inorg. Chem.* **2008**, *47* (1), 134–142.
- (4) Abragam, A.; Bleaney, B. *Electron Paramagnetic Resonance of Transition Ions*; OUP Oxford, 2012.
- (5) Pichon, C.; Mialane, P.; Rivière, E.; Blain, G.; Dolbecq, A.; Marrot, J.; Sécheresse, F.; Duboc, C. The Highest D Value for a MnIII Ion: Investigation of a Manganese(II) Polyoxometalate Complex by High-Field Electron Paramagnetic Resonance. *Inorg. Chem.* **2007**, *46* (19), 7710–7712.
- (6) (a) Dai, D.; Xiang, H.; Whangbo, M.-H. Effects of spin-orbit coupling on magnetic properties of discrete and extended magnetic systems. *J. Comput. Chem.* **2008**, *29* (13), 2187–2209. (b) Whangbo, M.-H.; Gordon, E. E.; Xiang, H.; Koo, H.-J.; Lee, C. Prediction of Spin Orientations in Terms of HOMO–LUMO Interactions Using Spin–Orbit Coupling as Perturbation. *Acc. Chem. Res.* **2015**, *48* (12), 3080–3087.
- (7) Jacobsen, C. J.; Pedersen, E.; Villadsen, J.; Weihe, H. ESR characterization of trans-diacidatotetrakis (pyridine) vanadium and-manganese trans-VII (py)₄X₂ and trans-MnII (py)₄X₂ (X= NCS, Cl, Br, I; py= pyridine). *Inorg. Chem.* **1993**, *32* (7), 1216–1221.
- (8) Azarkh, M.; Penkova, L. V.; Kats, S. V.; Varzatskii, O. A.; Voloshin, Y. Z.; Groenen, E. J. J. A Mononuclear Mn(II) Pseudocathrochelate Complex Studied by Multi-Frequency Electron-Paramagnetic-Resonance Spectroscopy. *J. Phys. Chem. Lett.* **2014**, *5* (5), 886–889.
- (9) Duboc, C.; Collomb, M.-N.; Pécaut, J.; Deronzier, A.; Neese, F. Definition of Magneto-Structural Correlations for the MnIII Ion. *Chem. -Eur. J.* **2008**, *14* (21), 6498–6509.

- (10) Duboc, C.; Phoeung, T.; Zein, S.; Pécaut, J.; Collomb, M.-N.; Neese, F. Origin of the Zero-Field Splitting in Mononuclear Octahedral Dihalide Mn(II) Complexes: An Investigation by Multifrequency High-Field Electron Paramagnetic Resonance and Density Functional Theory. *Inorg. Chem.* **2007**, *46* (12), 4905–4916.
- (11) Note, bismuth does undergo radioactive decay, but its half-life is 1.9×10^{19} years, or approximately 1.3 billion times the age of the universe. de Marcillac, P.; Coron, N.; Dambier, G.; Leblanc, J.; Moalic, J.-P. Experimental detection of α -particles from the radioactive decay of natural bismuth. *Nature* **2003**, *422* (6934), 876–878.
- (12) Condon, E.; Shortley, G. *The Theory of Atomic Spectra*; Cambridge University Press, 1957.
- (13) (a) Sunatsuki, Y.; Kishima, Y.; Kobayashi, T.; Yamaguchi, T.; Suzuki, T.; Kojima, M.; Krzystek, J.; Sundberg, M. R. A single tripodal ligand stabilizing three different oxidation states (II, III, and IV) of manganese. *Chem. Commun.* **2011**, *47* (32), 9149. (b) Costes, J.-P.; Yamaguchi, T.; Kojima, M.; Vendier, L. Experimental Evidence for the Participation of 5d Gd(III) Orbitals in the Magnetic Interaction in Ni-Gd Complexes. *Inorg. Chem.* **2009**, *48*(12), 5555–5561.
- (14) Kahn, O. *Molecular Magnetism*. VCH Publishers Inc., New York **1993**.
- (15) Azuah, R. T.; Kneller, L. R.; Qiu, Y.; Tregenna-Piggott, P. L. W.; Brown, C. M.; Copley, J. R. D.; Dimeo, R. M. DAVE: A Comprehensive Software Suite for the Reduction, Visualization, and Analysis of Low Energy Neutron Spectroscopic Data. *J. Res. Nat. Inst. Stand. Technol.* **2009**, *114* (6), 341.
- (16) Stoll, S.; Schweiger, A. EasySpin, a comprehensive software package for spectral simulation and analysis in EPR. *J. Magn. Reson.* **2006**, *178* (1), 42–55.

- (17) (a) Rado, G. T. Mechanism of the Magnetoelectric Effect in an Antiferromagnet. *Phys. Rev. Lett.* **1961**, *6* (11), 609–610. (b) Hornreich, R.; Shtrikman, S. Statistical Mechanics and Origin of the Magnetoelectric Effect in Cr₂O₃. *Phys. Rev.* **1967**, *161* (2), 506–512.
- (18) Qin, C.-J.; James, L.; Chartres, J. D.; Alcock, L. J.; Davis, K. J.; Willis, A. C.; Sargeson, A. M.; Bernhardt, P. V.; Ralph, S. F. An Unusually Flexible Expanded Hexaamine Cage and Its Cu(II) Complexes: Variable Coordination Modes and Incomplete Encapsulation. *Inorg. Chem.* **2011**, *50* (18), 9131–9140.
- (19) Sunatsuki, Y.; Kishima, Y.; Kobayashi, T.; Yamaguchi, T.; Suzuki, T.; Kojima, M.; Krzystek, J.; Sundberg, M. R. *Chem. Commun.* **2011**, *47*, 9149–9151.
- (20) Azuah, R. T.; Kneller, L. R.; Qiu, Y.; Tregenna-Piggott, P. L. W.; Brown, C. M.; Copley, J. R. D.; Dimeo, R. M. DAVE: A Comprehensive Software Suite for the Reduction, Visualization, and Analysis of Low Energy Neutron Spectroscopic Data. *J. Res. Nat. Inst. Stand. Technol.* **2009**, *114* (6), 341.
- (21) Stoll, S.; Schweiger, A. EasySpin, a comprehensive software package for spectral simulation and analysis in EPR. *J. Magn. Reson.* **2006**, *178* (1), 42–55.
- (22) APEX2, v. 2014 ; Bruker Analytical X-Ray Systems, Inc: Madison, WI, 2014.
- (23) Sheldrick, G. M. SADABS, Version 2.03; Bruker Analytical X-Ray Systems, Inc.: Madison, WI, 2000.
- (24) Sheldrick, G. M. SHELXTL, Version 6.12; Bruker Analytical X-ray Systems, Inc.: Madison, WI, 2000.

- (25) Dolomanov, O. V.; Bourhis, L. J.; Gildea, R. J.; Howard, J. A. K.; Puschmann, H. OLEX2: a complete structure solution, refinement and analysis program. *J. Appl. Crystallogr.* **2009**, *42* (2), 339–341.
- (26) Azarkh, M.; Penkova, L. V.; Kats, S. V.; Varzatskii, O. A.; Voloshin, Y. Z.; Groenen, E. J. J. A Mononuclear Mn(II) Pseudoclathrochelate Complex Studied by Multi-Frequency Electron-Paramagnetic-Resonance Spectroscopy. *J. Phys. Chem. Lett.* **2014**, *5* (5), 886–889.

References for Chapter Three

- (1) Moulder, J. F.; Stickle, W. F.; Sobol, P. E.; Bomben, K. D. *Handbook of Photoelectron Spectroscopy*; Perkin-Elmer Corporation: Eden Prairie, Mn, 1992.
- (2) Toro Iniesta, J. C. On the Discovery of the Zeeman Effect on the Sun and in the Laboratory. *Vistas Astron.* **1996**, *40*, 241–256.
- (3) Zeeman, P. The Effect of Magnetization on the Nature of Light Emitted by a Substance. *Nature* **1897**, *55*, 347.
- (4) Kong, D.; Cui, Y. Opportunities in Chemistry and Materials Science for Topological Insulators and their Nanostructures. *Nat. Chem.* **2011**, *3*, 845–849.
- (5) MÜchler, L.; Zhang, H.; Chadov, S.; Yan, B.; Casper, F.; Kübler, J.; Zhang, S.-C.; Felser, C. Topological Insulators from a Chemist's Perspective. *Angew. Chem. Int. Ed.* **2012**, *51*, 7221–7225.
- (6) Cava, R. J.; Ji, H.; Fuccillo, M. K.; Gibson, Q. D.; Hor, Y. S. Crystal Structure and Chemistry of Topological Insulators. *J. Mater. Chem. C* **2013**, *1*, 3176–3189.
- (7) Gatteschi, D.; Kahn, O.; Miller, J. S.; Palacio, F. *Magnetic Molecular Materials*; Springer Science & Business Media, 2012; Vol. 198.

- (8) Kahn, O. *Molecular Magnetism*; VCH: Weinheim, Germany, 1993.
- (9) Marian, C. M. Spin-Orbit Coupling and Intersystem Crossing in Molecules. *WIREs Comput. Mol. Sci.* **2012**, *2*, 187–203.
- (10) Tao, Y.; Yuan, K.; Chen, T.; Xu, P.; Li, H.; Chen, R.; Zheng, C.; Zhang, L.; Huang, W. Thermally Activated Delayed Fluorescence Materials towards the Breakthrough of Organoelectronics. *Adv. Mater.* **2014**, *26*, 7931–7958.
- (11) Yersin, H.; Rausch, A. F.; Czerwieniec, R.; Hofbeck, T.; Fischer, T. The Triplet State of Organo-Transition Metal Compounds. Triplet Harvesting and Singlet Harvesting for Efficient OLEDs. *Coord. Chem. Rev.* **2011**, *255*, 2622–2652.
- (12) Eaton, S. S.; Eaton, G. R. In *Biological Magnetic Resonance*; Berliner, L. J., Eaton, S. S., Eaton, G. R., Eds.; Kluwer Academic/Plenum Publishers: New York, 2000; Vol. 19, Distance Measurements in Biological Systems by EPR, pp 29–154.
- (13) Danovich, D.; Shaik, S. Spin-Orbit Coupling in the Oxidative Activation of H-H by FeO^+ . Selection Rules and Reactivity Effects. *J. Am. Chem. Soc.* **1997**, *119*, 1773–1786.
- (14) Schröder, D.; Shaik, S.; Schwarz, H. Two-State Reactivity as a New Concept in Organometallic Chemistry. *Acc. Chem. Res.* **2000**, *33*, 139–145.
- (15) Poli, R.; Harvey, J. N. Spin Forbidden Chemical Reactions of Transition Metal Compounds. New Ideas and New Computational Challenges. *Chem. Soc. Rev.* **2003**, *32*, 1–8.
- (16) Sun, Y.; Tang, H.; Chen, K.; Hu, L.; Yao, J.; Shaik, S.; Chen, H. Two-state Reactivity in Low-Valent Iron-Mediated C-H Activation and the Implications for Other First-Row Transition metals. *J. Am. Chem. Soc.* **2016**, *138*, 3715–3730.

- (17) Bellows, S. M.; Cundari, T. R.; Holland, P. L. Spin-Crossover During α -Hydride Elimination in High-Spin Fe(II)- and Co(II)-Alkyl Complexes. *Organometallics*, **2013**, *32*, 4741–4751.
- (18) Bunting, P. C.; Atanasov, M.; Damgaard-Møller, E.; Perfetti, M.; Crassee, I.; Orlita, M.; Overgaard, J.; van Slageren, J.; Neese, F.; Long, J. R. A Linear Cobalt(II) Complex with Maximal Orbital Angular Momentum from a Non-Aufbau Ground State. *Science* **2018**, *362*, eaat7319.
- (19) Guo, F.-S.; Day, B. M.; Chen, Y.-C.; Tong, M.-L.; Mansikkamäki, A.; Layfield, R. A. Magnetic Hysteresis Up to 80 Kelvin in a Dysprosium Metallocene Single-Molecule Magnet. *Science* **2018**, *362*, 1400–1403.
- (20) Thiele, S.; Balestro, F.; Ballou, R.; Klyatskaya, S.; Ruben, M.; Wernsdorfer, W. Electrically Driven Nuclear Spin Resonance in Single-Molecule Magnets. *Science* **2014**, *344*, 1135–1138.
- (21) Pyykkö, P. Relativistic Effects in Chemistry: More Common Than You Thought. *Annu. Rev. Phys. Chem.* **2012**, *63*, 45–64.
- (22) Pyykkö, P. The Physics Behind Chemistry and the Periodic Table. *Chem. Rev.* **2012**, *112*, 371–384.
- (23) Kasha, M. Collisional Perturbation of Spin-Orbital Coupling and the Mechanism of Fluorescence Quenching. A Visual Demonstration of the Perturbation. *J. Chem. Phys.* **1952**, *20*, 71–74.
- (24) Koziar, J. C.; Cowan, D. O. Photochemical Heavy-Atom Effects. *Acc. Chem. Res.* **1978**, *11*, 334–341.

- (25) Klemmer, T.; Hoydick, D.; Okumura, H.; Zhang, B.; Soffa, W. Magnetic Hardening and Coercivity Mechanisms in L10 Ordered FePd Ferromagnets. *Scr. Metall. Mater.* **1995**, *33*, 1793–1805.
- (26) Gutfleisch, O.; Lyubina, J.; Müller, K.-H.; Schultz, L. FePt Hard Magnets. *Adv. Eng. Mater.* **2005**, *7*, 208–212.
- (27) Adams, E.; Hubbard, W. M.; Syeles, A. M. A New Permanent Magnet from Powdered Manganese Bismuthide. *J. Appl. Phys.* **1952**, *23*, 1207–1211.
- (28) Yang, Y.; Chen, X.; Guo, S.; Yan, A.; Huang, Q.; Wu, M.; Chen, D.; Yang, Y.; Yang, J. Temperature Dependences of Structure and Coercivity for Melt-Spun MnBi Compound. *J. Magn. Magn. Mater.* **2013**, *330*, 106–110.
- (29) Jesche, A.; McCallum, R. W.; Thimmaiah, S.; Jacobs, J. L.; Taufour, V.; Kreyszig, A.; Houk, R. S.; Bud'ko, S. L.; Canfield, P. C. Giant Magnetic Anisotropy and Tunneling of the Magnetization in $\text{Li}_2(\text{Li}_{1-x}\text{Fe}_x)\text{N}$. *Nat. Commun.* **2014**, *5*, 3333.
- (30) Zadrozny, J. M.; Ziao, D. J.; Atanasov, M.; Long, G. J.; Grandjean, F.; Neese, F.; Long, J. R. Magnetic Blocking in a Linear Iron(I) Complex. *Nat. Chem.* **2013**, *5*, 577–581.
- (31) Abragam, A.; Bleaney, *Electron Paramagnetic Resonance of Transition Ions*; Clarendon Press: Oxford, 1970.
- (32) Duboc, C. Determination and Prediction of the Magnetic Anisotropy of Mn Ions. *Chem. Soc. Rev.* **2016**, *45*, 5834–5847.
- (33) Zein, S.; Duboc, C.; Lubitz, W.; Neese, F. A Systematic Density Functional Study of the Zero-Field Splitting in Mn(II) Coordination Compounds. *Inorg. Chem.* **2008**, *47*, 134–142.

- (34) Duboc, C.; Phoeung, T.; Zein, S.; Pécaut, J.; Collomb, M.-N.; Neese, F. Origin of the Zero-Field Splitting in Mononuclear Octahedral Dihalide Mn(II) Complexes: An Investigation by Multifrequency High-Field Electron Paramagnetic Resonance and Density Functional Theory. *Inorg. Chem.* **2007**, *46*, 4905–4916.
- (35) Brackett, G. C.; Richards, P. L.; Caughey, W. S. Far-infrared Magnetic Fe(III) and Mn(III) Porphyrins, Myoglobin, Hemoglobin, Ferrichrome A, and Fe(III) Dithiocarbamates. *J. Chem. Phys.* **1971**, *54*, 4383–4401.
- (36) Stavretis, S. E.; Atanasov, M.; Podlesnyak, A. A.; Hunter, S. C.; Neese, F.; Xue, Z.-L. Magnetic Transitions in Iron Porphyrin Halides by Inelastic Neutron Scattering and Ab Initio Studies of Zero-Field Splittings. *Inorg. Chem.* **2015**, *54*, 9790–9801.
- (37) Craig, G. A.; Murrie, M. 3d Single-Ion Magnets. *Chem. Soc. Rev.* **2015**, *44*, 2135–2147.
- (38) Zadrozny, J. M.; Telser, J.; Long, J. R. Slow Magnetic Relaxation in the Tetrahedral Cobalt (II) Complexes $[\text{Co}(\text{EPh})_4]^{2-}$ (E = O, S, Se). *Polyhedron* **2013**, *64*, 209–217.
- (39) Suturina, E. A.; Maganas, D.; Bill, E.; Atanasov, M.; Neese, F. Magneto-Structural Correlations in a Series of Pseudotetrahedral $[\text{Co}^{\text{II}}(\text{XR})_4]^{2-}$ Single Molecule Magnets: An ab Initio Ligand Field Study. *Inorg. Chem.* **2015**, *54*, 9948–9961.
- (40) Collingwood, J. C.; Day, P.; Denning, R. G. Magnetic Circular Dichroism Spectrum of the Tetraiodonickelate(II) Ion. *J. Chem. Soc., Faraday Trans. 2* **1973**, 591–607.
- (41) Atanasov, M.; Rauzy, C.; Baettig, P.; Daul, C. Calculation of Spin-Orbit Coupling within the LFDFT: Applications to $[\text{NiX}_4]^{2-}$ (X = F⁻, Cl⁻, Br⁻, I⁻). *Int. J. Quantum Chem.* **2005**, *102*, 119–131.

- (42) Krzystek, J.; Ozarowski, A.; Telser, J. Multi-Frequency, High-Field EPR as a Powerful Tool to Accurately Determine Zero-Field Splitting in High-Spin Transition Metal Coordination Complexes. *Coord. Chem. Rev.* **2006**, *250*, 2308–2324.
- (43) Desrochers, P. J.; Telser, J.; Zvyagin, S. A.; Ozarowski, A.; Krzystek, J.; Vicic, D. A. Electronic Structure of Four-Coordinate C_{3v} Nickel(II) Scorpionate Complexes: Investigation by High-Frequency and -Field Electron Paramagnetic Resonance and Electronic Absorption Spectroscopies. *Inorg. Chem.* **2006**, *45*, 8930–8941.
- (44) Ye, S.; Neese, F. How Do Heavier Halide Ligands Affect the Signs and Magnitudes of the Zero-Field Splittings in Halogenonickel(II) Scorpionate Complexes? A Theoretical Investigation Coupled to Ligand-Field Analysis. *J. Chem. Theory Comput.* **2012**, *8*, 2344–2351.
- (45) Karunadasa, H. I.; Arquero, K. D.; Berben, L. A.; Long, J. R. Enhancing Magnetic Anisotropy of Cyano-Ligated Chromium(II) and Chromium(III) Complexes via Heavy Halide Ligand Effects. *Inorg. Chem.* **2010**, *49*, 4738–4740.
- (46) Smolko, L.; Černák, J.; Dušek, M.; Miklovič, J.; Titiš, J.; Boča, R. Three Tetracoordinate Co(II) Complexes $[Co(biq)X_2]$ ($X = Cl, Br, I$) with easy-plane magnetic anisotropy as field-induced single-molecule magnets. *Dalton Trans.* **2015**, *44*, 17565–17571.
- (47) Brazzolotto, D.; Gennari, M.; Yu, S.; Pécaut, J.; Rouzières, M.; Clérac, R.; Orio, M.; Duboc, C. An Experimental and Theoretical Investigation on Pentacoordinated Cobalt(III) Complexes with an Intermediate $S = 1$ Spin State: How Halide Ligands Affect their Magnetic Anisotropy. *Chem. Eur. J.* **2016**, *22*, 925–933.

- (48) Smolko, L.; Černák, J.; Kuchár, J.; Rajnák, C.; Titiš, J.; Boča, R. Field-Induced Slow Magnetic Relaxation in Mononuclear Tetracoordinate Cobalt(II) Complexes Containing a Neocuproine Ligand. *Eur. J. Inorg. Chem.* **2017**, 2080–3086.
- (49) Wang, L.; Zlatar, M.; Vlahović, F.; Demeschko, S.; Philouze, C.; Molton, F.; Gennari, M.; Meyer, F.; Duboc, C.; Gruden, M. Experimental and Theoretical Identification of the Origin of Magnetic Anisotropy in Intermediate Spin Fe(III) Complexes. *Chem. Eur. J.* **2018**, *24*, 5091–5094.
- (50) Saber, M. R.; Dunbar, K. M. Ligands Effects on the Magnetic Anisotropy of Tetrahedral Cobalt Complexes. *Chem. Commun.* **2014**, *50*, 12266–12269.
- (51) Christian, J. H.; Brogden, D. W.; Bindra, J. K.; Kinyon, J. S.; van Tol, J.; Wang, J.; Berry, J. F.; Dalal, N. S. Enhancing the Magnetic Anisotropy of Linear Cr(II) Chain Compounds Using Heavy Metal Substitutions. *Inorg. Chem.* **2016**, *55*, 6376–6383.
- (52) Power, P. P. Main-Group Elements as Transition Metals. *Nature* **2010**, *463*, 171–177.
- (53) Pearson, T. J.; Fataftah, M. S.; Freedman, D. E. Enhancement of Magnetic Anisotropy in a Mn–Bi Heterobimetallic Complex. *Chem. Commun.* **2016**, *52*, 11394–11397.
- (54) Azarkh, M.; Penkova, L. V.; Kats, S. V.; Varzatskii, O. A.; Voloshin, Y. Z.; Groenen, E. J. A Mononuclear Mn(II) Pseudoclathrochelate Complex Studied by Multi-Frequency Electron-Paramagnetic-Resonance Spectroscopy. *J. Phys. Chem. Lett.* **2014**, *5*, 886–889.
- (55) Sunatsuki, Y.; Kishima, Y.; Kobayashi, T.; Yamaguchi, T.; Suzuki, T.; Kojima, M.; Krzystek, J.; Sundberg, M. R. A Single Tripodal Ligand Stabilizing Three Different Oxidation States (II, III, and IV) of Manganese. *Chem. Commun.* **2011**, *47*, 9149–9151.

- (56) Pichon, C.; Mialane, P.; Rivière, E.; Blain, G.; Dolbecq, A.; Marrot, J.; Sécheresse, F.; Duboc, C. The Highest D Value for a MnII Ion: Investigation of a Manganese(II) Polyoxometalate Complex by High-Field Electron Paramagnetic Resonance. *Inorg. Chem.* **2007**, *46*, 7710–7712.
- (57) Lomont, J. P.; Nguyen, S. C.; Harris, C. B. Ultrafast Studies of Stannane Activation by Triplet Organometallic Photoproducts. *Organometallics* **2012**, *31*, 3947–3957.
- (58) Lomont, J. P.; Nguyen, S. C.; Harris, C. B. Should External Heavy-Atom Effects be Expected in Transition Metal Complexes? *ChemRxiv* **2018**, DOI: 10.26434/chemrxiv.6987605.
- (59) Petz, W. Transition-Metal Complexes with Derivatives of Divalent Silicon, Germanium, Tin, and Lead as Ligands. *Chem. Rev.* **1986**, *86*, 1019–1047.
- (60) Lappert, M. F.; Rowe, R. S.; The Role of Group 14 Element Carbene Analogues in Transition Metal Chemistry. *Coord. Chem. Rev.* **1990**, *100*, 267–292.
- (61) Fischer, R. A. Weiß, J. Coordination Chemistry of Aluminum, Gallium, and Indium at Transition Metals. *Angew. Chem., Int. Ed.* **1999**, *38*, 2830–2850.
- (62) Braunschweig, H.; Cogswell, P.; Schwab, K. Synthesis, Structure, and Reactivity of Complexes Containing a Transition Metal-Bismuth Bond. *Coord. Chem. Rev.* **2011**, *255*, 101–117.
- (63) Rudd, P. A.; Liu, S.; Gagliardi, L.; Young, V. G., Jr.; Lu, C. C. Metal-Alane Adducts with Zero-Valent Nickel, Cobalt, and Iron. *J. Am. Chem. Soc.* **2011**, *133*, 20724–20727.
- (64) Rudd, P. A.; Planas, N.; Bill, E.; Gagliardi, L.; Lu, C. C. Dinitrogen Activation at Iron and Cobalt Metallaluminatranes. *Eur. J. Inorg. Chem.* **2013**, 3898–3906.

- (65) Cammarota, R. C.; Lu, C. C. Tuning Nickel with Lewis Acidic Group 14 Metalloligands for Catalytic Olefin Hydrogenation. *J. Am. Chem. Soc.* **2015**, *137*, 12486–12489.
- (66) Moore, J. T.; Smith, N. E.; Lu, C. C. Structure and Dynamic NMR Behavior of Rhodium Complexes Supported by Lewis Acidic Group 13 Metallatranes. *Dalton Trans.* **2017**, *46*, 5689–5701.
- (67) Vollmer, M. V.; Xie, J.; Lu, C. C. Stable Dihydrogen Complexes of Cobalt(-1) Suggest an Inverse trans-Influence of Lewis Acidic Group 13 Metalloligands. *J. Am. Chem. Soc.* **2017**, *139*, 6570–6573.
- (68) Cammarota, R. C.; Vollmer, M. V.; Xie, J.; Ye, J.; Linehan, J. C.; Burgess, S. A.; Appel, A. M.; Gagliardi, L.; Lu, C. C. A Bimetallic Nickel-Gallium Complex Catalyzes CO₂ Hydrogenation via the Intermediacy of an Anionic d¹⁰ Nickel Hydride. *J. Am. Chem. Soc.* **2017**, *139*, 14244–14250.
- (69) Vollmer, M. V.; Xie, J.; Cammarota, R. C.; Young, Jr, V. G.; Bill, E.; Gagliardi, L.; Lu, C. C. Formal Nickelate(-1) Complexes Supported by Group 13 Ions. *Angew. Chem., Int. Ed.* **2018**, *57*, 7815–7819.
- (70) Coste, S. C.; Vlasisavljevich, B.; Freedman, D. E. Magnetic Anisotropy from Main-Group Elements: Halides versus Group 14 Elements. *Inorg. Chem.* **2017**, *56*, 8195–8202.
- (71) Maser, L.; Schneider, C.; Vondung, L.; Alig, L.; Langer, R. Quantifying the Donor Strength of Ligand-Stabilized Main Group Fragments. *J. Am. Chem. Soc.* **2019**, *141* (18), 7596–7604.
- (72) Winterhalter, U.; Zsolnai, L.; Kircher, P.; Heinze, K.; Huttner, G. Reductive Activation of Tripod Cobalt Compounds: Oxidative Additions of H-H, P-H, and Sn-H Functions. *Eur. J. Inorg. Chem.* **2001**, 89–103.

- (73) Uehara, K.; Hikichi, S.; Akita, M. Highly Labile Cationic tris-acetonitrile Complexes, $[\text{Tp}^{\text{R}}\text{M}(\text{NCMe})_3]\text{OTf}$ (M = Ni, Co; Tp^{R} : hydrotrispyrazolylborato, R = Ph, Me, and $i\text{Pr}_2$): Versatile Precursors for Tp^{R} -Containing Nickel and Cobalt Complexes. *J. Chem. Soc., Dalton Trans.* **2002**, 3529–3538.
- (74) Whangbo, M.-H.; Gordon, E. E.; Xiang, H.; Koo, H.-J.; Lee, C. Prediction of Spin Orientations in Terms of HOMO-LUMO Interactions Using Spin-Orbit Coupling as a Perturbation. *Acc. Chem. Res.* **2015**, *48*, 3080–3087.
- (75) Cahier, B.; Maurice, R.; Bolvin, H.; Mallah, T.; Guihéry, N. Tools for Predicting the Nature and Magnitude of Magnetic Anisotropy in Transition Metal Complexes: Application to Co(II) Complexes. *Magnetochemistry* **2016**, *2*, 31.
- (76) Kameo, H.; Ishii, S.; Nakazawa, H. Synthesis and Reactivity of Rhodium Complexes Bearing $[\text{E}(\text{o-C}_6\text{H}_4\text{PPh}_2)_3]$ -Type Tetradentate Ligands (E = Si, Ge, and Sn) *Organometallics* **2012**, *31*, 2212–2218.
- (77) Kameo, H.; Ishii, S.; Nakazawa, H. Synthesis of Iridium Complexes Bearing $\{\text{o-Ph}_2\text{P}\text{C}_6\text{H}_4\}_3\text{E}$ type (E = Si, Ge, and Sn) Ligand and Evaluation of Electron Donating Ability of Group 14 Elements E. *Dalton Trans.* **2012**, 41, 8290–8296.
- (78) Figgis, B. N.; Hitchman, M. A. *Ligand Field Theory and its Applications*; Wiley-VCH: New Yor, 2000.
- (79) Telser, J. A Perspective on Applications of Ligand-Field Analysis: Inspiration from Electron Paramagnetic Resonance Spectroscopy of Coordination Complexes of Transition Metal Ions. *J. Braz. Chem. Soc.* **2006**, *17*, 1501–1505.

- (80) Bucinsky, L.; Breza, M.; Malček, M.; Power, D. C.; Hwang, S. J.; Krzystek, J.; Nocera, D. G.; Telser, J. High-Frequency and -Field EPR (HF-EPR) Investigation of a Pseudotetrahedral Cr^{IV} Siloxide Complex and Computational Studies of Related Cr^{IV}L₄ Systems. *Inorg. Chem.* **2019**, *58*, 4907–4920.
- (81) Krzystek, J.; Swenson, D. C.; Zvyagin, S. A.; Smirnov, D.; Ozarowski, A.; Telser, J. Cobalt(II) “Scorpionate” Complexes as Models for Cobalt-Substituted Zinc Enzymes: Electronic Structure Investigation by High-Frequency and -Field Electron Paramagnetic Resonance Spectroscopy. *J. Am. Chem. Soc.* **2010**, *132*, 5241–5253.
- (82) Winterhalter, U.; Zsolnai, L.; Kircher, P.; Heinze, K.; Huttner, G. *Eur. J. Inorg. Chem.* **2001**, *2001*, 89–103.
- (83) Uehara, K.; Hikichi, S.; Akita, M. *J. Chem. Soc., Dalton Trans.* **2002**, 3529–3538.
- (84) Bain, G. A.; Berry, J. F. *J. Chem. Educ.* **2008**, *85*, 532–536.

References for Chapter Four:

- (1) Kahn, O. *Molecular Magnetism*; VCH Publishers Inc. USA, 1993.
- (2) Danovich, D.; Shaik, S. Spin-Orbit Coupling in the Oxidative Activation of H-H by {FeO}⁺. Selection Rules and Reactivity Effects. *J. Am. Chem. Soc.* **1997**, *119* (7), 1773–1786.
- (3) Schröder, D.; Shaik, S.; Schwarz, H. Two-State Reactivity as a New Concept in Organometallic Chemistry. *Acc. Chem. Res.* **2000**, *33* (3), 139–145.
- (4) Poli, R.; Harvey, J. N. Spin forbidden chemical reactions of transition metal compounds. New ideas and new computational challenges. *Chem. Soc. Rev.* **2002**, *32* (1), 1–8.

- (5) Bellows, S. M.; Cundari, T. R.; Holland, P. L. Spin Crossover during α -Hydride Elimination in High-Spin Iron(II)- and Cobalt(II)-Alkyl Complexes. *Organometallics* **2013**, *32* (17), 4741–4751.
- (6) Figgis, B. N.; Hitchman, M. A. *Ligand Field Theory and its Applications*; Wiley-VCH New York, 2000; Vol. 158.
- (7) Chipman, J. A.; Berry, J. F. Paramagnetic Metal–Metal Bonded Heterometallic Complexes. *Chem. Rev.* **2020**, *120* (5), 2409–2447.
- (8) Aullón, G.; Alvarez, S. Oxidation states, atomic charges and orbital populations in transition metal complexes. *Theor. Chem. Acc.* **2009**, *123* (1-2), 67–73.
- (9) Holt, M. S.; Wilson, W. L.; Nelson, J. H. Transition metal-tin chemistry. *Chem. Rev.* **1989**, *89* (1), 11–49.
- (10) Weickgenannt, A.; Oestreich, M. Silicon- and Tin-Based Cuprates: Now Catalytic in Copper! *Chemistry - A European Journal* **2010**, *16* (2), 402–412.
- (11) Das, D.; Mohapatra, S. S.; Roy, S. Recent advances in heterobimetallic catalysis across a metal–tin”motif. *Chem. Soc. Rev.* **2015**, *44* (11), 3666–3690.
- (12) Buchwalter, P.; Rosé, J.; Braunstein, P. Multimetallic Catalysis Based on Heterometallic Complexes and Clusters. *Chem. Rev.* **2014**, *115* (1), 28–126.
- (13) Pereyre, M.; Quintard, J.-P.; Rahm, A. *Tin in Organic Synthesis*; Butterworth-Heinemann, 2013.
- (14) Cao, Y.; Petersen, J. L.; Stolzenberg, A. M. Metalloradical Chemistry of Cobalt(II) Porphyrins. The Syntheses, Structure, and Reactivity of Triphenyltin(II)- and Trihalomethylcobalt(III) Octaethylporphyrin. *Inorg. Chem.* **1998**, *37* (20), 5173–5179.

- (15) Smith, N. D.; Mancuso, J.; Lautens, M. Metal-Catalyzed Hydrostannations. *Chem. Rev.* **2000**, *100* (8), 3257–3282.
- (16) Wang, Z.; Yao, Z.; Lyu, Z.; Xiong, Q.; Wang, B.; Fu, X. Thermodynamic and reactivity studies of a tin corrole–cobalt porphyrin heterobimetallic complex. *Chem. Sci.* **2018**, *9* (22), 4999–5007.
- (17) McSkimming, A.; Harman, W. H. A Terminal N₂ Complex of High-Spin Iron(I) in a Weak, Trigonal Ligand Field. *J. Am. Chem. Soc.* **2015**, *137* (28), 8940–8943.
- (18) Uehara, K.; Hikichi, S.; Akita, M. Highly labile cationic tris-acetonitrile complexes, [TpRM(NCMe)₃OTf] (M = Ni, Co; {TpR}: hydrotrispyrazolylborato, R = Ph, Me and {iPr}₂): versatile precursors for {TpR}-containing nickel and cobalt complexes. *J. Chem. Soc., Dalton Trans.* **2002**, *18*, 3529.
- (19) Coste, S. C.; Pearson, T. J.; Freedman, D. E. Magnetic Anisotropy in Heterobimetallic Complexes. *Inorg. Chem.* **2019**, *58* (18), 11893–11902.
- (20) Cordero, B.; Gómez, V.; Platero-Prats, A. E.; Revés, M.; Echeverría, J.; Cremades, E.; Barragán, F.; Alvarez, S. Covalent radii revisited. *Dalton Trans.* **2008**, *21*, 2832.
- (21) Cotton, F. A.; Murillo, C. A.; Walton, R. A. *Multiple Bonds Between Metal Atoms*; Springer Science & Business Media, 2005.
- (22) Pauling, L.; Kamb, B. A revised set of values of single-bond radii derived from the observed interatomic distances in metals by correction for bond number and resonance energy. *Proc. Natl. Acad. Sci.* **1986**, *83* (11), 3569–3571.
- (23) Petz, W. Transition-metal complexes with derivatives of divalent silicon, germanium, tin, and lead as ligands. *Chem. Rev.* **1986**, *86* (6), 1019–1047.

- (24) Lappert, M. F.; Rowe, R. S. The role of group 14 element carbene analogues in transition metal chemistry. *Coord. Chem. Rev.* **1990**, *100*, 267–292.
- (25) Tereniak, S. J.; Carlson, R. K.; Clouston, L. J.; Young, V. G.; Bill, E.; Maurice, R.; Chen, Y.-S.; Kim, H. J.; Gagliardi, L.; Lu, C. C. Role of the Metal in the Bonding and Properties of Bimetallic Complexes Involving Manganese, Iron, and Cobalt. *J. Am. Chem. Soc.* **2013**, *136* (5), 1842–1855.
- (26) Eisenhart, R. J.; Carlson, R. K.; Clouston, L. J.; Young, V. G.; Chen, Y.-S.; Bill, E.; Gagliardi, L.; Lu, C. C. Influence of Copper Oxidation State on the Bonding and Electronic Structure of Cobalt–Copper Complexes. *Inorg. Chem.* **2015**, *54* (23), 11330–11338.
- (27) Eisenhart, R. J.; Clouston, L. J.; Lu, C. C. Configuring Bonds between First-Row Transition Metals. *Acc. Chem. Res.* **2015**, *48* (11), 2885–2894.
- (28) Vogler, A.; Kunkely, H. Photochemistry of $[MCo_2(CO)_8]$ ($M = Zn, Cd, Hg$) induced by metal to metal charge transfer excitation. *J. Organomet. Chem.* **1988**, *355* (1-3), 1–6.
- (29) Lever, A. P. *Inorganic Electronic Spectroscopy*; Elsevier Science Publishers B. V., 1984.
- (30) Krzystek, J.; Swenson, D. C.; Zvyagin, S. A.; Smirnov, D.; Ozarowski, A.; Telser, J. Cobalt(II) ”Complexes as Models for Cobalt-Substituted Zinc Enzymes: Electronic Structure Investigation by High-Frequency and -Field Electron Paramagnetic Resonance Spectroscopy. *J. Am. Chem. Soc.* **2010**, *132* (14), 5241–5253.
- (31) Scepianiak, J. J.; Harris, T. D.; Vogel, C. S.; Sutter, J.; Meyer, K.; Smith, J. M. Spin Crossover in a Four-Coordinate Iron(II) Complex. *J. Am. Chem. Soc.* **2011**, *133* (11), 3824–3827.
- (32) Creutz, S. E.; Peters, J. C. Spin-State Tuning at Pseudo-tetrahedral d_6 Ions: Spin Crossover in $[BP_3]Fe^{II}-X$ Complexes. *Inorg. Chem.* **2016**, *55* (8), 3894–3906.

- (33) Graham, W. A. Approach to the separation of inductive and mesomeric effects in complexes of the types $\text{LMn}(\text{CO})_5$ and $\text{LMo}(\text{CO})_5$. *Inorg. Chem.* **1968**, *7* (2), 315–321.
- (34) Kameo, H.; Ishii, S.; Nakazawa, H. Synthesis and Reactivity of Rhodium Complexes Bearing $[\text{E}(\text{o-C}_6\text{H}_4\text{PPh}_2)_3]$ -Type Tetradentate Ligands (E = Si, Ge, and Sn). *Organometallics* **2012**, *31* (6), 2212–2218.
- (35) Aldridge, S. Exploitation of a Very Strongly-Donating Sn(II) Ligand: Synthesis of a Homoleptic, Octahedral Ni(IV) Complex. *Angew. Chem. Int. Ed.* **2008**, *47* (13), 2348–2350.
- (36) Fox, M. A.; Marder, T. B.; Wesemann, L. DFT studies of the σ -donor/ π -acceptor properties of $[\text{SnCB}_{10}\text{H}_{11}]^-$ and its relationship to $[\text{SnCl}_3]^-$, CO, PF_3 , $[\text{SnB}_{11}\text{H}_{11}]^{2-}$, $\text{SnC}_2\text{B}_9\text{H}_{11}$, and related $\text{SnC}_2\text{B}_n\text{H}_n^{+2}$ compounds. *Can. J. Chem.* **2009**, *87* (1), 63–71.
- (37) Ye, S.; Neese, F. How Do Heavier Halide Ligands Affect the Signs and Magnitudes of the Zero-Field Splittings in Halogenonickel(II) Scorpionate Complexes? A Theoretical Investigation Coupled to Ligand-Field Analysis. *J. Chem. Theory Comput.* **2012**, *8* (7), 2344–2351.
- (38) Azuah, R. T.; Kneller, L. R.; Qiu, Y.; Tregenna-Piggott, P. L. W.; Brown, C. M.; Copley, J. R. D.; Dimeo, R. M. DAVE: A Comprehensive Software Suite for the Reduction, Visualization, and Analysis of Low Energy Neutron Spectroscopic Data. *J. Res. Nat. Inst. Stand. Technol.* **2009**, *114* (6), 341.
- (39) Desrochers, P. J.; Telser, J.; Zvyagin, S. A.; Ozarowski, A.; Krzystek, J.; Vicic, D. A. Electronic Structure of Four-Coordinate C_3v Nickel(II) Scorpionate Complexes: Investigation by High-Frequency and -Field Electron Paramagnetic Resonance and Electronic Absorption Spectroscopies. *Inorg. Chem.* **2006**, *45* (22), 8930–8941.

- (40) Rose, M. J.; Bellone, D. E.; Bilio, A. J. D.; Gray, H. B. Spectroscopic and magnetic properties of an iodo CoI tripodal phosphine complex. *Dalton Trans.* **2012**, 41 (38), 11788.
- (41) Krzystek, J.; Ozarowski, A.; Zvyagin, S. A.; Telser, J. High Spin Co(I): High-Frequency and -Field EPR Spectroscopy of CoX(PPh₃)₃ (X = Cl, Br). *Inorg. Chem.* **2012**, 51 (9), 4954–4964.
- (42) Freedman, D. E.; Harman, W. H.; Harris, T. D.; Long, G. J.; Chang, C. J.; Long, J. R. Slow Magnetic Relaxation in a High-Spin Iron(II) Complex. *J. Am. Chem. Soc.* **2010**, 132 (4), 1224–1225.
- (43) Harman, W. H.; Harris, T. D.; Freedman, D. E.; Fong, H.; Chang, A.; Rinehart, J. D.; Ozarowski, A.; Sougrati, M. T.; Grandjean, F.; Long, G. J.; Long, J. R.; Chang, C. J. Slow Magnetic Relaxation in a Family of Trigonal Pyramidal Iron(II) Pyrrolide Complexes. *J. Am. Chem. Soc.* **2010**, 132 (51), 18115–18126.
- (44) Pinkowicz, D.; Birk, F. J.; Magott, M.; Schulte, K.; Dunbar, K. R. Systematic Study of Open-Shell Trigonal Pyramidal Transition-Metal Complexes with a Rigid-Ligand Scaffold. *Chem. - Eur. J.* **2017**, 23 (15), 3548–3552.
- (45) Popescu, C. V.; Mock, M. T.; Stoian, S. A.; Dougherty, W. G.; Yap, G. P. A.; Riordan, C. G. A High-Spin Organometallic Fe-S Compound: Structural and Mössbauer Spectroscopic Studies of [Phenyltris((tert-butylthio)methyl)borate]Fe(Me). *Inorg. Chem.* **2009**, 48 (17), 8317–8324.
- (46) Stoll, S.; Schweiger, A. EasySpin, a comprehensive software package for spectral simulation and analysis in EPR. *J. Magn. Reson.* **2006**, 178 (1), 42–55.
- (47) Duboc, C.; Phoeung, T.; Zein, S.; Pécaut, J.; Collomb, M.-N.; Neese, F. Origin of the Zero-Field Splitting in Mononuclear Octahedral Dihalide Mn(II) Complexes: An Investigation by

- Multifrequency High-Field Electron Paramagnetic Resonance and Density Functional Theory. *Inorg. Chem.* **2007**, *46* (12), 4905–4916.
- (48) Duboc, C. Determination and prediction of the magnetic anisotropy of Mn ions. *Chem. Soc. Rev.* **2016**, *45* (21), 5834–5847.
- (49) Jain, V. K.; Lehmann, G. Electron Paramagnetic Resonance of Mn²⁺ in Orthorhombic and Higher Symmetry Crystals. *Phys. Stat. Sol. B* **1990**, *159* (2), 495–544.
- (50) Lee, V. Y.; Sekiguchi, A. *Organometallic Compounds of Low-Coordinate Si, Ge, Sn and Pb: From Phantom Species to Stable Compounds*; John Wiley & Sons, 2011.
- (51) Farges, F.; Linnen, R. L.; Brown, G. E. Redox and Speciation of Tin in Hydrous Silicate Glasses: A Comparison with Nb, Ta, Mo AND W. *Can. Mineral.* **2006**, *44* (3), 795–810.
- (52) Aluri, E. R.; Grosvenor, A. P. An X-ray absorption spectroscopic study of the effect of bond covalency on the electronic structure of Gd₂Ti_{2-x}Sn_xO₇. *Phys. Chem. Chem. Phys.* **2013**, *15* (25), 10477.
- (53) Wang, H.-T.; Srivastava, M. K.; Wu, C.-C.; Hsieh, S.-H.; Wang, Y.-F.; Shao, Y.-C.; Liang, Y.-H.; Du, C.-H.; Chiou, J.-W.; Cheng, C.-M.; Chen, J.-L.; Pao, C.-W.; Lee, J.-F.; Kuo, C. N.; Lue, C. S.; Wu, M.-K.; Pong, W.-F. Electronic and atomic structures of the Sr₃Ir₄Sn₁₃ single crystal: A possible charge density wave material. *Sci. Rep.* **2017**, *7* (1).
- (54) Masai, H.; Ina, T.; Okumura, S.; Mibu, K. Validity of Valence Estimation of Dopants in Glasses using XANES Analysis. *Sci. Rep.* **2018**, *8* (1).
- (55) Moore, C. E. *Ionization Potentials and Limits Derived from the Analyses of Optical Spectra* NSRDS-NBS 34; National Bureau of Standards, Washington DC, 1970.

- (56) Hoffmann, R.; Alvarez, S.; Mealli, C.; Falceto, A.; Cahill, T. J.; Zeng, T.; Manca, G. From Widely Accepted Concepts in Coordination Chemistry to Inverted Ligand Fields. *Chem. Rev.* **2016**, *116* (14), 8173–8192.
- (57) Puerta, D. T.; Cohen, S. M. [(TpMe,Ph)₂Zn₂(H₃O₂)]ClO₄: a new H₃O₂ species relevant to zinc proteinases. *Inorg. Chim. Acta* **2002**, *337*, 459–462.
- (58) McSkimming, A.; Harman, W. H. A Terminal N₂ Complex of High-Spin Iron(I) in a Weak, Trigonal Ligand Field. *J. Am. Chem. Soc.* **2015**, *137* (28), 8940–8943.
- (59) Uehara, K.; Hikichi, S.; Akita, M. Highly labile cationic tris-acetonitrile complexes, [{TpRM}({NCMe})₃]{OTf} (M = Ni, Co; {TpR}: hydrotrispyrazolylborato, R = Ph, Me and {iPr}₂): versatile precursors for {TpR}-containing nickel and cobalt complexes. *J. Chem. Soc., Dalton Trans.* **2002**, No. 18, 3529.
- (60) Abubekrov, M.; Gianetti, T. L.; Kunishita, A.; Arnold, J. Synthesis and characterization of coordinatively unsaturated nickel(ii) and manganese(ii) alkyl complexes supported by the hydrotris(3-phenyl-5-methylpyrazolyl)borate (TpPh,Me) ligand. *Dalton Trans.* **2013**, *42* (29), 10525.
- (61) Coste, S. C.; Pearson, T. J.; Freedman, D. E. Magnetic Anisotropy in Heterobimetallic Complexes. *Inorg. Chem.* **2019**, *58* (18), 11893–11902.
- (62) Bain, G. A.; Berry, J. F. Diamagnetic Corrections and Pascal Constants. *J. Chem. Educ.* **2008**, *85* (4), 532.
- (63) APEX3, v. 2017.3; Bruker Analytical X-ray Systems, Inc.: Madison, WI, 2017.
- (64) Sheldrick, G. M.; SADABS, Version2.03; Bruker Analytical X-ray Systems, Inc.: Madison, WI, 2000.

- (65) Sheldrick, G. M.; SHELXTL, Version 6.12; Bruker Analytical X-ray Systems, Inc.: Madison, WI, 2000.
- (66) Farrugia, L. J. WinGXsuite for small-molecule single-crystal crystallography. *J. Appl. Crystallogr.* **1999**, *32* (4), 837–838.
- (67) Stoll, S.; Schweiger, A. EasySpin, a comprehensive software package for spectral simulation and analysis in EPR. *J. Magn. Reson.* **2006**, *178* (1), 42–55.
- (68) Ravel, B.; Newville, M. ATHENA, ARTEMIS, HEPHAESTUS: Data analysis for X-ray absorption spectroscopy using IFEFFIT. *J. Synchrotron Rad.* **2005**, *12* (4), 537–541.
- (69). TURBOMOLE V6.5 2013, a development of University of Karlsruhe and Forschungszentrum Karlsruhe GmbH, 1989-2007, TURBOMOLE GmbH, since 2007; available from <http://www.turbomole.com>.
- (70) Tao, J.; Perdew, J. P.; Staroverov, V. N.; Scuseria, G. E. Climbing the Density Functional Ladder: Nonempirical Meta-Generalized Gradient Approximation Designed for Molecules and Solids. *Phys. Rev. Lett.* **2003**, *91* (14).
- (71) Staroverov, V. N.; Scuseria, G. E.; Tao, J.; Perdew, J. P. Comparative assessment of a new nonempirical density functional: Molecules and hydrogen-bonded complexes. *J. Chem. Phys.* **2003**, *119* (23), 12129–12137. [Erratum] **2004**, *121*, 11507(E).
- (72) Weigend, F.; Ahlrichs, R. Balanced basis sets of split valence, triple zeta valence and quadruple zeta valence quality for H to Rn: Design and assessment of accuracy. *Phys. Chem. Chem. Phys.* **2005**, *7* (18), 3297.
- (73) Eichkorn, K.; Treutler, O.; Öhm, H.; Häser, M.; Ahlrichs, R. Auxiliary basis sets to approximate Coulomb potentials. *Chem. Phys. Lett.* **1995**, *240* (4), 283–290.

- (74) Eichkorn, K.; Weigend, F.; Treutler, O.; Ahlrichs, R. Auxiliary basis sets for main row atoms and transition metals and their use to approximate Coulomb potentials *Theor. Chem. Acc.*, **1997**, *97*, 119–124.
- (75) Arnim, M. V.; Ahlrichs, R. Performance of parallel TURBOMOLE for density functional calculations. *J. Comput. Chem.* **1998**, *19* (15), 1746–1757.
- (76) Knizia, G. Intrinsic Atomic Orbitals: An Unbiased Bridge between Quantum Theory and Chemical Concepts. *J. Chem. Theory Comput.* **2013**, *9* (11), 4834–4843.
- (77) Mayer, I. Charge, bond order and valence in the AB initio SCF theory. *Chem. Phys. Lett.* **1983**, *97* (3), 270–274.
- (78) Lu, T.; Chen, F. Multiwfn: A multifunctional wavefunction analyzer. *J. Comput. Chem.* **2011**, *33* (5), 580–592.
- (79) Roos, B. O.; Taylor, P. R.; Sigbahn, P. E. M. A complete active space SCF method (CASSCF) using a density matrix formulated super-CI approach. *Chem. Phys.* **1980**, *48* (2), 157–173.
- (80) Andersson, K.; Malmqvist, P. A.; Roos, B. O.; Sadlej, A. J.; Wolinski, K. Second-order perturbation theory with a CASSCF reference function. *J. Phys. Chem.* **1990**, *94* (14), 5483–5488.
- (81) Andersson, K.; Malmqvist, P.-Å.; Roos, B. O. Second-order perturbation theory with a complete active space self-consistent field reference function. *J. Chem. Phys.* **1992**, *96* (2), 1218–1226.
- (82) Aquilante, F.; Autschbach, J.; Carlson, R. K.; Chibotaru, L. F.; Delcey, M. G.; Vico, L. D.; Galván, I. F.; Ferré, N.; Frutos, L. M.; Gagliardi, L.; Garavelli, M.; Giussani, A.; Hoyer, C. E.; Manni, G. L.; Lischka, H.; Ma, D.; Malmqvist, P. Å.; Müller, T.; Nenov, A.; Olivucci, M.;

- Pedersen, T. B.; Peng, D.; Plasser, F.; Pritchard, B.; Reiher, M.; Rivalta, I.; Schapiro, I.; Segarra-Martí, J.; Stenrup, M.; Truhlar, D. G.; Ungur, L.; Valentini, A.; Vancoillie, S.; Veryazov, V.; Vysotskiy, V. P.; Weingart, O.; Zapata, F.; Lindh, R. Molcas8: New capabilities for multiconfigurational quantum chemical calculations across the periodic table. *J. Comput. Chem.* **2015**, *37* (5), 506–541.
- (83) Douglas, M.; Kroll, N. M. Quantum electrodynamical corrections to the fine structure of helium. *Ann. Phys.* **1974**, *82* (1), 89–155.
- (84) Hess, B. A. Relativistic electronic-structure calculations employing a two-component no-pair formalism with external-field projection operators. *Phys. Rev. A* **1986**, *33* (6), 3742–3748.
- (85) Roos, B. O.; Lindh, R.; Malmqvist, P.-Å.; Veryazov, V.; Widmark, P.-O. Main group atoms and dimers studied with a new relativistic ANO basis set. *J. Phys. Chem. A* **2004**, *108* (15), 2851–2858.
- (86) Roos, B. O.; Lindh, R.; Malmqvist, P.-Å.; Veryazov, V.; Widmark, P.-O. New Relativistic ANO Basis Sets for Transition Metal Atoms. *J. Phys. Chem. A* **2005**, *109* (29), 6575–6579.
- (87) Aquilante, F.; Pedersen, T. B.; Lindh, R. Low-cost evaluation of the exchange Fock matrix from Cholesky and density fitting representations of the electron repulsion integrals. *J. Chem. Phys.* **2007**, *126* (19), 194106.
- (32) Scepaniak, J. J.; Harris, T. D.; Vogel, C. S.; Sutter, J.; Meyer, K.; Smith, J. M. Spin Crossover in a Four-Coordinate Iron(II) Complex. *J. Am. Chem. Soc.* **2011**, *133* (11), 3824–3827.
- (33) Creutz, S. E.; Peters, J. C. Spin-State Tuning at Pseudo-tetrahedral d6 Ions: Spin Crossover in [BP₃]Fe(II)–X Complexes. *Inorg. Chem.* **2016**, *55* (8), 3894–3906.

- (34) Poller, R. C.; Ruddick, J. N. R. Mössbauer spectra of organotin compounds. *J. Organomet. Chem.* **1972**, *39* (1), 121–128.

References for Chapter Five

- (1) Nielsen, M. A.; Chuang, I. L. Quantum computation and quantum information. *Phys. Today* **2001**, *54* (2), 60.
- (2) Feynman, R. P. Simulating physics with computers. *Int. J. Theor. Phys* **1982**, *21* (6/7).
- (3) Leuenberger, M. N.; Loss, D. Quantum computing in molecular magnets. *Nature* **2001**, *410* (6830), 789–793.
- (4) Graham, M. J.; Zadrozny, J. M.; Fataftah, M. S.; Freedman, D. E. Forging Solid-State Qubit Design Principles in a Molecular Furnace. *Chem. Mater.* **2017**, *29* (5), 1885–1897.
- (5) Aromí, G.; Aguilà, D.; Gamez, P.; Luis, F.; Roubeau, O. Design of magnetic coordination complexes for quantum computing. *Chem. Soc. Rev.* **2012**, *41* (2), 537–546.
- (6) Troiani, F.; Affronte, M. Molecular spins for quantum information technologies. *Chem. Soc. Rev.* **2011**, *40* (6), 3119.
- (7) Stamp, P. C. E.; Gaita-Ariño, A. Spin-based quantum computers made by chemistry: hows and whys. *J. Mater. Chem.* **2009**, *19* (12), 1718–1730.
- (8) Stanwix, P. L.; Pham, L. M.; Maze, J. R.; Sage, D. L.; Yeung, T. K.; Cappellaro, P.; Hemmer, P. R.; Yacoby, A.; Lukin, M. D.; Walsworth, R. L. Coherence of nitrogen-vacancy electronic spin ensembles in diamond. *Phys. Rev. B* **2010**, *82* (20).
- (9) Takahashi, S.; Hanson, R.; van Tol, J.; Sherwin, M. S.; Awschalom, D. D. Quenching Spin Decoherence in Diamond through Spin Bath Polarization. *Phys. Rev. Lett.* **2008**, *101* (4).

- (10) Pla, J. J.; Tan, K. Y.; Dehollain, J. P.; Lim, W. H.; Morton, J. J. L.; Jamieson, D. N.; Dzurak, A. S.; Morello, A. A single-atom electron spin qubit in silicon. *Nature* **2012**, *489* (7417), 541–545.
- (11) Wedge, C. J.; Timco, G. A.; Spielberg, E. T.; George, R. E.; Tuna, F.; Rigby, S.; McInnes, E. J. L.; Winpenny, R. E. P.; Blundell, S. J.; Ardavan, A. Chemical Engineering of Molecular Qubits. *Phys. Rev. Lett.* **2012**, *108* (10).
- (12) Morita, Y.; Suzuki, S.; Sato, K.; Takui, T. Synthetic organic spin chemistry for structurally well-defined open-shell graphene fragments. *Nat. Chem.* **2011**, *3* (3), 197.
- (13) Zadrozny, J. M.; Niklas, J.; Poluektov, O. G.; Freedman, D. E. Millisecond Coherence Time in a Tunable Molecular Electronic Spin Qubit. *ACS Cent. Sci.* **2015**, *1* (9), 488–492.
- (14) Bader, K.; Dengler, D.; Lenz, S.; Endeward, B.; Jiang, S.-D.; Neugebauer, P.; van Slageren, J. Room temperature quantum coherence in a potential molecular qubit. *Nat. Commun.* **2014**, *5* (1).
- (15) Morton, J. J. L.; Tyryshkin, A. M.; Ardavan, A.; Porfyrakis, K.; Lyon, S. A.; Briggs, G. A. D. Electron spin relaxation of N@C₆₀ in CS₂. *J. Chem. Phys.* **2006**, *124* (1), 14508.
- (16) Shiddiq, M.; Komijani, D.; Duan, Y.; Gaita-Ariño, A.; Coronado, E.; Hill, S. Enhancing coherence in molecular spin qubits via atomic clock transitions. *Nature* **2016**, *531* (7594), 348–351.
- (17) Godfrin, C.; Ferhat, A.; Ballou, R.; Klyatskaya, S.; Ruben, M.; Wernsdorfer, W.; Balestro, F. Operating Quantum States in Single Magnetic Molecules: Implementation of Grover's Quantum Algorithm. *Phys. Rev. Lett.* **2017**, *119* (18).

- (18) Moreno-Pineda, E.; Godfrin, C.; Balestro, F.; Wernsdorfer, W.; Ruben, M. Molecular spin qubits for quantum algorithms. *Chem. Soc. Rev.* **2018**, *47* (2), 501–513.
- (19) Mehring, M.; Mende, J.; Scherer, W. Entanglement between an Electron and a Nuclear Spin. *Phys. Rev. Lett.* **2003**, *90* (15).
- (20) Nakazawa, S.; Nishida, S.; Ise, T.; Yoshino, T.; Mori, N.; Rahimi, R. D.; Sato, K.; Morita, Y.; Toyota, K.; Shiomi, D.; Kitagawa, M.; Hara, H.; Carl, P.; Höfer, P.; Takui, T. A Synthetic Two-Spin Quantum Bit: g-Engineered Exchange-Coupled Biradical Designed for Controlled-NOT Gate Operations. *Angew. Chem. Int. Ed.* **2012**, *124* (39), 9998–10002.
- (21) Yamamoto, S.; Nakazawa, S.; Sugisaki, K.; Sato, K.; Toyota, K.; Shiomi, D.; Takui, T. Adiabatic quantum computing with spin qubits hosted by molecules. *Phys. Chem. Chem. Phys.* **2015**, *17* (4), 2742–2749.
- (22) Tesi, L.; Lucaccini, E.; Cimatti, I.; Perfetti, M.; Mannini, M.; Atzori, M.; Morra, E.; Chiesa, M.; Caneschi, A.; Sorace, L.; Sessoli, R. Quantum coherence in a processable vanadyl complex: new tools for the search of molecular spin qubits. *Chem. Sci.* **2016**, *7* (3), 2074–2083.
- (23) Atzori, M.; Morra, E.; Tesi, L.; Albino, A.; Chiesa, M.; Sorace, L.; Sessoli, R. Quantum Coherence Times Enhancement in Vanadium(IV)-based Potential Molecular Qubits: the Key Role of the Vanadyl Moiety. *J. Am. Chem. Soc.* **2016**, *138* (35), 11234–11244.
- (24) Frisch, J. Notitia coerulei Berolinensis nuper inventi. *Miscellanea Berolinensia ad incrementum Scientiorum* **1710**, *1710* (1), 377–378.
- (25) Dunbar, K. R.; Heintz, R. A. Chemistry of transition metal cyanide compounds: Modern perspectives. *Prog. Inorg. Chem.* **1997**, *45*, 283–392.

- (26) Birk, F. J.; Pinkowicz, D.; Dunbar, K. R. The Heptacyanotungstate(IV) Anion: A New 50.167emd Transition-Metal Member of the Rare Heptacyanometallate Family of Anions. *Angew. Chem.* **2016**, *128* (38), 11540–11543.
- (27) Qian, K.; Huang, X.-C.; Zhou, C.; You, X.-Z.; Wang, X.-Y.; Dunbar, K. R. A Single-Molecule Magnet Based on Heptacyanomolybdate with the Highest Energy Barrier for a Cyanide Compound. *J. Am. Chem. Soc.* **2013**, *135* (36), 13302–13305.
- (28) Pinkowicz, D.; Southerland, H. I.; Avendaño, C.; Prosvirin, A.; Sanders, C.; Wernsdorfer, W.; Pedersen, K. S.; Dreiser, J.; Clérac, R.; Nehr Korn, J.; Simeoni, G. G.; Schnegg, A.; Holldack, K.; Dunbar, K. R. Cyanide Single-Molecule Magnets Exhibiting Solvent Dependent Reversible "and "Exchange Bias Behavior. *J. Am. Chem. Soc.* **2015**, *137* (45), 14406–14422.
- (29) Ferlay, S.; Mallah, T.; Ouahès, R.; Veillet, P.; Verdaguer, M. A room-temperature organometallic magnet based on Prussian blue. *Nature* **1995**, *378* (6558), 701–703.
- (30) Ohkoshi, S.-I.; Nakagawa, K.; Tomono, K.; Imoto, K.; Tsunobuchi, Y.; Tokoro, H. High Proton Conductivity in Prussian Blue Analogues and the Interference Effect by Magnetic Ordering. *J. Am. Chem. Soc.* **2010**, *132* (19), 6620–6621.
- (31) Verdaguer, M.; Girolami, G. S. Magnetic Prussian blue analogs. *Magnetism: Molecules to Materials V* **2005**, *5*, 283–346.
- (32) Zadrozny, J. M.; Gallagher, A. T.; Harris, T. D.; Freedman, D. E. A Porous Array of Clock Qubits. *J. Am. Chem. Soc.* **2017**, *139* (20), 7089–7094.
- (33) Bok, L. D. C.; Leipoldt, J. G.; Basson, S. S. The preparation of $\text{Cs}_3\text{Mo}(\text{CN})_8 \cdot 2\text{H}_2\text{O}$ and $\text{Cs}_3\text{W}(\text{CN})_8 \cdot 2\text{H}_2\text{O}$. *Z. Anorg. Allg. Chem.* **1975**, *415*, 81–83.

- (34) Wang, Q.-L.; Zhang, Y.-Z.; Southerland, H.; Prosvirin, A. V.; Zhao, H.; Dunbar, K. R. Variations in topology and magnetic properties of hepta- and octacyanometallates of molybdenum with manganese(ii). *Dalton Trans.* **2014**, 43 (18), 6802–6810.
- (35) Zhao, H.; Brown, A. J.; Prosvirin, A. V.; Dunbar, K. R. One-dimensional square- and ladder-type architectures incorporating octacyanometallates of molybdenum(V) and tungsten(V). *Polyhedron* **2013**, 64, 321–327.
- (36) You, Y. S.; Kim, D.; Do, Y.; Oh, S. J.; Hong, C. S. One-Dimensional Octacyanomolybdate-Based Cu(II)-Mo(V) Bimetallic Assembly with a Novel Rope-Ladder Chain Structure. *Inorg. Chem.* **2004**, 43 (22), 6899–6901.
- (37) Ma, S.-L.; Ren, S.; Ma, Y.; Liao, D.-Z.; Yan, S.-P. Three types of heterometallic structural motifs based on $[\text{Mo}(\text{CN})_8]^{3-/4-}$ anion and Mn(II) cation as building blocks. *Struct. Chem.* **2008**, 20 (1), 145–154.
- (38) Nakabayashi, K.; Chorazy, S.; Miyamoto, Y.; Fujimoto, T.; Yazawa, K.; Takahashi, D.; Sieklucka, B.; Ohkoshi, S.-I. High thermal durability of a layered $\text{Cs}_4\text{Co}^{\text{II}}[\text{W}^{\text{V}}(\text{CN})_8]\text{Cl}_3$ framework: crystallographic and ^{133}Cs NMR spectroscopic studies. *CrystEngComm* **2016**, 18 (48), 9236–9242.
- (39) Arimoto, Y.; Ohkoshi, S.-I.; Zhong, Z. J.; Seino, H.; Mizobe, Y.; Hashimoto, K. Crystal Structure and Magnetic Properties of Two-dimensional Cyanide-bridged Bimetallic Assembly Composed of $\text{Cs}^{\text{I}}[\text{Mn}^{\text{II}}(3\text{-cyanopyridine})_2\text{W}^{\text{V}}(\text{CN})_8]\text{H}_2\text{O}$. *Chem. Lett.* **2002**, 31 (8), 832–833.
- (40) Nowicka, B.; Rams, M.; Stadnicka, K.; Sieklucka, B. Reversible Guest-Induced Magnetic and Structural Single-Crystal-to-Single-Crystal Transformation in Microporous Coordination Network $\{[\text{Ni}(\text{cyclam})]_3[\text{W}(\{\text{CN}\})_8]_2\}_n$. *Inorg. Chem.* **2007**, 46 (20), 8123–8125.

- (41) McGarvey, B. The Structure of the Octacyanomolybdate (V) and-tungstate (V) Ions from Electron Spin Resonance. *Inorg. Chem.* **1966**, 5 (3), 476–479.
- (42) Hayes, R. G. EPR Studies of the $\text{Mo}(\text{CN})_8^{3-}$ and $\text{W}(\text{CN})_8^{3-}$ Ions. The Geometry of the Ions. *J. of Chem. Phys.* **1966**, 44 (5), 2210–2212.
- (43) Nellutla, S.; Morley, G. W.; van Tol, J.; Pati, M.; Dalal, N. S. Electron spin relaxation and K^{39} pulsed ENDOR studies on Cr^{5+} -doped K_3NbO_8 at 9.7 and 240 GHz. *Phys. Rev. B* **2008**, 78 (5).
- (44) Fielding, A. J.; Fox, S.; Millhauser, G. L.; Chattopadhyay, M.; Kroneck, P. M. H.; Fritz, G.; Eaton, G. R.; Eaton, S. S. Electron spin relaxation of copper(II) complexes in glassy solution between 10 and 120K. *J. Magn. Reson.* **2006**, 179 (1), 92–104.
- (45) Berliner, L. J.; Eaton, S. S.; Eaton, G. R. *Distance Measurements in Biological Systems by EPR*; Springer Science & Business Media, 2006; Vol. 19.
- (46) Abragam, A.; Bleaney, B. *Electron Paramagnetic Resonance of Transition Ions*; OUP Oxford, 2012.
- (47) Escalera-Moreno, L.; Baldoví, J. J.; Gaita-Ariño, A.; Coronado, E. Spin states, vibrations and spin relaxation in molecular nanomagnets and spin qubits: a critical perspective. *Chem. Sci.* **2018**, 9 (13), 3265–3275.
- (48) Escalera-Moreno, L.; Suaud, N.; Gaita-Ariño, A.; Coronado, E. Determining Key Local Vibrations in the Relaxation of Molecular Spin Qubits and Single-Molecule Magnets. *J. Phys. Chem. Lett.* **2017**, 8 (7), 1695–1700.
- (49) Figgis, B. N.; Hitchman, M. A. *Ligand Field Theory and its Applications*; Wiley-VCH New York, 2000; Vol. 158.

- (50) Fielding, A. J.; Fox, S.; Millhauser, G. L.; Chattopadhyay, M.; Kroneck, P. M. H.; Fritz, G.; Eaton, G. R.; Eaton, S. S. Electron spin relaxation of copper(II) complexes in glassy solution between 10 and 120 K. *J. Magn. Reson.* **2006**, *179* (1), 92–104.
- (51) Flanagan, H. L.; Singel, D. J. Analysis of ^{14}N ESEEM patterns of randomly oriented solids. *J. Chem. Phys.* **1987**, *87* (10), 5606–5616.
- (52) Zecevic, A.; Eaton, G. R.; Eaton, S. S.; Lindgren, M. Dephasing of electron spin echoes for nitroxyl radicals in glassy solvents by non-methyl and methyl protons. *Mol. Phys.* **1998**, *95* (6), 1255–1263.
- (53) Eaton, G. R.; Eaton, S. S. Solvent and Temperature Dependence of Spin Echo Dephasing for Chromium(V) and Vanadyl Complexes in Glassy Solution. *J. Magn. Reson.* **1999**, *136* (1), 63–68.
- (54) Graham, M. J.; Yu, C.-J.; Krzyaniak, M. D.; Wasielewski, M. R.; Freedman, D. E. Synthetic Approach To Determine the Effect of Nuclear Spin Distance on Electronic Spin Decoherence. *J. Am. Chem. Soc.* **2017**, *139* (8), 3196–3201.
- (55) Yu, C.-J.; Graham, M. J.; Zadrozny, J. M.; Niklas, J.; Krzyaniak, M. D.; Wasielewski, M. R.; Poluektov, O. G.; Freedman, D. E. Long Coherence Times in Nuclear Spin-Free Vanadyl Qubits. *J. Am. Chem. Soc.* **2016**, *138* (44), 14678–14685.
- (56) Bok, L. D. C.; Leipoldt, J. G.; Basson, S. S. The preparation of $\text{Cs}_3\text{Mo}(\text{CN})_8 \cdot 2\text{H}_2\text{O}$ and $\text{Cs}_3\text{W}(\text{CN})_8 \cdot 2\text{H}_2\text{O}$. *Z. Anorg. Allg. Chem.* **1975**, *415*, 81–83.
- (57) Zadrozny, J. M.; Niklas, J.; Poluektov, O. G.; Freedman, D. E. Millisecond Coherence Time in a Tunable Molecular Electronic Spin Qubit. *ACS Cent. Sci.* **2015**, *1* (9), 488–492.

- (58) Chen, H.; Maryasov, A. G.; Rogozhnikova, O. Y.; Trukhin, D. V.; Tormyshev, V. M.; Bowman, M. K. Electron spin dynamics and spin–lattice relaxation of trityl radicals in frozen solutions. *Phys. Chem. Chem. Phys.* **2016**, *18* (36), 24954–24965.
- (59) Berliner, L. J.; Eaton, S. S.; Eaton, G. R. *Distance Measurements in Biological Systems by EPR*; Springer Science & Business Media, 2006; Vol. 19.
- (60) Flanagan, H. L.; Singel, D. J. Analysis of ^{14}N ESEEM patterns of randomly oriented solids. *J. Chem. Phys.* **1987**, *87* (10), 5606–5616.
- (61) Vennam, P. R.; Fisher, N.; Krzyaniak, M. D.; Kramer, D. M.; Bowman, M. K. A Caged, Destabilized, Free Radical Intermediate in the Q-Cycle. *ChemBioChem* **2013**, *14* (14), 1745–1753.
- (62) Abragam, A.; Bleaney, B. *Electron Paramagnetic Resonance of Transition Ions*; OUP Oxford, 2012.
- (63) Stoll, S.; Schweiger, A. EasySpin, a comprehensive software package for spectral simulation and analysis in EPR. *J. Magn. Reson.* **2006**, *178* (1), 42–55.

References for Chapter Six

- (1) Nielsen, M. A.; Chuang, I.; Grover, L. K. Quantum Computation and Quantum Information. *Am. J. Phys* **2002**, *70* (5), 558–559.
- (2) Feynman, R. P. Simulating physics with computers. *Int. J. Theor. Phys.* **1982**, *21* (6-7), 467–488.
- (3) Devoret, M. H.; Schoelkopf, R. J. Superconducting Circuits for Quantum Information: An Outlook. *Science* **2013**, *339* (6124), 1169–1174.

- (4) Leuenberger, M. N.; Loss, D. Quantum computing in molecular magnets. *Nature* **2001**, *410* (6830), 789–793.
- (5) Pla, J. J.; Tan, K. Y.; Dehollain, J. P.; Lim, W. H.; Morton, J. J. L.; Jamieson, D. N.; Dzurak, A. S.; Morello, A. A single-atom electron spin qubit in silicon. *Nature* **2012**, *489* (7417), 541–545.
- (6) Morita, Y.; Suzuki, S.; Sato, K.; Takui, T. Synthetic organic spin chemistry for structurally well-defined open-shell graphene fragments. *Nat. Chem.* **2011**, *3* (3), 197–204.
- (7) Zadrozny, J. M.; Niklas, J.; Poluektov, O. G.; Freedman, D. E. Millisecond Coherence Time in a Tunable Molecular Electronic Spin Qubit. *ACS Cent. Sci.* **2015**, *1* (9), 488–492.
- (8) Graham, M. J.; Zadrozny, J. M.; Shiddiq, M.; Anderson, J. S.; Fataftah, M. S.; Hill, S.; Freedman, D. E. Influence of Electronic Spin and Spin–Orbit Coupling on Decoherence in Mononuclear Transition Metal Complexes. *J. Am. Chem. Soc.* **2014**, *136* (21), 7623–7626.
- (9) Aromí, G.; Aguilà, D.; Gamez, P.; Luis, F.; Roubeau, O. Design of magnetic coordination complexes for quantum computing. *Chem. Soc. Rev.* **2012**, *41* (2), 537–546.
- (10) Troiani, F.; Affronte, M. Molecular spins for quantum information technologies. *Chem. Soc. Rev.* **2011**, *40*(6), 3119.
- (11) Stamp, P. C. E.; Gaita-Ariño, A. Spin-based quantum computers made by chemistry: hows and whys. *J. Mater. Chem.* **2009**, *19* (12), 1718–1730.
- (12) Doherty, M. W.; Manson, N. B.; Delaney, P.; Jelezko, F.; Wrachtrup, J.; Hollenberg, L. C. L. The nitrogen-vacancy colour centre in diamond. *Phys. Rep.* **2013**, *528* (1), 1–45.

- (13) Koehl, W. F.; Buckley, B. B.; Heremans, F. J.; Calusine, G.; Awschalom, D. D. Room temperature coherent control of defect spin qubits in silicon carbide. *Nature* **2011**, *479* (7371), 84–87.
- (14) Widmann, M.; Lee, S.-Y.; Rendler, T.; Son, N. T.; Fedder, H.; Paik, S.; Yang, L.-P.; Zhao, N.; Yang, S.; Booker, I.; Denisenko, A.; Jamali, M.; Momenzadeh, S. A.; Gerhardt, I.; Ohshima, T.; Gali, A.; Janzén, E.; Wrachtrup, J. Coherent control of single spins in silicon carbide at room temperature. *Nat. Mater.* **2014**, *14*(2), 164–168.
- (15) Christle, D. J.; Falk, A. L.; Andrich, P.; Klimov, P. V.; Hassan, J. U.; Son, N. T.; Janzén, E.; Ohshima, T.; Awschalom, D. D. Isolated electron spins in silicon carbide with millisecond coherence times. *Nat. Mater.* **2014**, *14* (2), 160–163.
- (16) Nellutla, S.; Morley, G. W.; van Tol, J.; Pati, M.; Dalal, N. S. Electron spin relaxation and K^{39} pulsed ENDOR studies on Cr^{5+} -doped K_3NbO_8 at 9.7 and 240 GHz. *Phys. Rev. B* **2008**, *78* (5).
- (17) Shiddiq, M.; Komijani, D.; Duan, Y.; Gaita-Ariño, A.; Coronado, E.; Hill, S. Enhancing coherence in molecular spin qubits via atomic clock transitions. *Nature* **2016**, *531* (7594), 348–351.
- (18) Bader, K.; Dengler, D.; Lenz, S.; Endeward, B.; Jiang, S.-D.; Neugebauer, P.; van Slageren, J. Room temperature quantum coherence in a potential molecular qubit. *Nat. Commun.* **2014**, *5* (1).
- (19) Morton, J. J. L.; Tyryshkin, A. M.; Ardavan, A.; Porfyrakis, K.; Lyon, S. A.; Briggs, G. A. D. Electron spin relaxation of $N@C_{60}$ in CS_2 . *J. Chem. Phys.* **2006**, *124* (1), 14508.

- (20) Takahashi, S.; Hanson, R.; van Tol, J.; Sherwin, M. S.; Awschalom, D. D. Quenching Spin Decoherence in Diamond through Spin Bath Polarization. *Phys. Rev. Lett.* **2008**, *101* (4).
- (21) Stanwix, P. L.; Pham, L. M.; Maze, J. R.; Sage, D. L.; Yeung, T. K.; Cappellaro, P.; Hemmer, P. R.; Yacoby, A.; Lukin, M. D.; Walsworth, R. L. Coherence of nitrogen-vacancy electronic spin ensembles in diamond. *Phys. Rev. B* **2010**, *82* (20).
- (22) Bertaina, S.; Gambarelli, S.; Tkachuk, A.; Kurkin, I. N.; Malkin, B.; Stepanov, A.; Barbara, B. Rare-earth solid-state qubits. *Nat. Nanotechnol.* **2007**, *2* (1), 39–42.
- (23) Pearson, T. J.; Laorenza, D. W.; Krzyaniak, M. D.; Wasielewski, M. R.; Freedman, D. E. Octacyanometallate qubit candidates. *Dalton Trans.* **2018**, *47* (34), 11744–11748.
- (24) Tesi, L.; Lucaccini, E.; Cimatti, I.; Perfetti, M.; Mannini, M.; Atzori, M.; Morra, E.; Chiesa, M.; Caneschi, A.; Sorace, L.; Sessoli, R. Quantum coherence in a processable vanadyl complex: new tools for the search of molecular spin qubits. *Chem. Sci.* **2016**, *7* (3), 2074–2083.
- (25) Atzori, M.; Benci, S.; Morra, E.; Tesi, L.; Chiesa, M.; Torre, R.; Sorace, L.; Sessoli, R. Structural Effects on the Spin Dynamics of Potential Molecular Qubits. *Inorg. Chem.* **2017**, *57* (2), 731–740.
- (26) Bar-Gill, N.; Pham, L. M.; Belthangady, C.; Sage, D. L.; Cappellaro, P.; Maze, J. R.; Lukin, M. D.; Yacoby, A.; Walsworth, R. Suppression of spin-bath dynamics for improved coherence of multi-spin-qubit systems. *Nat. Commun.* **2012**, *3* (1).
- (27) de Lange, G.; Wang, Z. H.; Riste, D.; Dobrovitski, V. V.; Hanson, R. Universal Dynamical Decoupling of a Single Solid-State Spin from a Spin Bath. *Science* **2010**, *330* (6000), 60–63.

- (28) Naydenov, B.; Dolde, F.; Hall, L. T.; Shin, C.; Fedder, H.; Hollenberg, L. C. L.; Jelezko, F.; Wrachtrup, J. Dynamical decoupling of a single-electron spin at room temperature. *Phys. Rev. B* **2011**, *83* (8).
- (29) Ryan, C. A.; Hodges, J. S.; Cory, D. G. Robust Decoupling Techniques to Extend Quantum Coherence in Diamond. *Phys. Rev. Lett.* **2010**, *105* (20).
- (30) Gordon, L.; Weber, J. R.; Varley, J. B.; Janotti, A.; Awschalom, D. D.; de Walle, C. G. V. Quantum computing with defects. *MRS Bull.* **2013**, *38* (10), 802–807.
- (31) Day, B. E.; Bley, N. D.; Jones, H. R.; McCullough, R. M.; Eng, H. W.; Porter, S. H.; Woodward, P. M.; Barnes, P. W. Structures of ordered tungsten- or molybdenum-containing quaternary perovskite oxides. *J. Solid State Chem.* **2012**, *185*, 107–116.
- (32) Stoll, S.; Schweiger, A. EasySpin, a comprehensive software package for spectral simulation and analysis in EPR. *J. Magn. Reson.* **2006**, *178* (1), 42–55.
- (33) Lamoreaux, R. H.; Hildenbrand, D. L.; Brewer, L. High-Temperature Vaporization Behavior of Oxides II. Oxides of Be, Mg, Ca, Sr, Ba, B, Al, Ga, In, Tl, Si, Ge, Sn, Pb, Zn, Cd, and Hg. *J. Phys. Chem. Ref. Data* **1987**, *16* (3), 419–443.
- (34) See Supplemental Material at <http://link.aps.org/supplemental/10.1103/PhysRevMaterials.3.125002> for more information on single-crystal characterization, refinement to synchrotron XRPD, and pulse EPR measurements.
- (35) Glazer, A. M. The classification of tilted octahedra in perovskites. *Acta Cryst. B* **1972**, *28* (11), 3384–3392.

- (36) Ramirez, A. P.; Kowach, G. R. Large Low Temperature Specific Heat in the Negative Thermal Expansion Compound ZrW_2O_8 . *Phys. Rev. Lett.* **1998**, *80* (22), 4903–4906.
- (37) Meng, J.; Lin, Q.; Chen, T.; Wei, X.; Li, J.; Zhang, Z. Oxygen vacancy regulation on tungsten oxides with specific exposed facets for enhanced visible-light-driven photocatalytic oxidation. *Nanoscale* **2018**, *10* (6), 2908–2915.
- (38) Salikhov, K. M.; Dzuba, S. A.; Raitsimring, A. M. The theory of electron spin-echo signal decay resulting from dipole-dipole interactions between paramagnetic centers in solids. *J. Magn. Reson.* **1981**, *42* (2), 255–276.
- (39) Eaton, S. S.; Eaton, G. R. Distance Measurements by CW and Pulsed EPR. In *Distance Measurements in Biological Systems by EPR*, series ed. Berliner, L. J., Eaton, G. R., Eaton, S. S.; Distance Measurements in Biological Systems by EPR; Springer US: Boston, MA, 2000.
- (40) Hoffmann, S. K.; Lijewski, S. Phonon spectrum, electron spin-lattice relaxation and spin-phonon coupling of Cu^{2+} ions in BaF_2 crystal. *J. Magn. Reson.* **2015**, *252*, 49–54.
- (41) Balasubramanian, G.; Neumann, P.; Twitchen, D.; Markham, M.; Kolesov, R.; Mizuochi, N.; Isoya, J.; Achard, J.; Beck, J.; Tissler, J.; Jacques, V.; Hemmer, P. R.; Jelezko, F.; Wrachtrup, J. Ultralong spin coherence time in isotopically engineered diamond. *Nat. Mater.* **2009**, *8* (5), 383–387.